DISSERTATION

NON-IONIZING TOMOGRAPHIC IMAGING MODALITIES FOR BEDSIDE LUNG MONITORING

Submitted by

Andre Vieira Pigatto

School of Biomedical Engineering

In partial fulfillment of the requirements

For the Degree of Doctor of Philosophy

Colorado State University

Fort Collins, Colorado

Spring 2023

Doctoral Committee:

Advisor: Jennifer L. Mueller

Jesse Wilson
Marlis Rezende
Zhijie Wang

ABSTRACT

NON-IONIZING TOMOGRAPHIC IMAGING MODALITIES FOR BEDSIDE LUNG MONITORING

The need for an accurate and non-ionizing imaging modality for pulmonary assessment of patients undergoing mechanical ventilation due to respiratory failure has increased due to COVID. The ability to quickly detect the development of pathologies at an early stage is highly desirable and could help reduce the incidence of complications. It is also clear that mechanical ventilation can cause ventilator-induced lung injuries, which can be avoided by adequately optimizing the positive end-expiratory pressure to induce alveolar recruitment while preventing hyperinflation. Here, I will explore two non-ionizing pulmonary imaging systems that could be used as monitoring systems in the intensive care unit: Ultrasound Computed Tomography (USCT) and Electrical Impedance Tomography (EIT).

The most comprehensive part of this research is the development of a Low-Frequency USCT system, which was motivated by recent studies demonstrating that acoustic waves transmitted at frequencies between 10 kHz and 750 kHz penetrate the lungs and may be useful for thoracic imaging. A novel transducer based on Tonpilz was designed, characterized, and calibrated through vibrational, electrical, and acoustic measurements, and a flexible belt that holds up to 32 transducers was constructed. A Verasonics Vantage^{TM} 64 Low-frequency Research Ultrasound system was programmed to collect data by transmitting and receiving signals at frequencies of 125 and 156 kHz. The data collection and processing algorithms were developed in MATLAB, and the system was tested on phantom and vertebrate animal experiments; image reconstructions were conducted using a Time-Of-Flight algorithm. As a secondary study, SMA-1, COVID, and regular patients were imaged and analyzed using EIT technology; these results are shown through journal and conference articles presented in the Appendix A and C of this document.

ACKNOWLEDGEMENTS

I am profoundly grateful for the extraordinary guidance, unwavering support, and unrelenting encouragement provided to me by my advisor, Dr. Jennifer Mueller, during my doctoral studies. Her steadfast commitment to mentorship has been critical in shaping the direction and excellence of this research, and I look forward to further collaborations with her in the future. In addition, I extend my immense appreciation to the members of my dissertation committee, Dr. Jesse Wilson, Dr. Marlis Rezende, and Dr. Zhijie Wang, whose invaluable comments and insightful suggestions were essential in elevating the quality of this work.

I extend my heartfelt gratitude to all my family, especially my parents, Rubens and Haide, and my brother, Daniel. Their unconditional support, understanding, love, and constant encouragement have been my source of strength, motivation, and inspiration throughout my life and this challenging journey. Furthermore, I wish to recognize the substantial aid and assistance given by my friends and colleagues, who have consistently provided me with encouragement, counsel, and backing throughout this expedition. Thank you, all, for being my rock and guiding light.

Finally, I wish to express my sincere appreciation to all the collaborators from Colorado State University's Veterinary Hospital, Children's Hospital Colorado, University of Colorado Anschutz Medical Campus, University of Sao Paulo, Bern University of Applied Sciences, and General Electric Research, whose invaluable contributions and cooperation have been critical to the success of this research. Without their support and assistance, this achievement would not have been possible.

Most of this doctoral research project was supported by Award Number R21EB024683 from the National Institute of Biomedical Imaging and Bioengineering. The content is solely my responsibility and does not necessarily represent the official view of the National Institute of Biomedical Imaging and Bioengineering or the National Institutes of Health.

DEDICATION

To all of those who contributed in any way, shape, or form to make this work possible.

TABLE OF CONTENTS

LIST OF TABLES

LIST OF FIGURES

Chapter 1

Introduction

Diagnostic imaging plays an important role in the detection of pathologies and monitoring the evolution of lung diseases. The current gold standard for lung imaging is Computerized Tomography (CT) and Chest X-Rays (CXR). CT scans provide rich information about the lung structures and have been used to understand several pathophysiological processes that underlie Acute Respiratory Distress Syndrome (ARDS), such as pulmonary edema [7], pleural effusion, pneumothorax, and atelectasis [8]. However, CT has three major disadvantages; the exposure of the patient to high doses of ionizing radiation, the long post-processing time for evaluation of the images by a specialized technician, and the difficulties in transporting critically ill patients from the ICU to the radiology facility [9]. CXR can be an option as a bedside lung imaging tool; however, besides exposing the patient to ionizing radiation, it provides less detailed images than CT scans, which can lead to misdiagnosis [10].

An alternative to CT scans and CXR is ultrasound (US), which has been studied as a thoracic bedside monitoring technology for years [11,12]. However, US waves from conventional handheld scanners do not penetrate the lungs, and thus, the information contained in US images is mostly artifacts instead of the physiological structures themselves [13]. It is important to point out that some of those artifacts carry information about potential pathologies, which spiked interest in exploring US as an option to monitor the progression of the disease and treatment of patients with COVID-19 [14–17]. For example, comet-tail-type artifacts arising from the pleural line (B-lines) could be associated with interstitial lung disease [18], and have been consistently reported in patients with COVID-19 pneumonia, being an indication of its severity [16, 19]. In addition, an indication of recovery could be the presence of A-lines, a horizontal reverberation artifact that occurs beneath the pleural line and is associated with an aerated lung [19].

All of the studies described above were performed using the conventional US imaging mode (B-Mode), which generates sound waves in frequencies of 2 to 10 MHz that propagate through

the tissue up to certain depths and then get reflected back into the probe. The technique produces a greyscale image, of which the pixel brightness is proportional to the amplitude of the logarithmically compressed envelope of echos produced by the interrogated tissues [20]. The caveat of B-Mode US is that it requires skilled technicians to collect the data and interpret the artifacts [21], which can be an obstacle when considering its use in intensive unit care. In addition, the propagation of acoustic waves is more complex and produces much richer information than just their reflection, which motivates the application of tomographic ultrasound for pulmonary imaging, as presented below.

The main contribution of this research was the development of a groundbreaking Low-Frequency USCT system for lung imaging applications. This topic was motivated by the absence of a radiation-free imaging tool for bedside lung monitoring applications and by recent studies that demonstrated that acoustic waves transmitted at frequencies between 10 kHz and 750 kHz penetrate the lungs and may be useful for thoracic imaging. A novel ultrasonic transducer based on Tonpilz was designed to operate on a tomographic configuration, characterized, and calibrated through vibrational, electrical, and acoustic measurements. The innovation of this design when compared to the current literature was the lateral distribution of the tail mass, the curvature of the piston head, and the integration of the stress rod into the piston. These modifications allowed the construction of a transducer that was compact enough to be fitted on a ring array configuration around the chest yet powerful and sensitive enough to transmit and receive signals through the thorax. A flexible belt that holds up to 32 transducers radially distributed and equally spaced was constructed and tested in various scenarios.

A Verasonics Vantage^{TM} 64 Low-frequency Research Ultrasound system was programmed to collect data by transmitting and receiving ultrasonic signals at frequencies of 125 to 156 kHz at one transducer at a time while listening in the remainder of the transducers. The transmitted waveform and other data collection parameters were set through MATLAB. Several datasets were collected and analyzed providing the necessary knowledge to develop the data processing algorithm, which used digital signal processing techniques to prepare the raw data collected with the Verasonics

system for Time-Of-Flight (TOF) reconstructions. In addition, an algorithm that determines the sample's boundary based on a 3D scan or an image was developed and utilized to calculate the transducer positions which were later used, in conjunction with the processed data, to compute TOF sound speed reconstructions. The system's performance was then assessed through several experiments conducted with various in-house made phantoms constructed using a standard mixture of ballistic gel. The experimental results indicated that the novel device was generally able to estimate the location and size of the targets and inhomogeneities of high and low sound speeds. These experiments allowed us to improve even more the data processing algorithms that were later used to process the data collected from vertebrate animals.

The final contribution was the assessment of the effectiveness of low-frequency sound waves for thoracic imaging using the developed USCT device in vertebrate animals. The first test involved collecting data during tidal breathing, which was used to reconstruct a TOF sound speed image showing low sound speed regions similar to the lungs' shape and location in the CT scan obtained after USCT data collection. The cyclic changes in the region's shape over time corresponded with the mechanical ventilator's settings, indicating the device's ability to detect the lungs and breathing changes. The second investigation used data collected during a pneumothorax-inducing protocol, revealing a low sound speed region comparable in size and location to the pneumothorax on the CT scan. The third investigation involved data collected during the pleural effusion protocol, showing high and low sound speed areas corresponding to the fluid and lung regions identified in the CT scan. The findings supported the efficacy of the USCT device for thoracic imaging, with potential applications for further animal and human studies.

Chapter 2

Literature Survey

2.1 Electrical Impedance Tomography (EIT)

Electrical impedance tomography (EIT) is an imaging modality that relies on the injection of small sinusoidal currents through an object and measurement of the voltage that arises on the electrodes attached to the object's boundaries to generate a conductivity or permittivity image [3, 22–25]. It is a safe, non-invasive, non-ionizing imaging modality that can be performed as often as needed. EIT has several applications in different fields of study, such as civil, chemical, electrical, and materials engineering [26], but we are interested in the medical field here. Thoracic imaging can be performed by using the measured data to numerically solve an inverse problem that computes the conductivity distribution in the chest. Since air, blood, muscle, and lung tissue all have different conductivity values, dynamic images of ventilation and perfusion can be formed from the reconstructions. Clinical validation against CT images has shown that EIT is effective for obtaining images of regional ventilation distribution [27–32]. Figure 2.1 shows an example of regional ventilation distribution imaging performed with EIT on a patient with Spinal muscular atrophy 1 (SMA1) disorder.

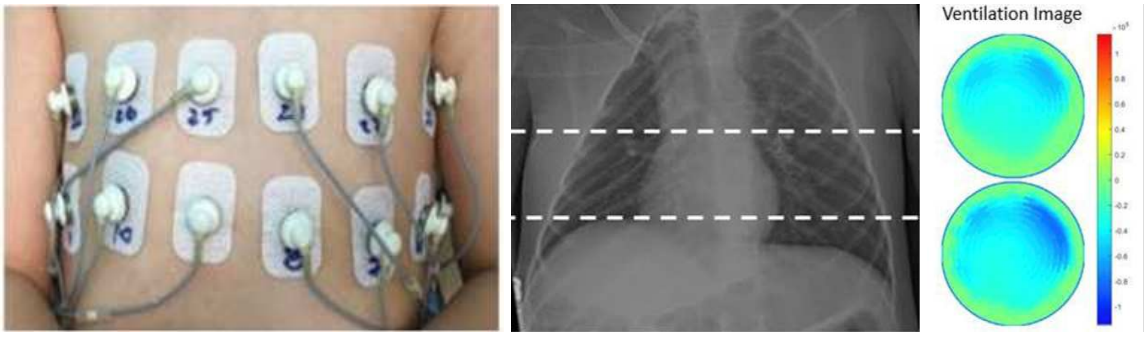

(a) Five-year old patient. **(b)** Chest X-Ray. **(c)** EIT image.

Figure 2.1: SMA-1 patient regional ventilation analysis through EIT imaging (presented in DICOM orientation); figure from [3], provided in Appendix A.

The patient shown in Figure 2.1a was imaged using two rows of 16 pediatric electrodes each, which enabled the reconstruction and volume calculation of two different portions of the lung. When analyzing the chest cross-sectional conductivity reconstruction shown in Figure 2.1c, it is possible to notice a mismatch in ventilation of the left and right lungs; the air volume on the left lung was higher than on the right lung. Those results agree with the chest shape seen on the X-Ray shown in Figure 2.1c, which was collected on the same date as the EIT data, and show that the patient had a conical chest shape and smaller right lung. Regional information used to derive measures of spatial and temporal ventilatory heterogeneity has been used to detect changes in patients with chronic asthma pre- and post-bronchodilator inhalation [33], and cystic fibrosis [34]. Cystic fibrosis patients were also the subjects of studies in which changes in EIT-derived spirometry measures demonstrated a positive correlation with standard spirometry [35, 36], and regions of air trapping were identified using EIT-derived ventilation/perfusion maps [37]. Changes in lung volume using EIT images collected during spirometry have shown excellent correlation with pneumotachograph measurements [38,39]. EIT has also been shown to be effective for monitoring pulsatile pulmonary perfusion [29, 40, 41], which is also relevant for SMA-1 patients because of the ventilation/perfusion mismatch that can result from their respiratory weakness [42]. Moreover, EIT has been used to evaluate changes in ventilation in SMA-1 patients before and after airway clearance [3].

2.2 Ultrasound Computed Tomography (USCT)

Ultrasound computed tomography is a non-ionizing, non-invasive imaging technique that aims to reconstruct a cross-section of an object based on computing its acoustic properties. The process begins by using a set of transducers to transmit sound waves through the object while measuring the reflected and transmitted portions of the signal on the object's boundaries. Next, the collected data is processed and used to estimate the target's regional acoustic characteristics, such as sound speed and attenuation [43–45]. Then, the measurements are used to generate a qualitative image that has the same shape as the object and shows its regional acoustic properties, which directly depend

on the materials that compose it. Therefore, in a controlled environment, where the materials that compose the sample, and their acoustic properties, are known, USCT can be used to determine the boundaries of each material. USCT has several applications, such as the characterization of hydraulic fracture [46], detection of internal defects of concrete [47], and imaging of the flow behavior of fluid foods [48]. However, there are also several applications in the medical field, such as the characterization of biological tissues [49], and the detection and characterization of breast cancer [50–56].

2.2.1 Breast Diagnostics

USCT is a very promising alternative to the traditional mammography diagnostic system using X-rays. Some of the main reasons for choosing ultrasound are that it does not introduce any ionizing radiation to the patient's body and also does not require compression of the breasts, which is deemed painful by most patients. An example of a breast diagnostic USCT system is the SoftVue™ [57], from Delphinus Medical Technologies, Inc, which is shown in Figure 2.2. The system works by suspending the breasts in a water bath while a transducer ring array that sits around the breast, shown in detail in Figure 2.2b, moves up and down while transmitting and receiving ultrasonic signals. The collected data is used to compute a reconstruction of the breast image, and abnormalities can be detected [57].

(a) Full USCT system. **(b)** Transducer ring array detail.

Figure 2.2: SoftVue™ breast imaging system, figures reproduced from [4].

In research, a computer simulation study of breast imaging with USCT in the frequency range of 300 - 500 kHz demonstrated that a spatial resolution of about 2–3 mm can be achieved when operating at the wavelength of about 5 mm, even using a stationary 3D scheme with a few fixed sources and no rotating elements [49], but existing experimental and commercial systems operate above 1 MHz.

2.2.2 Lung Imaging

The application of USCT as a bedside monitoring and diagnostics tool is very attractive since it is radiation-free and less expensive than the current diagnostic methods, such as CT scans and MRIs. In addition, it could provide early detection of common pathologies in acute respiratory distress syndrome patients, such as pneumothorax, pleural effusion, and air trapping [58]. However, all of the equipment available in the market operates in the megahertz frequency range, which poses a problem for pulmonary imaging, as the acoustic waves primarily reflect off of the lung pleura with little to no penetration through the lung tissue. Research [59] has shown that there are three frequency bands in which acoustic signals behave in distinct ways in the human thorax. Between 1 and 10 kHz, transmission is absent. Above 1 MHz, there is also no transmission through healthy lungs. However, there is an efficient frequency range for acoustic transmission between 10 and 750 kHz, with signal attenuation increasing as frequency increases. These properties pose an opportunity for bedside pulmonary monitoring in the ICU using low-frequency ultrasound tomography. Recent studies have found promising results when detecting pneumothorax on simulated low-frequency ultrasonic data implemented using K-wave and reconstructed through the distorted Born iterative method (DBIM) and Tikhonov regularization [1]. Three types of pneumothorax were simulated using trigonometric and single transmission excitation patterns, and the phantoms shown in Figure 2.3, which were developed based on the tissue properties presented in Table 2.1.

Table 2.1: Tissue acoustic properties used by [1] to simulate USCT pneumothorax detection feasibility.

Simulated Organ	Sound speed (m/s)	Attenuation (dB/MHz cm)
Medium	1540	0.002200
Torso	1550	0.01000
Healthy lungs	1440	0.8000
Pneumothorax	1360	1.200
Spine	1640	2.000
Heart	1580	0.2000

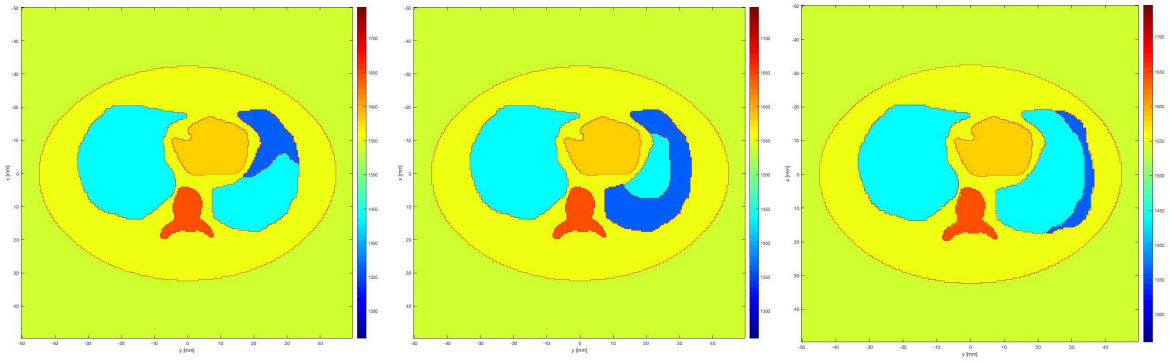

(a) Pneumothorax one. **(b)** Pneumothorax two. **(c)** Pneumothorax three.

Figure 2.3: Phantoms used by [1] to simulate USCT pneumothorax detection feasibility.

As seen in Table 2.1, the author set medium properties that match those of water, whereas the torso has been assigned a slightly higher sound speed but more attenuation, healthy lungs had a higher attenuation and lower sound speed due to their composition (blood and cellular matter) [59]. Moreover, the pneumothorax values were set lower for sound speed and higher for attenuation when compared to healthy lungs since it contains little blood or cellular structure. Finally, the spine and heart were modeled with higher sound speeds and attenuation than the medium. In that

study, the organs were modeled with constant density. Figure 2.4 shows the reconstructions for all of the pneumothoraces using two different transmission patterns.

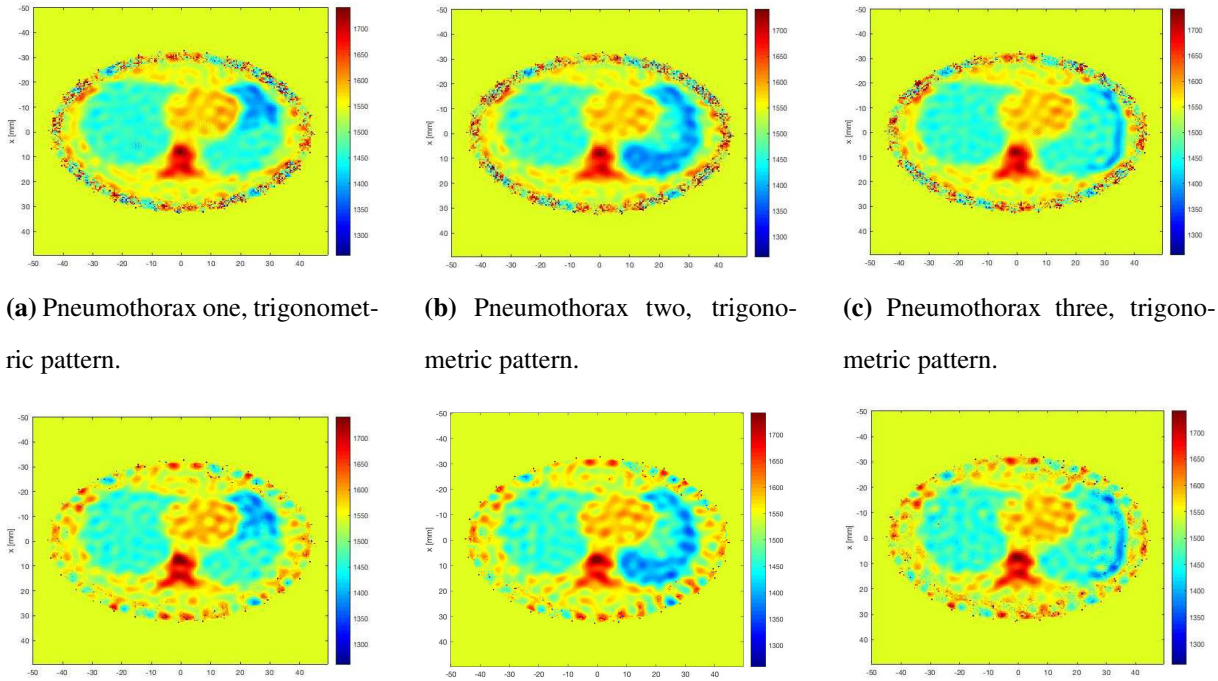

(a) Pneumothorax one, trigonometric pattern.

(b) Pneumothorax two, trigonometric pattern.

(c) Pneumothorax three, trigonometric pattern.

(d) Pneumothorax one, single transmission.

(e) Pneumothorax two, single transmission.

(f) Pneumothorax three, single transmission.

Figure 2.4: Reconstructions computed by [1] when simulating the USCT pneumothorax detection feasibility.

Trigonometric excitation patterns are defined in [1] and are achieved by firing all of the transducers simultaneously while setting the amplitude of the transmitted waveform of each transducer based on a trigonometric function, such as sine and cosine, and the transducer angular position. For example, for a system with 32 transducers, if the transmission pattern was $\cos(\theta)$ and transducer one corresponded to angle $\theta = 0$, it would receive the maximum transmission amplitude (V_{max}). In contrast, transducer 17, of which the angular position would be $\theta = 180°$, would receive -V_{max}, and nine, of which the angular position would be $\theta = 90°$, would receive zero [1]. Single transmission is when only one transducer is fired at a time, with a voltage value common to all transmissions.

When comparing the reconstructions computed with the simulated ultrasonic data, it is seen that the author's method was able to reproduce the organs, tissues, and pathology. For all of the sizes and regions of pneumothoraces, the data simulated based on a trigonometric excitation produced better images than those based on a single transmission. Those differences could result from the higher SNR achieved when all of the transducers are fired at the same time [1]. Another study has shown even better reconstructions by implementing an imaging method that combines Electrical Impedance Tomography (EIT) with USCT [2]. The advantage of using both systems is that the currents injected by the EIT system penetrate the lungs well, whereas USCT provides sharper edge detection but poor internal resolution due to the significant attenuation of the ultrasound waves in the lungs. Combining both methods and using one as a priori information for the reconstruction of the other achieved an overall better image reconstruction. The reconstructions are computed iteratively using D-BAR [60] for EIT, and DBIM for USCT, as follows:

- 1. Compute initial USCT reconstruction.
- 2. Construct an EIT prior based on the USCT reconstruction.
- 3. Compute an EIT reconstruction based on the prior created in the step above.
- 4. Construct a USCT prior based on the EIT image and recompute the USCT reconstruction using the prior.
- 5. Repeat steps 2 - 4 as necessary.

To evaluate the novel method, the author ran simulations using phantoms with pneumothoraces and air trapping regions, shown in Figure 2.5, which were developed based on the tissue properties presented in Table 2.2. It is essential to mention that, unlike USCT, the phantoms used for the EIT reconstructions are developed based on a conductivity map since this technology measures the impedance of the sample instead of the sound speed.

Table 2.2: Tissue acoustic properties used by [2] to simulate USCT and EIT pneumothorax and air trapping detection feasibility.

Simulated Organ	Sound speed (m/s)	Conductivity (S/m)
Medium	1540	N/A
Torso	1540	1.00
Healthy lungs	1440	0.600
Air trapping and pneumothorax	1400	0.250
Spine	1640	0.126
Heart	1560	1.50

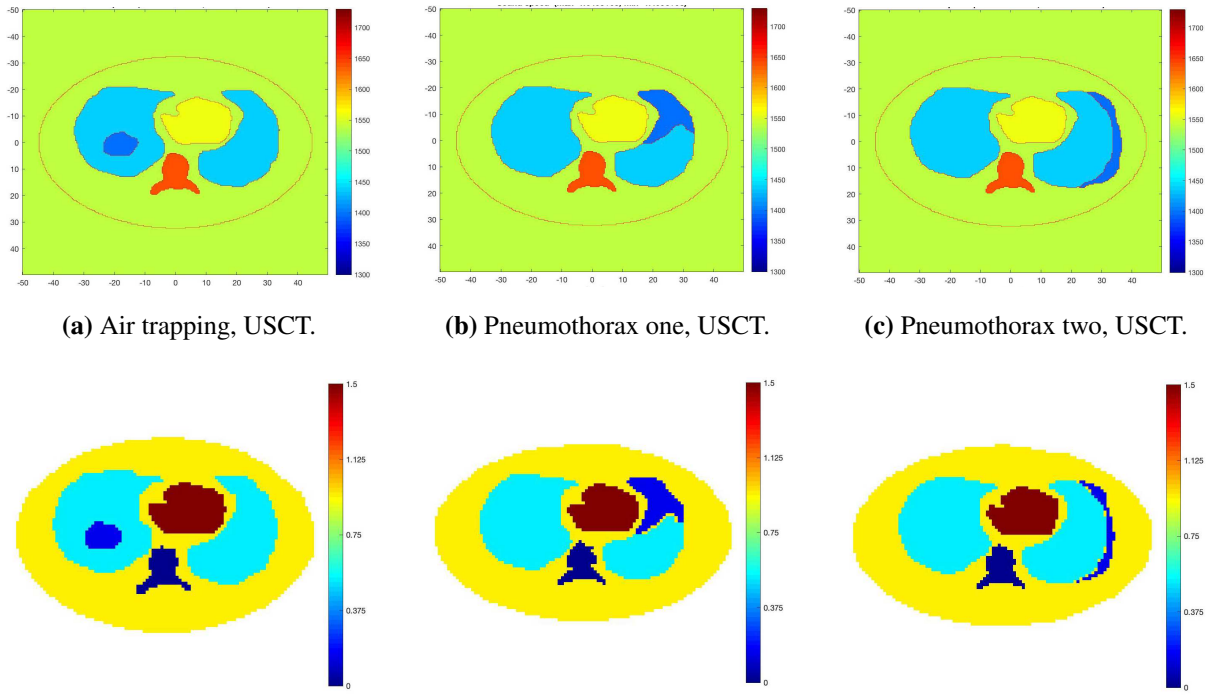

(a) Air trapping, USCT. **(b)** Pneumothorax one, USCT. **(c)** Pneumothorax two, USCT.

(d) Air trapping, EIT. **(e)** Pneumothorax one, EIT. **(f)** Pneumothorax two, EIT.

Figure 2.5: Simulated phantoms used by [2] when simulating the USCT-EIT pneumothorax and air trapping detection feasibility; USCT and EIT phantoms are presented on the top and bottom row, respectively.

From Figure 2.5 it is seen that the organs and tissues from both sound speed and conductivity maps were developed with the same shapes, positions, and boundaries, which would be the equiv-

alent of imaging an object or subject with both pieces of equipment simultaneously. The results achieved by the author when reconstructing the images are shown in Figure 2.6.

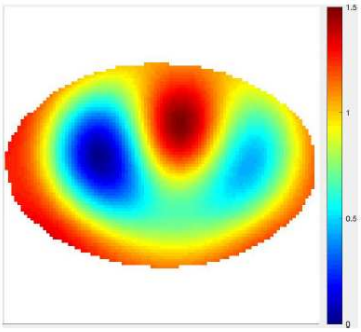

(a) Air trapping: D-Bar EIT recon, no prior.

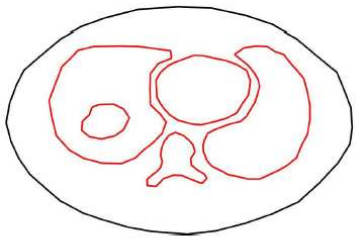

(b) Air trapping: USCT-derived organ boundaries.

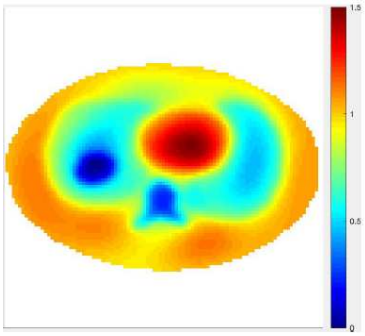

(c) Air trapping: final EIT recon with USCT prior.

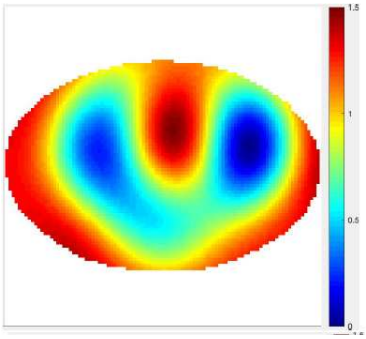

(d) Pneumothorax one: D-Bar EIT recon, no prior.

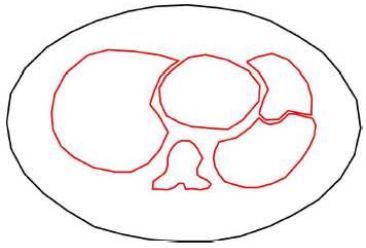

(e) Pneumothorax one: USCT-derived organ boundaries.

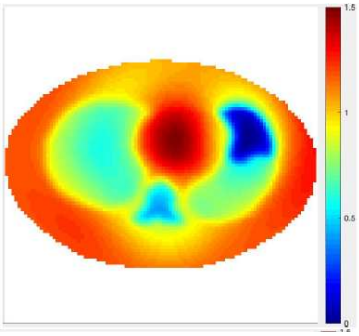

(f) Pneumothorax one: final EIT recon with USCT prior.

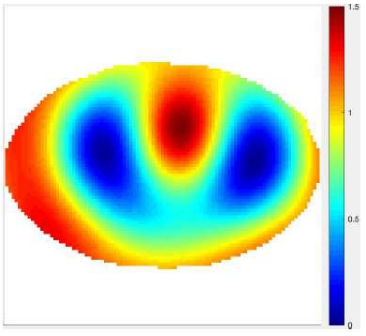

(g) Pneumothorax two: D-Bar EIT recon, no prior.

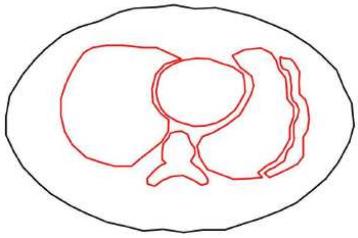

(h) Pneumothorax two: USCT-derived organ boundaries.

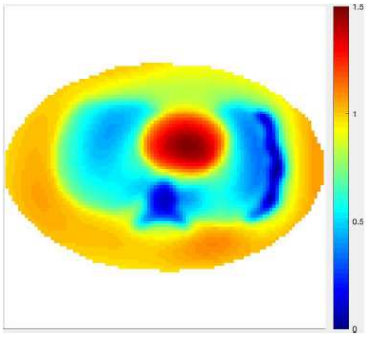

(i) Pneumothorax two: final EIT recon with USCT prior.

Figure 2.6: Reconstructions computed by [2] when simulating the USCT-EIT lung diagnostic feasibility.

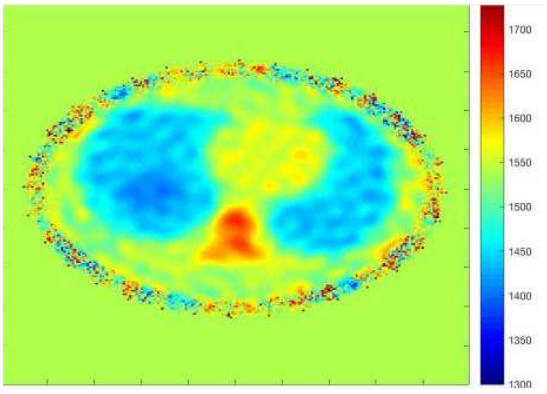

(a) Air trapping: DBIM recon, no prior.

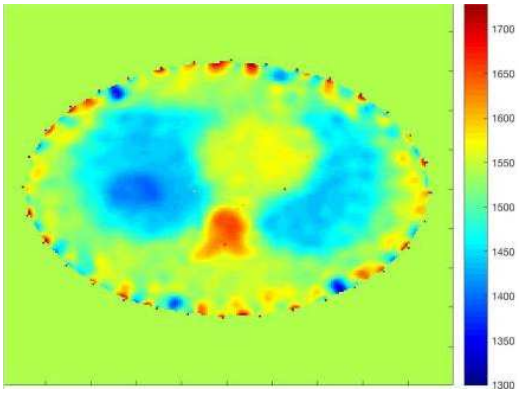

(b) Air trapping: DBIM recon with EIT prior.

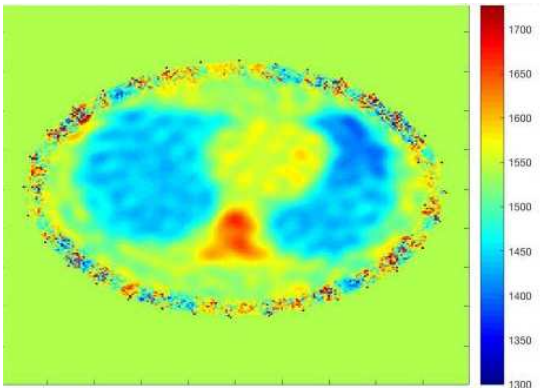

(c) Pneumothorax one: DBIM recon, no prior.

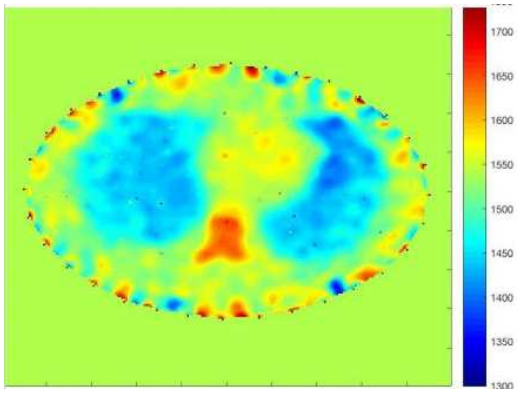

(d) Pneumothorax one: DBIM recon with EIT prior.

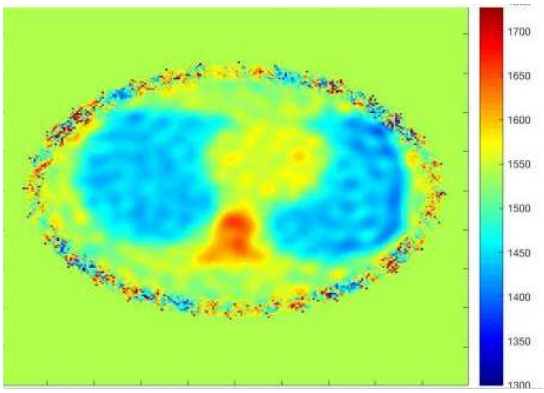

(e) Pneumothorax two: DBIM recon, no prior.

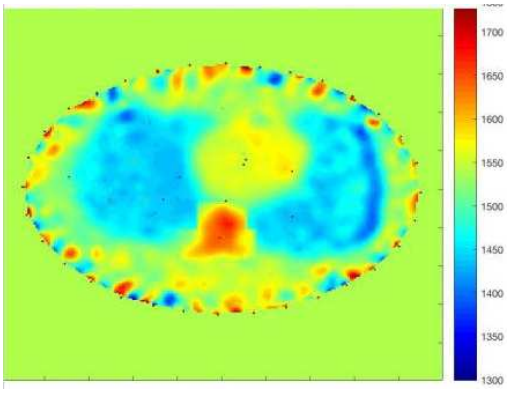

(f) Pneumothorax two: DBIM recon with EIT prior.

Figure 2.7: Reconstructions computed by [2] when simulating the USCT-EIT lung diagnostic feasibility.

When analyzing Figure 2.6, it is clear that the methods complement each other; while EIT was able to detect ventilation, it did not detect the pathologies. As for the USCT reconstructions, the organs' boundaries are clear, but, as shown in the results from the first study (Figure 2.4), their interior content is not as clear as when using the EIT information as prior. Therefore, within the results presented in this chapter, Figures 2.6c, 2.6f, 2.6i, 2.7b, 2.7d, and 2.6i created using the combination of both methods, are the ones that achieved the best overall definition of the organs and pathologies.

So far, it has been shown that low-frequency USCT has great potential when used for lung imaging by itself or in combination with more established methods, such as EIT. However, the low-frequency signal, the thorax's geometry, and the medical ultrasound's safety constraints pose a challenge in transducer design, and commercial transducers are not available for this application. Low-frequency guided waves have been demonstrated to have the potential for complementing dual X-ray absorptiometry in screening for osteoporosis [61], but require separate transducers for transmitting and receiving. A low-frequency transducer design for quantitative cortical bone assessment was proposed in [62] with the main broadband response ranging from about 70 to 110 kHz. A few research studies have shown new designs of low-frequency ultrasound transducers for chronic wound treatment [63], transdermal drug transport [64], and accurate placement of spine screws [65]. However, those transducers are designed for their specific application and would not be suitable for USCT due to their operating frequency range, dimensions, or sensitivity.

2.2.3 Low-Frequency Transducers

One of the goals of this project is to develop a novel version of the Tonpilz design [66] as a solution for low-frequency medical ultrasound tomography. Tonpilz transducers are composed of a stack of piezoelectric materials pressed between a light head and a heavy tail mass [67], and can operate as either a transmitter or receiver, being commonly utilized in underwater sonar applications. The main interest in this constructive topology is that the transducer's resonance frequency can be adjusted based on its design and the masses of its components instead of solely

on the piezoelectric components. Thus, it can generate high power while operating in the low-frequency range (below 500 kHz) [68, 69]. A typical Tonpilz transducer is illustrated in Figure 2.8.

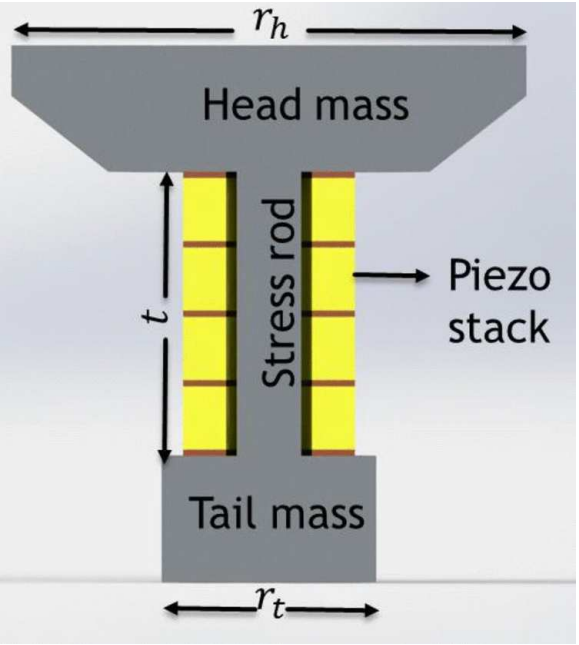

Figure 2.8: Typical Tonpilz transducer illustration from [5].

As seen in the illustration, the tail mass and head mass are connected by a stress rod that ensures that the piezoelectric rings (PZTs) are well compressed, also known as pre-stressed. The PZTs are stacked but separated with a copper ring, which connects them to the signal transmitter or receiver. This illustration is not to scale since the tail mass is typically larger than the head mass since the technique requires the tail mass to be much heavier than the piston. One way of reducing the size of the tail mass is to fabricate the piston with a void space which decreases its weight and enables the use of a smaller tail mass [70]. Previous work on the Tonpilz design includes the use of stacked PZTs to facilitate lower frequency resonant operation than would be possible with a single layer and electrical impedance matching to typical transmission circuitry [71]. An equivalent circuit method was proposed in [72] to analyze the transmitting voltage response spectrum of a planar array of Tonpilz transducers with a center frequency of 100 kHz and then used to improve the design to maximize the bandwidth.

One of the limitations of Tonpilz transducers is that they have a very narrow bandwidth, which can be a problem for certain applications. Thus, a lot of studies explored alternatives to the typical constructive methodology in order to widen the bandwidth, such as using PZTs with different thicknesses [73], adding flexural vibration mode to the piston [74–76], and fabricating the head mass with a void space [74]. With the goal of tomographic thoracic imaging, an understanding of the transducer properties, such as temperature sensitivity, directivity, and acoustic power, is necessary for obtaining optimal performance and assessing the safety of its use. An alternative numerical/analytical method for determining the directivity-dependent receiving sensitivity of general electro-acoustic transducers is presented in [77] and demonstrated on a Tonpilz transducer. A non-resonant design for low-frequency transducers proposed in [78] for disbond detection in the automotive industry and has promise as an alternative to the Tonpilz design presented here if sufficient amplitude could be achieved, which would require further study beyond the results presented in [78].

A second limitation of Tonpilz transducers is that they are oddly shaped and usually fairly long, which is undesirable for a tomographic application. In our design, we developed a more compact transducer by distributing the tail mass laterally, using different materials, and integrating the stress rod into the piston, providing casing and protection to the internal components. We also developed a piston with a curved head to achieve a broader angular dependence than a typical transducer. Through simulations and experiments, we demonstrate that the design and prototype presented here meet design and safety considerations for the application of pulmonary imaging, paving the way for future work in animal studies.

Chapter 3

Proposed USCT Overview

The hardware presented in this work uses a planar ring array of transducers to transmit and receive sound waves at a frequency range of 125 to 156 kHz. The electric signals injected and received from the transducers are generated by a Verasonics Vantage 64 Low-Frequency Research ultrasound system. Figure 3.1 illustrates the main components of the proposed solution.

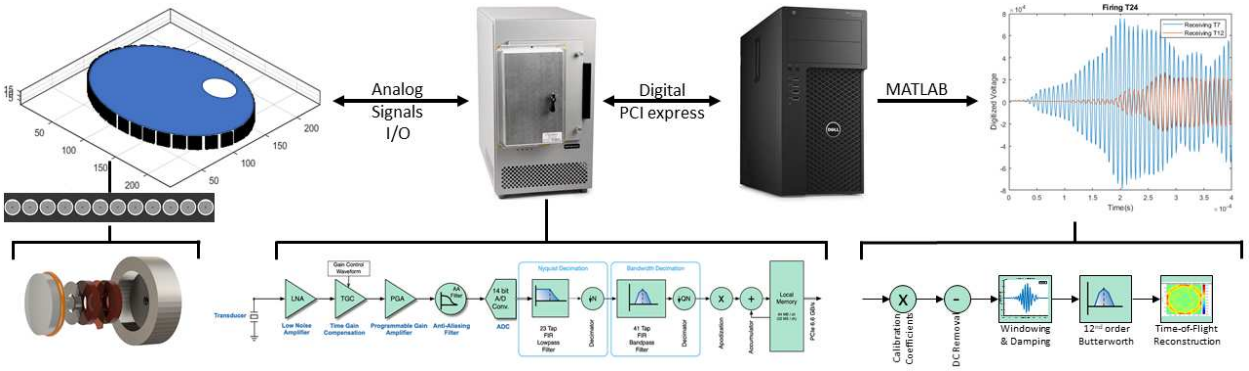

Figure 3.1: Simplified system block diagram.

As seen in Figure 3.1, a belt with up to 32 transducers is attached to the phantom, and the active transducer is fed with an electrical sinusoidal signal generated by the Verasonics System. The wavefront travels through the phantom, reaching the passive transducers on the belt, generating electrical signals with an amplitude proportional to the sound pressure received at the transducer piston. The analog signals are then measured by the Verasonics system, filtered, digitized, and sent to a host computer running MATLAB. The communication between the host computer and the hardware is bidirectional. The host controls all parameters, such as the acquisition frequency, the transmission pattern, and the voltage, through a customized MATLAB script.

The raw digitized signals are then processed and prepared for reconstruction. First, the calibration coefficients corresponding to the transmitting and receiving transducers are applied to the signal. Next, the DC and drifts are removed, the signal is windowed, filtered using a 12^{th} order

Butterworth band-pass filter, and sent to a Time-of-Flight (TOF) reconstruction algorithm, which computes the sound speed in the phantom's domain. The location and size of irregularities are then determined based on regional sound speed. More details of each part of the developed system are shown in Sections 3.1 to 3.7, of which the text and images presented in Section 3.1 were re-purposed from the article attached in Appendix B, which was presented at the 2022 IEEE EMBC Conference, and is available under the DOI: 10.1109/EMBC48229.2022.9872007 or [79].

3.1 Low-Frequency Custom Transducer Design

The transducer design presented in Sections 3.1.1 to 3.1.2 of this document was conducted in collaboration with Ely Mendes Lopes Filho, from the University of São Paulo, São Paulo, Brazil.

The transducer parameters were carefully crafted to achieve specific design objectives. These included the ability to operate within a frequency range of 20 kHz to 750 kHz, while also maintaining a slim profile with an external diameter of 25 mm or less and a thickness of 11 mm or less. These dimensional limitations were strategically imposed to meet the demands of thoracic USCT imaging, which required the placement of two rows of transducers around the chest circumference.

3.1.1 Simulation

Tonpilz transducers are widely used in sonar applications due to their low cost, high acoustic power, and simple structure [80, 81]. A standard Tonpilz transducer is composed of a tail mass, a stack of piezoelectric ceramic rings (PZT) and a head mass that weighs less than half of the tail mass [67, 82]. This design is known for achieving a resonance frequency that no longer depends only on the PZT but on the masses of the parts used in its construction [68,69]. Furthermore, lower working frequencies can be achieved than those found on commercial transducers, motivating an adaptation of the traditional Tonpilz construction method. Therefore, this was the construction methodology adopted in this project; a model of the experimental transducer was developed and analyzed using the Finite Element Method (FEM). A render of the 3D model is found in Figure 3.2.

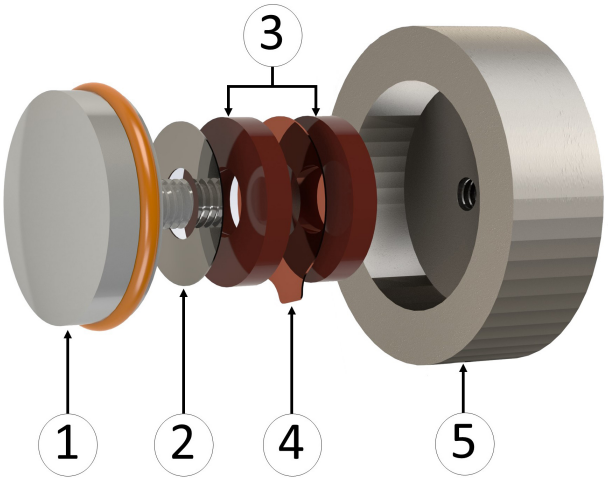

Figure 3.2: Virtual model of the experimental transducer.

As shown in Figure 3.2, the transducer is composed of the tail mass (5), two PZT8 ceramics (3) separated by a thin copper sheet (4), a washer (2) and a piston (1); a silicone rubber o-ring is used to seal the gap between the piston and the housing. A cylindrical spacer (not shown in Figure 3.2) is used to ensure proper alignment of the PZTs and washers by filling the gap between the PZTs and the piston's bolt.

The main constructive novelties, when compared to the standard Tonpilz are the following:

- The tail mass is laterally distributed, providing housing for the ceramics and piston, and reducing the overall transducer thickness.
- The stress rod is integrated into the piston structure, enabling the development of a thinner and lighter piston
- The piston head is curved, increasing the beam divergence, which is essential for the application.

Several characteristics of the transducer were simulated and analyzed through the design process, such as the resonance frequency modes, the directivity, and the mechanical stresses on each part. The final physical dimensions and construction materials were determined iteratively based on the application requirements.

The final virtual transducer design was implemented with a tail mass of external diameter 25 mm, a thickness of 8 mm, and a piston of size 16 mm wide and 10 mm tall. The depth and width of the cavity on the tail mass were set to 5 mm and 17 mm, respectively. The curvature of the surface of the piston head was optimized using FEM simulations. The goal was to obtain the highest total radiated acoustic power and a radiation pattern suitable for the application.

Acoustic Data

To determine the optimal curvature of the piston head, heights (denoted by hini in Figure 3.3) from 0.5 mm to 1.5 mm were primarily evaluated using a step size of 0.1 mm. After the first round of simulations, the range from 0.885 mm to 0.905 mm was examined with a higher resolution (0.05 mm), leading to Figure 3.3.

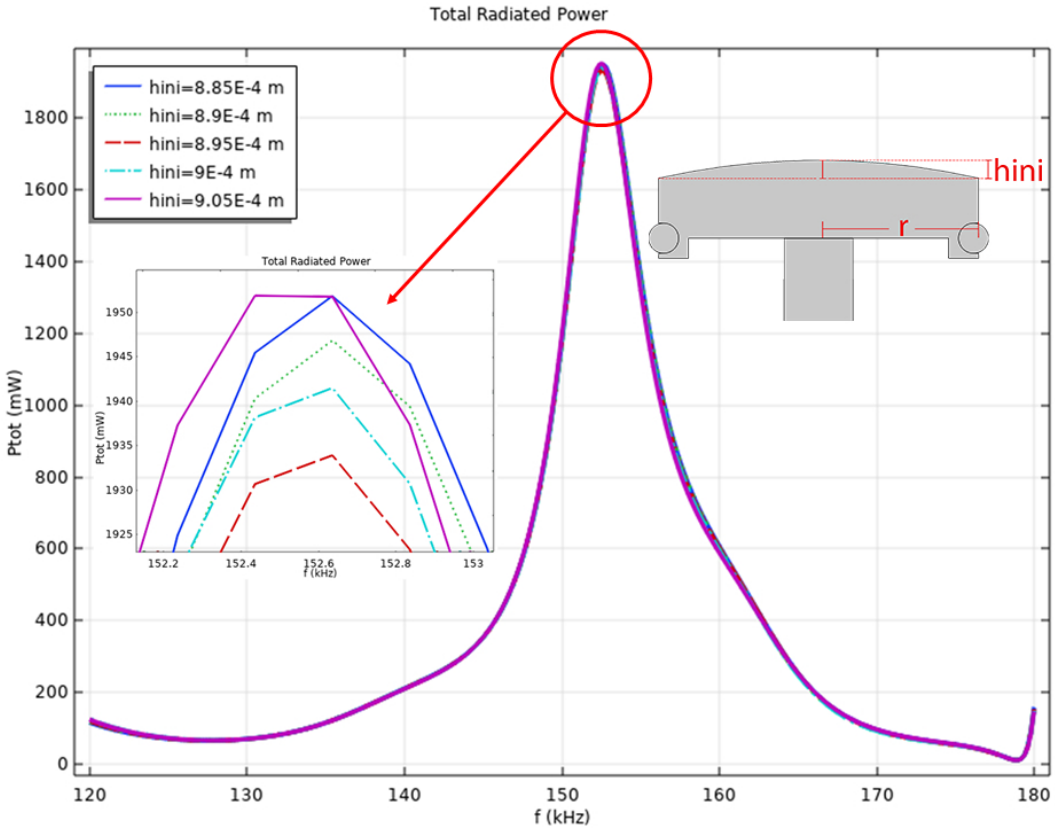

Figure 3.3: Maximum irradiated power for different piston head curvatures.

From Figure 3.3, one sees that the piston head curvature height that results in the highest total radiated power is 0.885 mm. However, through further analysis of the radiation pattern, a curvature height of 0.895 mm was chosen for the final design. Even though that lowers the total radiated power by 18 mW, corresponding to a decrease of approximately 1%, a more desirable radiation pattern was achieved. Moreover, the resonance frequency was found to be 152.6 kHz, and the peak radiated power at that frequency was 1934 mW. The thermal index (TI) that can be achieved when operating at this frequency at maximum power is 1.40 [83], which represents 23% of the maximum value approved by the FDA [84], and, thus, is considered safe.

Figure 3.4 illustrates the transducer's radiation pattern and acoustic pressure map when excited with a sinusoidal source with an amplitude of 84.5 V_{pp} and a frequency of 153 kHz.

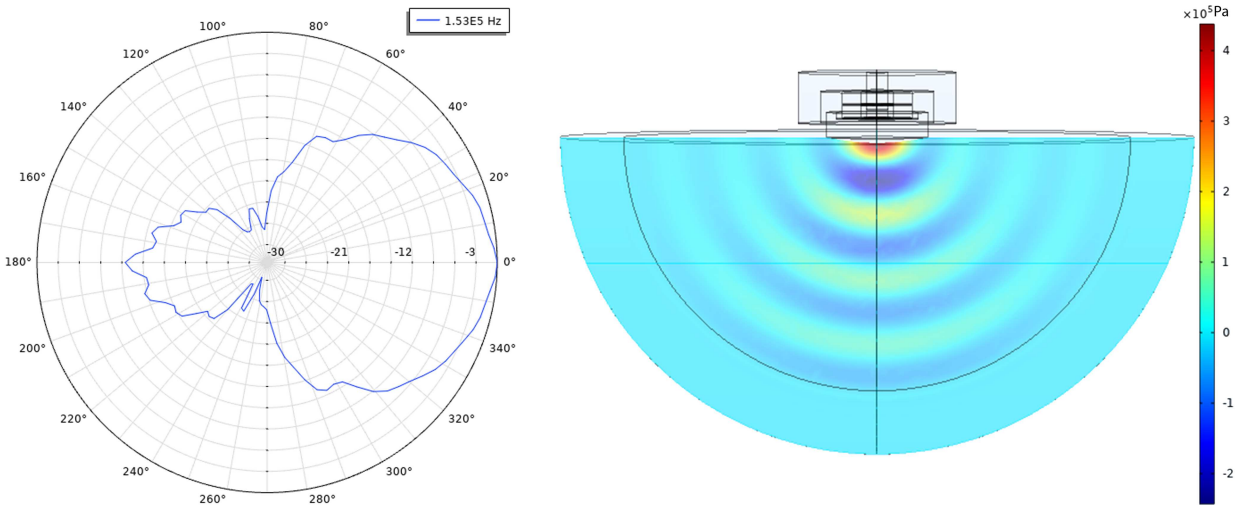

(a) radiation pattern in dB.

(b) acoustic pressure map for a height h of 8.95e-4 m (denoted $hini$ in Figure 3.3) and a frequency of 153 kHz.

Figure 3.4: Acoustic simulations in water

As seen in Figure 3.4 (a), the beam divergence, that is, the angle from the acoustic axis to the point where the acoustic pressure on the far-field has decreased to one-half (-6dB) [85], is 40°. The maximum acoustic pressure achieved was found to be 0.438 MPa. The mechanical index (MI) was introduced by Apfel and Holland in 1991 [86], for the purpose of quantifying the potential for

bio-effects due to transient cavitation. Acoustic cavitation is a concern at this frequency range and has been studied in [87–89]. Maximum acoustic pressure of 0.438 MPa results in a mechanical index of 1.12 using the formula in [86]. The FDA-approved maximum MI for diagnostic imaging is 1.9 [84].

Structural Analysis

To analyze the structural behavior of the transducer, a static and dynamic stress analysis was conducted. The von Mises stress study was determined by applying the maximal voltage to the transducer and a torque of 0.3 N-m is used during its assembly. The results are shown on Figure 3.5.

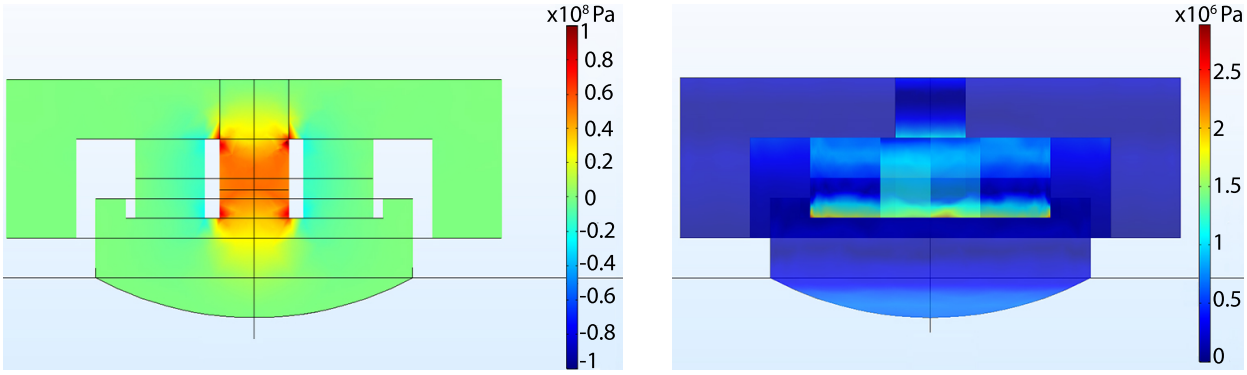

(a) static mechanical stress.

(b) dynamic mechanical stress.

Figure 3.5: Simulated mechanical stresses.

As shown in Figure 3.5 (a), the maximum static stress of 100 MPa occurs on the piston bolt. This static stress is caused by the force necessary to compress the PZTs and internal parts of the transducer and is solely dependent on the manual torque applied to the piston during assembly. In Figure 3.5 (b) one sees that the maximum stress of 2.8 MPa, caused by the vibration of the PZTs, occurs on the piston's rear surface. Therefore, considering that the weakest material has a yield strength of 240 MPa, when both sources of deformation were combined, a safety factor of 2.33 was achieved. Furthermore, different tightening torques were simulated, and the results have

shown that the application of a torque larger than 0.3 Nm did not improve the transducers' acoustic characteristics.

3.1.2 Fabrication

After determining the optimal dimensions and materials through computational analysis, the transducer parts were fabricated with the aid of a milling machine with a tolerance of ±0.001". The tail mass was built using 304 stainless steel, the washer was manufactured on stainless steel 301, and the piston was machined in 6061 T6 aluminum. The application of different materials to the tail mass and piston increases the disparity between these two masses and ensures that the highest fraction of the displacement generated by the PZTs is transferred to the piston and not to the tail mass. Both the tail mass and piston are connected to the electric ground, while the internal copper sheet supplies the excitation signal to the PZTs, ensuring a safe operation. The cable that connects the transducer to the UST system was built using an RG-316 shielded cable and a male SMT terminal as shown in Figure 3.6.

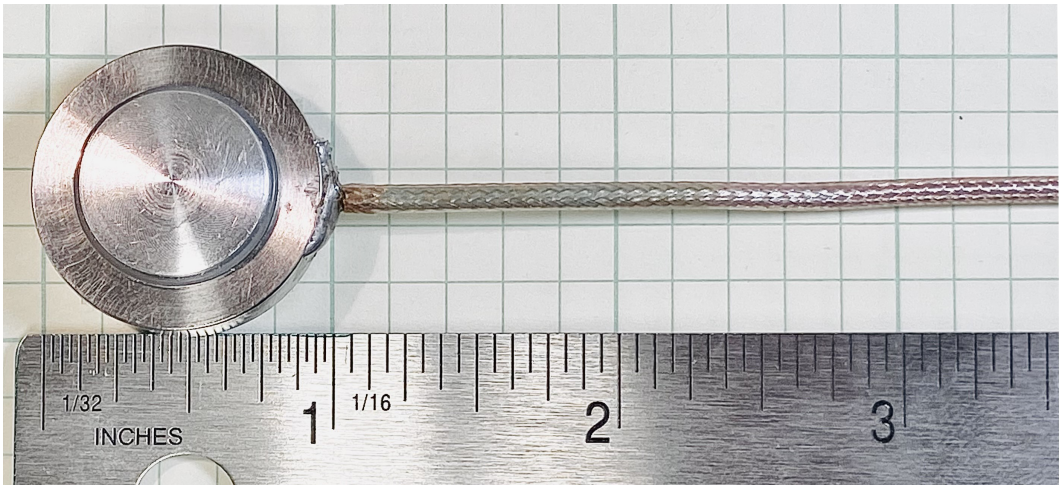

Figure 3.6: Final assembled transducer.

As seen in Figure 3.6, no bolts are used to attach the piston to the tail mass since the threads were already machined on the piston's structure. An ACT Piezoclamping ® prestress measurement tool was used to ensure the application of a prestress load of 16.4 ± 0.45 MPa to the PZTs.

3.1.3 Electrical Impedance and Displacement Experimental Evaluation

The impedance and vibrational amplitude of each transducer was experimentally measured within the selected frequency range of 120 to 170 kHz. The collected data was then compared to the simulation results aiming at the evaluation of the variability of the electrical impedance, resonance frequencies, and displacement amplitude among the 35 custom-built transducers.

Impedance Measurement

The transducer impedance was measured in an open-air configuration using a continuous sinusoidal sweep signal with a voltage amplitude of 20 V_{pp} for the selected frequency range. Figure 3.7 shows the configuration of the hardware used in the experiment.

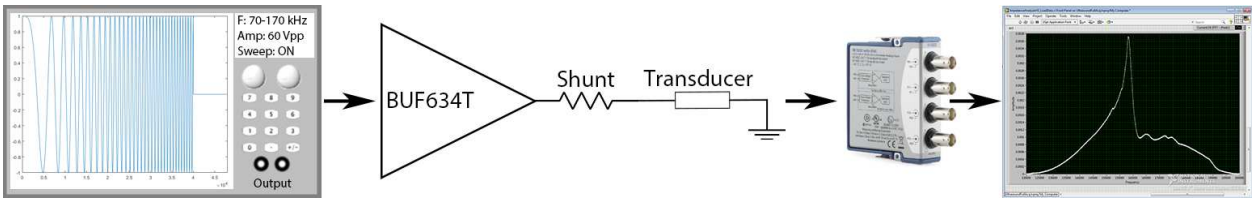

Figure 3.7: Impedance measurement experimental setup.

As shown in Figure 3.7, a function generator (SRS DS360 Ultra Low Distortion) was used to generate a voltage sweep, which was amplified by a BUF634T high-speed buffer, and excited the shunt resistor and transducer. The voltage was measured on the buffer's output and on the shunt using a NI-9775 Digitizer Module at a sampling rate of 2 MHz. The signal was collected using LabVIEW and processed in MATLAB to determine the impedance and resonance frequencies.

The measurements were taken in the selected range of 120 kHz to 170 kHz to focus on the operational frequency range used for this application. Figure 3.8 shows the magnitude of the electrical impedance of four representative transducers.

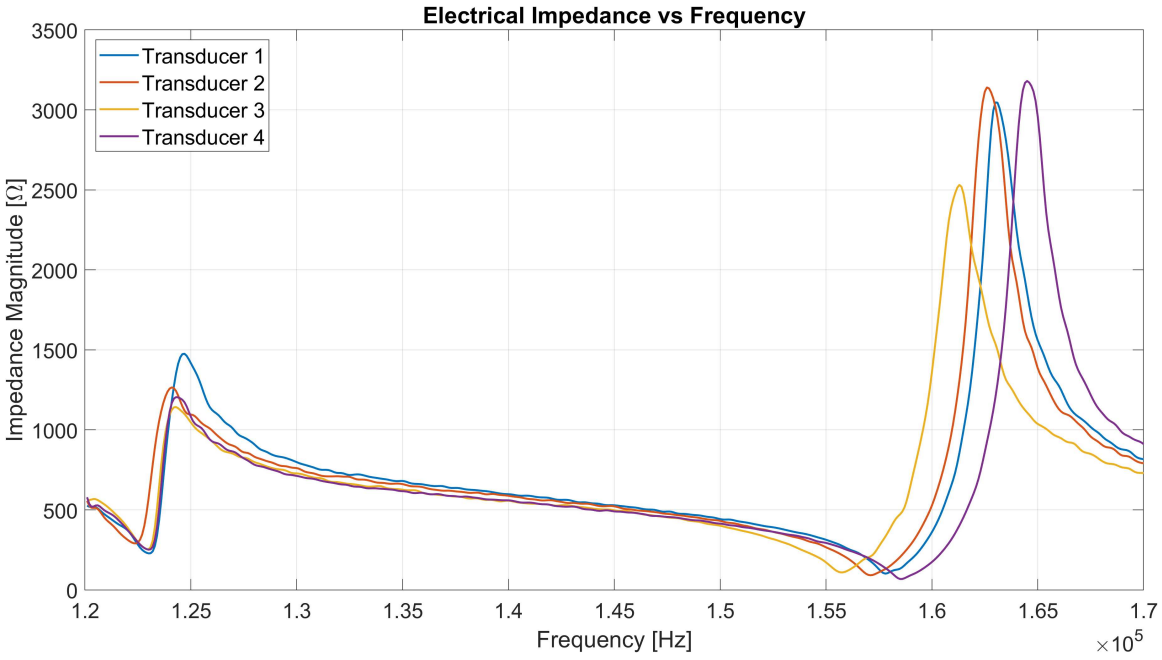

Figure 3.8: Electrical impedance magnitude as a function of the applied signal frequency of transducers 1, 2, 3, and 4.

As seen in Figure 3.8, there is a substantial variation in the magnitudes of the electrical impedance, depending on the frequency and the transducer.

- The extremal values for the different transducers occur at different frequencies and have different values.
- The variations at the second peaks are considerably larger than the variations around 125 kHz .

These differences are important since they are related to the transducer sensitivity when operating at a specific frequency [90]. Therefore, after analyzing all of the data collected for all transducers, it was determined that the USCT will be operated at the frequencies of 125 kHz and 156 kHz in future studies. By operating the system at two frequencies, one can explore the characteristics of the received signal at two different operation regimens; at the resonance frequency (156 kHz) and between the two resonance frequency modes (125 kHz). When operating between resonance modes, the sensitivity per transducer is lower, but the sensitivity variability among transducers is also lower, which is desirable when collecting data on a tomographic configuration. The individ-

ual sensitivity is higher when operating at 156 kHz; however, more variation among transducers is expected. Thus, since this is a pilot study, we decided to investigate both options.

Displacement Measurement

The displacement measurements presented in Section 3.1.3 of this document were conducted by Luca Giacobbo, from Bern University of Applied Sciences, Bern, Switzerland. A PSV 300 vibrometer was used to measure the velocity and displacement of the transducer's piston. A sinusoidal sweep with a selected frequency range and an amplitude of 60 V_{pp} was applied to the transducer. Figure 3.9 shows the hardware configuration used for the experiment.

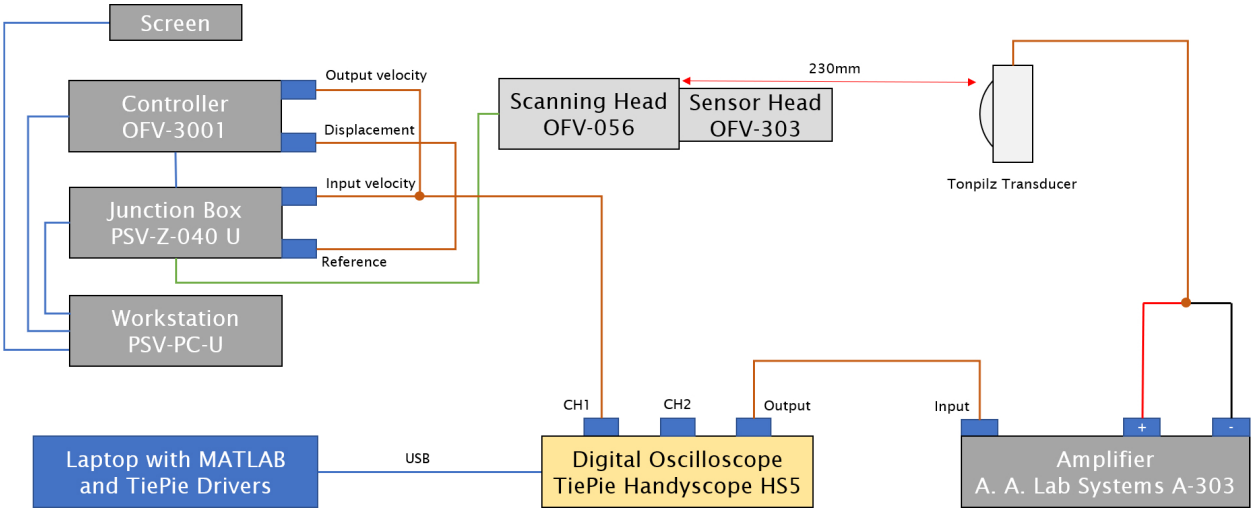

Figure 3.9: Displacement measurement experimental setup.

As shown in Figure 3.9, a TiePie Handyscope HS5 Digital oscilloscope is controlled by a laptop with MATLAB, which sets the frequency and amplitude of the excitation signal. The generated signal was amplified by an A-303 amplifier and supplied to the transducer at 230 mm from the vibrometer. The vibration characteristics of the center piston were measured. The velocity and displacement amplitudes are converted to a voltage signal by the controller and junction box, then digitized by the oscilloscope. The signal was sent to MATLAB to calculate the velocity and displacement for the current frequency. The frequency increments were 100 Hz, and the vibrome-

ter displacement range was set to 0.5 μm/V. After collecting the data, the transmission sensitivity (displacement per unit input voltage) was determined.

The displacement amplitude measurement data were analyzed, and the characteristics of each transducer were extracted. A subset of the measurements are shown in Figure 3.10, where a substantial variation in the displacement magnitude is observed, again, depending on frequency and transducer.

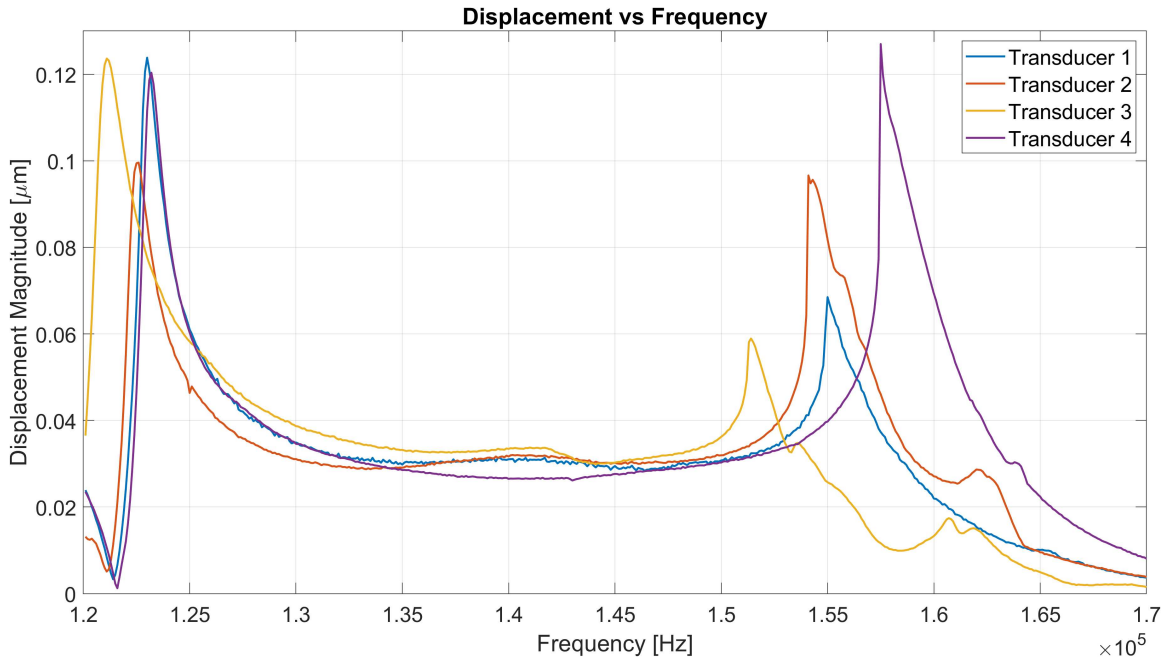

Figure 3.10: Displacement magnitude as a function of the applied signal frequency of transducers 1, 2, 3, and 4.

It is clear that not only the magnitude varies with frequency and among transducers, but the maximal values do not necessarily occur for the same resonance mode. For transducer 3, a higher displacement magnitude was achieved on the resonance mode closer to 122 kHz, whereas, for transducer 4, it was achieved closer to 156 kHz. In the region between the 125 kHz and 150 kHz, the magnitude for all transducers is between 0.027 μm and 0.033 μm. Similar behavior was also observed in the electrical impedance measurements, and therefore, agrees with the frequency previously chosen to be used on the application.

Statistical Analysis

The statistical significance of the impedance and displacement data collected during the experiment was analyzed through an analysis of variance test with a confidence interval of 99% (F-Table α=0.01). The controlled variable considered was the transducer, and the response factors were the maximum and minimum impedance, displacement, and sensitivity values, and also, the frequency to which they occur. The ANOVA residuals for all of the response variables showed a normal distribution, and the equal variances premise was not violated, and thus, it was considered that ANOVA is an adequate test for this experiment [91]. ANOVA has shown that the resonance frequency, the maximum and minimum displacement, the electrical impedance, and the sensitivity when the transducer is operating on its own resonance frequency and at fixed frequencies of 125 kHz and 156 kHz, significantly vary among transducers (f-values $\geq$ 27.08 and p-values $\leq$ 0.001).

The results in Table 3.1 and Figure 3.11 show that even though the average electrical impedance is higher at 125 kHz, the displacement of the piston is larger at that frequency. Also, the variability at 125 kHz is lower than at 156 kHz, thus, it is considered that 125 kHz might be the best operation frequency for the transducers.

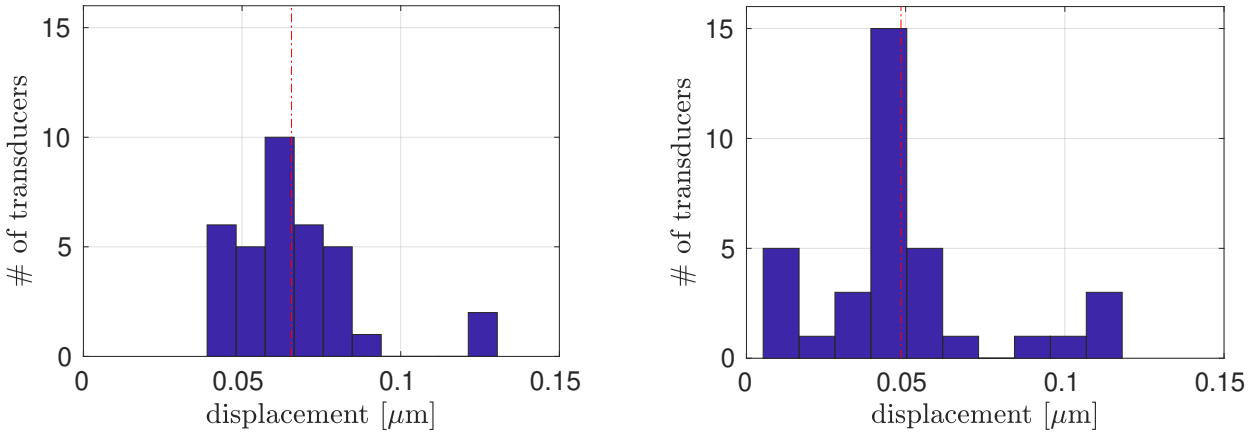

(a) 125 kHz. **(b)** 156 kHz.

Figure 3.11: Histograms for the displacements.

Table 3.1: The average impedance and displacement of the transducers at the two frequencies.

Frequency	**125 kHz**	**156 kHz**
Electrical impedance	$955 \pm 210\ \Omega$	$433 \pm 242\ \Omega$
Displacement	$0.066 \pm 0.02\ \mu m$	$0.049 \pm 0.03\ \mu m$

If each transducer was operated at its resonance frequency, displacements of 0.110 ± 0.03 μm and 0.109 ± 0.03 μm could be achieved for the first and second resonant modes. However, each transducer is used to emit and receive signals in a tomographic configuration, and thus, varying the frequency of the transmitted signal would make the image reconstruction process more complicated, and also increase the disparity between the sensitivity of the transmitting and receiving transducers that compose the array.

Transducer Calibration

As seen in section 3.1.3, there was significant variability in the sensitivity of the transducers. After analyzing and comparing the magnitude of the impedance and displacement, a strong correlation ($r = 0.91$) was found between the frequency corresponding to the minimum impedance and maximum displacement for both resonance modes (around 125 kHz and 156 kHz). However, there was no correlation ($r = -0.07$) between the impedance magnitude at the resonance frequency and displacement. Therefore, a calibration approach based only on impedance would not be sufficient to compensate for the sensitivity variation of the transducers, and hence a calibration based on the displacement is proposed. The vibrometer measured the displacement magnitude at the center of the transducer's piston three times. The variability among samples collected per transducer was evaluated, and only the third sample was used for calibration under the assumption that the vibrometer had reached steady-state temperature by the third measurement. The measurements were then analyzed, and the absolute value of displacement at the operating frequencies of 125 kHz and 156 kHz was determined for each transducer.

The sensitivity of each transducer was determined based on the displacement reached at the operating frequency and the excitation voltage. The average sensitivity was 1.809 $\pm$ 0.5879 nm/V and 1.812 $\pm$ 0.5979 nm/V for the frequencies of 125 and 156 kHz, respectively. A calibration table was filled with the sensitivity coefficients. The rows represent the transducer number, and the columns the normalized sensitivity at each operating frequency.

The table was used to calibrate data collected in a tomographic configuration (32 transducers radially distributed on the same plane). The coefficients are applied to the raw, time-dependent data twice; once for the transmitting transducer and once for each of the receiving transducers, as shown in Equation (1).

$$\text{Voltage}_c = \frac{\text{Voltage}_r}{\text{Coeff}_r.\text{Coeff}_t}, \tag{3.1}$$

where Voltage_c is the calibrated voltage, Voltage_r is the raw received signal, and Coeff_r and Coeff_t are the calibration coefficients of the receiving and transmitting transducers.

For a segment of data collected on transducer 25, when the signal is transmitted by transducer 32, for example, the data is divided by the normalized sensitivity coefficient of transducer 25 and 32. That approach compensates for the differences in sensitivity for both sending and receiving channels individually, which is essential for a proper tomographic reconstruction.

3.2 Acoustic Calibration

An acoustic calibration was conducted to determine the transducers' acoustical properties and their variance among different samples. The maximum acoustic pressure and pressure field when the transducers were driven by a sinusoidal signal of frequencies 125 and 156 kHz and amplitudes of 0 to 32 V_{pp} were analyzed. The data was collected in an acoustic tank platform, developed in-house, and used to determine the transducers' sensitivity for transmitting and receiving ultrasonic signals; Figure 3.12 shows the configuration of the hardware developed for this experiment.

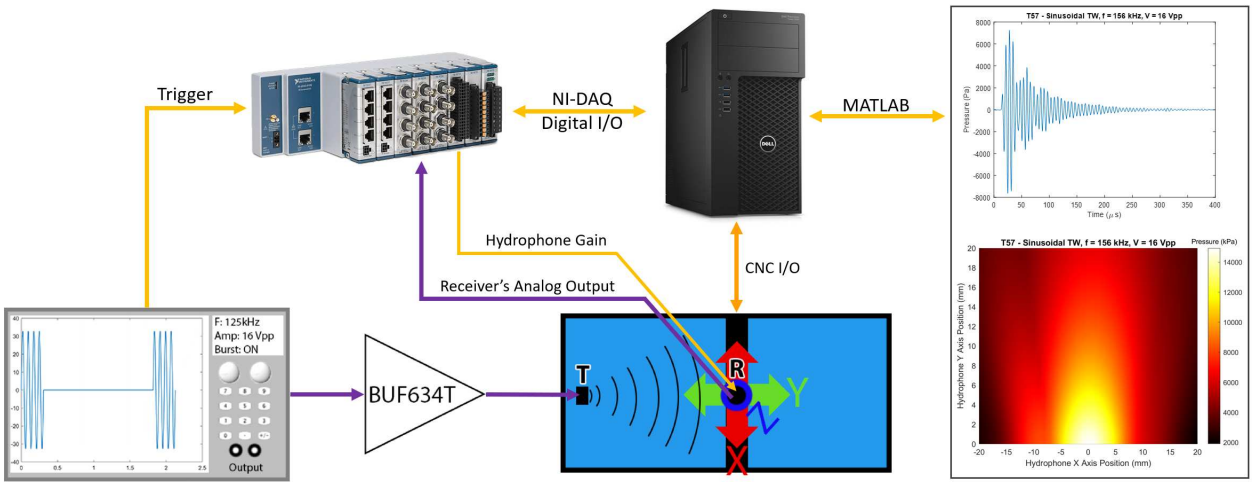

Figure 3.12: Acoustical measurement tank setup: digital signals and analog signals are represented by yellow and purple arrows, respectively.

As seen in Figure 3.12, a function generator (SRS DS360 Ultra-Low Distortion Function Generator) was used to generate a sinusoidal burst that was amplified by a high-speed buffer (BUF634T) which drives the transmitting transducer (T), attached to a fixed beam and completely submerged in a water tank. The pressure wave produced by T hit the receiver (R), which was either another transducer or a pre-amplified hydrophone with adjustable gain (Benthowave BII-7015PG), and the analog voltage that arose on the receiver was measured by a digitizer module (NI-9775) at a sampling rate of 5 MHz. When acquiring data with the hydrophone, a digital I/O module (NI-9401) was used to set the hydrophone's pre-amplifier gain to 0, 20, 40, or 60 dB. The receiver was attached to a vertical beam connected to the head of a modified CNC router (FoxAlien Masuter 4040 CNC) with three degrees of movement, denoted by X, Y, and Z. The entire calibration procedure and data processing were controlled over MATLAB.

3.2.1 Tank Dimensions

A free-field calibration of an underwater transducer requires the measurements to be conducted on a free-field environment, i.e., an infinite reservoir, where propagation losses completely attenuate the reflected waves before they reach the receiver [92]. This would require a deep-water facility, such as a lake or the ocean, making the measurement logistically challenging. It is pos-

sible, however, to create an echo-free environment by using gating techniques and proper tank size to allow measuring the first received lobe before interference occurs [93]. The minimum tank dimensions will then depend on several factors, including the sound speed, the characteristics of the transmitted waveform, the desired distance between the source and the receiver (direct signal path), and the shortest distance between the receiver and the first reflected signal [93]. For all the transducers measured, the maximum distance between the transmitter and receiver was 223 mm, and the tank's dimensions were 919.2 mm in length, 430.1 mm in height, and 463.6 mm in width. The time between the transmission of the signal and the arrival of the first reflected signal can be determined according to equation 3.2, [94].

$$\tau = \frac{\sqrt{l^2 + d^2} - d}{\mathrm{c}_{water}}, \tag{3.2}$$

where τ is the time of arrival of the first reflected pulse, c_{water} is the speed of sound in water, l is the shortest tank dimension, and d is the distance between the transmitter and receiver. Considering the tank's shortest dimension, a sound speed in water at 70°F of 1485 m/s [95] and a maximum distance of interest, the expected time for the arrival of the first reflected pulse was 176.1 μs. Therefore, since we were interested in determining the transducers' sound pressure map at 125 kHz and 156 kHz when transmitting a sinusoidal signal of six half-cycles (HC), which had a maximum duration of 24 μs, the first lobe was received without interference.

3.2.2 Mechanical Assembly

The mechanical structure of the acoustic tank was composed of a modified CNC router (Fox-Alien Masuter 4040 CNC), two beams that hold the transmitter and receiver in place, a sturdy structure that suspends the CNC router, and a water tank. The transmitter holding beam was fixed to the structure and thus immobile. In contrast, the receiver's beam is fixed to the CNC head and can freely move within a range of 380 mm for the X and Y axes and 55 mm for the Z axis (refer to Figure 3.12) and a step size of 0.01 mm. The water tank was placed under the structure, which allowed for measuring the acoustic pressure received at the receiver in multiple locations, which

composed the transducers' acoustic map. The beams that hold the transducer and receiver in place were composed of PVC pipes with custom 3D-printed ends to ensure proper alignment of devices and, thus, the repeatability of the measurements. Figure 3.13 shows the 3D model of the developed parts.

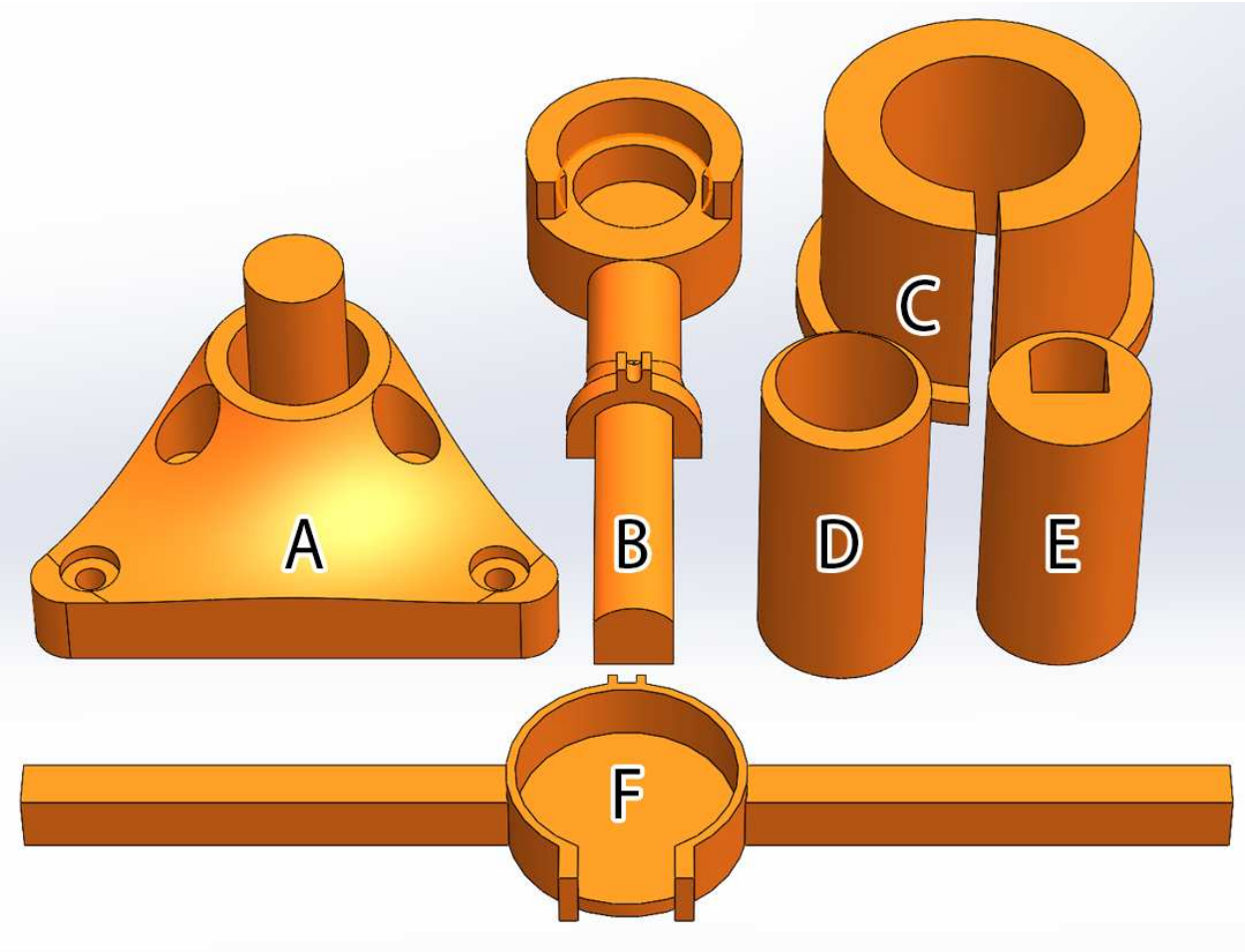

Figure 3.13: Acoustic tank 3D printer holders: a) transmitter upper fixture, b) transmitter lower fixture, c) receiver upper fixture, d) hydrophone lower fixture, e) transducer (when receiving) lower fixture adapter, and f) transducer alignment tool.

As seen in Figure 3.13, parts A and B were connected to the ends of a PVC pipe and composed of the beam fixed to the bottom of the main structure and used to suspend the transmitting transducer away from the tank walls. Part C was used to connect the upper part of the beam that suspends the receiver to the CNC head, while parts D and E are interchangeable and permit a

transducer or a hydrophone to be used as a receiver. Finally, part F was attached to the back of part B to enhance misalignment visualization and enable a proper calibration of the equipment. A cross-line laser level (TB-H2-LL-30-L2) was used to level and align all the structures used in the building and ensure the receiver moves freely in the X and Y directions while remaining in the measurement plane; Figure 3.14 shows some of the measurements taken.

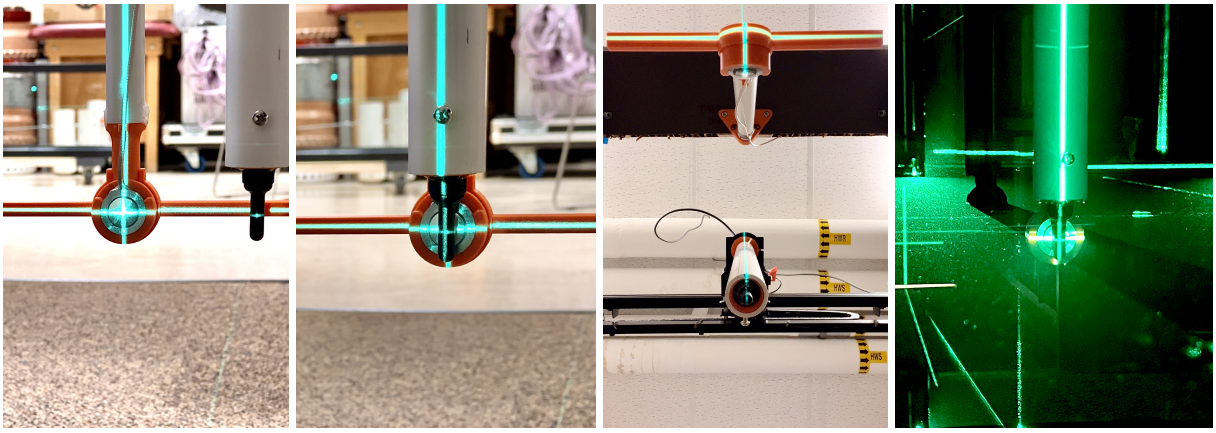

(a) Transmitter centering. **(b)** Hydrophone alignment. **(c)** Hydrophone alignment. **(d)** In water measurement.

Figure 3.14: Acoustic tank mechanical alignment.

From Figures 3.14a and 3.14b, it is seen that the hydrophone's height did not change when it moved on the X axis. From Figure 3.14c, it is noticeable that the hydrophone remained centered with the transducer when it moved on the Y axis and that the transducer holder's longitudinal axis was parallel to the X axis.

3.2.3 Hardware Control

All the hardware was controlled through MATLAB, including the analog data acquisition, hydrophone gain, and CNC position. The communication between MATLAB and the NI-DAQ and CNC router was established through USB. Once the systems were started, their behavior could be represented by the workflow diagram in Figure 3.15.

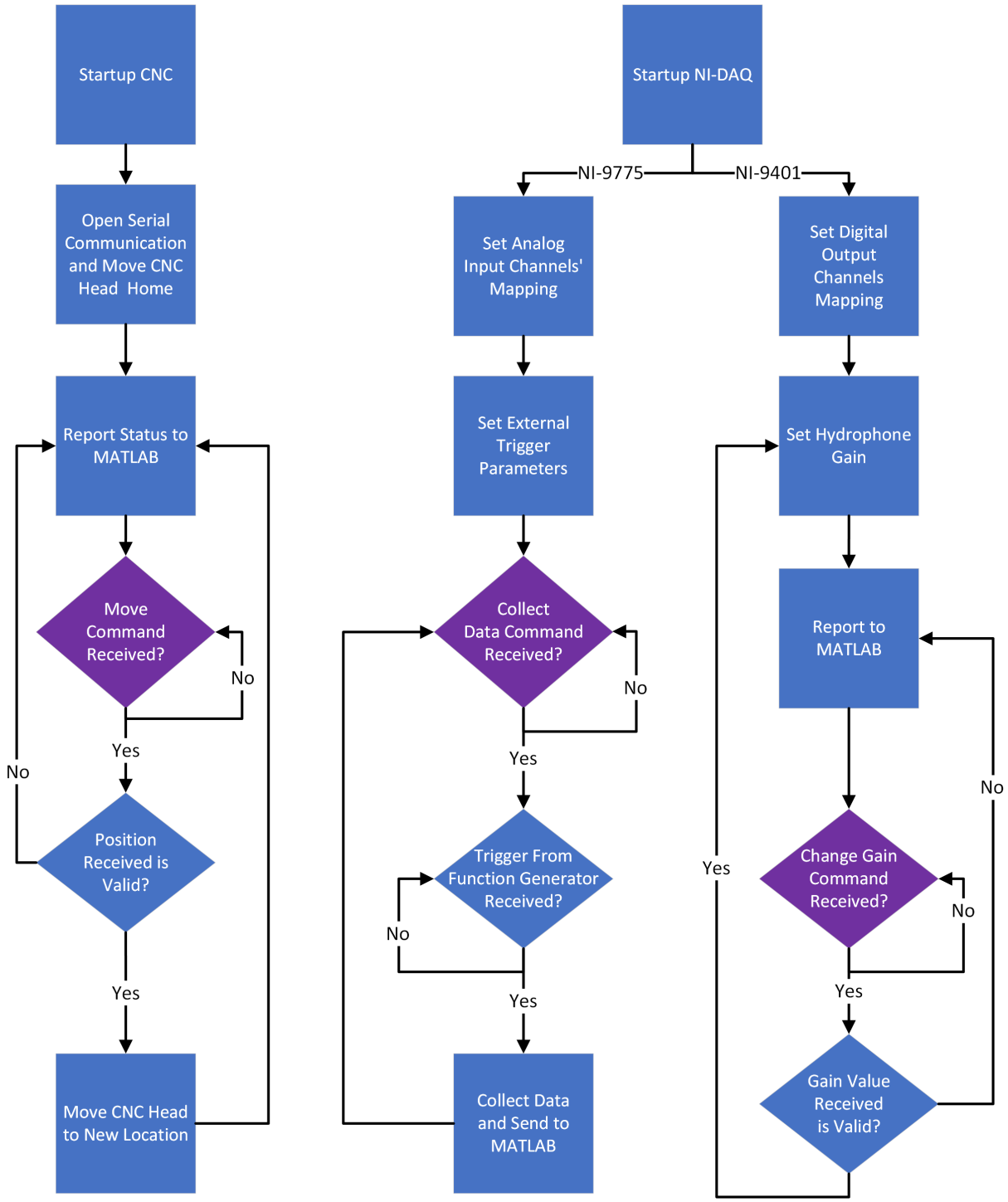

Figure 3.15: CNC and NI-DAQ behavior diagram.

As seen in Figure 3.15, both systems had a main state (represented by the purple diamond shape) where they waited for MATLAB's command to perform their action. Once the command

was received and evaluated, it was either executed or flagged as an error and reported to MATLAB. For the NI-9775 path, it is important to notice that the data collection was synced to the function generator's trigger, i.e., once the Data Collection Command was received, it waited for the digital trigger and then collected the data and sent it to MATLAB. That ensured a consistent data collection time window, which improved repeatability and facilitated the post-processing procedure.

3.2.4 Acoustic Pressure Measurement

The acoustic pressure was measured using an omnidirectional needle hydrophone. This underwater device produces an electrical signal of amplitude proportional to the pressure's magnitude it is exposed to and its free-field voltage sensitivity (FFVS). The electrical signal is then measured and used to determine the acoustic pressure experienced at the active element by using Equation 3.3, [96].

$$\mathrm{p(t)} = \frac{\mathrm{V(t)}}{\mathrm{M(f)}}, \tag{3.3}$$

where p(t) is the pressure of the received signal, V(t) is the voltage of the received signal, and M(f) is the sensitivity of the hydrophone on the frequency of the received signal in $\frac{\mu V}{Pa}$.

The hydrophone (BII-7015PG) used in this project was custom-built by Benthowave Instrument Inc. It had a built-in programmable gain pre-amplifier, with gain levels pre-set to 0, 20, 40, and 60 dB, and it can be operated underwater on frequencies of 1 to 400 kHz. The hydrophone came with a calibration certificate, and its beam pattern and FFVS were provided by the manufacturer for its entire operational range, as shown in Figure 3.16.

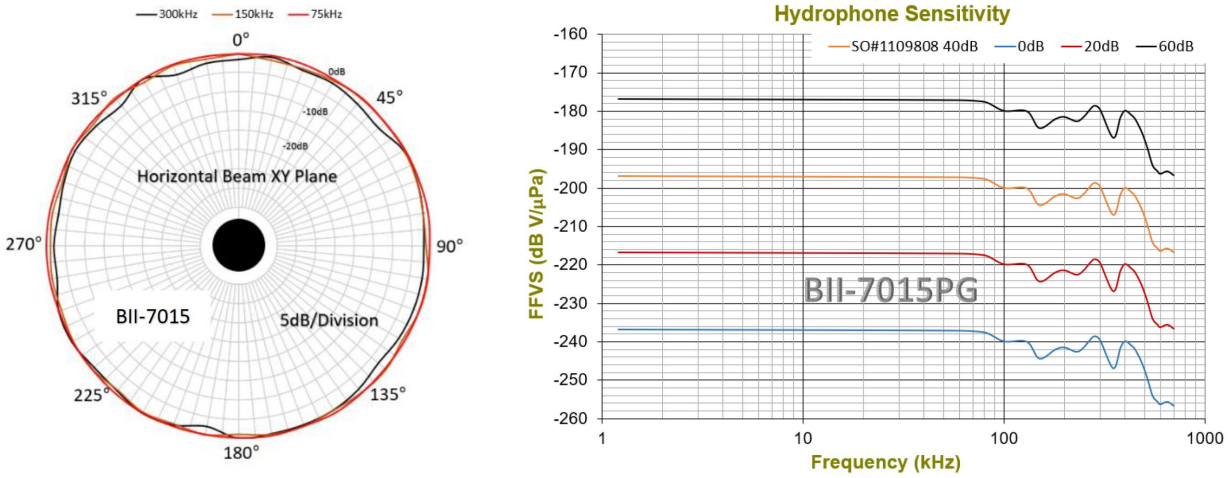

(a) Beam pattern.

(b) FFVS.

Figure 3.16: Hydrophone FFVS and beam pattern curves provided by Benthowave Instrument Inc.

As seen in Figure 3.16, the hydrophone's response is not flat, especially within the range of interest. However, since the transmitted waveform is a single-frequency sinusoidal burst, and the sensor's sensitivity is known for 125 and 156 kHz, as shown in Table 3.2, it was considered suitable to determine the transducers' output pressure map.

Table 3.2: Hydrophone FFVS sensitivity at 125 and 156 kHz; values provided by Benthowave Instrument Inc.

Pre-amp gain level (dB)	Sensitivity at 125 kHz ($\frac{\mu V}{Pa}$)	Sensitivity at 156 kHz ($\frac{\mu V}{Pa}$)
60	1002.31	636.795
40	100.231	63.6795
20	10.0231	6.36795
0	1.00231	0.636795

3.2.5 Calibration Routine

The calibration procedure was mostly automated, except for swapping transducers and adjusting the frequency and voltage of the transmitted waveform through the function generator, which was user-done. A representation of the calibration workflow is shown in Figure 3.17.

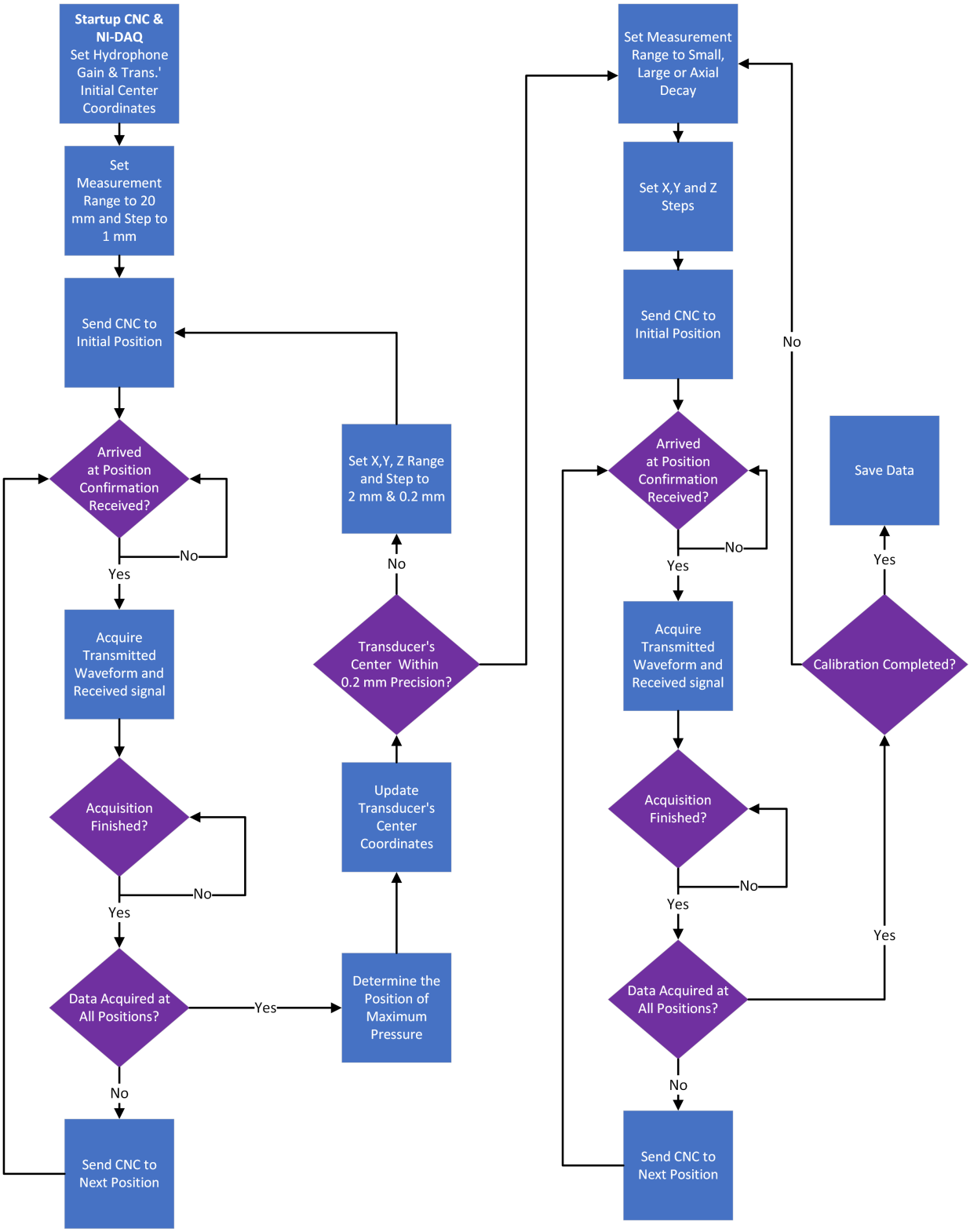

Figure 3.17: Calibration procedure diagram.

As seen in Figure 3.17, the first step of the calibration procedure was to find the center by sweeping the X and Z axes on a range of 20 mm with a 1 mm step. The initial center coordinates were pre-defined based on the geometrical position of the transducer and had absolute values X = -200 mm, Y = -376 mm, and Z = - 20 mm. Once the maximum absolute pressure point was found, the center was updated, and the routine was rerun with a range of 2 mm and a step of 0.2 mm. That procedure ensured that the hydrophone center was aligned with the transducers' piston geometrical center with a precision of 0.2 mm, thus, compensating for small physical misalignments or differences among transducers. After that, the transmitted waveform and the acoustic pressure of the wave produced by the transducer at each map point were measured. The spatial resolution (step) and map dimensions were determined based on the wavelength of the transmitted signal, calculated using Equation 3.4, and preliminary measurements.

$$\lambda_{TW} = \frac{\mathrm{c}_{water}}{\mathrm{f}_{TW}}, \tag{3.4}$$

where λ_{TW} is the wavelength of the transmitted waveform, c_{water} is the speed of sound in water, and f_{TW} is the frequency of the transmitted waveform. When driving the transducer with signals of frequency 125 and 156 kHz, the wavelengths in water were 11.93 and 9.558 mm, respectively. Therefore, to avoid aliasing, the spatial resolution chosen for all pressure maps was 1 mm; the dimensions and other details regarding all the calibration modes are shown in Table 3.3.

Table 3.3: Calibration modes spatial specifications.

Calibration mode	**Range (mm)**			**Step (mm)**			**Num. Measurements**
Axis	**X**	**Y**	**Z**	**X**	**Y**	**Z**	**Total**
Find max. coarse	11	0	11	1	0	1	121
Find max. fine	11	0	11	0.2	0	0.2	121
Small	41	21	0	1	1	0	861
Large	201	101	0	1	1	0	20301
Axial decay	1	201	0	0	1	0	201

Transmitted Waveform

The transducer under calibration was driven by a single-tone sinusoidal burst of frequencies 125 or 156 kHz with amplitudes within 0 to 32 V_{pp}, six half-cycles of length, and an interburst interval of 100.74 ms. Considering that the transmitted waveform had a maximum duration of 24 μs, that left an interval of approximately 100.71 ms where the transducer was not driven. The interval duration is critical and was considered long enough for the reflected signals to be attenuated by the medium, thus, preventing interference. Figure 3.18 shows a segment of the transmitted waveform and electrical signal received at the hydrophone.

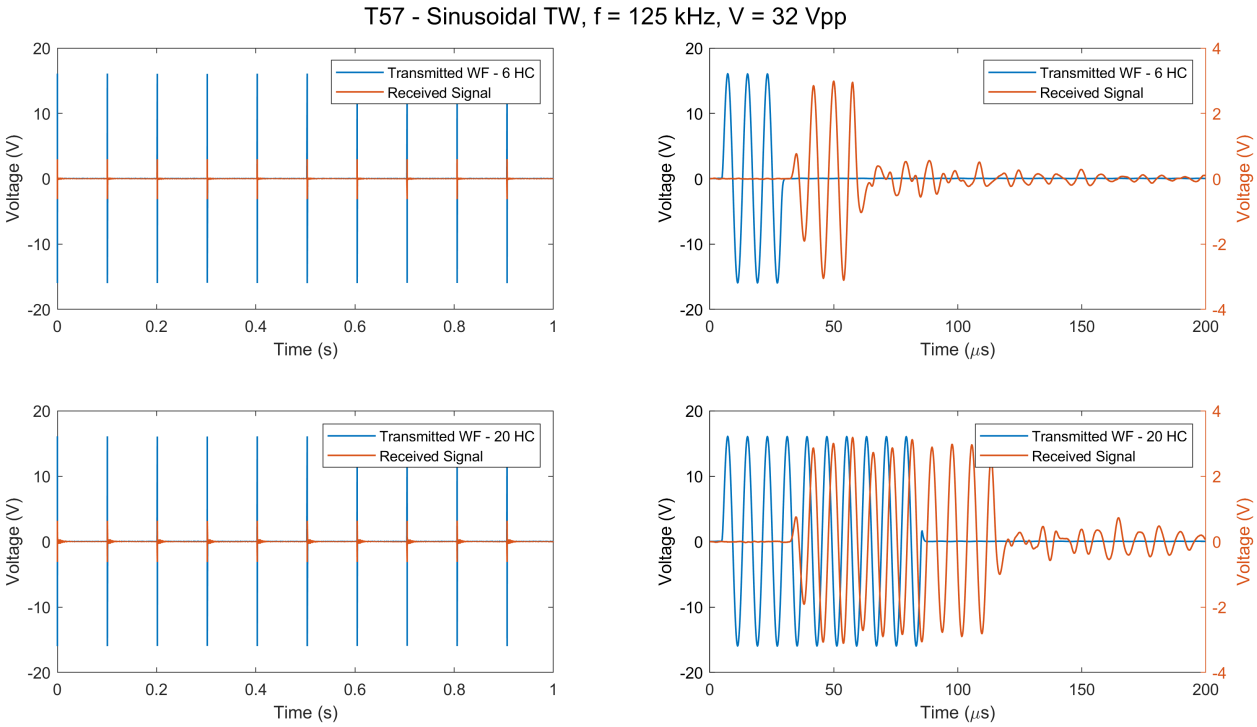

Figure 3.18: Transmitted and received signals for a sinusoidal TW with the frequency of 125 kHz, amplitude of 32 V_{pp}, six HC (top) and 20 HC (bottom).

When analyzing Figure 3.18, it is seen that when a new signal was transmitted, the previous one, and its reflections, had been attenuated by the medium to a level that could not be measured by the digitizer. Thus, confirming that the chosen transmission interburst interval was sufficient. Moreover, when comparing the case where 20 HC were transmitted to the one when six were,

it is seen that the maximum peak-to-peak voltage of the received signal did not change, i.e., the transducer steady-state was achieved in both cases. Therefore, a shorter burst was adopted for the remainder of the experiment to increase the time between transmissions and help prevent interference.

Another important aspect of the transmitted waveform parameters was to ensure that the transducers were driven on a voltage range that would not saturate the PZTs, which would have created non-linear conditions on the propagated wave [97]. Different voltages within the proposed range of 0 to 32 V_{pp} were used to drive the transducers while their pressure output was measured by the hydrophone; the results obtained with T47 are shown in Figure 3.19.

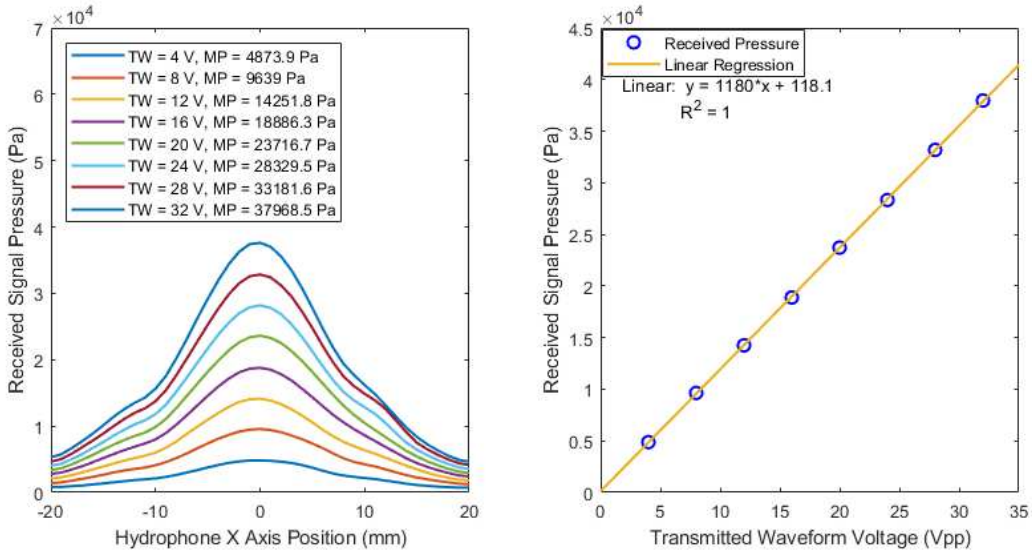

Figure 3.19: Peak-to-peak acoustic pressure output as a function of the driving voltage when the hydrophone is at a distance of 13.94 mm from the transducer.

As seen in Figure 3.19, the transducer's pressure output linearly increased while the transmitted waveform voltage was increased. Furthermore, the spatial pressure profile was similar for driving voltages, thus, indicating that the PZTs were not saturated, i.e., the transducer was being operated on its linear range.

Received Signals

The received signals were analyzed for a variety of transmission and reception configurations. An example of unfiltered received signals, acquired when transducer T59 transmitted a sine-wave burst of frequency 125 kHz and 16 V_{pp} amplitude on the same axis as the hydrophone at three distinct distances, is provided in Figure 3.20. It is important to point out that the right side of the received signals was zero-padded after the first received lobe to improve visualization and that the excitation signal was transmitted at time = 0 μs.

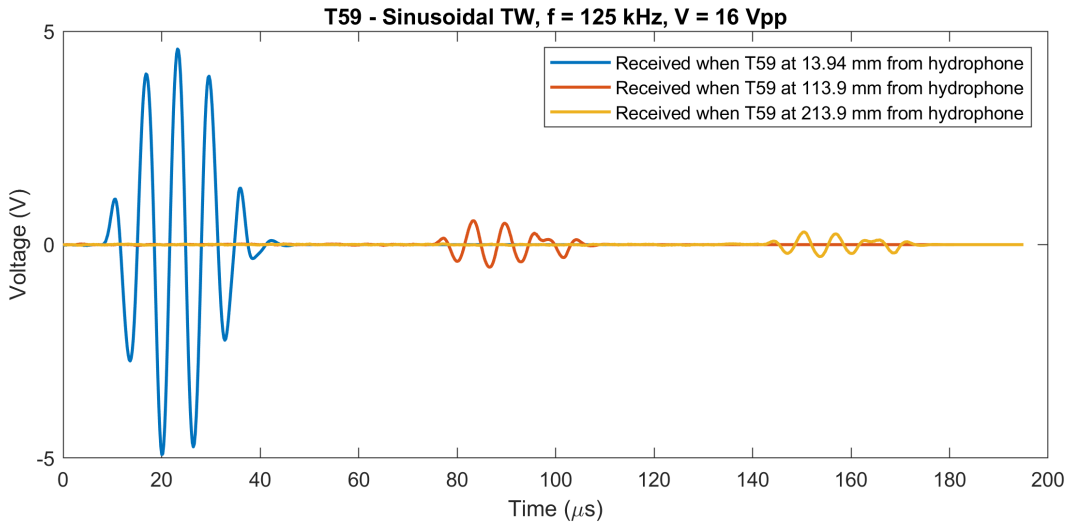

Figure 3.20: Received signals when T59 is transmitting in the same axis as the hydrophone for three distances.

When observing the received signals, it is noticeable that the amplitude decreased as the transducer moved away from the hydrophone, whereas the TOF increased. The TOF when the transducer was at distances of 13.94, 113.9, and 213.9 mm from the hydrophone were 9.609 μs, 76.28 μs, and 143.8 μs, respectively. Considering the speed of sound in water and the TOF, the computed distances between the transmitter and the hydrophone were 14.27, 113.3, and 213.5 mm, representing a maximum error of 0.6768 mm. This analysis was carried out for multiple transducers using 201 axial positions per transducer; the maximum error observed was 0.7820 mm. An example of the data collected with T57 is shown in Figure 3.21.

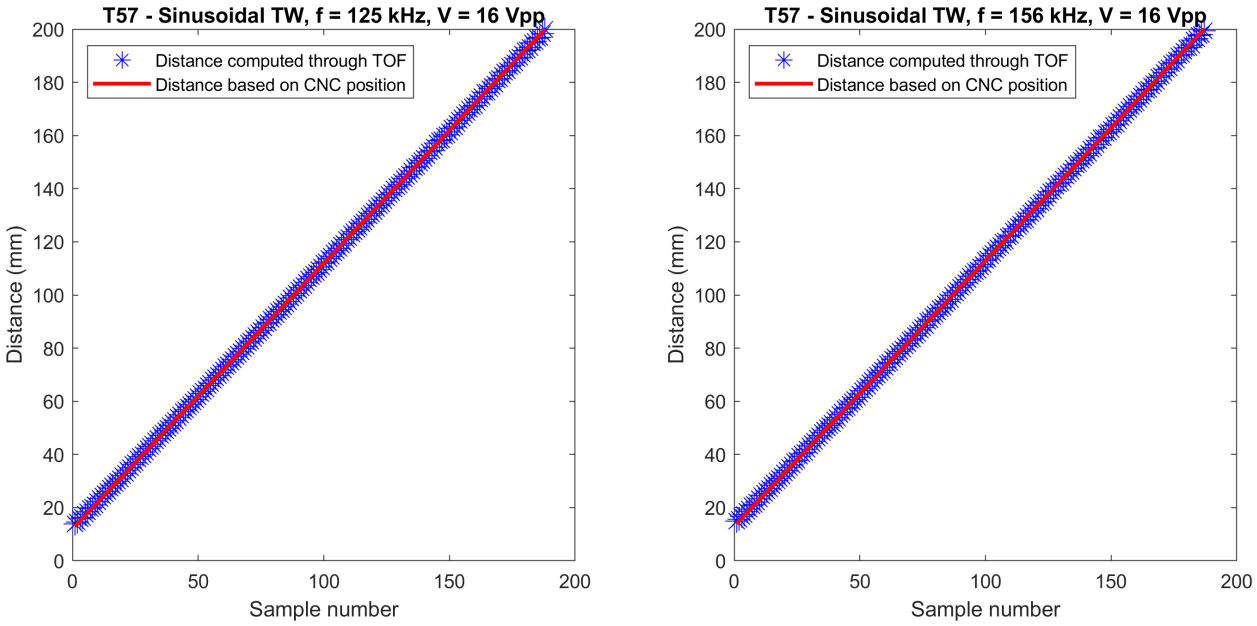

Figure 3.21: Distance computed through TOF and based on the CNC position.

3.2.6 Transmitting Pressure Maps

As previously outlined in Section 3.2.5, the transducers' acoustic pressure maps were evaluated in various spatial configurations, including small and large ones. An example of a large pressure map generated using measurements obtained with the hydrophone when transmitting with transducer 57, is provided in Figure 3.22

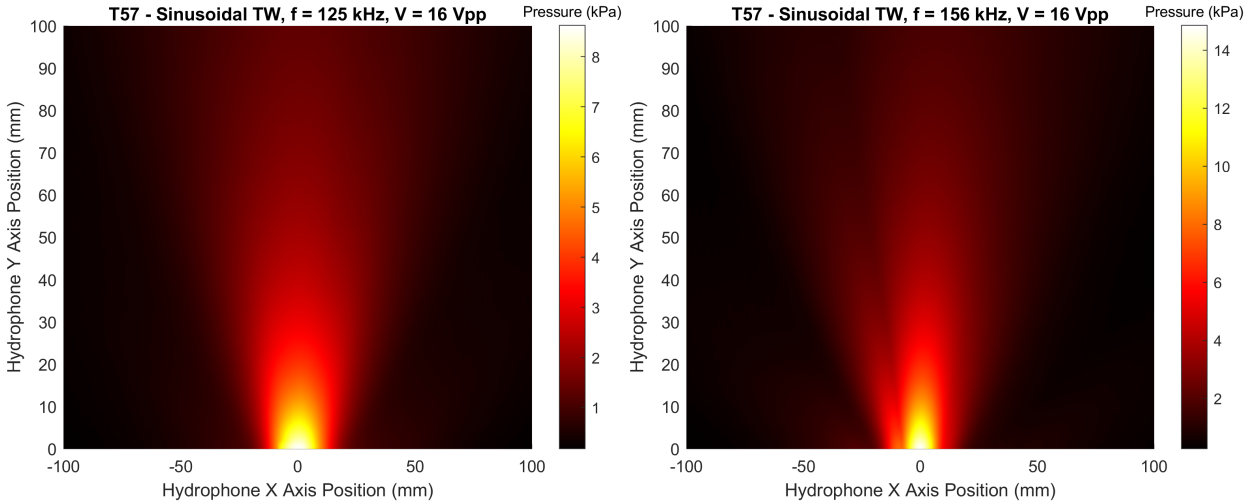

(a) Transducer 57, F = 125 kHz.

(b) Transducer 57, F = 156 kHz.

Figure 3.22: Acoustic pressure maps of transducer 57 when transmitting a sinusoidal signal.

Upon comparison of the acoustic pressure maps generated by a single transducer at varying frequencies, it is apparent that there exist differences in both the maximum pressure and beam pattern. The peak-to-peak pressures achieved were 8.620 kPa and 14.85 kPa for 125 and 156 kHz, respectively, representing a difference of 53.09%. At first, this suggests that the optimal frequency for the transducer operation may be 156 kHz, as it can generate greater pressure using the same peak-to-peak voltage. However, the beam pattern is observed to be more uniform and wider when the transducer is operated at 125 kHz, which is critical for this application. Furthermore, a lower sensitivity can be compensated by driving the transducers with a higher voltage as long as it operates on its linear range, whereas the beam pattern is primarily frequency dependent.

Most of the energy transmitted by the transducer, and, thus, the information about the beam pattern and its maximum pressure, was concentrated within X = - 20 to 20 mm and Y = 0 to 20 mm. Therefore, these dimensions were adopted as the standard for the analysis conducted with the remainder of the transducers since they enhance those features. Examples of the acoustic pressure maps computed for transducers 57, 59, and 60 are shown in Figures 3.23 to 3.25; all the acoustic maps collected for the remainder of the transducers can be found on Appendix D.

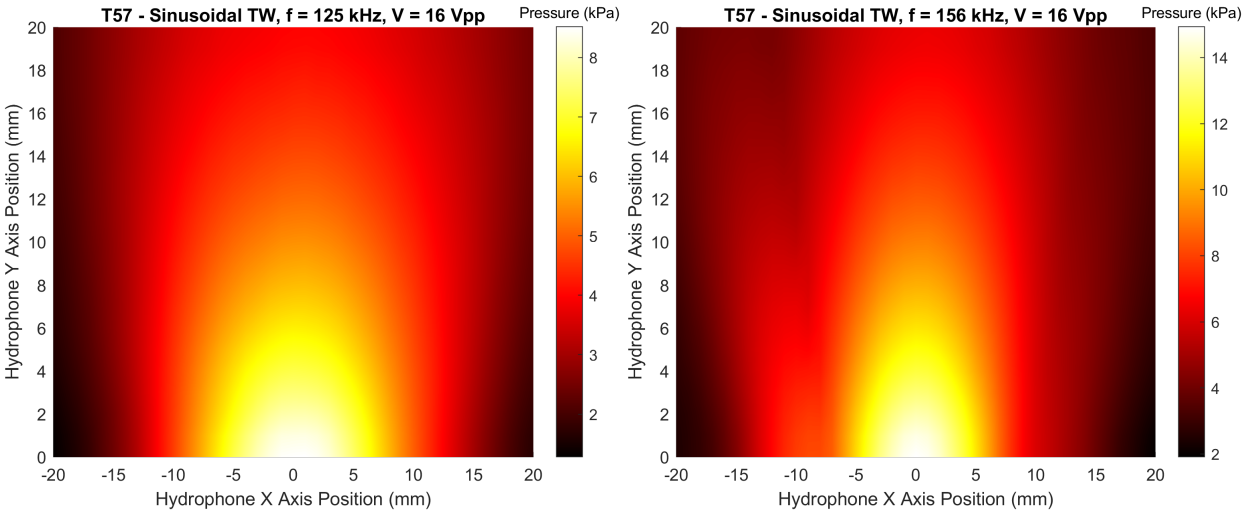

(a) Transducer 57, F = 125 kHz.

(b) Transducer 57, F = 156 kHz.

Figure 3.23: Acoustic pressure maps of transducer 57 when transmitting a sinusoidal signal.

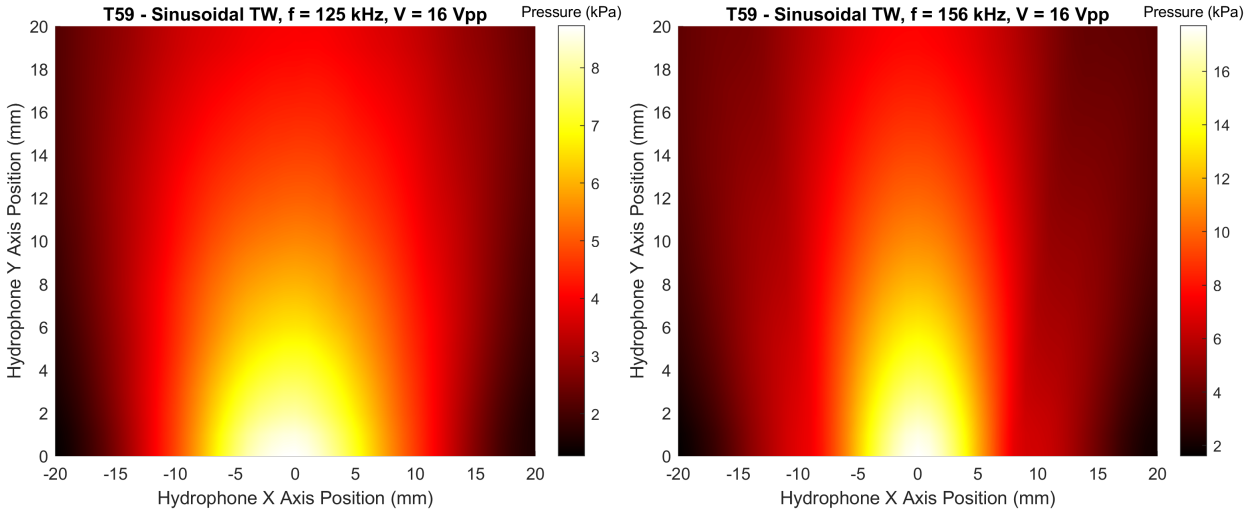

(a) Transducer 59, F = 125 kHz. **(b)** Transducer 59, F = 156 kHz.

Figure 3.24: Acoustic pressure maps of transducer 59 when transmitting a sinusoidal signal.

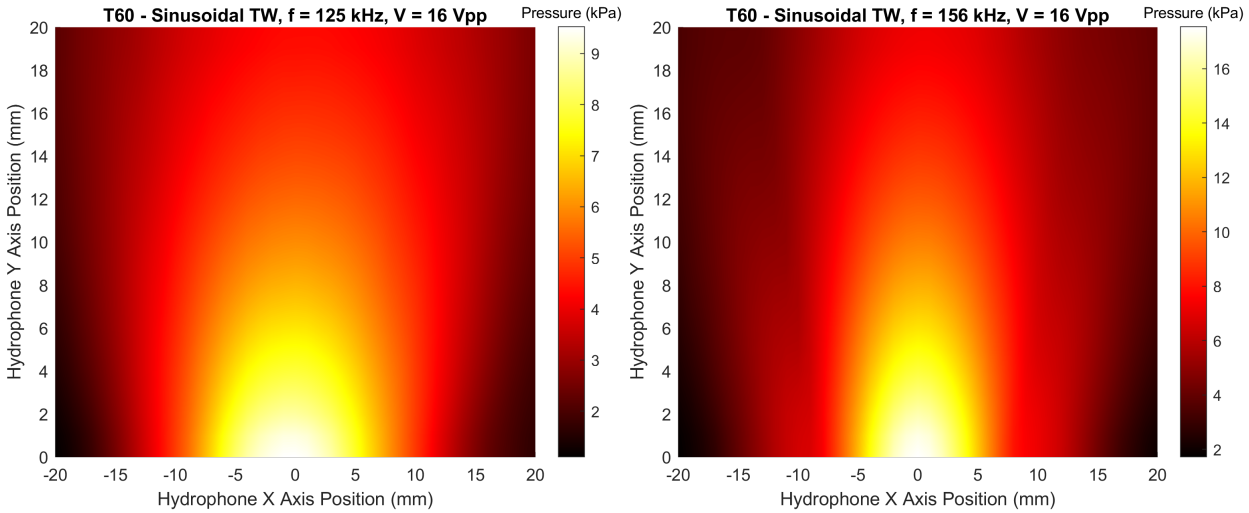

(a) Transducer 60, F = 125 kHz. **(b)** Transducer 60, F = 156 kHz.

Figure 3.25: Acoustic pressure maps of transducer 60 when transmitting a sinusoidal signal.

All the transducers' acoustic maps analyzed presented a similar behavior; when transmitting at 125 kHz, the beam was wider and more uniform, and the maximum achieved pressure was lower than when operating at 156 kHz. For transducers 57, 59, and 60, the beam angles were 39.43°, 38.15°, and 37.53°when operating at 125 kHz and 36.02°, 29.89°, and 31.18° when operating at 156 kHz. The maximum acoustic pressures achieved by transducers 57, 59, and 60 at a frequency

of 125 kHz were 8.516, 8.725, and 9.520 kPa, whereas, at 156 kHz, they were 14.928, 17.699, and 17.542 kPa, respectively. Therefore, the maximum pressure and beam angle variation among these samples was greater when they were operated at 156 kHz (16.99 $\%$ and 18.60 $\%$) than at 125 kHz (11.13 $\%$ and 4.93 $\%$), which encourages their use at 125 kHz. Moreover, the differences among the transducers' transmission characteristics can also be evaluated through their acoustic profile as shown in Figure 3.26.

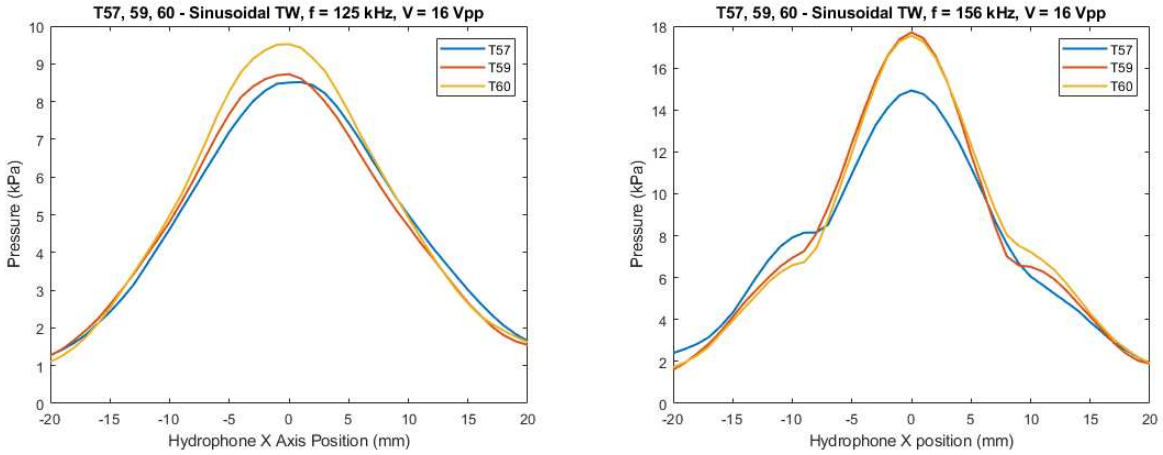

(a) Transducers 57, 59 and 60, F = 125 kHz.

(b) Transducers 57, 59 and 60, F = 156 kHz.

Figure 3.26: Acoustic pressure profiles of transducers 57, 59, and 60 when the hydrophone is at a 13.94 mm distance from the transducer.

Upon comparison of the pressure profiles generated when the transducer was transmitting at a frequency of 125 and 156 kHz, it is clear that the decrease in pressure when the hydrophone moved away from the axial center of the transducer is different among transducers and frequencies. When transmitting at 156 kHz, instead of a continuous attenuation of the signal as the hydrophone moves to the left and right of the center axis, there are recovery lobes between the positions $|X| = 8$ to $|X| = 12$, which could have been caused by constructive interference between the acoustic front wave (transmitted by the center of the transducer's piston) and the side wave (transmitted by the edges of the transducer's piston). This phenomenon is known as flapping and can happen in some

of the transducer's vibration modes [81]. This analysis was conducted with all the transducers, and the remainder of their pressure profiles can be found in Appendix E.

3.2.7 Receiving Voltage Maps

The receiving voltage map of the transducers was assessed by driving a reference transducer (T57 or T49) with a sinusoidal signal of 32 V_{pp} and with a frequency of either 125 or 156 kHz while receiving the signal with another transducer. The reception was performed with one transducer at a time, under various spatial configurations, as described in Table 3.3. The collected data were processed to create a receiving voltage map, which, along with the reference transducer's transmitted pressure map, was used to determine the sensitivity of each transducer in receiving signals. Figures 3.27 to 3.29 provide examples of the received voltage maps generated from the measurements obtained using transducers 57, 59, and 60. The voltage maps for the remaining transducers can be found in Appendix F.

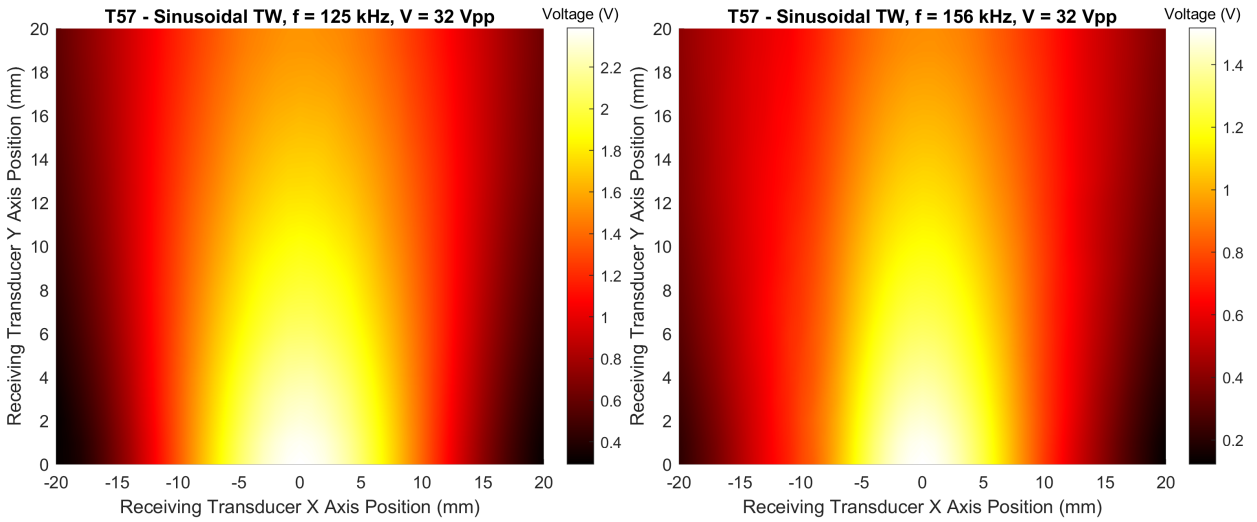

(a) Transducer 57, F = 125 kHz.

(b) Transducer 57, F = 156 kHz.

Figure 3.27: Receiving voltage maps of transducer 57 when T49 was transmitting a sinusoidal signal.

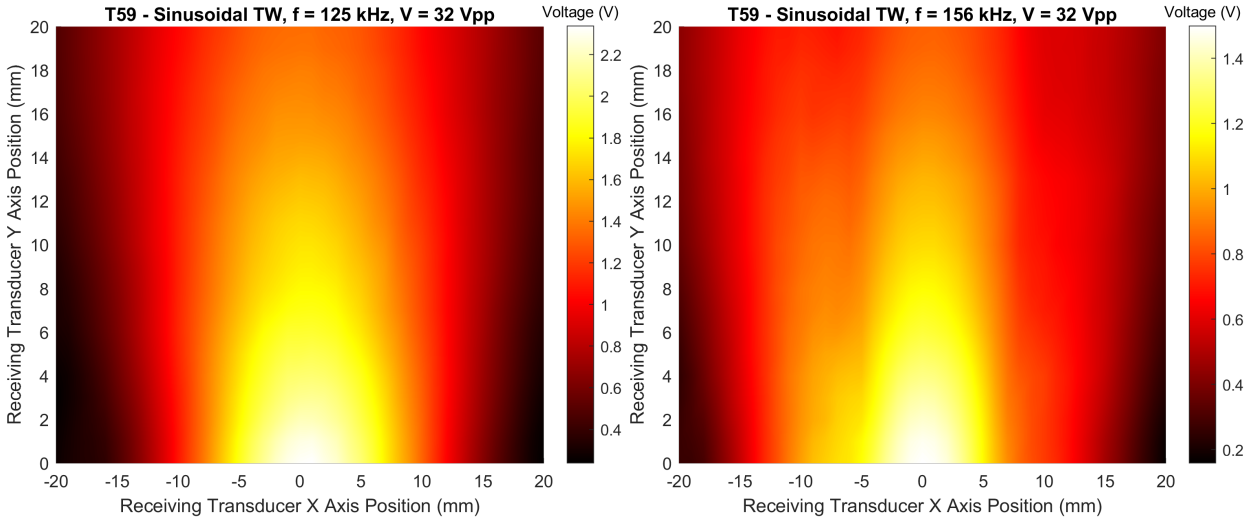

(a) Transducer 59, F = 125 kHz.

(b) Transducer 59, F = 156 kHz.

Figure 3.28: Receiving voltage maps of transducer 59 when T57 was transmitting a sinusoidal signal.

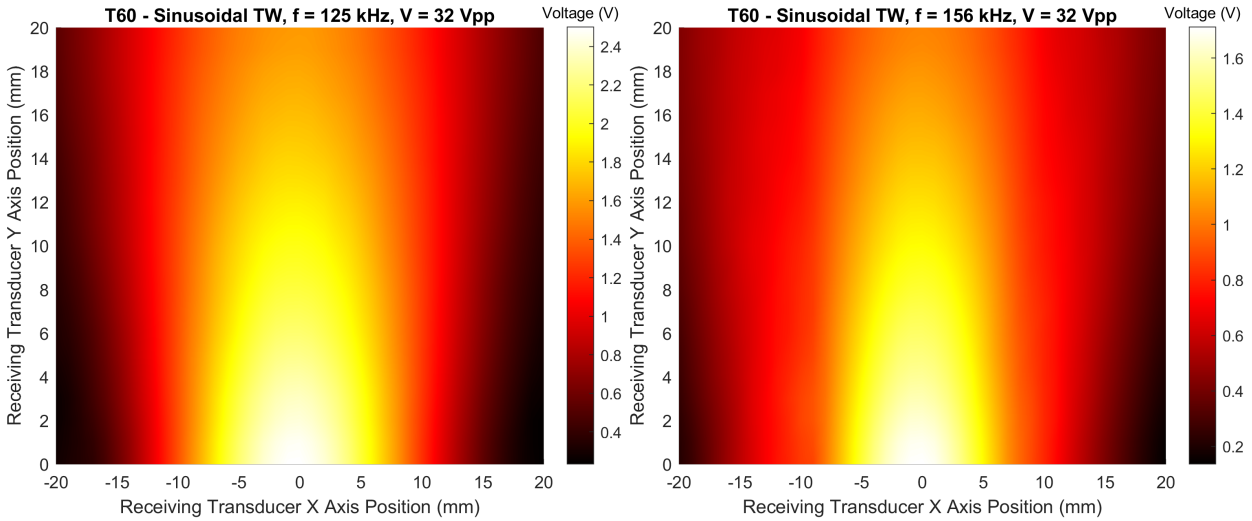

(a) Transducer 60, F = 125 kHz.

(b) Transducer 60, F = 156 kHz.

Figure 3.29: Receiving voltage maps of transducer 60 when T57 was transmitting a sinusoidal signal.

The voltage maps of all the transducers showed similar characteristics. When operating at a frequency of 125 kHz, the beam was wider and more uniform, and the maximum received voltage was greater than when receiving at 156 kHz. Upon comparing the voltage maps with the pressure maps obtained through the hydrophone, it was observed that the main beam was wider and longer in both frequencies. This is a predictable outcome, given that the area of the piston and transducer's

PZT responsible for receiving signals was much larger than the area of the needle hydrophone, resulting in increased sensitivity in receiving signals but decreased spatial resolution. For transducers 57, 59, and 60, the maximum received voltage achieved when operating at a frequency of 125 kHz were 2.388, 2.337, and 2.500 V, whereas, at 156 kHz, they were 1.516, 1.499, and 1.711 V, respectively. Therefore, the maximum voltage variation among these samples was greater when they were operated at 156 kHz (12.09 $\%$) than at 125 kHz (4.583 $\%$), which encourages their use at 125 kHz. Moreover, the differences among the transducers' receiving characteristics can also be evaluated through their voltage profile as shown in Figure 3.30.

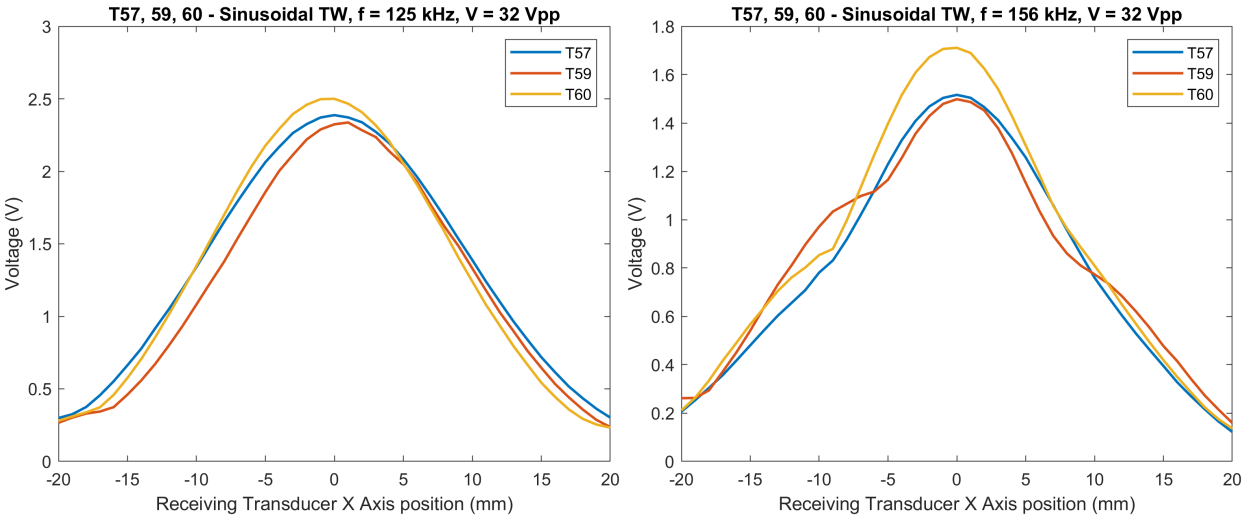

(a) Transducers 57, 59 and 60, F = 125 kHz.

(b) Transducers 57, 59 and 60, F = 156 kHz.

Figure 3.30: Acoustic pressure profiles of transducers 57, 59, and 60 when the receiving transducer is at a 13.94 mm distance from the transducer.

Upon comparison of the voltage profiles computed when the transducer was receiving signals of frequencies of 125 and 156 kHz, it is clear that the decrease in voltage when the receiving transducer moved away from the axial center of the transducer is different among receivers and frequencies. When receiving a signal of frequency 156 kHz, instead of a continuous attenuation of its amplitude as the receiver moves to the left and right of the center axis, there are recovery lobes between the positions $|X| = 6$ to $|X| = 13$. This behavior is similar to the one found when measuring the pressure profile with the hydrophone and could be caused by head flapping [81].

However, when receiving with a transducer instead of the hydrophone, the phenomenon can be accentuated or diminished by the flapping characteristic of the receiver. This analysis was conducted with all the transducers, and the remainder of their pressure profiles can be found in Appendix G.

3.2.8 High-Voltage Operation

The transducers' transmission pressure output and its linearity as a function of the driving voltage, when driven by the Verasonics Vantage™ 64, were analyzed for transmitting signals of frequencies 125 and 156 kHz, a voltage range of 6 to 192 V_{pp}, and five transmitted half-cycles. A segment of the data collected with transducer 39 (transducer with the highest transmission sensitivity) is shown in Figure 3.31

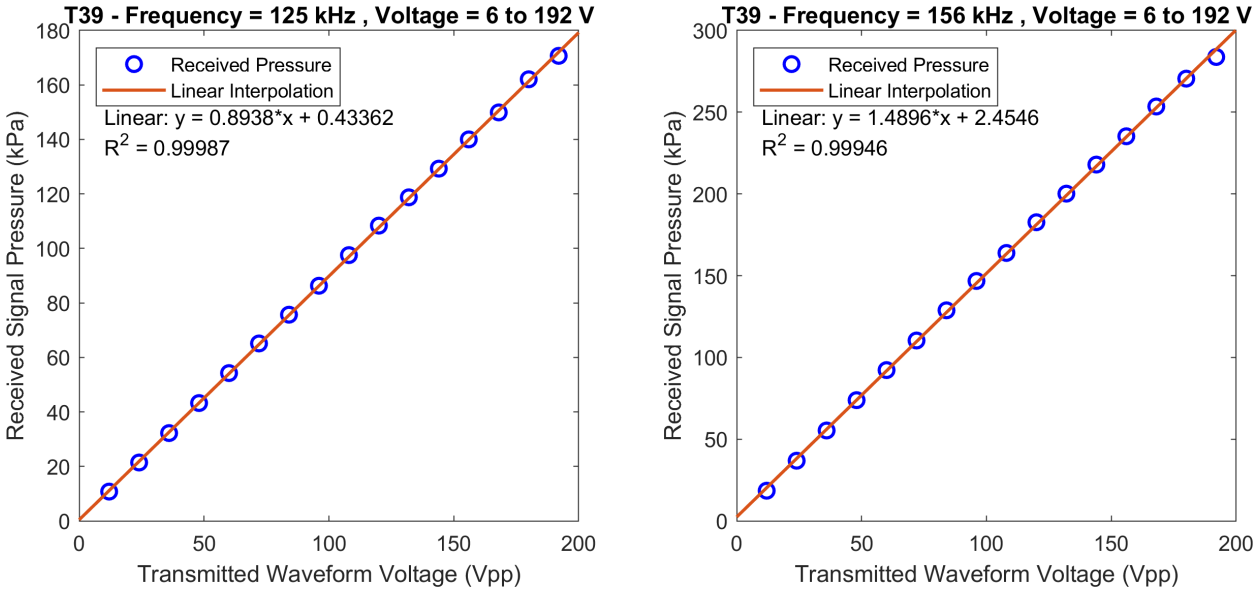

Figure 3.31: Peak-to-peak acoustic pressure output as a function of the driving voltage when the hydrophone was at a distance of 13.94 mm from the transducer.

As observed, the maximum peak-to-peak acoustic pressure achieved by the transducers when driving them with the Verasonics Vantage™ 64 ultrasound tomography system at its maximum driving voltage amplitude (192 V_{pp}) was 170.6 kPa and 283.7 kPa, when operating at 125 and 156 kHz, respectively. The acoustic pressure output as a function of the transmitted waveform voltage presented a linear behavior ($R^2 \geq 0.99946$) for driving voltages within the range of 0 to 196 V_{pp}.

However, it is important to point out that the pressure measured for a transmitted voltage of 192 V_{pp} was the one that presented the highest deviation from the linear interpolation (residual), and could be an indication that the transducers' PZTs had reached their saturation threshold. Therefore, the maximum recommended operational voltage for both frequencies was 180V_{pp}. When the system was operated at the maximum voltage (192 V_{pp}), transmitting with one transducer at a time, the thermal and mechanical indexes, computed as in [84], were 0.1466 and 0.2413 for a frequency of 125 kHz and 0.5059 and 0.3591 for a frequency of 156 kHz, respectively.

3.2.9 Statistical Analysis

The statistical analysis of the data collected during the experiment was performed using an Analysis of Variance (ANOVA) test with a 99% confidence level (F-Table $\alpha = 0.01$). The controlled factors were the transducer and its frequency of operation, while the response variables were the maximum received voltage and transmitted pressure, beam angle, and sensitivities. The residuals of the ANOVA test for all response variables were determined to have a normal distribution and the equal variance assumption was not violated. As such, it was concluded that ANOVA was an appropriate test for this experiment [91]. The results of the ANOVA test indicated that both the transducer and frequency of operation had a significant effect on the response variables (f-values ≥ 3.06 and p-values ≤ 0.001). A descriptive statistics summary and histograms of the response variables are presented in Table 3.4 and Figure 3.32.

Table 3.4: Acoustic calibration descriptive statistics summary.

Frequency	**125 kHz**	**156 kHz**
Max. transmitted pressure (peak-to-peak)	9.837 ± 0.9650 kPa	18.44 ± 2.123 kPa
Beam angle	$35.70 \pm 1.430°$	$30.93 \pm 2.361°$
Max. received voltage	2.638 ± 0.3313 V_{pp}	1.843 ± 0.3082 V_{pp}
Receiving sensitivity	211.3 ± 25.53 $\frac{\mu V}{Pa}$	93.73 ± 15.68 $\frac{\mu V}{Pa}$
Transmitting sensitivity	614.8 ± 60.32 $\frac{Pa}{V}$	1152 ± 132.7 $\frac{Pa}{V}$

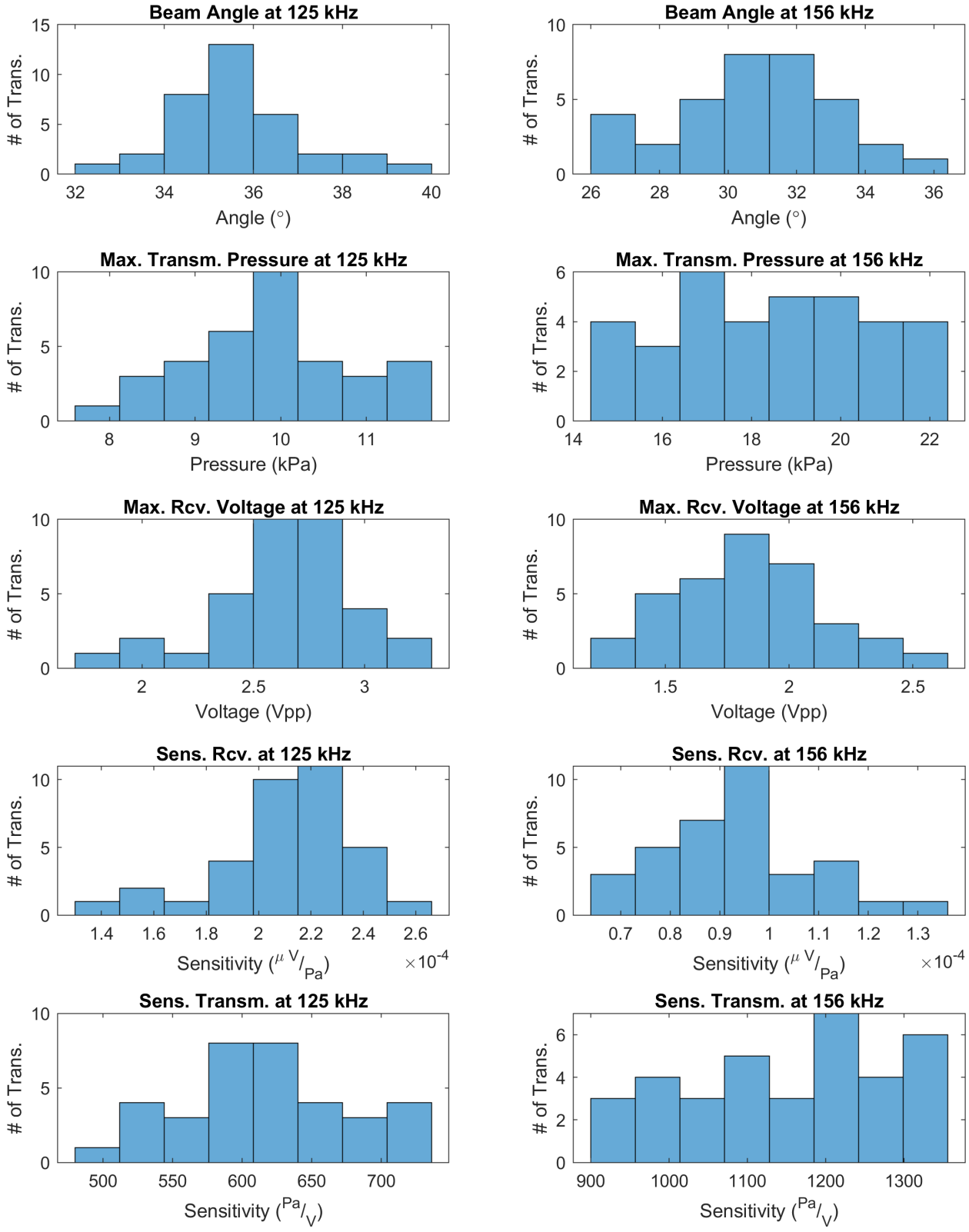

Figure 3.32: Histograms of the maximum voltage and pressure, the beam angle, and the receiving and transmitting sensitivities.

The acoustic properties of all of the built transducers were similar to the ones of transducers 57, 59, and 60, previously presented in Sections 3.2.6 and 3.2.7. The maximum transmitted pressure and its variance were greater when transmitting at a frequency of 156 kHz, while the beam angle was wider and had a lower variance when transmitting at 125 kHz. The maximum received voltage occurred at 125 kHz, even though the transmitter transducers were driven with the same peak-to-peak voltage for both frequencies, and their transmitting sensitivity was higher when operating at 156 kHz. That can be explained by the fact that the receiving sensitivity for signals of frequency 125 kHz is more than double the receiving sensitivity for signals of frequency 156 kHz. Previous studies have shown that the peak of receiving sensitivity can occur at a different frequency than the peak of transmitting sensitivity [98–102]. The differences can be related to several factors, including if the transducer is operating at the longitudinal or flexural (flapping) mode [81, 102], which could explain why the receiving sensitivity was lower at 156 kHz than at 125 kHz. Therefore, it was considered that operating at a frequency of 125 kHz might be advantageous since the beam angle was wider and a lower transmitting pressure was necessary for the received signals to achieve the same or higher amplitude than at 156 kHz. Furthermore, reducing the transmitted acoustic pressure results in a decrease in the Thermal and Mechanical Indices, which is highly desirable in medical imaging.

3.3 Transducer Belt

The transducer belt was designed to hold 32 transducers radially distributed and equally spaced in the same plane. It was constructed in neoprene with two Velcro straps at the end, which confers flexibility and adjustable length, enabling the use of as many transducers as can be fit on the phantom or patient-to-be imaged. This characteristic allows the belt to be used in targets of different shapes and sizes while achieving the best resolution feasible for this particular technology and application. Figure 3.33 shows an illustration of the belt assembly.

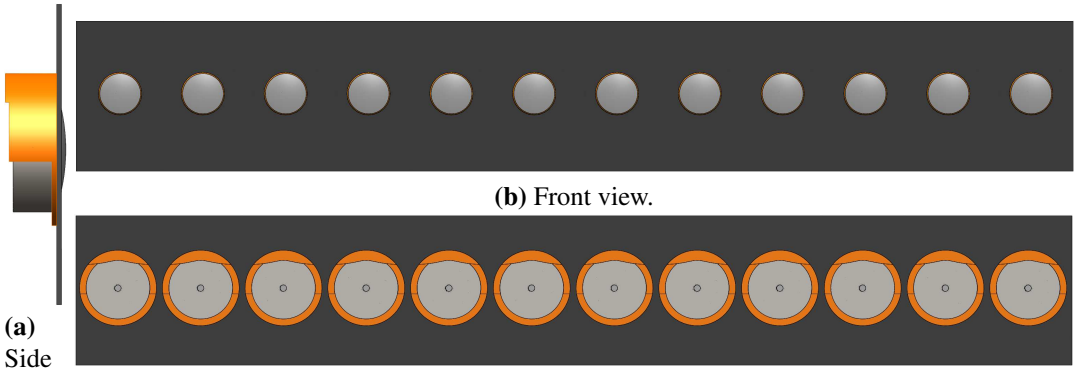

(a) Side view.

(b) Front view.

(c) Back view.

Figure 3.33: Belt design illustration.

As seen in Figure 3.33a, the transducer's tail mass sits flush against the holder, whereas the piston head protrudes from the neoprene, ensuring proper acoustic coupling with the sample, especially when the ultrasonic gel is used. From Figures 3.33b and 3.33c, one sees that the transducers are held horizontally aligned and equally spaced, which is necessary to achieve proper reconstructions. The sensors are attached to the belt using 3D-printed custom-built holders, similar to the ones illustrated in Figure 3.34.

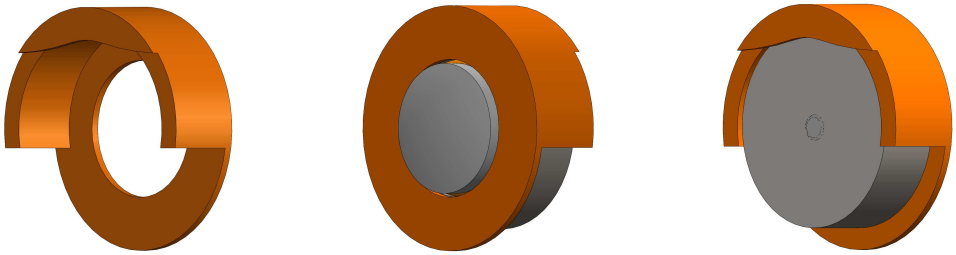

(a) Solo. **(b)** Assembly front. **(c)** Assembly rear.

Figure 3.34: Custom-built transducer holder.

When assembling the belt, the holders are precisely positioned and glued to the neoprene using a spacing and alignment jig, and the holes are cut using a sharp blade right after. Thus, a proper horizontal alignment is achieved when the belt is positioned and stretched out. Furthermore, the holder was designed so that a transducer can be easily replaced without needing to remove the belt

from the imaging target. This feature is essential to ensure that the belt will be kept in the same position during the entire data collection, especially when the subject is lying down.

3.4 Verasonics Vantage 64 Ultrasound System

3.4.1 Data Acquisition Hardware

The Verasonics Vantage^{TM} 64 Ultrasound System offers 64 independent channels with a receive path composed of several stages of analog and digital signal conditioning each, making it a robust system for ultrasound data acquisition. It is offered in three versions, low-frequency, standard, and high-frequency, which operate in the frequency ranges of 50 kHz to 1.5 MHz, 0.5 MHz to 20 MHz, and 2.0 MHz to 42 MHz, respectively. All Vantage^{TM} versions and their channels use a similar data acquisition structure [6], as shown in Figure 3.35.

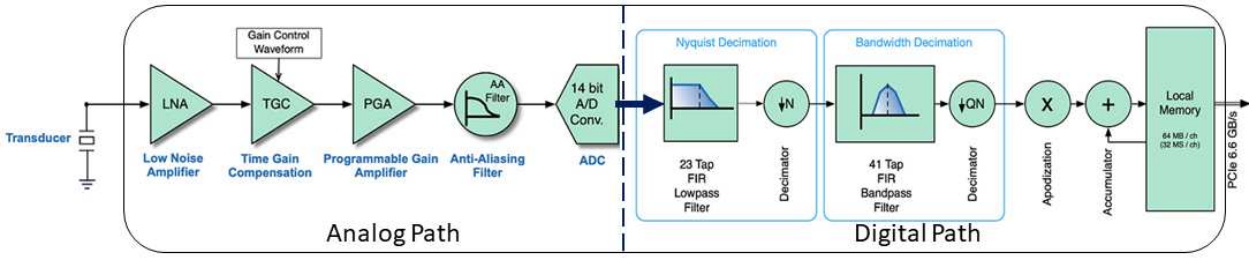

Figure 3.35: Verasonics Vantage 64 Low-Frequency Research Ultrasound System receive path diagram block [6].

A low-noise amplifier receives the electrical signal generated by the transducer with a programmable gain and electrical impedance. This feature enables the gain to be adjusted between 15 and 24 dB and the input impedance to be set to a value within a range of 110 to 3000 Ω, matching the transducers' electrical impedance at the desired operating frequency. Next, the signal is attenuated using a time gain compensation (TGC) block, which aims to reduce the impact of ultrasound wave-front attenuation when traveling through the medium by decreasing the electrical signal's attenuation over time [103]. For this system, the TGC waveform has eight user-defined control points, which determine the attenuation waveform at eight equally spaced steps where the

maximum and minimum attenuation values are -40 dB and 0 dB, respectively. Figure 3.36 shows the effect of using a higher input gain combined with a TGC attenuation compensation technique applied to a segment of data collected with an agar phantom.

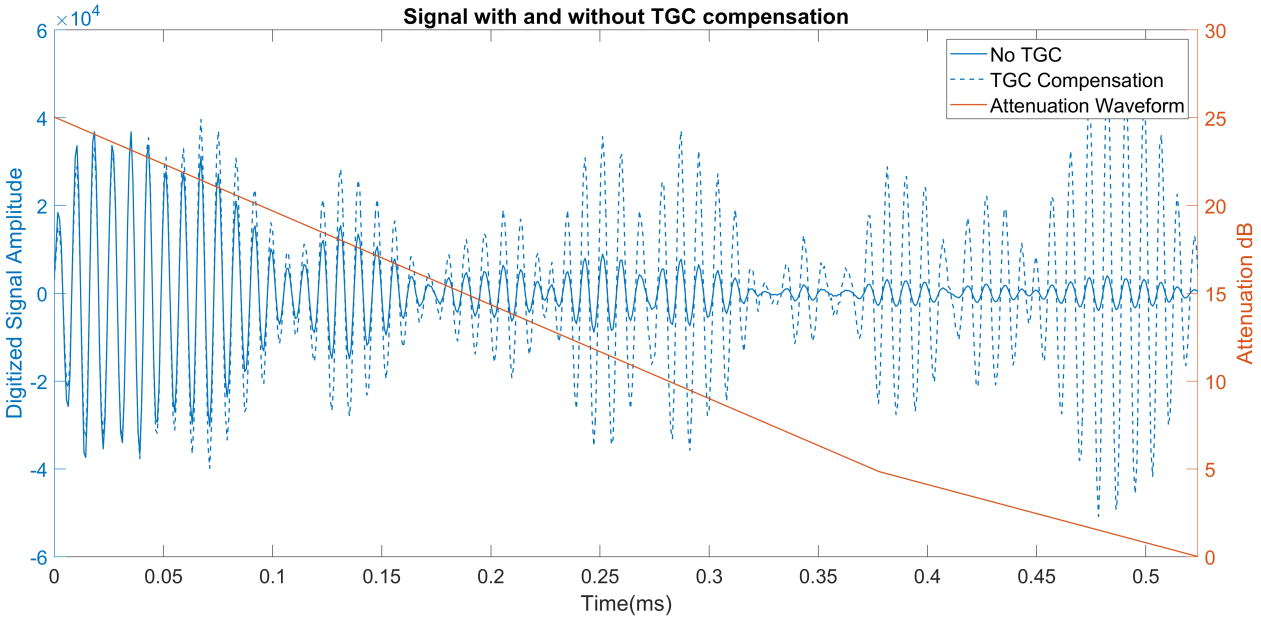

Figure 3.36: Electrical signals received by transducer five with and without TGC compensation.

When analyzing Figure 3.36, one sees that the signal's amplitude without TGC compensation decreases a lot faster over time than the compensated one, which is undesirable. In pulse-echo ultrasound systems, commonly used in medical diagnostics, the echoes returning from the tissue are used to reconstruct the image [104]. Thus, meaningful information about the tissue at higher depths might get lost if the TGC is not used. Properly adjusting the TGC has been shown to be critical in medical procedures that require deeper tissue visualization, such as image-guided biopsy [105] and ultrasound-guided anesthesia [106]. For tomographic ultrasound imaging, where the interest resides in the signal transmitted through the tissue, the application of an adaptive TGC algorithm has shown an increase in SNR and a decrease in RMS error during breast ultrasound tomography, which improved the ability to detect masses [65]. Furthermore, adjusting the TGC in the analog path enables more gain before digitizing the signal and, thus, better utilization of the ADC range, which leads to a better SNR. The final conditioning stages in the analog path are

a programmable gain amplifier (PGA), which can be set to provide a gain of 24 or 30 dB, and a third-order anti-aliasing filter (AA Filter) with a cut-off frequency that can be adjusted from 10 to 50 MHz. The signal is then digitized by a 14-bit ADC with programmable sample rates from 10 to 62.5 MHz.

The digitized signal is further processed at the digital path, of which the first block is a 23 Tap FIR low-pass filter and a decimator. In this step, the data collected at a frequency of up to 62.5 MHz is filtered to prevent aliasing and then downsampled; the filtering frequency and decimation rate will depend on the transmitted signal and transducer's frequency and bandwidth. Next, the signal is filtered by a 41 Tap FIR bandpass filter and decimated again. By filtering and decimating the signal, a portion of out-of-band noise is eliminated while lowering the data rate transmitted to the host. The final stage of the digital processing path is apodization, which is the application of weights with values within the range of -4 to 4 to the acquired signal, enabling, for example, compensation for differences in the transducer's sensitivity. An accumulator is also available and permits averaging several samples when conducting repeatable experiments that would typically generate small signals with poor SNR.

3.4.2 Signal Transmission Hardware

The Vantage^{TM} platform can generate arbitrary waveforms through a high-voltage tri-state PWM module which can output three voltage levels, +V, 0 V, and -V, at clock intervals of 4 ns [107]. The output voltage is adjustable and symmetric, having a maximum absolute value of 96 V_p or 192 V_{pp}. A change in voltage takes at least three clock cycles, which must be taken into account when programming the system. Even though the arbitrary waveform is generated through PWM, high fidelity is achieved due to the presence of an inductive load in series with the output, in addition to the nature of the transducer's frequency response, which typically has a narrow bandwidth, behaving as a band-pass filter [107, 108]. Therefore, multiple transducers can be driven by the power supply as long as the total power drained does not exceed 50 W. For this application, considering the transducers described in Section 3.1 of this document, ten sensors

could be concurrently fired at a voltage of 84.5 V_{pp}, which would translate to an acoustic pressure of 0.438 MPa per actuator.

To define the transmitted waveform (TWF) characteristics, one has to set four main parameters: the center frequency of the equivalent sinusoidal signal, the PWM duty cycle, the number of HCs to be transmitted, and the polarity of the first HC. Figure 3.37 shows the transmitted signal for a sinusoidal waveform with 125 kHz center frequency, 67% duty cycle, 10 and 20 HCs of length, and negative polarity. The TWF can be retrieved from the system through a MATLAB command after each data collection section; more details are shown in Section 3.4.3. When connecting multiple transducers to the system, an apodization vector is used per transmission to define which sensors are active (transmitting signal) and passive (receiving only).

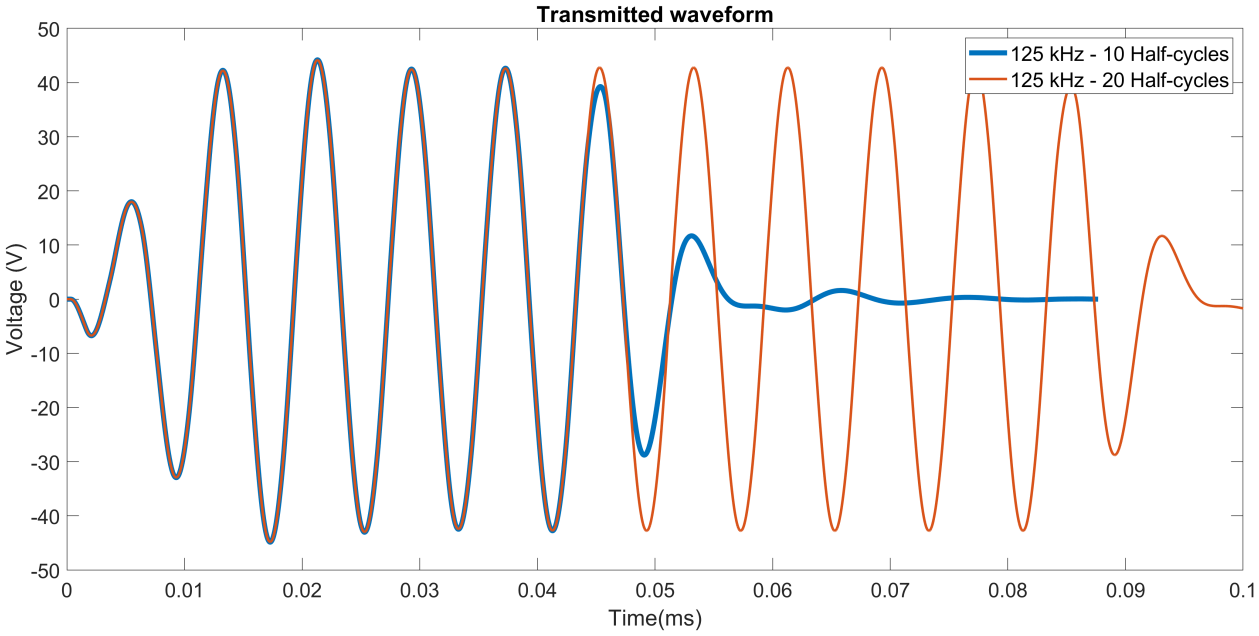

Figure 3.37: Transmitted waveform example for a center frequency of 125 kHz, 50% duty cycle, 10-20 HC, and negative polarity.

3.4.3 Sequence Control

All of the processes and user-defined parameters are controlled through MATLAB, which runs on the host computer, and are specified by global or event objects. Figure 3.38 illustrates the primary event sequence (ES) used in most of the data collections presented in this document.

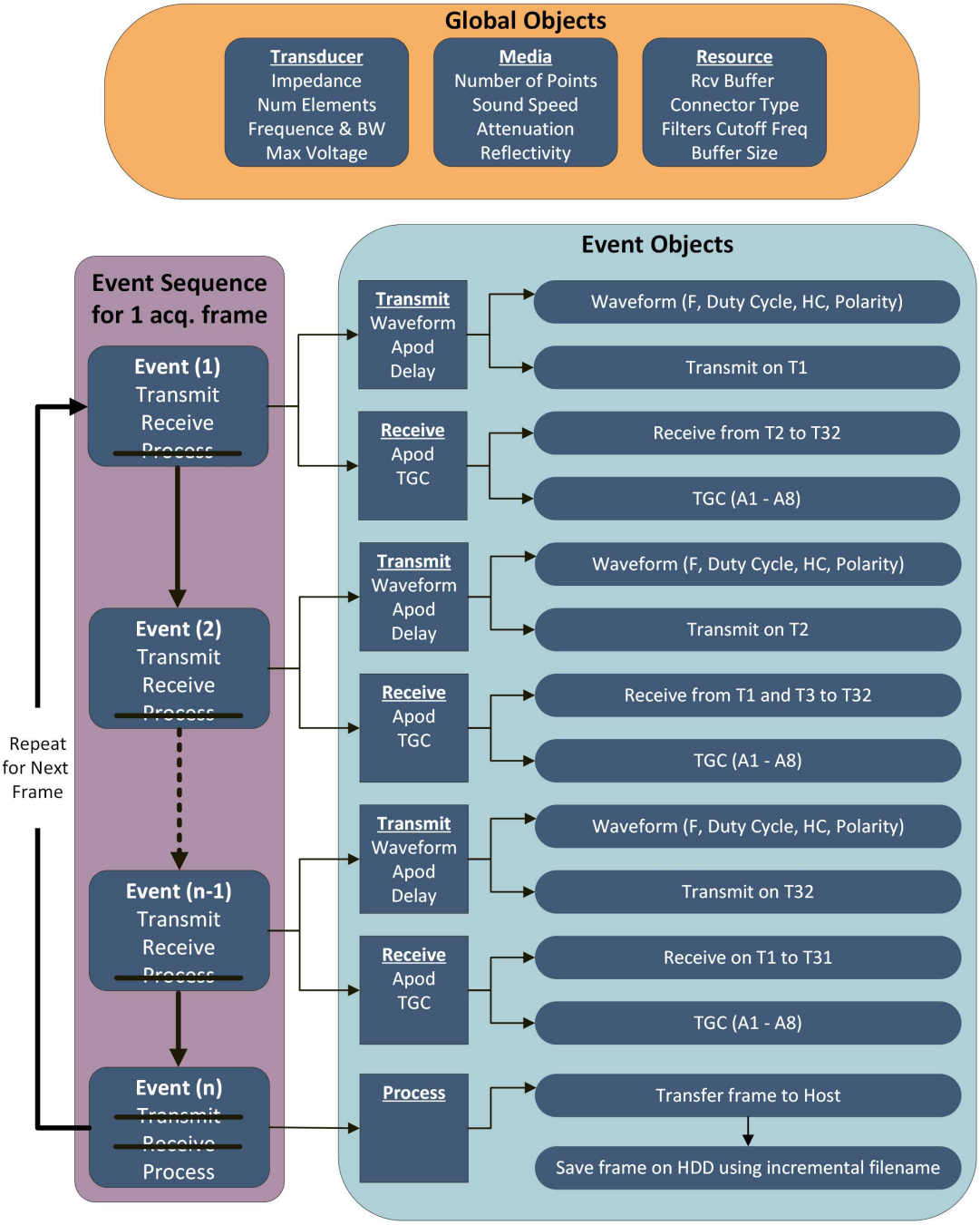

Figure 3.38: Basic event sequence used in most data collections.

The global objects (GO) define fixed parameters during the entire data collection algorithm execution, i.e., the settings cannot be altered between frames. They determine the transducer number, their physical location, electrical characteristics, transmitted waveform attributes, etc. The event objects (EO) determine settings specific to each event that compose the entire data collection individually. When analyzing Figure 3.38, it is essential to notice that a frame is composed of a set of **n** events that can perform multiple tasks, such as transmitting and receiving data, or a process, that can be, for example, the data transference to the host computer. It is also important to point out that the EO varies among events, e.g., for the first event, the transmit Apod will enable transducer one and disable the remainder, whereas, on the second, only transducer two will be active. Furthermore, even though the EOs vary among events, they will be repeated on the subsequent frame acquisition since the ES represents the data collection of one frame only. Figure 3.39 illustrates the execution of the first three consecutive events; the transducers are always fired clockwise. Table 3.5 shows the parameters used as global objects for all of the conducted data collections.

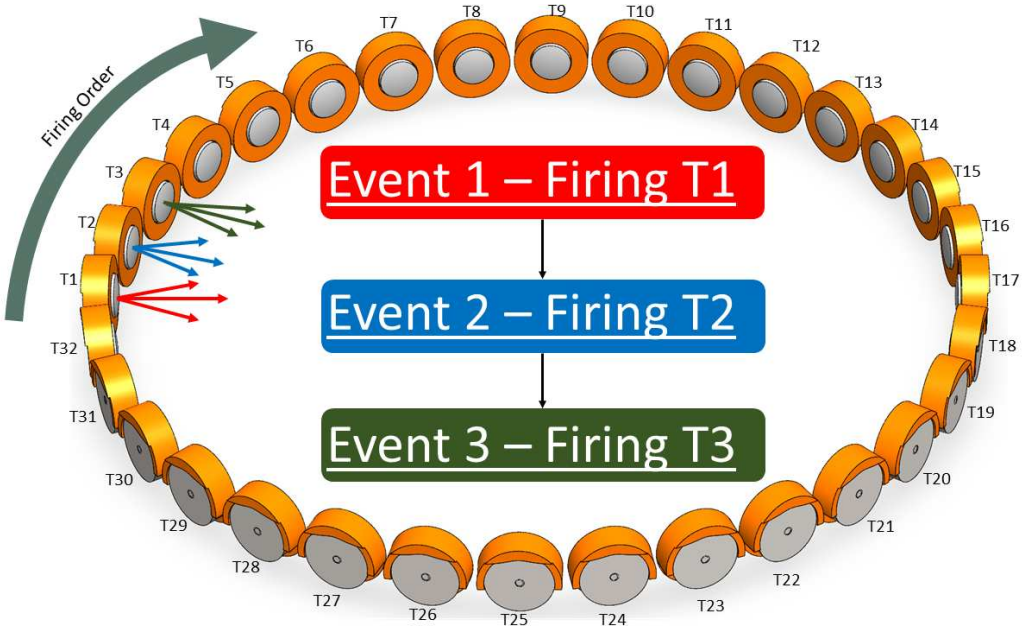

Figure 3.39: Transducer ring-array numbering and firing order.

Table 3.5: Resource global objects' attributes for all data collections.

Transducer	
Frequency (kHz)	125 or 156
Impedance (Ω)	955 or 433
Bandwidth (%)	33
Max. allowed voltage (V_{pp})	130
Num. elements	32
Element width (in)	1
Position	Ring Array, Radius = 6 in
Num. of transmitted half-Cycles	5, 10, 20 and 40
Resource	
Connector type	UA-260 MUX
LNA gain (dB)	18
TGC	Enabled
PGA gain (dB)	24
AA filter cutoff freq (MHz)	5
ADC sampling frequency (MHz)	10
23 TAP FIR filter cutoff freq (MHz)	0.5
Decimator factor	8
41 Tap FIR bandpass filter	Disabled
Quad decimator factor	Disabled
Receive apodization	Disabled
Receive accumulator	Disabled
Final sampling frequency (MHz)	1.25
Rcv. buffer rows per frame	40960
Time to next acquisition (μs)	4365

Notice that there are two frequency and impedance values in the transducer section of Table 3.5; for each data collection, the system was run twice, once in each frequency, and at least two datasets were collected. The number of transmitted HC was selected based on the application, and more than one value was often used for the same experiment for comparison.

The resource parameters shown in the Resource section of Table 3.5 refer to the stages shown in Figure 3.35 and are common to all data collections except for the TGC, which was manually adjusted on every experiment based on the attenuation of the signals on that particular sample. A few features on the digital path were disabled to prevent further data downsampling. Thus, the data were collected at a frequency rate of 1.25 MHz, approximately eight times higher than the highest operating frequency, and considered adequate for the transducers' bandwidth.

Before transferring the data to the host, a full frame of ultrasonic measurements is stored in the system's buffer in a matrix with 40960 rows and 32 columns where each received signal has a length of 1280 rows, and each column represents the received signal in all transducers when the transducer that has the same number as the column is active. For example, the signals received by transducers one to thirty-one when transducer thirty-two is active are stored in column thirty-two. Finally, at the end of the data collection of each frame, the buffer content is transferred to the host and stored in its main hard drive.

3.5 Data Processing

The first step of the developed data processing procedure is to import the files into MATLAB's workspace and transform the extended 2D matrix of size 40960 x 32 into a 3D array of size 32 x 32 x 1280, where the rows and columns represent the receiving and transmitting transducer, respectively, and the 3rd dimension, the data. Next, each array is stored in a structure array, where the first field has the dataset name, which includes information such as the target, experiment date, and the transmitted waveform parameters. In contrast, the sub-fields carry information about any post-processing performed.

All of the data is handled offline, and the processing depth will depend on whether the measurement's nature is time-dependent. The steps illustrated in Figure 3.40, however, are common to all types of data.

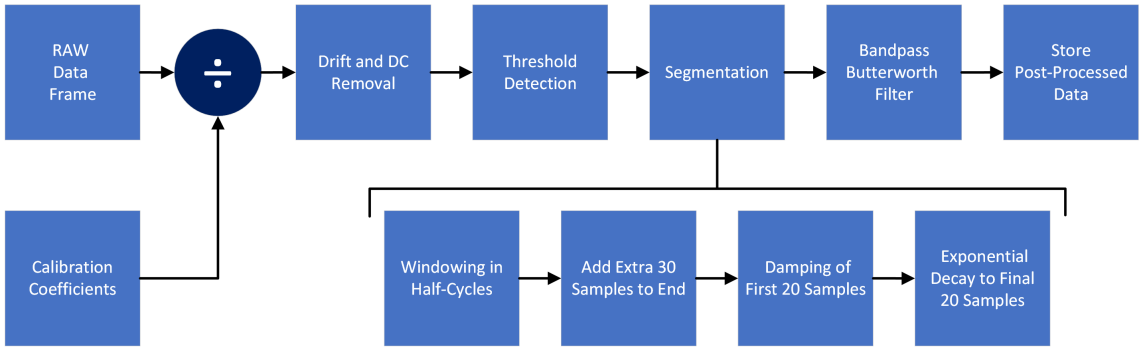

Figure 3.40: Basic ultrasonic signals' post-processing procedure.

The first step of the data processing procedure is the application of the calibration coefficients to each data segment based on its transmitting and receiving transducers. For the data analyzed prior to the transducers' acoustic calibration, the coefficients applied were the ones shown in Section 3.1.3, which resulted in an output data named Digitized Voltage since it refers to the corrected value of the voltage measured by the ADC. For the data analyzed after the transducers' acoustic calibration, the output variable is given in pressure since it was computed based on the received voltage and the transmitter and receiver sensitivities as determined in Section 3.2. After applying the calibration coefficients, the DC and voltage drift is removed by computing and subtracting the moving average from each data section; the window length is adjusted based on the dataset. The third step is the application of a threshold, which is determined per file based on the calculation of the noise level of the first fifty samples of the data section. The algorithm determines the index of the first non-zero element and sends it to the segmentation function with the original data.

The segmentation function uses the index previously calculated to apply the threshold to the dataset by adding zeros from the beginning of the data segment to the first non-zero element. Next, it performs the signal segmentation; the window width is determined based on the number of listening HC desired; for example, for a twenty HC listening period, considering data collected at

125 kHz, a window width of 100 samples is used. Next, an extra 30 samples of data are added to the end of the segment, and an exponential decay is applied to those samples to avoid discontinuities. In addition, logarithmic damping is applied to the first 20 samples of data. After that, the segment of pre-processed data passes through a 12^{th} order band-pass Butterworth filter with a pass-band width of 30 kHz, and the center frequency equals the transmitted frequency used on the particular dataset. Finally, the data segment is stored into a vector with a fixed length and filled initially with zeros; the beginning of the segment is inserted at the original first non-zero element, previously calculated. Therefore, the time-of-flight information is preserved during data processing. Figure 3.41 shows a segment of RAW and post-processed data.

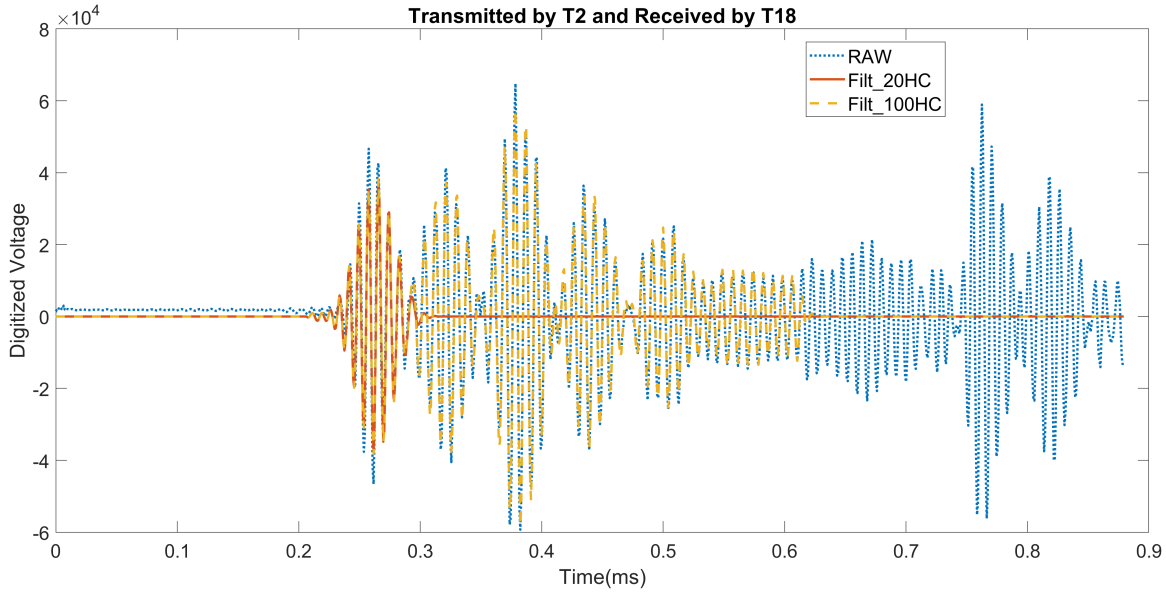

Figure 3.41: RAW and filtered experimental data received on transducer eighteen when transmitted by transducer two through a circular, intact agar phantom.

When comparing the RAW signal with the filtered ones using a segmentation window of 20 and 100 HC, it is clear that the temporal information is not lost; all of the segments have their first received lobe starting at the same point in time. It is also noticeable that both yellow and red signals have a dampened beginning and end and different lengths, as expected. Furthermore, it is shown that the noise that precedes the first lobe, the DC, and the drift were removed in both filtered segment lengths.

3.6 Boundary Detection

Differently from a traditional CT device, the sensors that compose the developed system are not fixed to a mechanical apparatus that would enable their position to be tracked at all times. Instead, the transducers are attached to a flexible belt whose shape conforms to the sample, implying that their position will depend on the belt length, their number, and the phantom or subjects' shape. When conducting image reconstructions based on data collected on a tomographic configuration, it is imperative to determine the position of the sensors to allow an accurate reconstruction of the internal structures of the object being scanned. If the position of the sensors is unknown or incorrect, the resulting image might be distorted, show artifacts, or mimic actual anatomical structures, which is highly undesirable. Therefore, a boundary detection method based on 3D scanning or image processing was developed for this project and is illustrated in Figure 3.42.

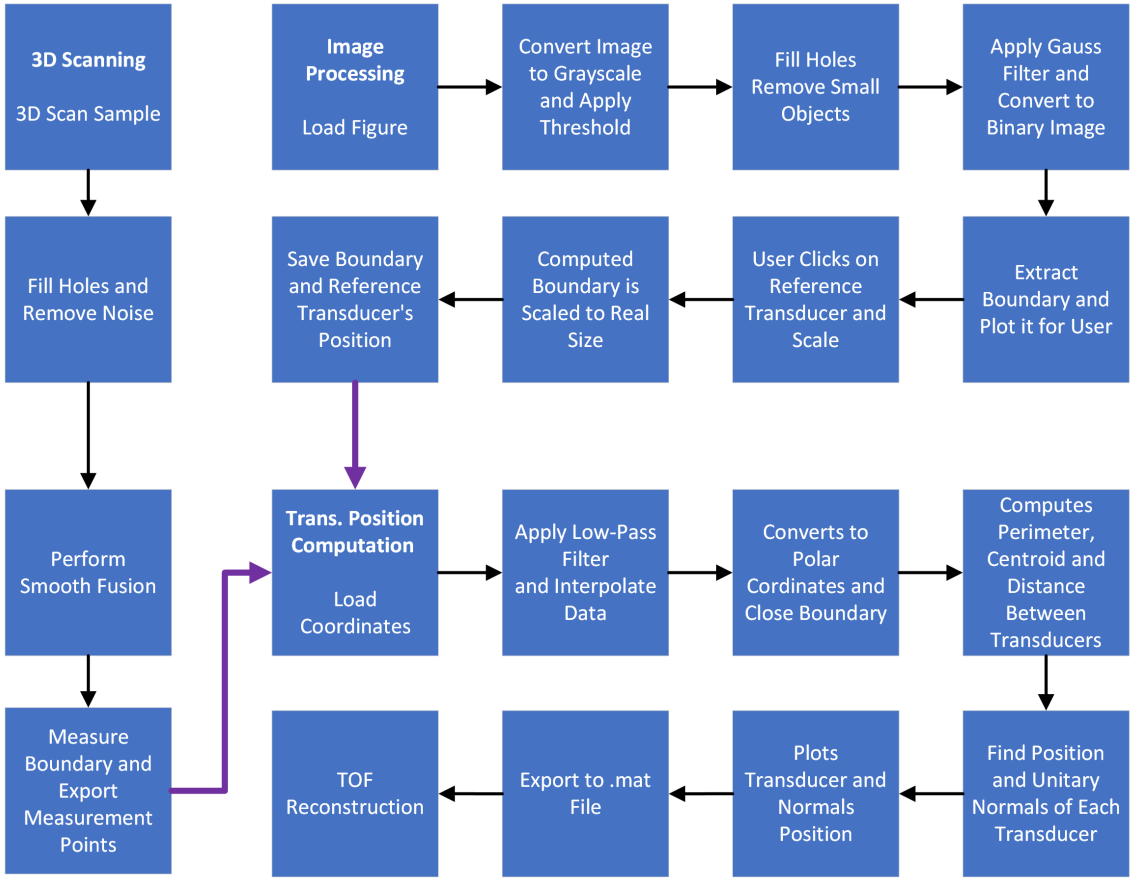

Figure 3.42: Boundary detection method diagram.

The first step towards calculating the transducers' position is to determine the domain boundary coordinates, which can be accomplished by performing a 3D scanning of the sample using a professional 3D scanner (Artec Eva Lite) or through image processing. When using the 3D scanning method, a sample is scanned, generating a cloud of points which is processed to remove noise and holes and is measured, generating a list of coordinates representing the object's shape where the belt was located during the experiment. The second method is to extract the boundary from an image, such as a CT scan, for example. That image is processed and filtered, and a boundary is generated and shown to the user as a form of a plot. The user then clicks on the reference transducer and the extremities of the scale, and the real-sized boundary is computed. Next, the data is exported and loaded into the main algorithm (Trans. Position Processing), which computes the position of each transducer and a unitary component that is normal to its piston. These coordinates are used by the TOF reconstruction algorithm to determine each transducer's position and which direction it is pointing toward. Examples of boundaries computed from a 3D scan and a CT scan are shown in Figures 3.43 and 3.44, respectively.

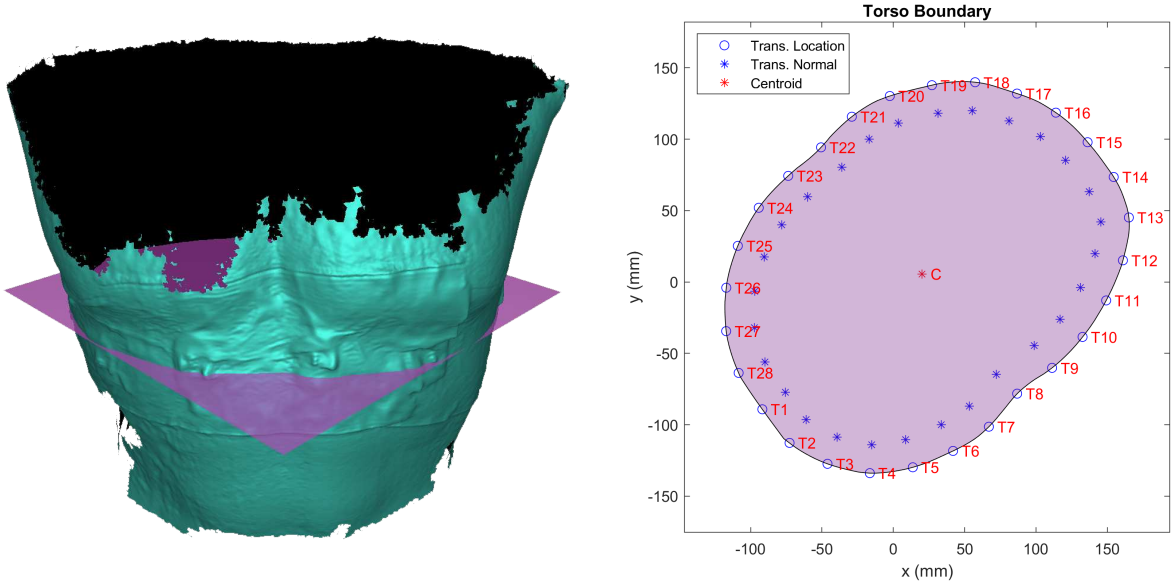

(a) 3D scanned torso. **(b)** Computed boundary.

Figure 3.43: Boundary determined based on the torso's 3D scan.

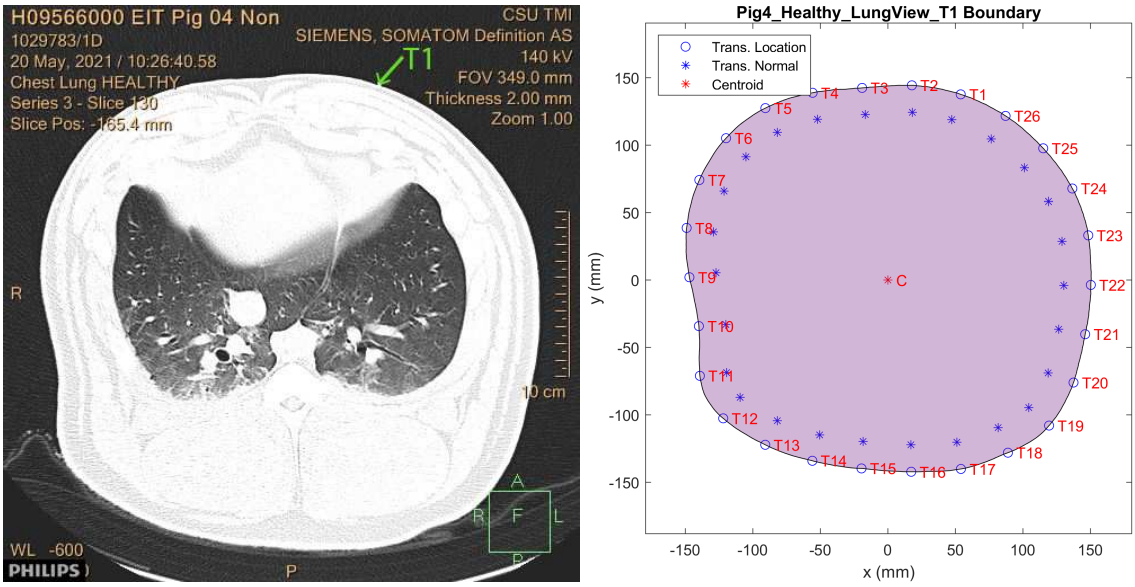

(a) CT scan from Pig 4.

(b) Computed boundary.

Figure 3.44: Boundary determined based on Pig Four CT scan.

The algorithm developed was able to properly detect the boundary and compute the transducers' position, and normals from the 3D scanned coordinates and CT scan image. In Figure 3.43a, the purple square represents the auxiliary cross-sectional plane used to slice the 3D scanned surface and determine its boundary on the transducer belt plane. As seen in Figure 3.43b, the noise and irregularities caused by the 3D scanning procedure were eliminated, and the transducers' location and normal were accurately computed. The same behavior is observed in Figure 3.44, where it is noticeable that the detected boundary shape and transducer one location are similar to the one shown on the CT scan.

3.7 Final Assembly

The USCT system was assembled in a modified rugged utility cart to enable easy and safe transportation. Figure 3.45 shows the final system's assembly, where some constructive details can be seen, such as the oversized pneumatic tires, the 3D printed transducer connection panel, the Verasonics^{TM} system with the Ribbon Cable Break-out Board adapter, the transducer cables, belt, and host computer. It is also vital to notice that the critical parts of the system were securely

strapped to the cart, which prevents them from tipping over, even if the cart is rolled on non-level terrain. In addition, a 50 ft long power cord was incorporated into the system, which, combined with the 7 ft long transducer cables, enables the system to be used in most typical hospital room layouts.

(a) Front view. **(b)** Side view.

Figure 3.45: USCT system fully assembled.

Chapter 4

Experimental Data

The system was evaluated through several experiments conducted with various in-house developed phantoms made using different materials and dimensions. The first test was conducted on a solid agar slab, followed by a water-filled bucket-shaped ballistic gel phantom and a torso-shaped ballistic gel phantom with two internal cavities that simulated lungs. Each experimental iteration had its complexity increased and allowed us to refine the data processing and reconstruction algorithms that were later used to assess data collected with vertebrate animals, shown in Section 5.

All the TOF image reconstructions shown in this document were computed by Jennifer L. Mueller from Colorado State University, Fort Collins, CO, USA, using a sequence of linear least-squares problems solved by the Gauss-Newton method and conjugate gradients, as in [109]. Refraction correction was applied to the signal using a Fast Marching Method [110]. The algorithm computes the sound speed distribution of the sample based on the travel time of the sound waves transmitted through it during USCT [111]. However, it is crucial to point out that, unlike X-Rays, used in CT Scans, the sound waves do not follow a straight line from the source to the detector; they follow a refracted path that minimizes the travel time between two points. The method proposed by [109] takes the refraction of the waves into account when computing sound speed maps, which is more accurate than traditional TOF methods; hence it was chosen for this application.

4.1 Agar Phantom Data

The experiment was conducted using an agar-made circular phantom with 14 inches in diameter and four inches in thickness. Thirty-two transducers were used to collect ultrasonic data; the transmitted waveform frequency and amplitude were set to 125 kHz and $20V_{pp}$, respectively, and five HC were transmitted. Data was collected in different configurations, first with an intact slab and then by adding non-homogeneity by cutting cylindrical holes in the agar and plugging them with targets of various densities. Figure 4.1 shows the experimental setup for three cases.

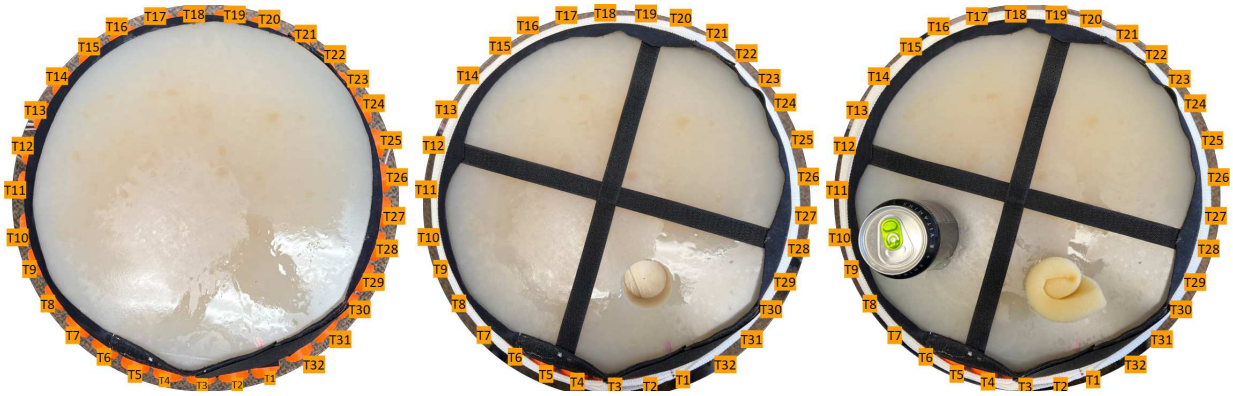

(a) Intact. **(b)** One Hole. **(c)** Two plugged holes.

Figure 4.1: Experimental setup for data collection using an agar phantom.

As seen in Figure 4.1, the transducer belt was strapped around the circular phantom, and an elastic bandage and Velcro were used to ensure a steady positioning of it during the entire experiment. In addition, the transducers' pistons and agar surfaces were coated with ultrasonic gel to improve their acoustic coupling. It is essential to point out that agar is stiffer than human skin; thus, it does not properly conform to the transducer shape, making using ultrasonic gel imperative. After conducting the experiment, the data were analyzed offline and processed using the procedures described in Section 3.5; Figure 4.2 shows a few segments of data collected from transducer four when sixteen is firing for different phantom conditions.

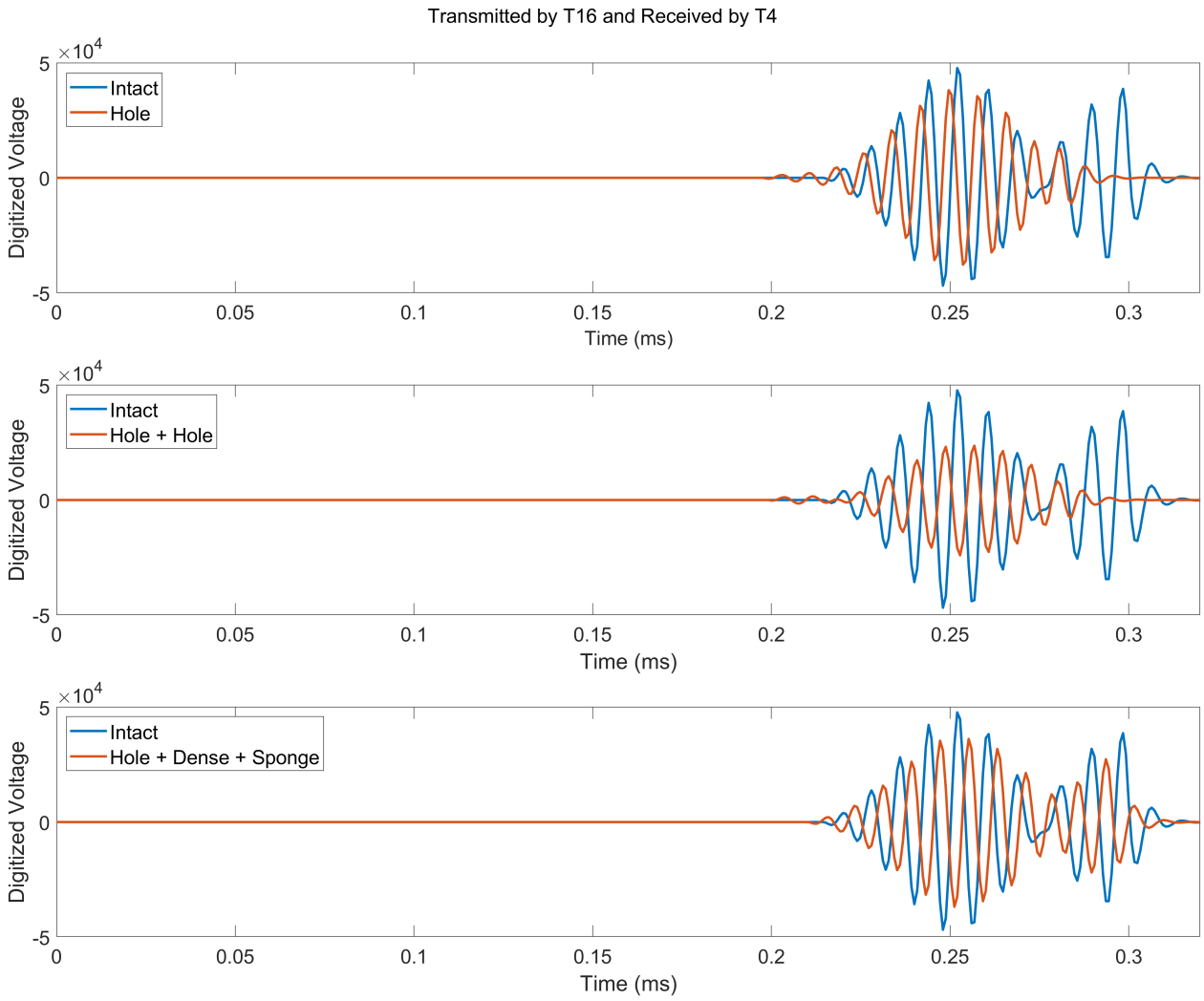

Figure 4.2: Segments of data received by transducer four when sixteen is firing for all phantom conditions.

The nomenclature used to define the agar phantom conditions when collecting the data shown in Figure 4.2 is:

- Hole: the phantom had one empty hole near transducer one.
- Hole + Hole: the phantom had two empty holes, one next to transducer one and another next to transducer 10.
- Hole + Dense + Sponge: the phantom had two holes, of which the one next to transducer one was plugged with a sponge soaked in ultrasonic gel, and the one next to transducer 10 was plugged with a can full of liquid.

The signals received by transducer four were analyzed for a listening period of forty HC, which is typically equivalent to the first received lobe. A few conclusions can be drawn from the study, which are:

- The received signal after the first hole was drilled in the phantom, refer to Figure 4.1b, had a smaller amplitude than the one received when the agar slab was intact; it also presented a phase-shift of 54°.
- When the second hole was drilled in the agar slab, the amplitude of the received signal decreased more, and the phase shift changed to 108°.
- Once the holes were plugged with the unopened can of soda, which had a higher density than air, the amplitude of the received signal had almost the same level as when there was only one hole, and the phase changed to 72°, which was in between the two previous cases.

When looking at the wavefront path between transducers sixteen and four, in Figure 4.2 , it is seen that it was not completely blocked by any of the holes. However, since the transducer had a beam angle of 35°, the agar-air interface created by the holes caused reflections that interfered with the wavefront and, thus, changed the signal received on transducer four. Moreover, the second hole obstructed a larger area of the transverse section path between T16 and T4 than the first one, which explains the more drastic decrease in the amplitude and change in phase. It could also explain why these characteristics improved when the second hole was plugged with the dense object.

To examine the effect of sponge addition to the first hole, the signal transmitted by transducer sixteen and received by thirty-two was analyzed for all conditions. As shown in Figure ,4.3 there was no difference in the signal received when having one or two plugged or empty holes. When observing the path between T16 and T32, Figure 4.1c, it is clear that the hole plugged with the sponge obstructed most of the wavefront, and that could explain why the signal's behavior was different from the previous case. Moreover, since the sponge insertion caused no measurable difference in the received signal, it was considered that it did not improve the transmission of the sound waves through the hole.

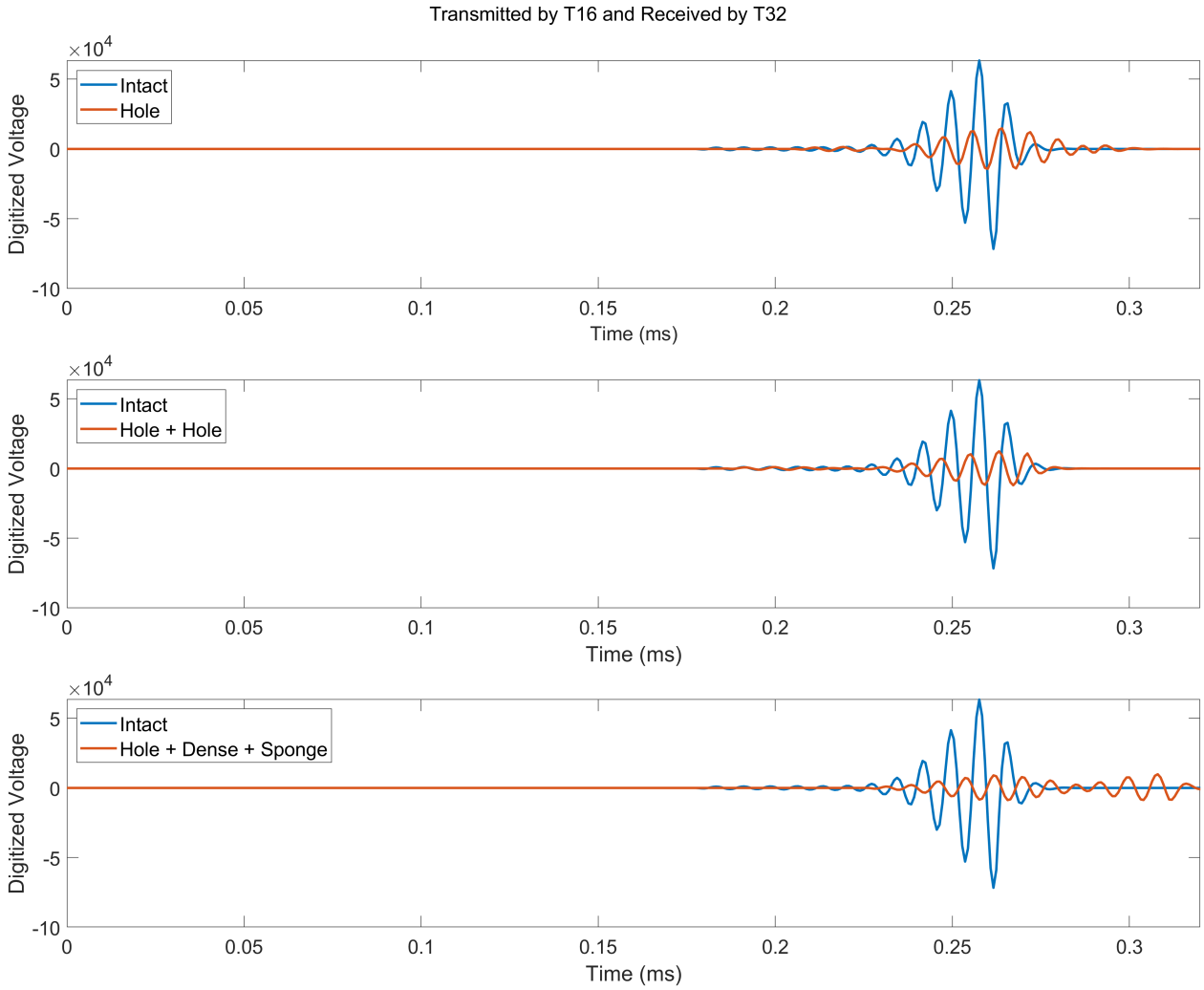

Figure 4.3: Segments of data received by transducer four when sixteen is firing for all phantom conditions.

4.1.1 Time-of-Flight Reconstructions

The reconstructions depicted in this chapter were computed using calibration coefficients determined from the transducers' piston displacement, as explained in Section 3.1.3 of this document. However, they were computed as difference images, with the dataset collected when the agar phantom was intact as a reference. This likely compensated for the uncertainty arising from the absence of an acoustic calibration. It is essential to note that this was merely a preliminary test and that a reference dataset would not be available in a practical setting. Therefore, this issue was addressed beginning in Section 4.2.2; all the reconstructions shown in subsequent sections are absolute images that require no prior knowledge of the medium.

Figure 4.4 shows the preliminary TOF reconstructions of the data collected from the agar slab with different inhomogeneities, collected at a frequency of 125 kHz, an amplitude of 20 V_{pp}, five transmitted HC, and a listening period of 60 HC. The transducers are represented by the red dots; transducer one is located in position $x = 177\ mm$ and $y = 0\ mm$, and the numbering is incremented counterclockwise, e.g., transducer 17 is located in position $x = -177\ mm$ and $y = 0\ mm$.

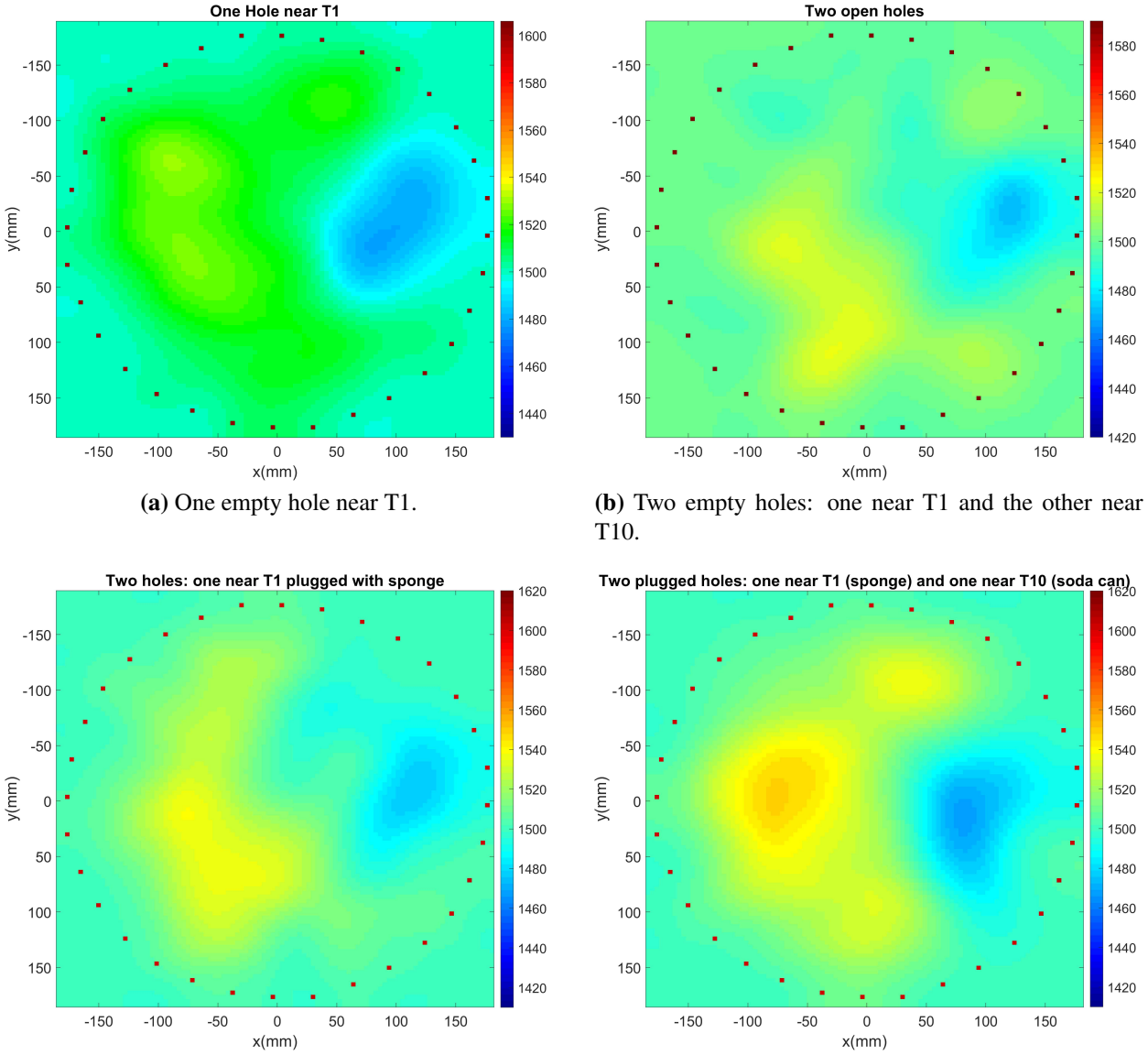

(a) One empty hole near T1.

(b) Two empty holes: one near T1 and the other near T10.

(c) Two holes: one near T1 (plugged with sponge) and the other near T10 (empty).

(d) Two holes: one near T1 (plugged with sponge) and the other near T10 (plugged with soda can).

Figure 4.4: TOF reconstructions of the agar phantom experiment.

The first characteristic of the sound speed maps computed through TOF reconstruction is that the different inhomogeneities configurations resulted in slightly different images, which was considered promising due to the fact that the agar slab was only 4 inches thick, leading to undesirable levels of reflections of the ultrasonic signals. An interpretation of the figures computed is itemized below:

- Figure 4.4a: the data was collected with only one empty 50 mm diameter hole that can be identified in the reconstruction by the dark blue region centered around the coordinates $x = 105\ mm$ and $y = -4\ mm$, which is very close to where it was physically located in the phantom.

- Figure 4.4b: the data was collected with two empty holes, one with 50 mm diameter and the other with 66 mm. The first hole can be identified in the reconstruction by the dark blue region centered around the coordinates $x = 105\ mm$ and $y = -4\ mm$, and the second caused a light blue shadowing close to transducer 10, which is where it was located on the agar slab.

- Figure 4.4c: the data was collected with one empty hole (65 mm diameter, located next to transducer 10) and a plugged one (50 mm diameter, located next to transducer 1, plugged with sponge). The plugged hole can still be identified in the reconstruction by the dark blue region centered around the coordinates $x = 105\ mm$ and $y = -4\ mm$, and the second caused a light blue shadowing close to the transducer 10, which is where it was located on the agar slab. That indicates, as expected that the sponge has not caused any measurable changes to the sound transmission and refraction through the phantom.

- Figure 4.4d: the data was collected with two plugged holes, one with a can of soda (65 mm diameter, located next to transducer 10), and one with the sponge (50 mm diameter, located next to transducer 1). The hole plugged with the sponge could still be identified in the reconstruction by the dark blue region centered around the coordinates $x = 105\ mm$ and $y = -4\ mm$, and the one plugged with the can of soda caused a light yellow area close to

the transducer 10, which is where it was located in the agar slab. That indicates, as expected that the sponge has not caused any visible changes to the sound transmission and refraction through the phantom, but the soda can (high-density object) has increased the sound speed in that area.

As a very preliminary study, it was considered that the results achieved were promising; even with the experiment's limitations, the first hole punched into the agar slab was identified in the proper location. In addition, inserting the can of soda on the agar slab seemed to have increased the sound speed on the second hole, which was an expected behavior due to its density, which is higher than air or agar. It is imperative to mention, though, that the shape of the targets was not accurate and that there were notable artifacts in the reconstructions that could have been caused by several reasons, such as the presence of non-visible cracks and inhomogeneities in the agar slab, its thickness, or even a non-ideal listening period and signal filtration process. Therefore, we believe that conducting an experiment with a thicker and better-constructed phantom could lead to signals with fewer reflections, facilitating the data interpretation and processing and enabling better reconstructions.

4.2 Ballistic Gel Phantom Data

The phantoms used in the experiments shown in this section were made in-house using a standard ballistic gel mixture with a density of 18% in weight. For each experiment, a mold was built in the desired shape and filled with the ballistic gel mixture, which was later cooled to 40° F for at least 48 hours and then unmolded. The experiments were then conducted in various configurations to evaluate the ability of the system to detect targets of distinct dimensional and acoustical properties.

4.2.1 Bucket-Shaped Phantom

To mimic a simplified torso, a ballistic gel cylindrical phantom shaped like a bucket was constructed with 281 mm diameter, 205 mm depth, and 26.1 mm wall thickness. The phantom was

made using two cylindrical molds of different sizes; a large mold was used to externally shape the gel, while a small one was used to create the cavity. Figure 4.5 shows more details of the experimental setup.

(a) Top view. **(b)** Side view. **(c)** phantom with the belt.

Figure 4.5: The ballistic gel phantom and experimental setup.

As shown in Figure 4.5c, the transducer belt was positioned mid-height on the phantom. A layer of ultrasonic gel was applied to the transducers to improve the acoustic coupling between the transducer and the ballistic gel. A self-adhesive bandage strap was used to secure the belt in place and compensate for the slippery nature of the phantom's surface. Next, a plastic cylinder rim was positioned right above the belt to reference transducer numbering and to prevent the phantom from overstretching due to the water pressure applied to its walls when filled up. Twenty-four transducers were used to collect ultrasonic data; the transmitted waveform frequency and amplitude were set to 125 kHz and 10 V_{pp}, respectively, and five HC were transmitted on one transducer at a time, in clockwise firing order, while listening on all the remainder.

Two balloons filled with air were used as targets to simulate an air-filled lung, whereas an empty glass bottle was used to simulate a high-density organ such as the heart. The diameter of the targets was: 48 mm for the green balloon, 41 mm for the blue balloon, and 57 mm for the glass bottle. The targets were positioned in different locations of the tank. The results were evaluated

by reconstructing the sound speed map in the plane of the transducer array using a TOF algorithm applied to the post-processed data. All of the targets used in the experiment were fully submerged in the water solution during the data collection. The signals received by the transducers were analyzed for each test case before reconstruction based on the target's type and position relative to the transducer number, as defined in Figure 4.6.

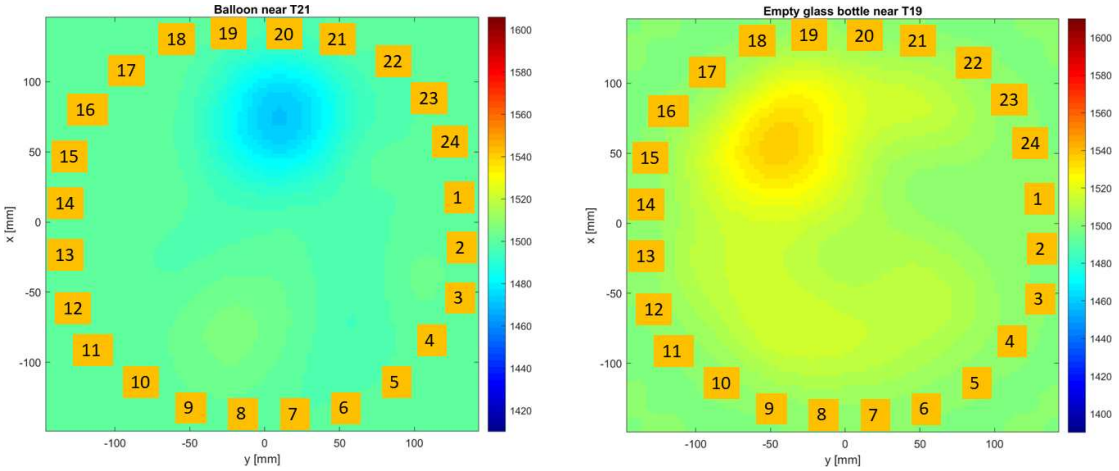

(a) Balloon near transducer 21. **(b)** Glass bottle near transducer 19.

Figure 4.6: Transducer numbering reference for all reconstructions.

A segment of digitized electrical signals received by all the transducers when transducers 19 or 21 are individually fired, with and without targets with different properties, is shown in Figures 4.7 and 4.8.

When analyzing the received signals shown in Figures 4.7 and 4.8, it is clear that their amplitude, phase, and TOF vary among transducers depending on their position on the ring array and the target's properties and location on the tank. A summary of the findings when comparing the signals received by all transducers when the balloon was placed near transducer 21 versus with a water-filled phantom is shown below:

- Transducers 20 to 24: similar behavior in terms of TOF, amplitude, and phase with and without the balloon.

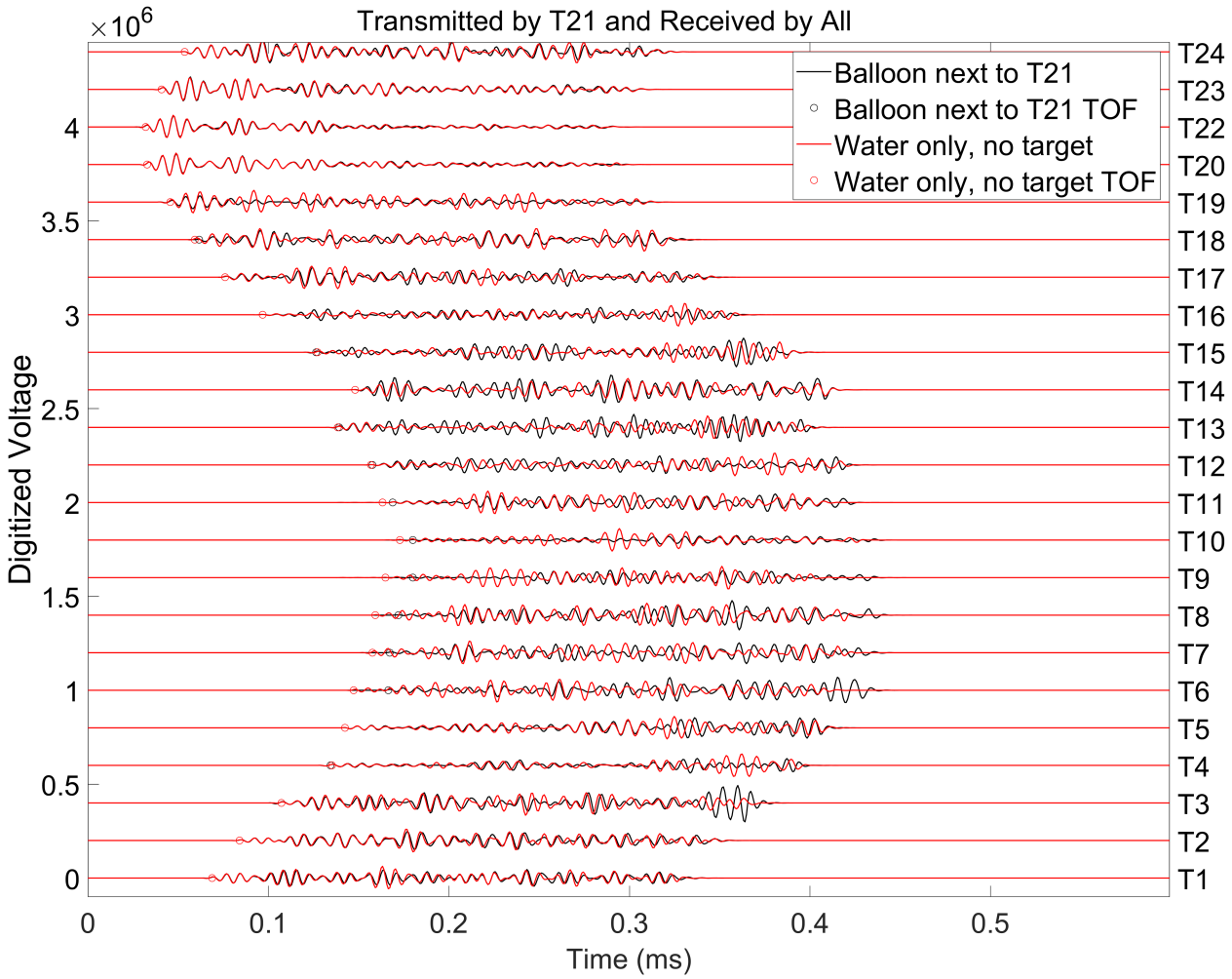

(a) Balloon near transducer 21.

Figure 4.7: Signals received on transducers one to 24 when transmitting with transducer 19 or 21 for two cases: balloon near transducer 21 and glass bottle next to transducer 19.

- Transducers one to five and 12 to 19: similar TOF but a 6.68% lower peak-to-peak digitized voltage amplitude when the balloon was inserted.
- Transducers six to 11: increase of 6.75% in TOF and a decrease of 14.1% in the peak-to-peak digitized voltage amplitude when the balloon was present.

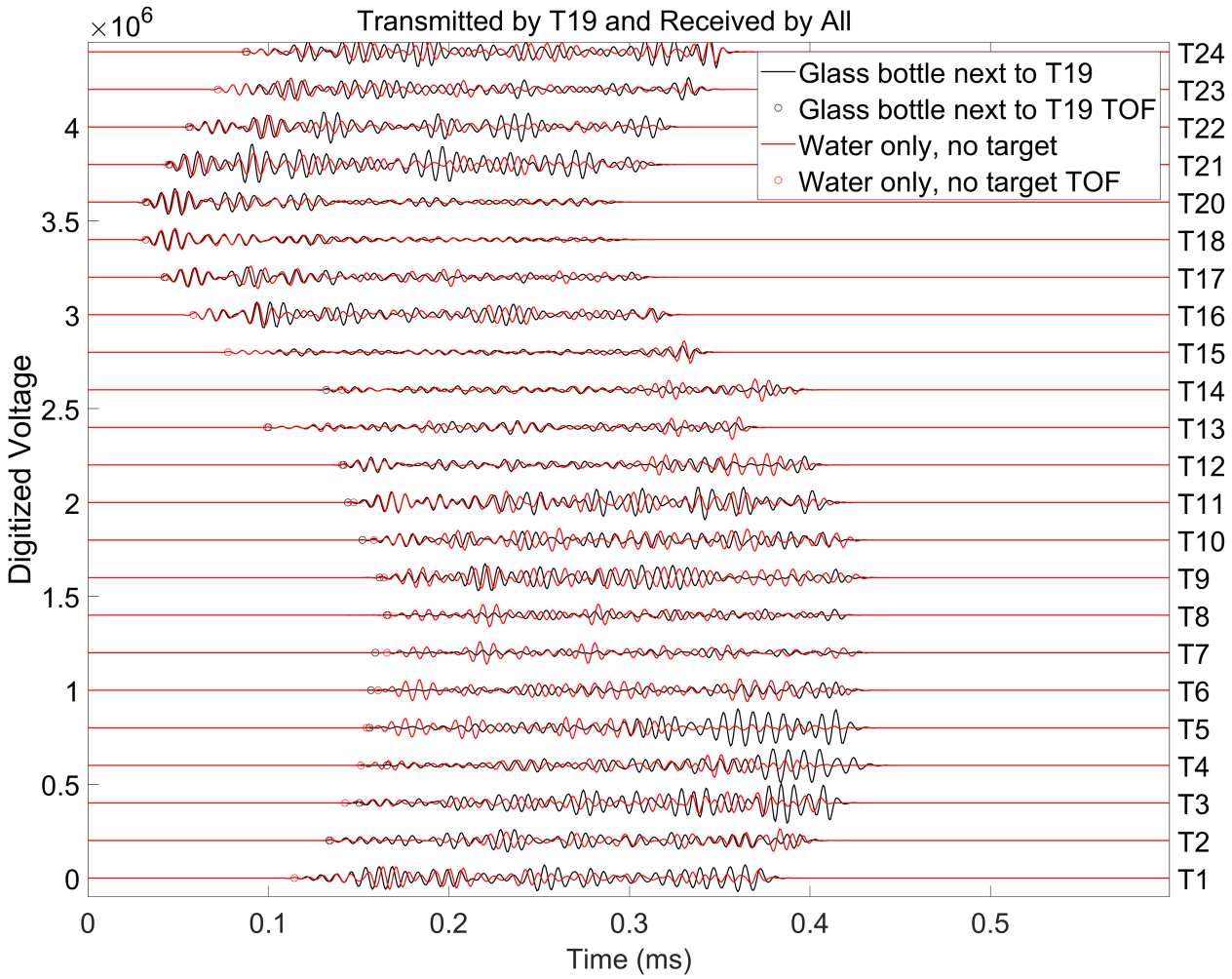

(a) Water bottle near transducer 19.

Figure 4.8: Signals received on transducers one to 24 when transmitting with transducer 19 or 21 for two cases: balloon near transducer 21 and glass bottle next to transducer 19.

A summary of the findings when comparing the signals received by all transducers when the glass bottle was placed near transducer 19 versus with a water-filled phantom is shown below:

- Transducers one, two, 12, 13 and 15 to 24: increase in the peak-to-peak digitized voltage amplitude of 5.07% when the target was submerged but made no difference in TOF.
- Transducers six to 11 and 14: decrease in TOF of and the peak-to-peak digitized voltage amplitude of 3.09% and 20.4%, respectively.
- Transducers three to five: increase of 5.39% in TOF and 63.8% in the peak-to-peak digitized voltage amplitude.

TOF Reconstructions

The reconstructions shown in this chapter were computed using the calibration coefficients calculated based on the transducers' piston displacement, as shown in Section 3.1.3 of this document. They were, however, computed as difference images, using the dataset collected when the phantom was filled with water only as a reference, which likely has partially compensated for the uncertainty introduced by the lack of an acoustic calibration. It is important to point out that this was a preliminary test, and that a reference dataset would not be available on a real application. Therefore, this problem was addressed starting in Section 4.2.2; all the reconstructions shown in that and further sections are absolute images that did not require any prior knowledge of the medium. Figures 4.9 to 4.11 show the targets' locations and sound speed reconstructions computed based on the data collected in this experiment.

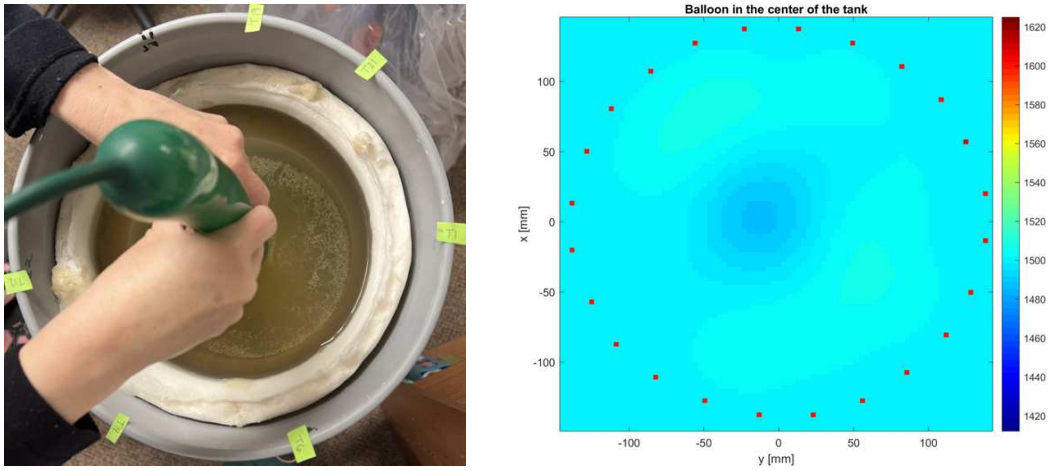

(a) One balloon in the center of the water-filled tank.

(b) TOF sound speed reconstruction.

Figure 4.9: Single targets in different positions in the water-filled tank.

(a) One balloon in the water-filled tank near transducer 21.

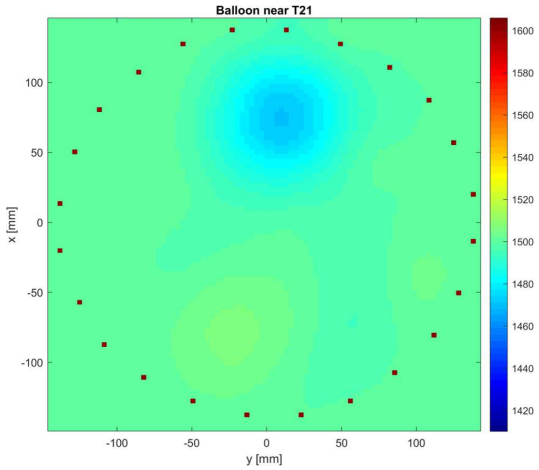

(b) TOF sound speed reconstruction.

(c) The glass bottle in the water-filled tank near transducer 19.

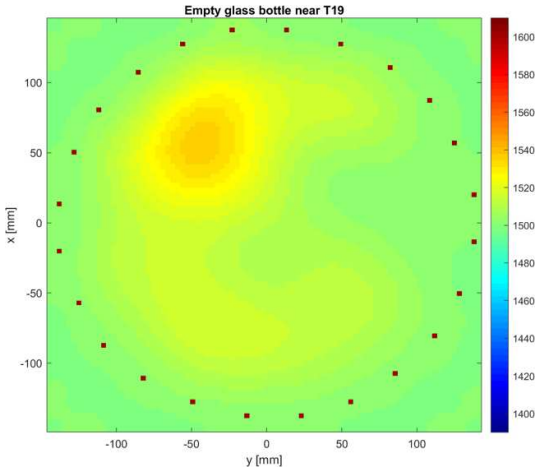

(d) TOF sound speed reconstruction.

(e) One balloon in the water-filled tank near transducer 6.

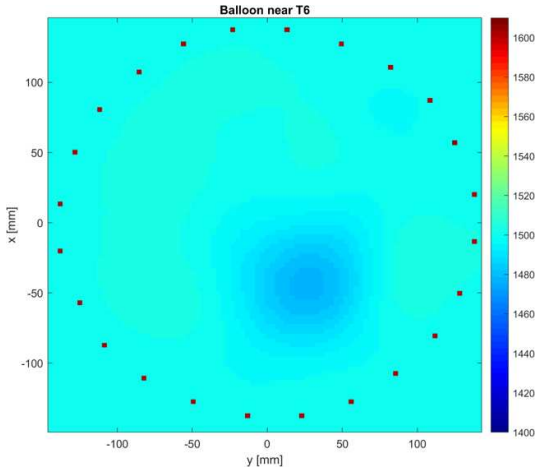

(f) TOF sound speed reconstruction.

Figure 4.10: Single targets in different positions in the water-filled tank (Cont.).

(a) The glass bottle in the water-filled tank near transducer 16 and the balloon near transducer 6.

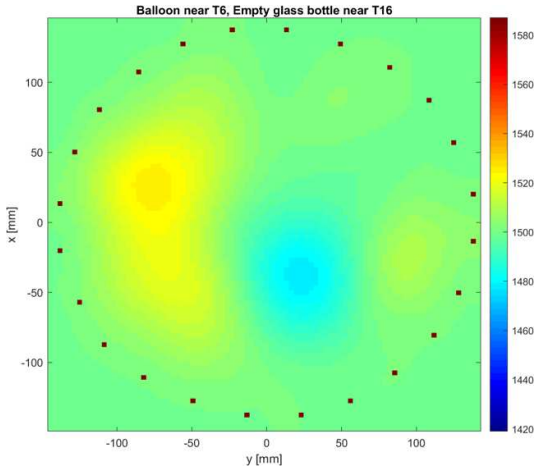

(b) TOF sound speed reconstruction.

(c) The glass bottle in the water-filled tank near transducer three and the balloons near transducers 9 and 19.

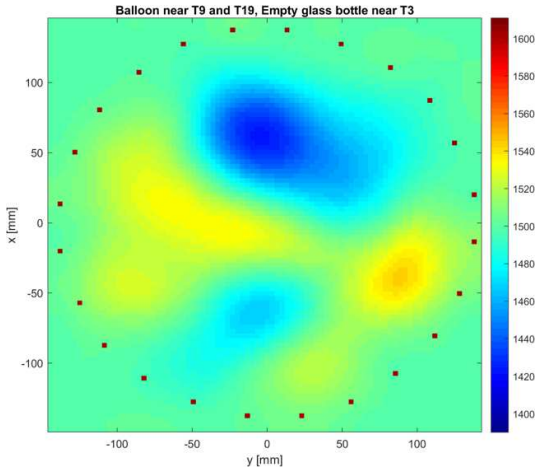

(d) TOF sound speed reconstruction.

Figure 4.11: Multiple targets in different positions in the water-filled tank.

The results show that targets of low (balloons) and high (glass) sound speeds are detected by the system, and their size and location are generally well-estimated. The balloon in the center of the tank showed the least contrast in sound speed. More blurring occurred in the cases with multiple targets. We surmise this can be attributed to the motion of the targets since it was difficult to hold them steady due to their buoyancy in the water, especially the balloons. The presence of multiple targets did not mask the presence of the others.

4.2.2 Torso-Shaped Phantom

To mimic the boundary conditions of a thorax, a ballistic gel phantom shaped like a human torso was constructed with a chest circumference of 854 mm, measured at the inframammary fold line, and two internal cavities with 110 mm diameter and 200 mm depth. The phantom was made using a standard mannequin and two PVC pipes; the mannequin was used to externally shape the gel, while the PVC pipes were used to create the cavities. Figure 4.12 shows more details of the experimental setup.

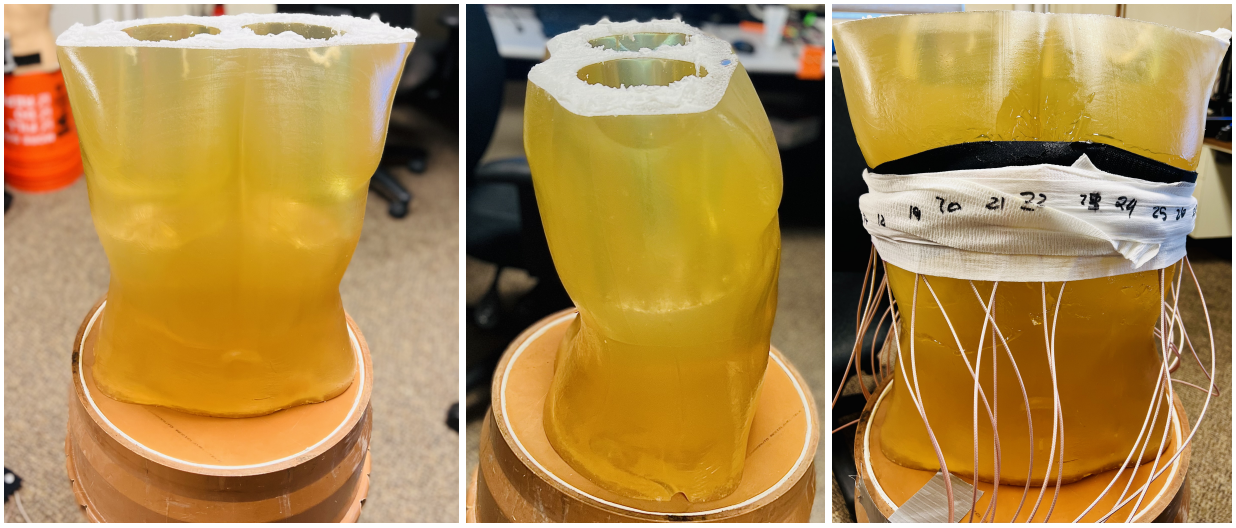

(a) Frontal view. **(b)** Side view. **(c)** phantom with the belt.

Figure 4.12: The ballistic gel torso and experimental setup.

As shown in Figure 4.12c, the transducer belt was placed right below the inframammary fold line. A layer of ultrasonic gel was applied to the transducers to improve their acoustic coupling with the ballistic gel. A self-adhesive bandage strap was used to secure the belt in place and compensate for the slippery nature of the phantom's surface. Twenty-eight transducers were used to collect ultrasonic data; the transmitted waveform frequency and amplitude were set to 125 kHz and 10 V_{pp}, respectively. Five HC were transmitted on one transducer at a time, in clockwise firing order, while listening on all the remainder. Data were collected in various configurations, including with both cavities empty (filled with air only), one empty and one filled with water, and both full

of water and with an empty plastic bottle of diameter 60 mm as a target (fully submerged). The post-processed data was used to reconstruct the sound speed map in the plane of the transducer ring array in each of the experimental configurations. The results were evaluated by comparing the real dimensions and location of the target with the ones detected by the system. An annotated picture and illustration used as a spatial reference in the experiment are shown in Figure 4.13.

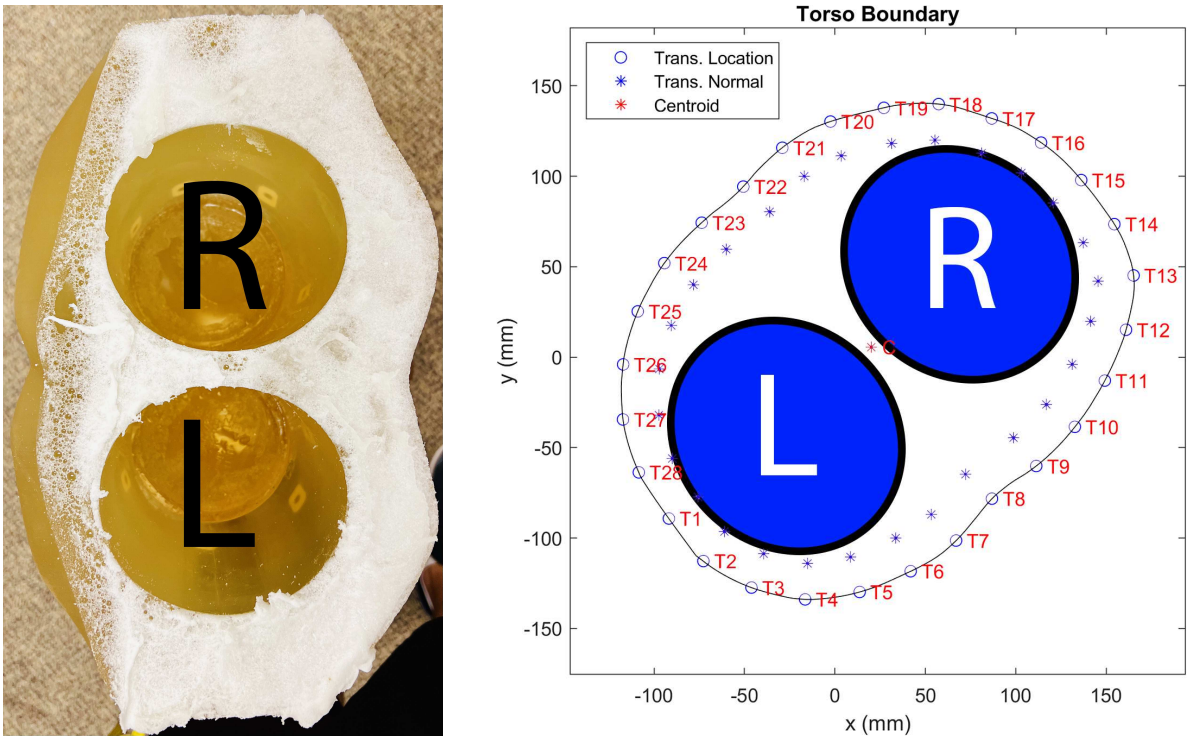

(a) Phantom's top view with cavities referenced.

(b) Transducer numbering and phantom cavities reference (R - right, L - left) at the belt height.

Figure 4.13: Transducer numbering and position reference for all reconstructions.

TOF Reconstructions

The sound speed map reconstructions obtained using TOF methodology, as presented in this section, were computed utilizing an absolute image approach. Notably, no prior domain knowledge or reference image was employed in the computation process. The reconstructions were determined solely based on the post-processed data, calibrated using the transducers' acoustic properties determined in Section 3.2, and the transducer positions, determined using the algorithm

presented in Section 3.6 of this document. The speed of sound of map reconstruction of each case study, as well as a detailed version of the region of interest are shown in Figures 4.14 to 4.16.

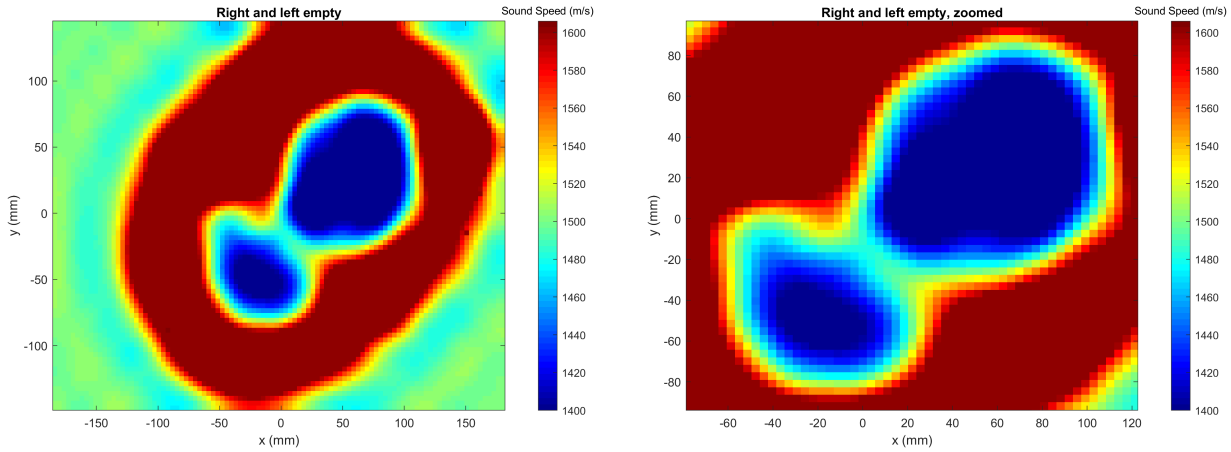

(a) Full reconstruction. **(b)** Detailed view of the area of interest.

Figure 4.14: TOF sound speed reconstruction of the torso with both cavities empty (filled with air).

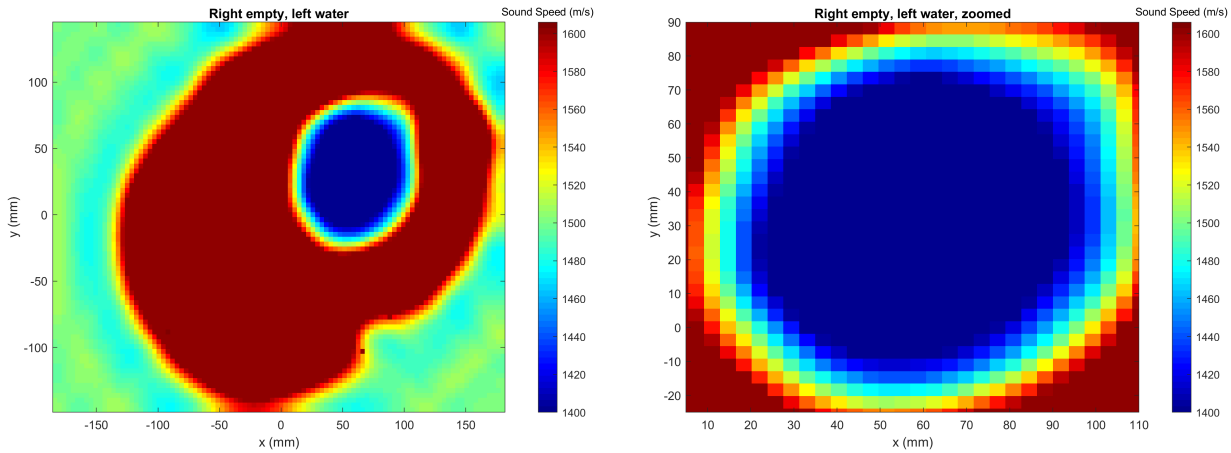

(a) Full reconstruction. **(b)** Detailed view of the area of interest.

Figure 4.15: TOF sound speed reconstruction of the torso with its right and left cavities filled with air (empty) and water.

The results have shown that the system effectively detected the cavities and targets, exhibiting a notable aptitude for estimating their respective position and size. Upon comparison of all cases, it is visible that the system displayed greater precision in target detection when at least one of

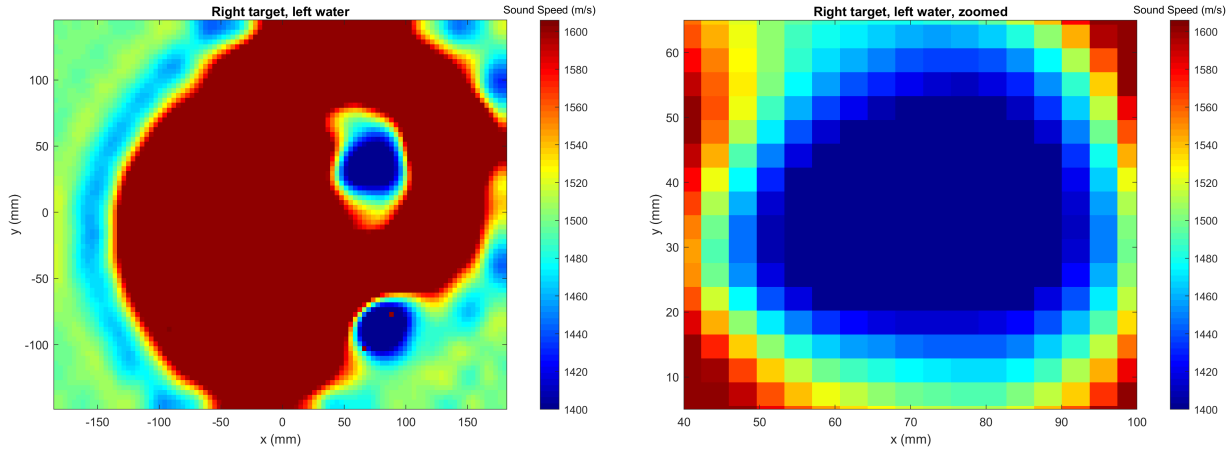

(a) Full reconstruction.

(b) Detailed view of the area of interest.

Figure 4.16: TOF sound speed reconstruction of the torso with both cavities filled with water and an empty plastic bottle target submerged in the right cavity.

the cavities was filled with water, as opposed to when both cavities were empty. A quantitative overview of these findings is presented below:

- Both cavities empty: both chambers were detected; their left and right diameters were 106 and 173 mm, and their centroids coordinates were x = -44.1 mm, y = -17.2 mm, and x = 25.2 mm, y = 55.0 mm, respectively.

- Right cavity empty and left cavity filled with water: the right chamber was detected; its calculated diameter was 104 mm, and its centroid coordinates were x = 31.6 mm, y = 58.7 mm.

- Both cavities filled with water and an empty plastic bottle submerged at the center of the right cavity: the empty water bottle was detected; its calculated diameter was 55.0 mm, and its centroid coordinates were x = 35.7 mm, y = 72.1 mm.

When comparing the reconstructed cavity sizes to their actual dimensions, we found a maximum diameter estimation error of 3.71% when the left cavity was filled with water, and the right was empty. However, when both cavities were empty, the error increased to 44.5%. We attribute this dramatic increase to the air's limited ability to transmit acoustic waves, which is further compounded by the fact that the cavities occupy a significant portion of the torso cross-section, limiting

the number of potential paths between the source and detectors and leading to a reduction in the system's accuracy. When both cavities were filled with water, and a plastic bottle was submerged in the right cavity, we observed an error of 8.69% between the detected diameter and the bottle's actual diameter. Notably, our analysis of the target and cavity dimensions and centroids confirmed that the plastic bottle was detected within the cavity limits. Furthermore, when comparing the TOF reconstructions shown in this section to the ones presented in Section 4.2.1, an improvement in contrast and boundary definition is seen. We surmise that the enhancement of these attributes was caused by applying the updated acoustic calibration coefficients to the data processing phase, which better compensated for the variation in the transducers' acoustic properties across samples.

Chapter 5

Vertebrate Animal Studies

Animal experimentation is a crucial step in the development and testing of novel medical devices; the safety and efficacy of equipment must be thoroughly evaluated before it can be tested on humans [112]. That allows researchers to assess the device's performance in a living system and to gather data on its safety and potential adverse effects without exposing a human subject to unnecessary risks. While animal experimentation is a contentious issue, it remains a necessary step in medical research to ensure the safety and efficacy of medical devices before they are tested on human subjects. Ultimately, this research helps to advance our understanding of the human body and contributes to the development of innovative medical technologies that improve patient care and outcomes [113].

Therefore, a vertebrate animal study (Protocol number: 17-7247A, Animal welfare assurance number: A3572-01) was conducted at the Translational Medicine Institute, Colorado State University in Fort Collins, CO, and aimed to analyze the behavior of the novel USCT equipment and the feasibility of the application of UCST for lung imaging and assessment of the development of respiratory complications. Five Landrace pigs weighing approximately 170 lbs were obtained from a USDA-approved vendor and used for the study. These pig species were chosen for their strong morphologic and hemodynamic behavior resembling human lungs. The study consisted of several steps of data collection with USCT and standard CT scan data to assess the pulmonary health of the subjects before and after induced acute lung injury, as described in Subsections 5.1 to 5.6.

The USCT data collected during the experiment were further processed and analyzed regarding the amplitude of the received signals over time and through TOF sound speed map reconstructions. The first analysis, shown in Section 5.7, aimed to evaluate the changes in the characteristics of the received signals as a function of the animal's lung condition at the time when the data was collected. The second analysis, presented in Section 5.8, was conducted to evaluate the system's capacity to detect changes in the medium's acoustic properties caused by the inflation and deflation

of the lungs and also the induced pathologies. Several TOF reconstructions were computed and evaluated. The shape and location of low (air) and high (tissue or fluids) sound speed areas were analyzed and compared against the images collected using a CT scan machine, which was used as the ground truth to evaluate the animal's lung condition at the time of each data collection.

5.1 Preparation

The animals were anesthetized and orotracheally intubated using a laryngoscope and an endotracheal tube number 7.5. Anesthesia was maintained with a continuous infusion of intravenous anesthetic and analgesic drugs. Once the depth of anesthesia was considered adequate, a neuromuscular blocker was administered to avoid any interference, such as spontaneous breathing, during data collection. Animals were mechanically ventilated during anesthesia. A board-certified veterinary anesthesiologist (Dr. Marlis Rezende) continuously evaluated anesthesia and muscle relaxation levels through indirect signals such as direct arterial blood pressure, heart rate and rhythm, arterial oxygen and CO2 blood gas content, muscle tone, and animal movements; these vital signals and ventilator settings were annotated during the entire experiment. Next, the animal was placed in a CT scan bed, where the entire data study was conducted. The area between the 4 th and 8 th intercostal space was shaved and disinfected with alcohol to improve the acoustic coupling between the transducer and the animal's skin.

5.2 Baseline Assessment

A section of USCT data was collected before any lung injury. The transducers and the animal's skin were coated with ultrasound gel, the belt was strapped to the pig's chest at mid-lung height, and data was collected at 125 and 156 kHz frequencies. Next, the belt was removed, the ultrasound gel was cleaned from the skin, and self-adhesive fiducial markers were carefully positioned where the transducers were previously located; a permanent marker was used to indicate the belt height, location, and the number of each transducer. After that, a CT scan was taken to evaluate the lung health condition of the animal before acute lung injury was induced.

5.3 Pneumothorax Protocol

Pneumothorax is a medical condition where gas accumulates in the space between the lungs and the chest wall [114]. To detect the presence of this disorder, our protocol seeks to evaluate the system's ability to identify a region of slow sound speed (air) within the thoracic cavity that agrees with the location of the induced pneumothorax (confirmed through a CT scan). To accomplish that, minimally invasive surgery was performed to insert a 5 mm thick intrathoracic tube into the 8 th posterior space. The transducer belt was prepared with ultrasonic gel and re-strapped to the pig, and USCT data was collected continuously while the air was injected into the chest through the chest tube in increments of 300 ml until a change in systemic arterial pressure was detected. Once the pneumothorax was considered established, the data collection was stopped and restarted with a new dataset name. After that, the belt was removed, the fiducial markers were placed to represent the transducers, and a new CT scan was performed. Finally, the belt was replaced, and USCT data was collected while the air was removed in 300 ml increments.

5.4 Atelectasis Protocol

Atelectasis was produced by ventilating the subject with a high concentration of oxygen (100% FiO_2) and small tidal volumes (4 ml/kg). USCT data was collected during the entire procedure and restarted once the atelectasis was considered established by the veterinarian based on changes in the arterial partial pressure of oxygen (blood gas). After that, the belt was removed, the fiducial markers were installed, and a new CT scan was taken to confirm the health condition of the lungs.

5.5 Pleural Effusion Protocol

Pleural effusion is a medical condition where fluid accumulates in the space between the lungs and the chest wall [115]. To detect the presence of this disorder, our protocol seeks to evaluate the system's ability to identify a region of high sound speed (fluid) within the thoracic cavity that agrees with the location of the induced pleural effusion (confirmed through a CT scan). The pleural effusion injury procedure was conducted last due to the high level of trauma caused by this

complication. USCT data was collected while injecting a saline solution into the thorax through the catheter and restarted when a liquid volume of approximately 1.5 l was injected. Next, the belt was removed, the fiducial markers were installed, and a final CT scan was collected.

5.6 Euthanasia and Animal Disposal

Following the American Veterinary Medical Association guidelines, an additional bolus of anesthetic was used preceding the injection of KCL to induce euthanasia through rapid and painless cardiac arrest. After confirming the full cardiac arrest, the animal was placed in a specific plastic bag for animal disposal and forwarded to the deposit of organic waste, properly identified, for later incineration.

5.7 UCST and CT Scan Data Analysis

The experimental USCT data collected with the animals were post-processed using the approach explained in Section 3.5 and the calibration coefficients determined in Section 3.1.3. However, a few more steps are required to analyze the respiratory signals since they are not static in time, unlike the phantom data explored in Section 4.1. Thus, the peak-to-peak voltage of each received signal for each frame was extracted and concatenated onto a new array of size 32x32xNFrames, where NFrames is the number of frames collected for that particular dataset. Next, the signal was filtered using a 4 th order Butterworth low-pass filter with a cutoff frequency of 3 Hz (approximately ten times larger than the breathing frequency set on the ventilator). Several data characteristics were analyzed, such as the amplitude of the cyclic waveform and an increase or decrease in amplitude over time. The regional information was also taken into account based on the position of the transducers transmitting and receiving the signals and the pathologies seen on the CT scans. Figure 5.1 shows a segment of respiratory data collected from pig five during baseline (healthy lungs).

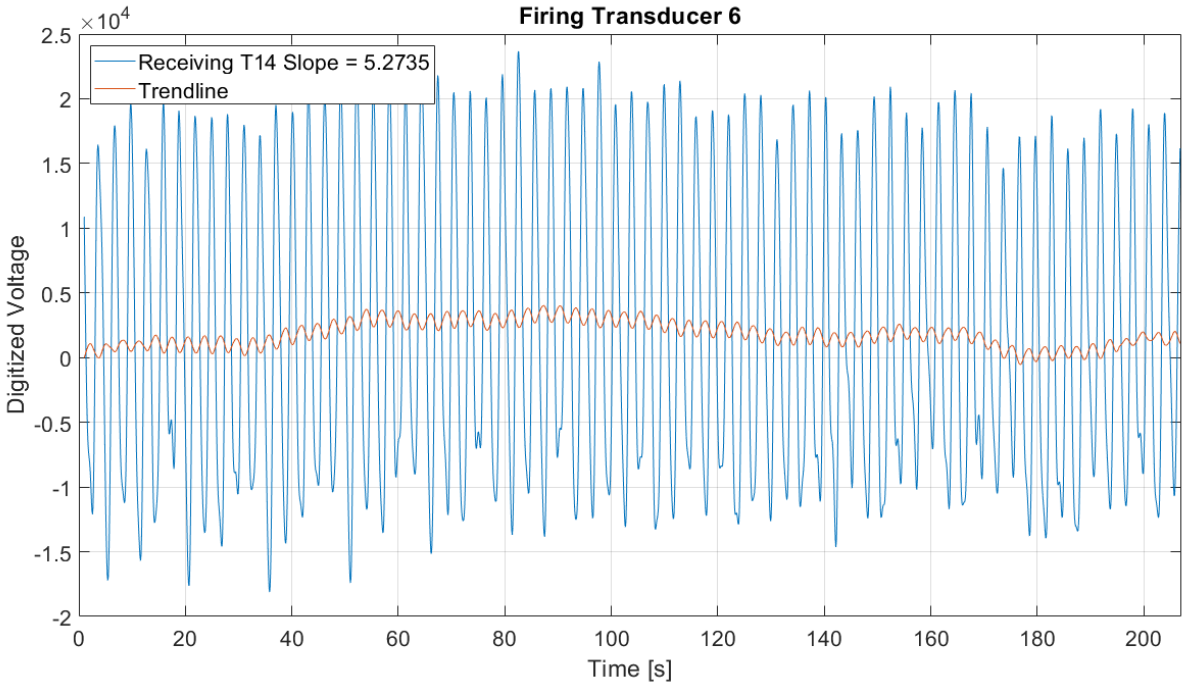

(a) All frames, approximately 210 s duration.

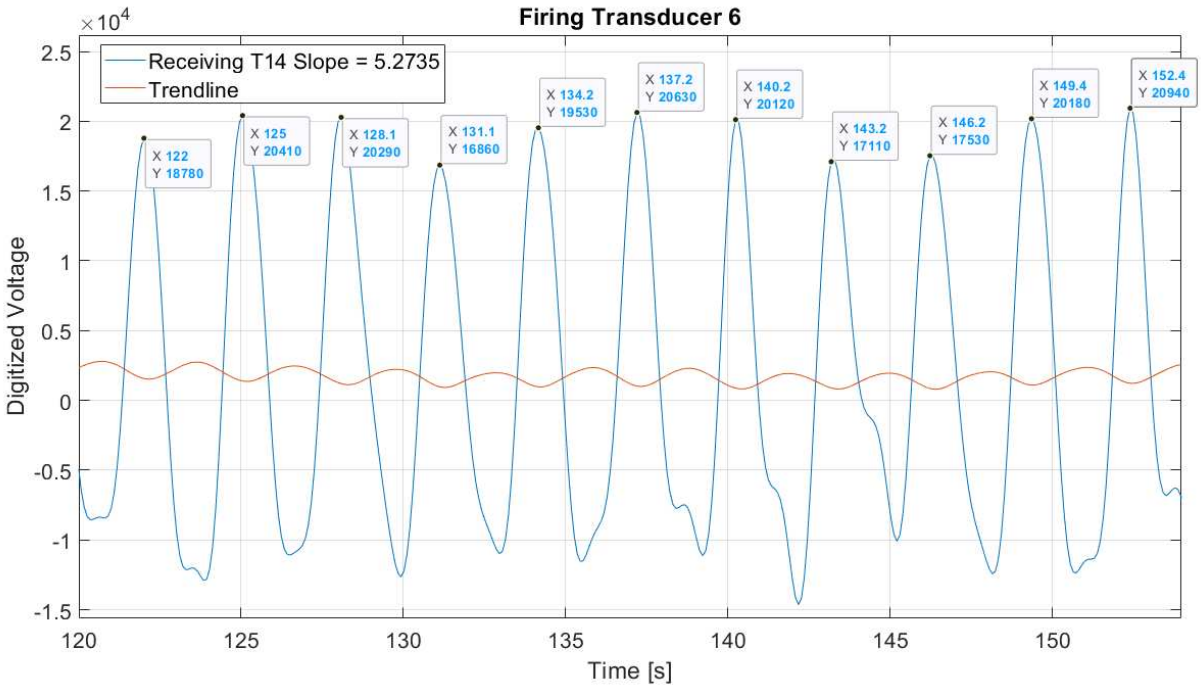

(b) Detailed view of a segment of data extracted from Figure 5.1a.

Figure 5.1: Baseline segment of data collected from pig five; signal received by transducer six when transducer 14 was firing.

When analyzing the signals shown in Figure 5.1, some important features can be seen, such as a cyclic behavior, shown in detail in Figure 5.1b, and a consistent peak-to-peak amplitude and trend. The average period of the waveform was 3 s, which matched the breathing parameters set on the ventilator (20 breaths per minute), and the average amplitude and trendline were stable during the entire data collection, which might indicate that there was not an expressive change in the acoustic characteristics of the medium during the procedure. An analysis of the CT scan performed right after the USCT data collection led to the conclusion that the animal had healthy lungs at that time of the experiment, as shown in Figure 5.2.

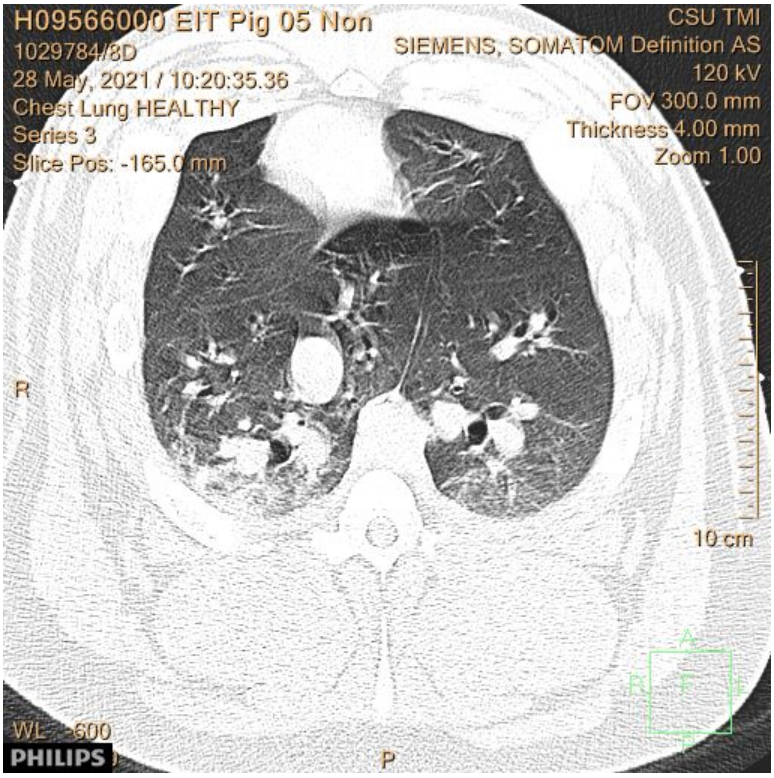

Figure 5.2: Lung CT scan from pig five performed right after baseline USCT data collection.

Next, the data collected during the pneumothorax injury protocol were analyzed, and some of the signals received by specific transducers showed some important differences when compared to the baseline. Figure 5.3 shows a segment of the signals received by transducer 18 when 11 was firing.

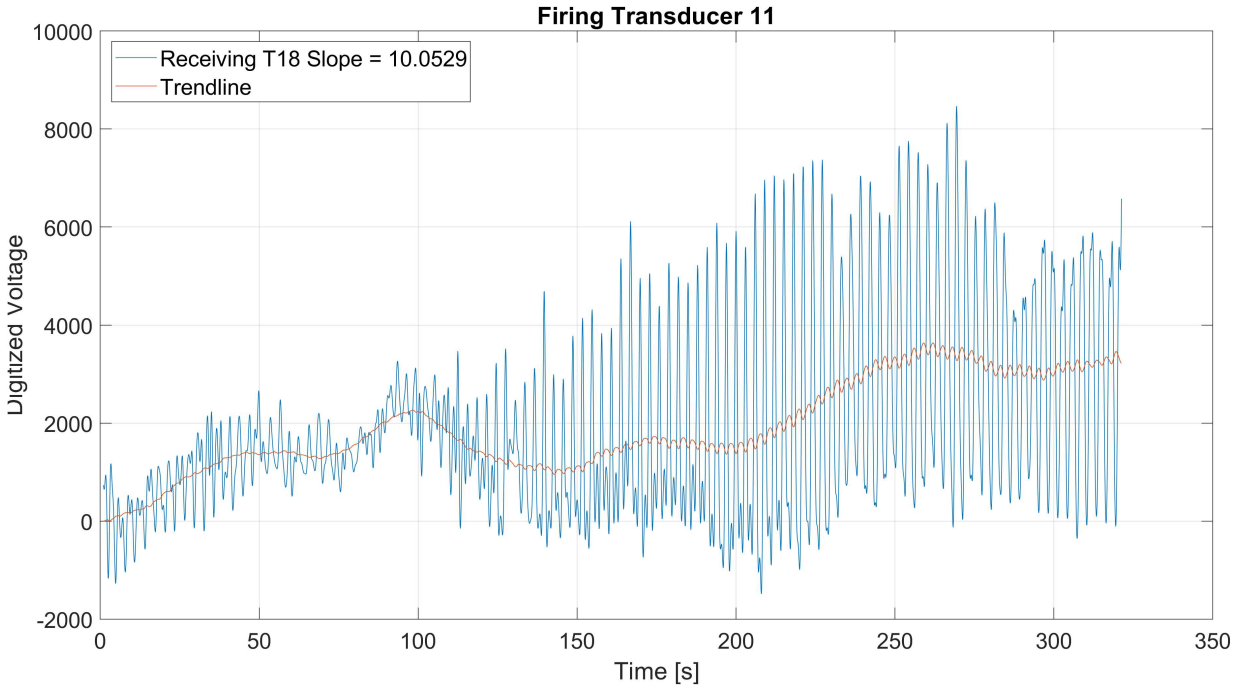

(a) All frames, approximately 325 s duration.

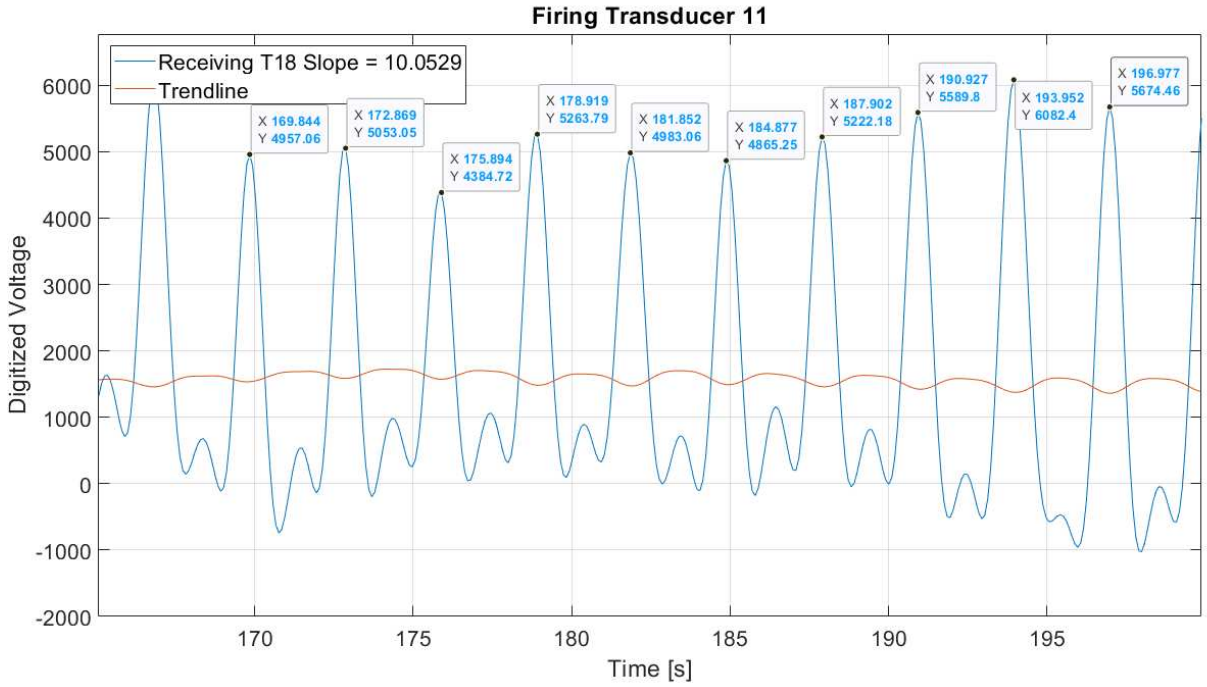

(b) Detailed view of a segment of data extracted from Figure 5.3a.

Figure 5.3: Segment of data collected from Pig Four during the pneumothorax protocol; signal received by transducer 18 when transducer 11 was firing.

When comparing Figure 5.1a with Figure 5.3a, one of the clear differences is that there was an increase in the peak-to-peak amplitude (about 3.2 fold) and the DC level over time. That indicates that the injection of air into the animals' thorax was not only increasing the overall sound wave transmission, due to an increase in the DC level but also the amplitude of the breathing signal, due to the peak-to-peak amplitude increase. Those differences might have been caused by several factors, such as the compression of the animal's organs, which could improve the transmission by filling up gaps between them, the presence of the air bubble in the chest cavity, which could increase the reflections by creating other tissue-air interfaces, or even the movement of the skin, due to chest inflation. When looking at the CT scan slice that represents the height where the belt was positioned, shown in Figure 5.4, it is noticeable that there was a massive air bubble in the animal's thorax that caused the compression of the organs towards the pig's back. Therefore, since the path between transducers 11 and 18 was located across the region where the compression occurred, it could be responsible for the change in the acoustic wave transmission over time.

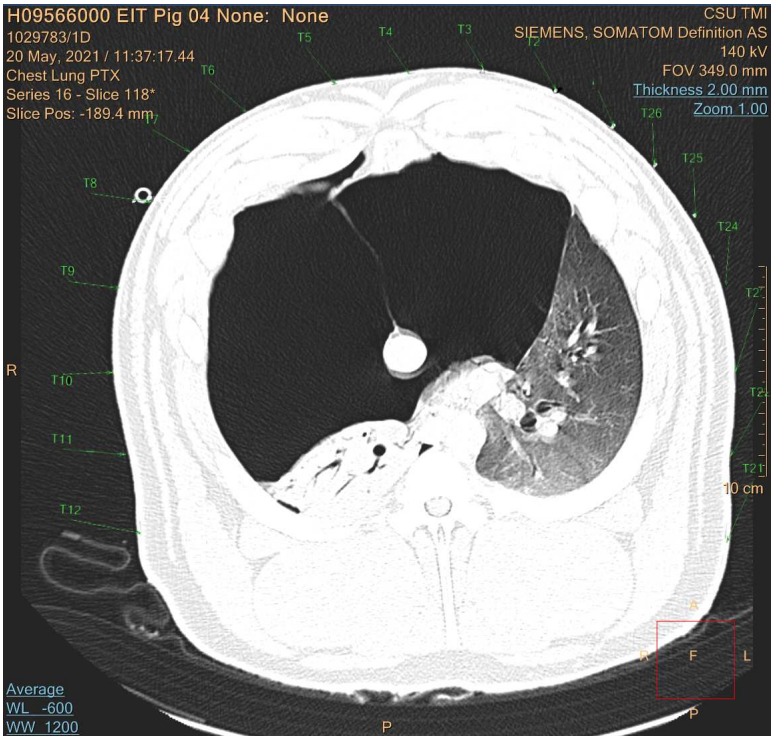

Figure 5.4: Lung CT scan from Pig Four performed right after the pneumothorax was established.

As a final data exploration, the USCT data collected during the pleural effusion procedure were analyzed; a segment of data is shown in Figure 5.6, where features similar to the ones seen in the pneumothorax case were found. When looking at the signals, an increase in the peak-to-peak voltage and DC over time is clear. However, in this case, the difference was in the order of 35-fold instead of 3.2. The trendline's slope was also much higher, reaching a value of 735 instead of 10.05. The reason for such an increase in transmission could be explained by the presence of a large amount of fluid on the pathway between the transmitting (T11) and receiving (T5) transducers, which is shown in Figure 5.5. The attenuation coefficient of water can be up to 450 times smaller than certain tissues [116]. Thus, that could be a reasonable explanation for the transmission improvement in this experiment.

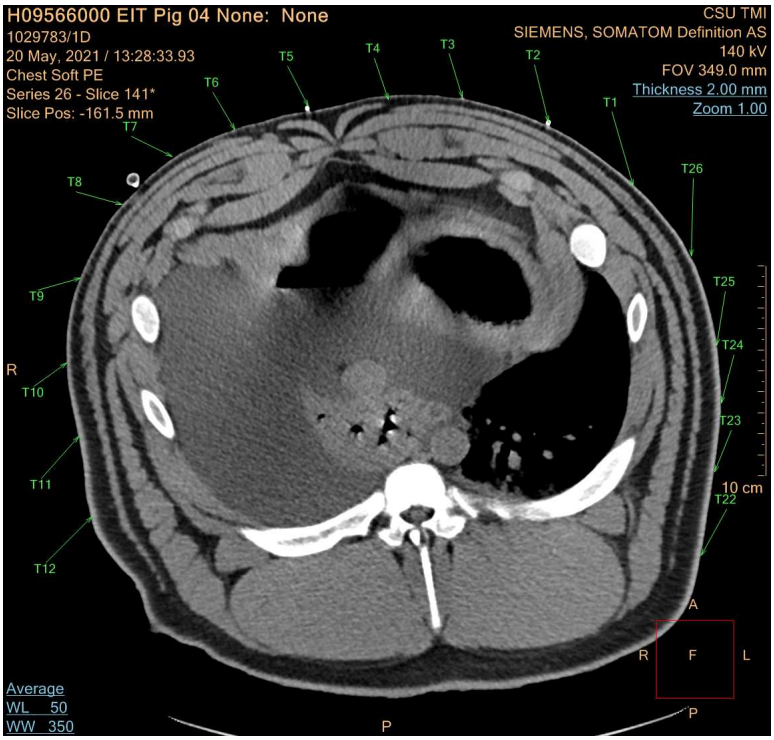

Figure 5.5: Lung CT scan from Pig Four performed right after the pleural effusion was established.

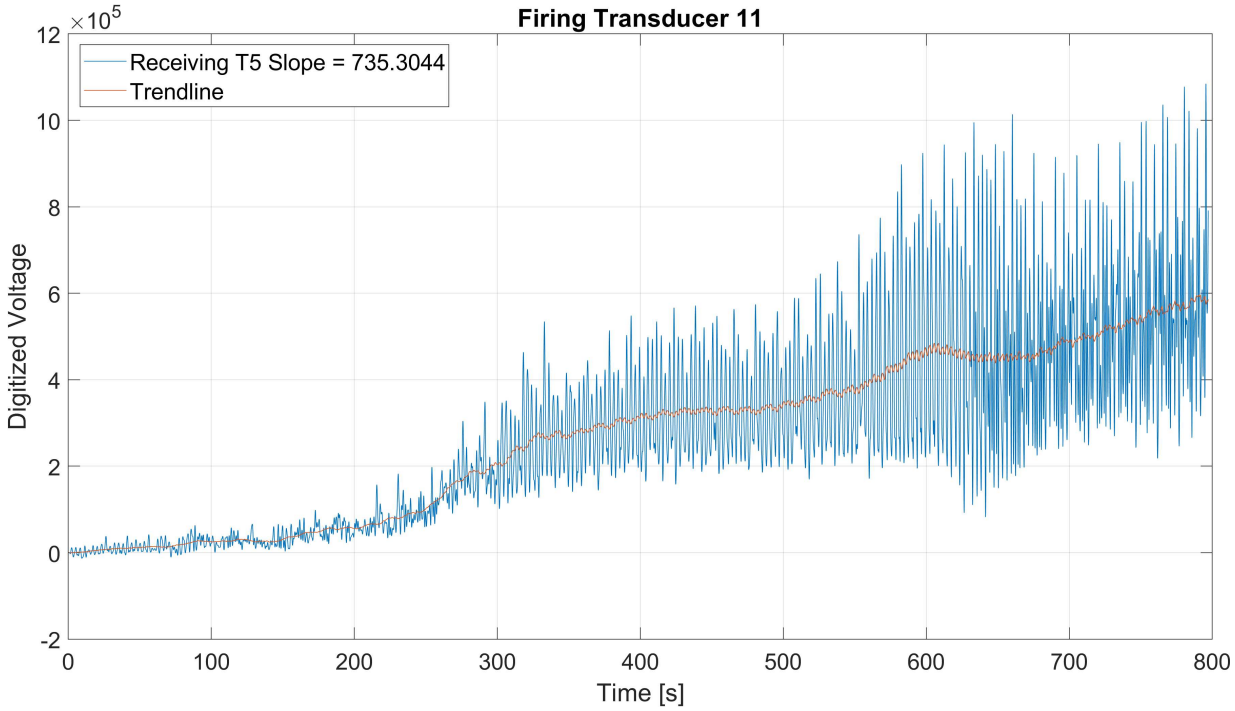

(a) All frames, approximately 800 s duration.

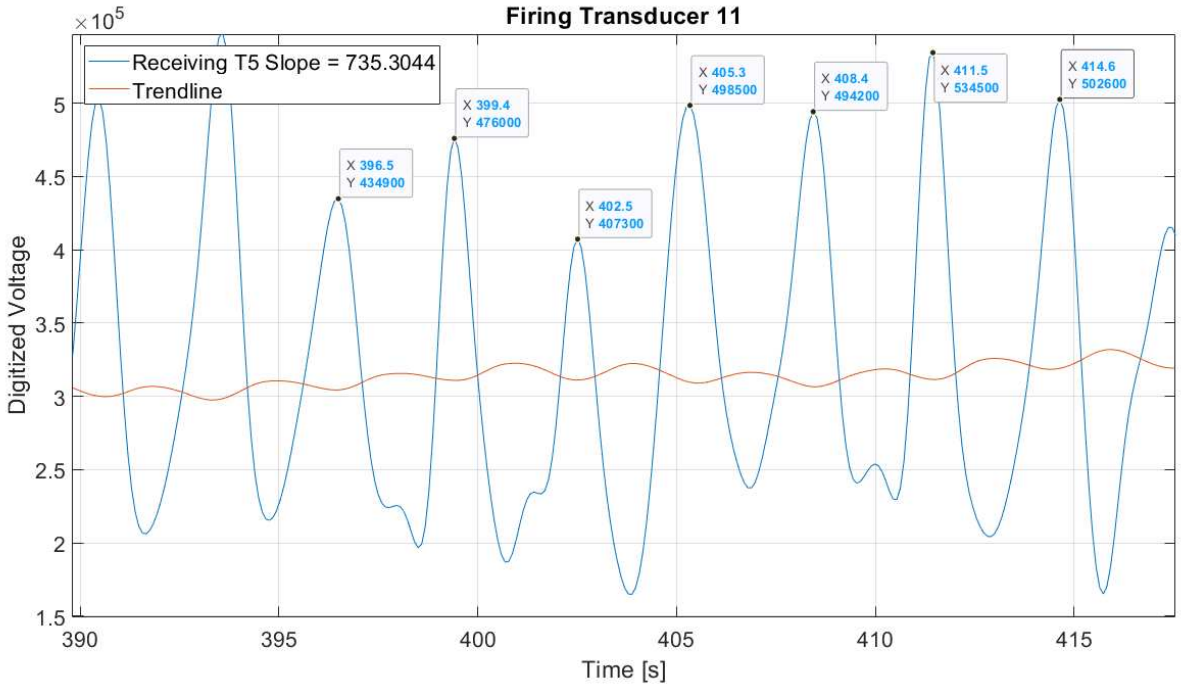

(b) Detailed view of a segment of data extracted from Figure 5.6a.

Figure 5.6: A segment of data collected from Pig Four during the pleural effusion protocol; signal received by transducer 5 when transducer 11 was firing.

5.8 TOF Reconstructions

This section presents the sound speed map reconstructions obtained using TOF methodology applied to the data collected from Pig Four during baseline, pneumothorax, and pleural effusion protocols, as previously described. Notably, an absolute image approach was utilized, and no prior domain knowledge or reference image was employed in the computation process. The reconstructions were computed using the post-processed data, calibrated with the acoustic properties of the transducers identified in Section 3.2, and the positions of the transducer, determined through the algorithm presented in Section 3.6. Twenty-six transducers were used in the experiment; the transmitted waveform frequency and amplitude were set to 125 or 156 kHz and 120 V_{pp}, respectively, and 40 HC were transmitted on one transducer at a time, in clockwise firing order, while listening on all the remainder.

5.8.1 Baseline

USCT data was gathered continuously during a three-minute period while the subject was mechanically ventilated at a rate of 20 breaths per minute. The data were acquired at a frame rate of 10.9 frames per second (FPS) and subsequently analyzed. A subset of frames was then selected, reconstructed, and compared to a CT scan obtained right after the USCT data collection, as demonstrated in Figure 5.7.

Upon comparing the sound speed map obtained through the TOF reconstruction and the CT scan slice obtained at the same cross-sectional height as the transducer belt, a notable similarity between the two was observed. The TOF reconstruction's low sound speed areas, marked as blue, and high sound speed areas, marked as red, demonstrate a similar shape and location as the corresponding lung (low sound speed) and bone/soft tissue regions (high sound speed) in the CT scan. Notably, the speed of sound in porcine tissues varies significantly; previous studies have found values ranging from 1423 to 1682 m/s [117–119] for soft tissue and from 2854 to 3252 m/s [120] for bone, which corroborates with the values found on the TOF reconstruction. Moreover, when

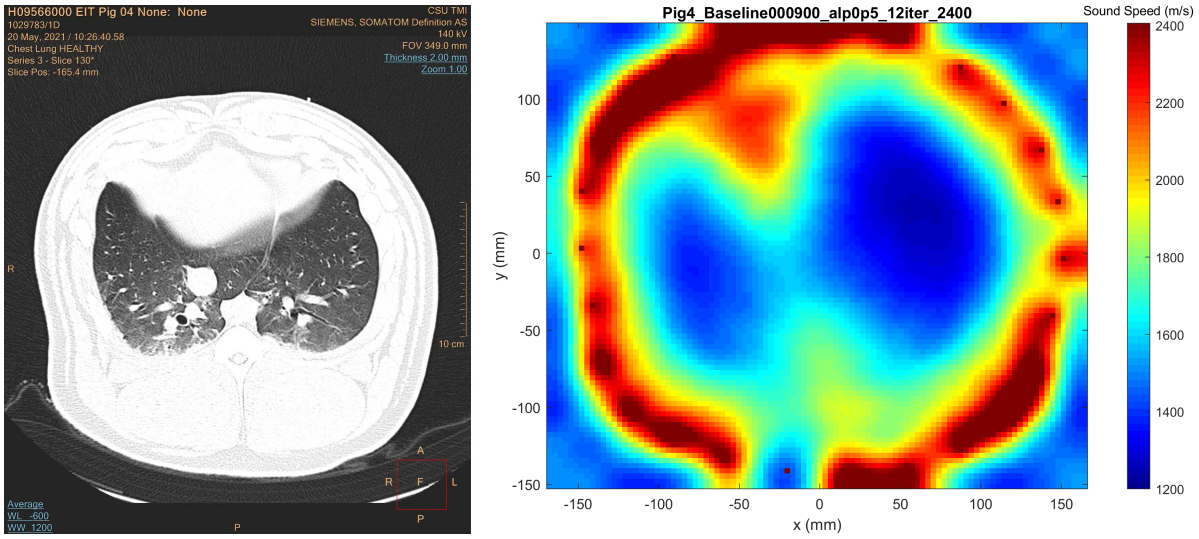

(a) CT Scan (DICOM format). **(b)** TOF reconstruction (DICOM format).

Figure 5.7: CT scan and TOF sound speed reconstruction of the data collected from Pig Four during mechanical ventilation.

analyzing the left and right lung sizes, it is clear that the right lung area is smaller both on the reconstruction and the CT scan.

Further analysis was conducted to investigate the possible presence of a cyclic pattern within a sequence of USCT frames, which may correspond to the detection of a breathing cycle. To examine this, the ventilator was configured to a breathing rate of 20 breaths per minute and an inspiratory-to-expiratory ratio of 1:2. This resulted in an average breath cycle of 3 seconds, with the inspiration and expiration phases lasting approximately 1 and 2 seconds, respectively. Given that the data was captured at a rate of 10.9 FPS, a complete breath cycle would span approximately 33 frames, with 11 frames for inspiration and 22 for expiration. Therefore, a sequence of 60 consecutive frames was randomly selected, reconstructed, and analyzed; a portion of the TOF reconstructions is presented in Figure 5.8.

Upon analyzing the reconstructed frames from 900 to 960, a complete breathing cycle was potentially identified between frames 900 and 934. This was evidenced by a consistent increase in the blue-colored area, of which the computed value is shown in Figure 5.9, depicting lower sound speed from frames 900 to 907, followed by a consistent decrease from frames 908 to 917,

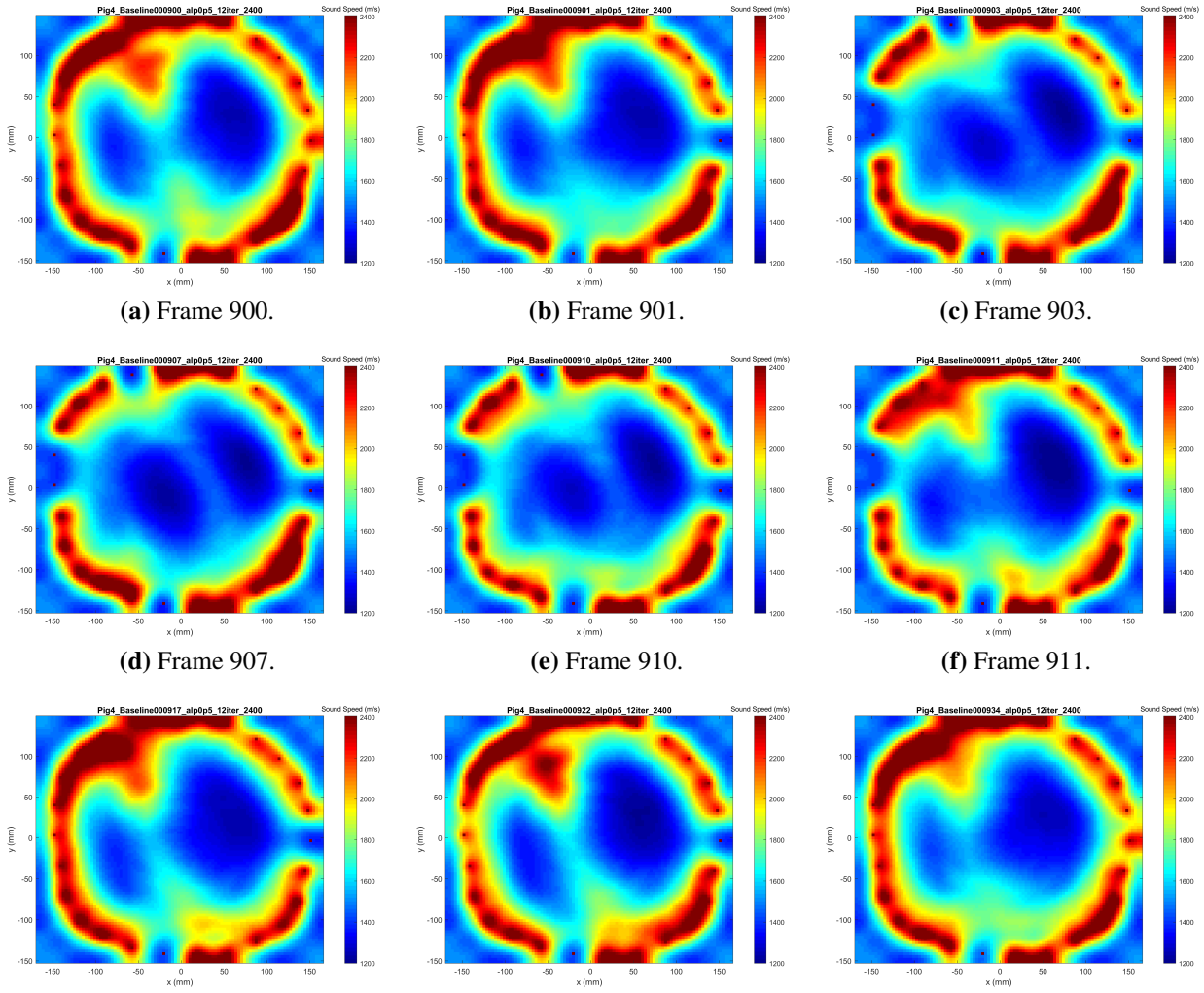

(a) Frame 900. **(b)** Frame 901. **(c)** Frame 903.

(d) Frame 907. **(e)** Frame 910. **(f)** Frame 911.

(g) Frame 917. **(h)** Frame 922. **(i)** Frame 934.

Figure 5.8: TOF sound speed reconstructions (DICOM) of the data collected from Pig Four during baseline; sequence of selected frames from one breathing cycle.

ultimately returning to a shape and area similar to that of frame 900. This suggests that the system may have detected changes in lung volume during breathing. Moreover, the calculated breath rate based on the frame number aligns with the setting on the mechanical ventilator, further supporting the system's accuracy.

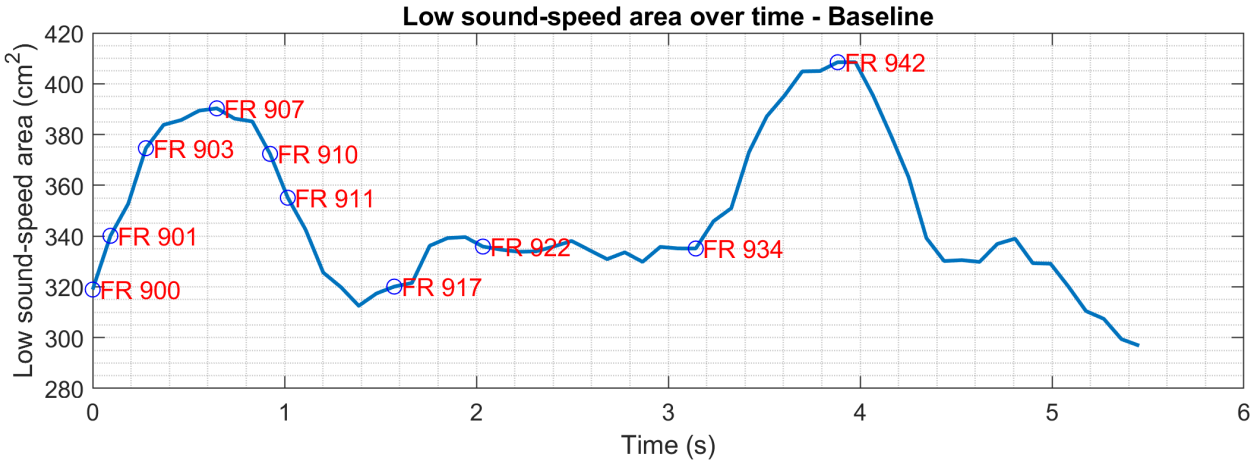

Figure 5.9: Low sound speed area computed from Pig Four's TOF sound speed reconstructions (DICOM) of the data collected during baseline.

5.8.2 Pneumothorax

USCT data was gathered continuously for 5.4 minutes while the pneumothorax was induced. The data were acquired at a rate of 10.9 FPS and subsequently analyzed. A subset of frames was then selected, reconstructed, and compared to a CT scan obtained post-procedure, as demonstrated in Figure 5.10.

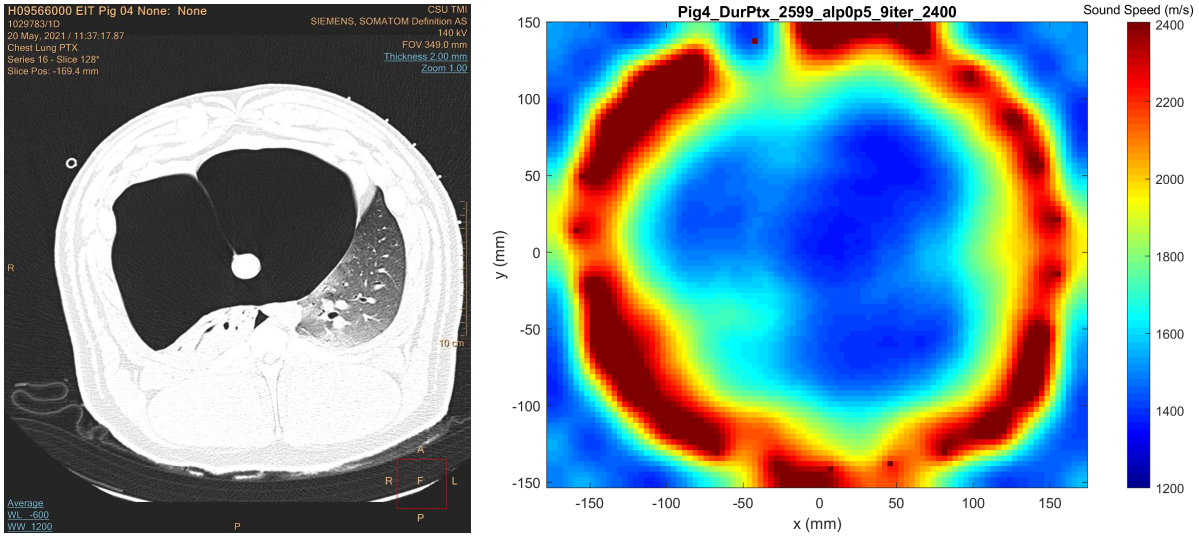

(a) CT Scan (DICOM format). **(b)** TOF reconstruction (DICOM format).

Figure 5.10: CT scan and TOF sound speed reconstruction of the data collected from Pig Four after the pneumothorax was established.

Similar to the previous case, a significant resemblance was observed between the sound speed map obtained through TOF reconstruction and the CT scan slice taken at the same cross-sectional level as the transducer belt. The central blue region of the reconstruction represents a substantial portion of the reconstructed slice, which aligns with the location of the pneumothorax found on the CT scan. Additionally, a comparison between this reconstruction and the previous ones (baseline) reveals the absence of the high sound speed area observed at the 11 o'clock position in all baseline reconstructions. This may be attributed to the compression of the tissue that was originally present in that area. The relocation of tissues and lung collapse is confirmed through the CT scan, which resulted from the pressure exerted by the air injected during the pneumothorax protocol. Since the data was continuously collected for the duration of the experiment, further investigation was conducted to analyze if the progression of the pneumothorax resulted in differences in the reconstructions over time. A selection of frames spaced between 500 and 1000 frames (550 and 1100 s) between each other was reconstructed and analyzed; a portion of the TOF reconstructions is presented in Figure 5.11.

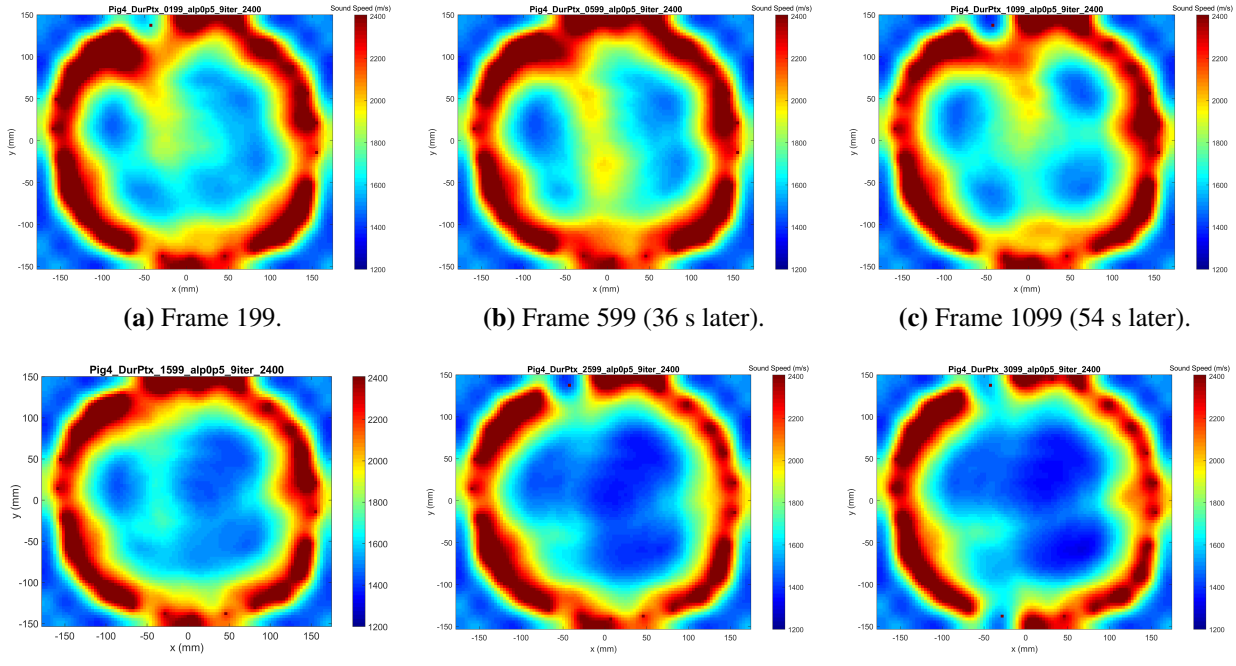

(a) Frame 199. **(b)** Frame 599 (36 s later). **(c)** Frame 1099 (54 s later).

(d) Frame 1599 (54 s later). **(e)** Frame 2599 (108 s later). **(f)** Frame 3099 (54 s later).

Figure 5.11: TOF sound speed reconstructions (DICOM) of the data collected from Pig Four during the pneumothorax protocol; sequence of selected frames showing the condition's progression.

Upon analyzing the reconstructed frames between 199 and 3099, the progression of the pneumothorax was evident. Over time, a consistent increase in the blue-colored area was observed, likely caused by the accumulation of air volume in the animal's thorax. This led to a collapse of the right lung, resulting in an overall decrease in sound speed in that area. Additionally, the high sound speed region near the 11 o'clock position, which was visible in the baseline reconstructions, can be seen in Figures 5.11a to 5.11c, but not in subsequent frames. This could be attributed to the compression of the tissue against the thoracic wall, which occurred due to the enlargement of the pneumothorax and was confirmed through the CT scan.

5.8.3 Pleural Effusion

USCT data was collected continuously for approximately 14 minutes while the pleural effusion was induced. The data were acquired at a rate of 10.9 FPS and subsequently analyzed. A subset of frames was then selected, reconstructed, and compared to a CT scan obtained post-procedure, as demonstrated in Figure 5.12.

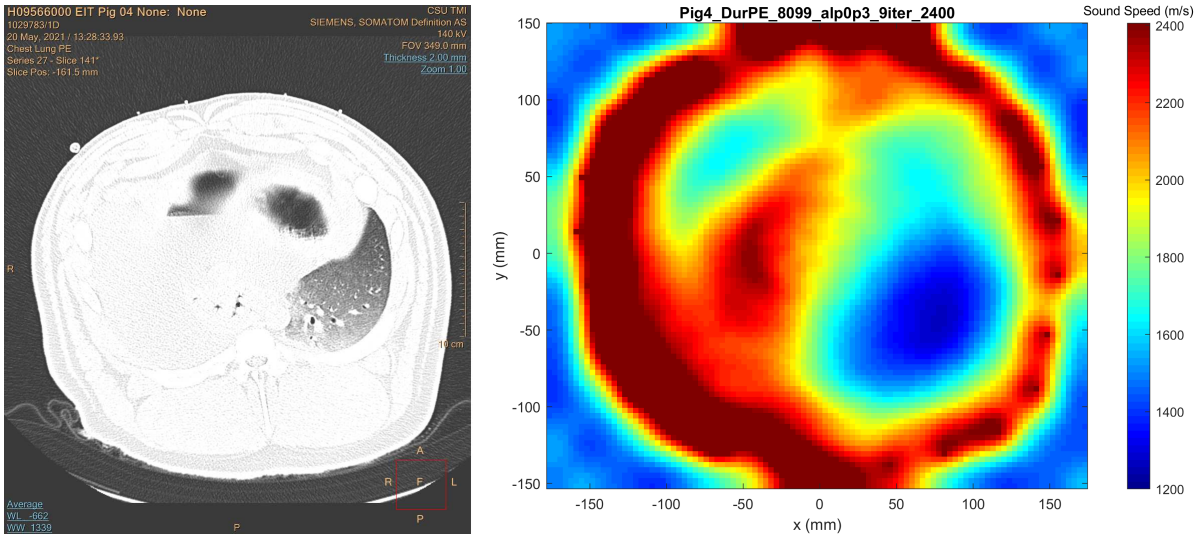

(a) CT Scan (DICOM). **(b)** TOF reconstruction (DICOM).

Figure 5.12: CT scan and TOF sound speed reconstruction of the data collected from Pig Four after the pleural was established.

The study's results revealed a remarkable level of correspondence between the data collected through the post-procedure CT scan and the sound speed map reconstructions. The CT scan highlighted the presence of fluid throughout the thoracic cavity, except the left lung and the area immediately above it (between 10 o'clock and 2 o'clock). Similarly, the TOF reconstruction demonstrated a low sound speed region at the 4 o'clock position, corresponding to the lung position on the CT scan. Additionally, the high sound speed area located in the center of the reconstruction coincided with the fluid region identified by the CT scan, while the low sound speed area in the northwest region corresponded with the fluid-free region (CT). To investigate the system's ability to track the progression of the pleural effusion condition, multiple frames spaced 1000 frames apart (1100 s) were reconstructed and analyzed. The selected reconstructed frames are presented in Figure 5.13, providing evidence of the system's capacity to detect changes in the pleural effusion condition over time.

Upon analyzing the reconstructed frames between 199 and 8099, clear evidence of the pleural effusion progression was observed. A consistent migration of the high sound speed region, initially concentrated around the 10 o'clock position, was observed, and likely caused by the spread of the fluid injected in the chest tube, which was inserted in the right side of the pig's thorax. Frame 199, obtained at the beginning of the experiment, shows that most of the fluid was concentrated in the top right region of the thorax, while the subsequent frames indicate fluid migration towards the back and center of the thoracic cavity. The final frame showed fluid accumulation around the left lung and the thoracic cavity center, which agrees with the previously analyzed CT scan. Notably, the reconstructed image corresponds to one data slice, with thickness determined by the transducer diameter and beam angle, which affects the ultrasonic wave path throughout the chest. Therefore, when the fluid was injected, it could have followed various paths not covered by the analyzed slice, explaining why the high sound speed area increased towards the thorax's left side from frames 1099 to 3099 before moving towards the pig's back.

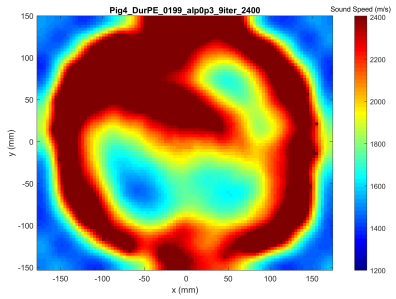

(a) Frame 199.

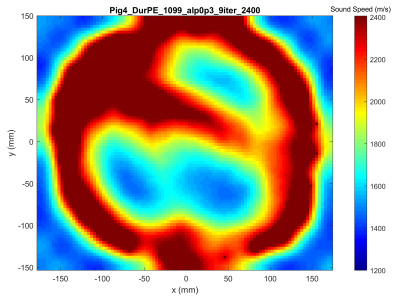

(b) Frame 1099 (82 s later).

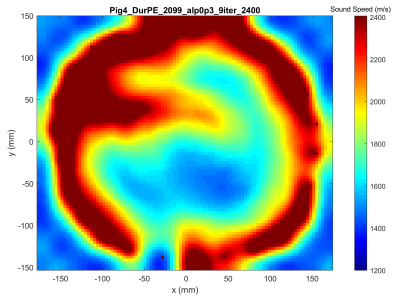

(c) Frame 2099 (108 s later).

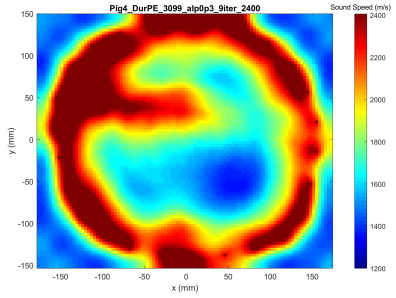

(d) Frame 3099 (108 s later).

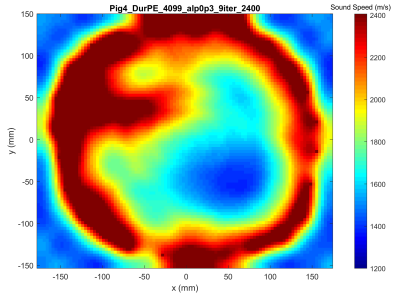

(e) Frame 4099 (108 s later).

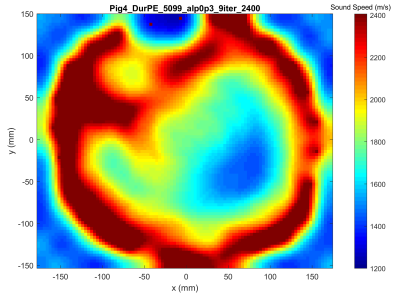

(f) Frame 5099 (108 s later).

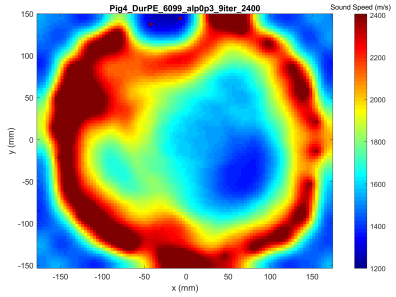

(g) Frame 6099 (108 s later).

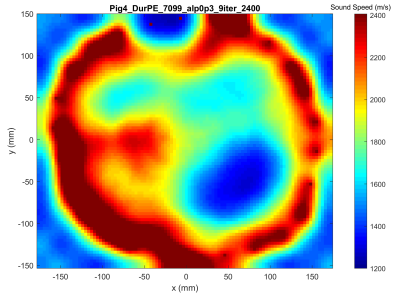

(h) Frame 7099 (108 s later).

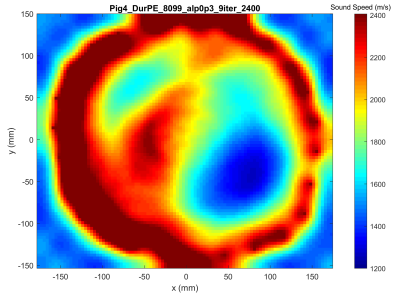

(i) Frame 8099 (108 s later).

Figure 5.13: TOF sound speed reconstructions (DICOM) of the data collected from Pig Four during the pleural effusion protocol; sequence of selected frames showing the condition's progression.

Chapter 6

Conclusion

The objective of this work was to create and assess a groundbreaking low-frequency USCT system for the application of lung imaging. Motivated by the lack of a radiation-free imaging tool for bedside lung imaging applications and by previous studies showing that low-frequency ultrasonic waves can be transmitted through the thorax, a complete USCT system was developed based on the Verasonics platform. To accomplish that, a modified Tonpilz transducer was designed to operate on a tomographic configuration. The newly designed transducer comprised a tail mass that had its mass distributed laterally, two PZT ceramics, and a curved-headed piston that included an integrated stress rod. These innovative design features allowed for the creation of a transducer that was both compact enough to fit in a ring array with up to 32 sensors and also powerful and sensitive enough to emit sound waves that could permeate the lungs and be detected around the subject's torso. The transducer's electrical, mechanical, and acoustical characteristics were experimentally determined and used to develop a calibration method that compensates for the sensitivity differences amongst samples. Next, a flexible belt of adjustable length that can hold up to 32 transducers radially distributed and equally spaced was developed and tested, showing that it was able to conform to the phantom or patient-to-be imaged while supporting all the transducers in a ring array configuration.

After that, a data collection routine that uses the Verasonics system to transmit ultrasonic signals in one transducer at a time while listening in the remainder was developed in MATLAB. The script determines a series of parameters that impact the transmitted and received signals, such as the transmitted waveform frequency, number of half-cycles, and voltage amplitude, as well as the gain and filtering features that compose the system's receive path. In addition, the algorithm generates the sequence that controls which transducer is active at a time and when to transfer the collected data from the system's buffer to the host's hard drive. The system's behavior was assessed through many tests, including using the transducer and a hydrophone in a water bath to determine

the acoustic pressure generated and the electric signal received as a function of the transmitted waveform and receive path settings.

The following step was to conduct experiments with various phantoms of different acoustic and dimensional properties and analyze the unprocessed signals received by the Verasonics system when used in a tomographic configuration. This step was essential to better understand the characteristics of the signals and later develop the data processing algorithms, which were responsible for removing the drift and DC, detecting the beginning of the received lobe, segmenting the signals, and storing the processed data. A section of data collection was composed of several frames, and each frame consisted of up to 1024 signals with 1280 samples each, which made comprehending and extracting the information contained in those signals a challenging task. Therefore, several studies were conducted with a gradual increase in phantom complexity, allowing the necessary knowledge build-up to develop a robust algorithm that was used to process the data employed in the computation of the time-of-flight reconstructions. In addition, since the position of the transducers is not fixed to a mechanical apparatus, as, for example, the sensors in a CT scan device, their position is not known by the system. However, having the transducer's position and their normals is essential to allow a tomographic reconstruction, and thus, an algorithm that calculates their location and normals based on a 3D scanned surface of the sample or an image that shows its boundary was developed.

The system's performance was assessed through several tests conducted with different phantoms, which indicated that it was generally able to well estimate the location and size of targets and phantom inhomogeneities' of different acoustic properties. The TOF reconstructions computed using the acoustic calibration coefficients determined in Section 3.2 were generally better defined and had more contrast than the ones computed with the data calibrated based on the displacement measurement only (Section: 3.1.3). That showed the importance of thoroughly characterizing all the sensors that were used on the USCT device.

The USCT device underwent a vertebrate animal study, and the results corroborated the hypothesis that low-frequency sound waves can penetrate the lungs, making them suitable for tho-

racic imaging. As a first test, data collected during tidal breathing were used to reconstruct a TOF sound speed image that revealed low sound speed regions with a shape and location similar to that of the lungs on the CT scan obtained after the USCT data collection. Moreover, the changes in the shape of the region over time exhibited a cyclic pattern in which the duration of each cycle corresponded with the duration of the inflation and deflation phases of the mechanical ventilator's settings, indicating the system's capability to detect the lungs and the changes caused due to breathing.

As a second investigation, data collected during a pneumothorax-inducing protocol were used to compute a TOF sound speed reconstruction which showed a low sound speed region that was comparable in both size and location to the pneumothorax that was identified on the CT scan. Furthermore, the progression of the condition could be identified by reconstructing multiple frames collected at different times during the procedure.

Finally, the TOF reconstructions computed with the data collected during the pleural effusion protocol revealed a remarkable level of correspondence between the size and location of the high and low sound speed areas and the size and location of the fluid and lung regions identified on the CT scan. Further analysis of the data collected during the experiment showed the migration of the high sound speed region over time which could be rated to the progression of the condition. These findings lend further support to the efficacy of the USCT device for thoracic imaging, paving the way for further work in animal studies and potentially humans.

Chapter 7

Future Work

7.1 Data Processing

One of the most complicated procedures of the data processing algorithm is to determine how to segment the received ultrasonic signals. The current approach determines the beginning of the first received lobe and segments the signal based on the number of listening half cycles pre-determined by the user, which resulted in well-defined TOF reconstructions. However, it is known that a lot of information about the medium might be contained in the reflected signal. Thus, exploring the reflected signals and performing reconstructions based on them might be a way of detecting certain pathologies or conditions that would not be visible otherwise.

7.2 Reconstructions

All the data processing and reconstructions presented in this document were conducted offline. As an implication, most of the parameters that define the transmitted waveform and receive path were adjusted on the fly during the experiments, and their values were based solely on the characteristics of the unprocessed received signal. Having a reconstructed image readily available, even if not computed at the same frame rate as the equipment can reach, would provide better feedback that could be used to tune the parameters that directly affect its quality. Therefore, implementing an algorithm that can process the data and generate the reconstructions online would be a great addition to the system. In addition, it would be worth exploring different reconstruction algorithms, such as the distorted Born iterative method (DBIM) and full-waveform inversion (FWI).

7.3 Experiments

While the data obtained from the vertebrate animal study has yielded promising results, there are still areas that warrant further exploration. For instance, the data was collected using a consis-

tent number of transmitted half-cycles, which may have restricted the system's ability to resolve smaller objects that were not detected in the reconstructions. Additionally, it would be interesting to investigate vertebrate animals with less severe conditions to assess the system's capability in detecting subtle variations in the medium's acoustical properties.

7.4 Safety

In order to proceed with collecting human data through the USCT system, it is imperative to ensure its safety. While the system's mechanical and thermal indexes have been assessed according to FDA regulations and found to fall within acceptable limits, additional factors must be thoroughly investigated to determine how to safely operate it [121]. As such, it is highly recommended to conduct a comprehensive review of the current literature regarding safety standards before conducting human trials.

Bibliography

[1] J. L. Mueller, D. Cardenas, and S. Furuie. A preclinical simulation study of ultrasound tomography for pulmonary bedside monitoring. In *Proceedings of the Second International Workshop on Medical Ultrasound Tomography (MUSTII)*, 2019.

[2] Melody Alsaker, Diego Armando Cardona Cárdenas, Sérgio Shiguemi Furuie, and Jennifer L Mueller. Complementary use of priors for pulmonary imaging with electrical impedance and ultrasound computed tomography. *Journal of Computational and Applied Mathematics*, 395:113591, 2021.

[3] Andre Viera Pigatto, Tzu-Jen Kao, Jennifer L. Mueller, Christopher D. Baker, Emily M. DeBoer, and Oren Kupfer. Electrical impedance tomography detects changes in ventilation after airway clearance in spinal muscular atrophy type i. *Respiratory Physiology and Neurobiology*, 294:103773, December 2021.

[4] Elizabeth AM O'Flynn, Jeremie Fromageau, Araminta E Ledger, Alessandro Messa, Ashley D'Aquino, Minouk J Schoemaker, Maria Schmidt, Neb Duric, Anthony J Swerdlow, and Jeffrey C Bamber. Ultrasound tomography evaluation of breast density: a comparison with noncontrast magnetic resonance imaging. *Investigative radiology*, 52(6):343, 2017.

[5] Farzad Karami and Reza Morsali. Optimization of sonar transducers via evolutionary algorithms. *SN Applied Sciences*, 1(12), November 2019.

[6] Verasonics. Signal conditioning in the vantage research ultrasound system receive path adds flexibility and efficiency to research projects, Jan. 13, 2020 [Online].

[7] Thomas Gluecker, Patrizio Capasso, Pierre Schnyder, François Gudinchet, Marie-Denise Schaller, Jean-Pierre Revelly, René Chiolero, Peter Vock, and Stéphan Wicky. Clinical and radiologic features of pulmonary edema. *Radiographics*, 19(6):1507–1531, 1999.

[8] Luciano Gattinoni, Pietro Caironi, Franco Valenza, and Eleonora Carlesso. The role of ct-scan studies for the diagnosis and therapy of acute respiratory distress syndrome. *Clinics in chest medicine*, 27(4):559–570, 2006.

[9] Marine Aliaga, Jean-Marie Forel, Sophie De Bourmont, Boris Jung, Guillemette Thomas, Martin Mahul, Magali Bisbal, Stephanie Nougaret, Sami Hraiech, Antoine Roch, et al. Diagnostic yield and safety of ct scans in icu. *Intensive Care Medicine*, 41(3):436–443, 2015.

[10] Wesley H Self, D Mark Courtney, Candace D McNaughton, Richard G Wunderink, and Jeffrey A Kline. High discordance of chest x-ray and computed tomography for detection of pulmonary opacities in ed patients: implications for diagnosing pneumonia. *The American journal of emergency medicine*, 31(2):401–405, 2013.

[11] D.A. Lichtenstein. Ultrasound in the management of thoracic disease. *Crit. Care Med.*, 35:S250–S261, 2007.

[12] Y. Beaulieu and P.E. Marik. Bedside ultrasonography in the ICU: part 2. *Chest*, 128(3):1766–1781, 2005.

[13] C.L. Tobin, Y.C. Lee, F. Gleeson, D. Feller-Kopman, and N. Rahman. *Pleural ultrasound for clinicians: a text and e-book*. CRC Press, 2014.

[14] David L. Convissar, Lauren E. Gibson, Lorenzo Berra, Edward A. Bittner, and Marvin G. Chang. Application of lung ultrasound during the COVID-19 pandemic: A narrative review. *Anesthesia & Analgesia*, 131(2):345–350, 2020.

[15] Luna Gargani, Hatem Soliman-Aboumarie, Giovanni Volpicelli, Francesco Corradi, Maria Concetta Pastore, and Matteo Cameli. Why, when, and how to use lung ultrasound during the COVID-19 pandemic: enthusiasm and caution. *European Heart Journal - Cardiovascular Imaging*, 21(9):941–948, 06 2020.

[16] J. A Shaw, E. H Louw, and C. F. N. Koegelenberg. Lung ultrasound in COVID-19: Not novel, but necessary. *Respiration*, 99:545–547, 2020.

[17] Yao Zhang, Heng Xue, Mixue Wang, Nan He, Zhibin Lv, and Ligang Cui. Lung ultrasound findings in patients with coronavirus disease (COVID-19). *American Journal of Roentgenology*, 216(1):80–84, 2021.

[18] J.A. Shaw, F. von Groote-Bidlingmaier, and C.F.N. Koegelenberg. Transthoracic ultrasound, Palange P, Rhode G, editors: ERS. In *Handbook of Respiratory Medicine. 3rd ed.*, pages 160–167. European Respiratory Society (ERS), 2019.

[19] QY. Peng, XT. Wang, LN. Zhang, and Chinese Critical Care Ultrasound Study Group (CCUSG). Findings of lung ultrasonography of novel corona virus pneumonia during the 2019-2020 epidemic. *Intensive Care Med*, 46:849–850, 2020.

[20] Roberto J. Lavarello and Andrew J. Hesford. Methods for forward and inverse scattering in ultrasound tomography. In *Quantitative Ultrasound in Soft Tissues*, pages 345–394. Springer Netherlands, 2013.

[21] M. Blaivas, A. Kirkpatrick, and A. Sustic. Future directions and conclusions. *Crit. Care Med.*, 35:S305–S307, 2007.

[22] DS Holder. Introduction to biomedical electrical impedance tomography electrical impedance tomography methods, history and applications ed ds holder, 2005.

[23] Brian H Brown. Electrical impedance tomography (eit): a review. *Journal of medical engineering & technology*, 27(3):97–108, 2003.

[24] Thiago de Castro Martins, André Kubagawa Sato, Fernando Silva de Moura, Erick Dario León Bueno de Camargo, Olavo Luppi Silva, Talles Batista Rattis Santos, Zhanqi Zhao, Knut Möeller, Marcelo Brito Passos Amato, Jennifer L Mueller, et al. A review of electrical impedance tomography in lung applications: Theory and algorithms for absolute images. *Annual Reviews in Control*, 48:442–471, 2019.

[25] Inéz Frerichs, Marcelo BP Amato, Anton H Van Kaam, David G Tingay, Zhanqi Zhao, Bartłomiej Grychtol, Marc Bodenstein, Hervé Gagnon, Stephan H Böhm, Eckhard

Teschner, et al. Chest electrical impedance tomography examination, data analysis, terminology, clinical use and recommendations: consensus statement of the translational eit development study group. *Thorax*, 72(1):83–93, 2017.

[26] Tushar Kanti Bera. Applications of electrical impedance tomography (EIT): A short review. *IOP Conference Series: Materials Science and Engineering*, 331:012004, March 2018.

[27] Eduardo LV Costa, R Gonzalez Lima, and Marcelo BP Amato. Electrical impedance tomography. *Yearbook of Intensive Care and Emergency Medicine*, pages 394–404, 2009.

[28] Inéz Frerichs, José Hinz, Peter Herrmann, Gerald Weisser, Gunter Hahn, Taras Dudykevych, Michael Quintel, and Gerhard Hellige. Detection of local lung air content by electrical impedance tomography compared with electron beam ct. *Journal of applied physiology*, 93(2):660–666, 2002.

[29] Henk J Smit, Anton Vonk Noordegraaf, J Tim Marcus, Anco Boonstra, Peter M de Vries, and Pieter E Postmus. Determinants of pulmonary perfusion measured by electrical impedance tomography. *European journal of applied physiology*, 92(1):45–49, 2004.

[30] Inéz Frerichs, José Hinz, Peter Herrmann, Gerald Weisser, Günter Hahn, Michael Quintel, and Gerhard Hellige. Regional lung perfusion as determined by electrical impedance tomography in comparison with electron beam ct imaging. *IEEE transactions on medical imaging*, 21(6):646–652, 2002.

[31] João Batista Borges, Fernando Suarez-Sipmann, Stephan H. Bohm, Gerardo Tusman, Alexandre Melo, Enn Maripuu, Mattias Sandström, Marcelo Park, Eduardo L. V. Costa, Göran Hedenstierna, and Marcelo Amato. Regional lung perfusion estimated by electrical impedance tomography in a piglet model of lung collapse. *Journal of Applied Physiology*, 112(1):225–236, January 2012.

[32] Gerhard K. Wolf and John H. Arnold. Noninvasive assessment of lung volume: Respiratory inductance plethysmography and electrical impedance tomography. *Critical Care Medicine*, 33(Supplement):S163–S169, March 2005.

[33] Inez Frerichs, Zhanqi Zhao, Tobias Becher, Peter Zabel, Norbert Weiler, and Barbara Vogt. Regional lung function determined by electrical impedance tomography during bronchodilator reversibility testing in patients with asthma. *Physiological measurement*, 37(6):698, 2016.

[34] Sylvia Lehmann, Steffen Leonhardt, Chuong Ngo, Lukas Bergmann, Ines Ayed, Simone Schrading, and Klaus Tenbrock. Global and regional lung function in cystic fibrosis measured by electrical impedance tomography. *Pediatric pulmonology*, 51(11):1191–1199, 2016.

[35] Peter A Muller, Jennifer L Mueller, Michelle Mellenthin, Rashmi Murthy, Michael Capps, Brandie D Wagner, Melody Alsaker, Robin Deterding, Scott D Sagel, and Jordana Hoppe. Evaluation of surrogate measures of pulmonary function derived from electrical impedance tomography data in children with cystic fibrosis. *Physiological measurement*, 39(4):045008, 2018.

[36] Sabine Krueger-Ziolek, Benjamin Schullcke, Zhanqi Zhao, Bo Gong, and Knut Moeller. Determination of regional lung function in cystic fibrosis using electrical impedance tomography. *Current Directions in Biomedical Engineering*, 2(1):633–636, 2016.

[37] Jennifer L Mueller, Peter Muller, Michelle Mellenthin, Rashmi Murthy, Michael Capps, Melody Alsaker, Robin Deterding, Scott D Sagel, and Emily DeBoer. Estimating regions of air trapping from electrical impedance tomography data. *Physiological measurement*, 39(5):05NT01, 2018.

[38] Francois Marquis, Nicolas Coulombe, Roberta Costa, Hervé Gagnon, Robert Guardo, and Yoanna Skrobik. Electrical impedance tomography's correlation to lung volume is not

influenced by anthropometric parameters. *Journal of clinical monitoring and computing*, 20(3):201–207, 2006.

[39] Nicolas Coulombe, Herve Gagnon, Francois Marquis, Yoanna Skrobik, and Robert Guardo. A parametric model of the relationship between eit and total lung volume. *Physiological measurement*, 26(4):401, 2005.

[40] Henrik Reinius, João Batista Borges, Filip Fredén, Lena Jideus, EDLB Camargo, MBP Amato, Göran Hedenstierna, Anders Larsson, and Fredrik Lennmyr. Real-time ventilation and perfusion distributions by electrical impedance tomography during one-lung ventilation with capnothorax. *Acta Anaesthesiologica Scandinavica*, 59(3):354–368, 2015.

[41] Hazel R Carlisle, Ruth K Armstrong, Peter G Davis, Andreas Schibler, Inéz Frerichs, and David G Tingay. Regional distribution of blood volume within the preterm infant thorax during synchronised mechanical ventilation. *Intensive care medicine*, 36(12):2101–2108, 2010.

[42] Agus Iwan Foead, Wendy Wai Yeng Yeo, Thirupathirao Vishnumukkala, Michael Larvin, et al. Rehabilitation in spinal muscular atrophy. *The Journal of the International Society of Physical and Rehabilitation Medicine*, 2(1):62, 2019.

[43] Fong Ming Hooi, Oliver Kripfgans, and Paul L. Carson. Acoustic attenuation imaging of tissue bulk properties with a priori information. *The Journal of the Acoustical Society of America*, 140(3):2113–2122, September 2016.

[44] M. Pérez-Liva, J. L. Herraiz, J. M. Udías, E. Miller, B. T. Cox, and B. E. Treeby. Time domain reconstruction of sound speed and attenuation in ultrasound computed tomography using full wave inversiona). *The Journal of the Acoustical Society of America*, 141(3):1595–1604, March 2017.

[45] Hang Yin, Yun Wu, Xiaoyue Fang, Junjie Song, Liang Zhou, Qiude Zhang, Zhaohui Liu, Jupeng Ni, Mingyue Ding, and Ming Yuchi. Sound speed image reconstruction of ultrasound

computed tomography based on gpu acceleration. In *2021 IEEE International Conference on Medical Imaging Physics and Engineering (ICMIPE)*, pages 1–6, 2021.

[46] Wei Zhu, Xu Chang, Yibo Wang, Hongyu Zhai, and Zhenxing Yao. Reconstruction of hydraulic fractures using passive ultrasonic travel-time tomography. *Energies*, 11(5):1321, 2018.

[47] Hajin Choi and John S. Popovics. NDE application of ultrasonic tomography to a full-scale concrete structure. *IEEE Transactions on Ultrasonics, Ferroelectrics, and Frequency Control*, 62(6):1076–1085, June 2015.

[48] Y.J. Choi, K.L. Mccarthy, and M.J. Mccarthy. Tomographic techniques for measuring fluid flow properties. *Journal of Food Science*, 67(7):2718–2724, September 2002.

[49] A.V. Goncharsky, S.Y. Romanov, and S.Y. Seryozhnikov. A computer simulation study of soft tissue characterization using low-frequency ultrasonic tomography. *Ultrasonics*, 67:136–150, April 2016.

[50] Arthorn Sanpanich, Kazuhiko Hamamoto, and Chuchart Pintavirooj. An investigation on attenuation UCT with wave paths enhancement for breast ultrasound. *IEEJ Transactions on Electrical and Electronic Engineering*, 7(S1):S105–S113, December 2012.

[51] Chang Liu, Chenyang Xue, Binzhen Zhang, Guojun Zhang, and Changde He. The application of an ultrasound tomography algorithm in a novel ring 3d ultrasound imaging system. *Sensors*, 18(5):1332, 2018.

[52] Matthias Birk, Sven Koehler, Matthias Balzer, Michael Huebner, Nicole V. Ruiter, and Juergen Becker. FPGA-based embedded signal processing for 3-d ultrasound computer tomography. *IEEE Transactions on Nuclear Science*, 58(4):1647–1651, August 2011.

[53] Neb Duric, Peter Littrup, Cuiping Li, Olivier Roy, Steve Schmidt, John Seamans, Andrea Wallen, and Lisa Bey-Knight. Whole breast tissue characterization with ultrasound tomog-

raphy. In Johan G. Bosch and Neb Duric, editors, *Medical Imaging 2015: Ultrasonic Imaging and Tomography*, volume 9419, pages 81 – 88. International Society for Optics and Photonics, SPIE, 2015.

[54] Mark Sak, Peter Littrup, Rachel Brem, and Neb Duric. Whole Breast Sound Speed Measurement from US Tomography Correlates Strongly with Volumetric Breast Density from Mammography. *Journal of Breast Imaging*, 2(5):443–451, 07 2020.

[55] Gursharan Yash Sandhu, Erik West, Cuiping Li, Olivier Roy, and Neb Duric. 3D frequency-domain ultrasound waveform tomography breast imaging. In Neb Duric and Brecht Heyde, editors, *Medical Imaging 2017: Ultrasonic Imaging and Tomography*, volume 10139, pages 56 – 69. International Society for Optics and Photonics, SPIE, 2017.

[56] G Y Sandhu, C Li, O Roy, S Schmidt, and N Duric. Frequency domain ultrasound waveform tomography: breast imaging using a ring transducer. *Physics in Medicine & Biology*, 60(14):5381, 2015.

[57] Elizabeth AM O'Flynn, Jeremie Fromageau, Araminta E Ledger, Alessandro Messa, Ashley D'Aquino, Minouk J Schoemaker, Maria Schmidt, Neb Duric, Anthony J Swerdlow, and Jeffrey C Bamber. Ultrasound tomography evaluation of breast density: a comparison with noncontrast magnetic resonance imaging. *Investigative radiology*, 52(6):343, 2017.

[58] Kahdi F Udobi, ED Childs, and Karim Toujier. Acute respiratory distress syndrome. *American family physician*, 67(2):315–322, 2003.

[59] D. Rueter, H. P. Hauber, D. Droeman, P. Zabel, and Stefan Uhlig. Low-frequency ultrasound permeates the human thorax and lung: A novel approach to non-invasive monitoring. *Ultraschall in der Medizin*, 31(1):53–62, 2010.

[60] Melody Dodd and Jennifer L Mueller. A real-time d-bar algorithm for 2-d electrical impedance tomography data. *Inverse problems and imaging (Springfield, Mo.)*, 8(4):1013, 2014.

[61] Florian Vogl, Bernd Friesenbichler, Laura Hüsken, Inès A. Kramers de Quervain, and William R. Taylor. Can low-frequency guided waves at the tibia paired with machine learning differentiate between healthy and osteopenic/osteoporotic subjects? a pilot study. *Ultrasonics*, 94:109–116, April 2019.

[62] Koussila Kassou, Youcef Remram, Pascal Laugier, and Jean-Gabriel Minonzio. Dispersion characteristics of the flexural wave assessed using low frequency (50–150 kHz) point-contact transducers: A feasibility study on bone-mimicking phantoms. *Ultrasonics*, 81:1–9, November 2017.

[63] Olivia Ngo, Evan Niemann, Vivinya Gunasekaran, Prabagar Sankar, Miriam Putterman, Alec Lafontant, Sumati Nadkarni, Rose Ann Dimaria-Ghalili, Michael Neidrauer, Leonid Zubkov, Michael Weingarten, David J. Margolis, and Peter A. Lewin. Development of low frequency (20-100 kHz) clinically viable ultrasound applicator for chronic wound treatment. *IEEE Transactions on Ultrasonics, Ferroelectrics, and Frequency Control*, 66(3):572–580, 2019.

[64] Seungjun Lee, N.B. Smith, and K.K. Shung. Ultrasound mediated transdermal in vivo transport of insulin with low profile cymbal arrays. In *2002 IEEE Ultrasonics Symposium, 2002. Proceedings.*, volume 2, pages 1423–1426 vol.2, 2002.

[65] Peiyang Li, Weiwei Shao, Tingyi Jiang, Zhangjian Li, Suoyuan Li, Junjie Fan, Liming Cai, Yaoyao Cui, and Jun Shen. Development of a miniaturized low-frequency transducer for accurate placement of screw implants in the spine. In *2019 IEEE International Ultrasonics Symposium (IUS)*, pages 1815–1818, 2019.

[66] Robert J. Urick. *Principles of Underwater Sound*. (McGraw–Hill, New York, 1893.

[67] Charles H. Sherman and John L. Butler. *Transducers and Arrays for Underwater Sound*. Springer New York, 2007.

[68] Chunying Wang, Yu Lan, and Wenwu Cao. Tonpilz transducer head mass selection based on excitation signal type. *Applied Acoustics*, 176:107852, 2021.

[69] Valsala Kurusingal. Tonpilz transducer array for wideband sonar applications. In *2019 IEEE International Ultrasonics Symposium (IUS)*, pages 1750–1752, 2019.

[70] Hyunki Kim and Yongrae Roh. Design and fabrication of a wideband tonpilz transducer with a void head mass. *Sensors and Actuators A: Physical*, 239:137–143, March 2016.

[71] A Cochran, P Reynolds, and G Hayward. Progress in stacked piezocomposite ultrasonic transducers for low frequency applications. *Ultrasonics*, 36(10):969–977, October 1998.

[72] Seonghun Pyo and Yongrae Roh. Structural design of an acoustic planar array transducer by using the equivalent circuit method. *Ultrasonics*, 108:106219, December 2020.

[73] Seonghun Pyo, Muhammad Shakeel Afzal, Youngsub Lim, Seungjin Lee, and Yongrae Roh. Design of a wideband tonpilz transducer comprising non-uniform piezoceramic stacks with equivalent circuits. *Sensors*, 21(8):2680, April 2021.

[74] Jinwook Kim, Hoeyong Kim, and Yongrae Roh. Design and fabrication of multi-mode wideband tonpilz transducers. *The Journal of the Acoustical Society of Korea*, 32(3):191–198, 2013.

[75] Kenji Saijyou and Tomonao Okuyama. Design optimization of wide-band tonpilz piezoelectric transducer with a bending piezoelectric disk on the radiation surface. *The journal of the acoustical society of America*, 127(5):2836–2846, 2010.

[76] BUTLER JL; CIPOLLA JR; BROWN WD. Radiating head flexure and its effect on transducer performance. *J. ACOUST. SOC. AM.; ISSN 0001-4966; USA; DA. 1981; VOL. 70; NO 2; PP. 500-503; BIBL. 9 REF.*, 1981.

[77] Christian Henke. A numerical modeling strategy for passive electro-acoustic transducers. *Ultrasonics*, 102:106065, March 2020.

[78] J.M. Allin and P. Cawley. Design and construction of a low frequency wide band non-resonant transducer. *Ultrasonics*, 41(3):147–155, May 2003.

[79] A. V. Pigatto, L. Giacobbo, A. Lisibach, E. M. Lopes Filho, R. G. Lima, and J. L. Mueller. Design and calibration of a tonpilz transducer for low frequency medical ultrasound tomography. In *2022 44th Annual International Conference of the IEEE Engineering in Medicine & Biology Society (EMBC)*, pages 4611–4617, 2022.

[80] Ahmad Safari and E Koray Akdogan. *Piezoelectric and acoustic materials for transducer applications*. Springer Science & Business Media, 2008.

[81] Qingshan Yao and Leif Bjørnø. Broadband tonpilz underwater acoustic transducers based on multimode optimization. *IEEE Transactions on Ultrasonics, Ferroelectrics, and Frequency Control*, 1997.

[82] R.J. Meyer, T.C. Montgomery, and W.J. Hughes. Tonpilz transducers designed using single crystal piezoelectrics. In *OCEANS '02 MTS/IEEE*, volume 4, pages 2328–2333 vol.4, 2002.

[83] Hazel C. Starritt and Francis A. Duck. Safety. In *Clinical Ultrasound*, pages 51–60. Churchill Livingstone, jan 2011.

[84] FDA. Marketing Clearance of Diagnostic Ultrasound Systems and Transducers; Guidance for Industry and Food and Drug Administration Staff. *U.S. Department of Health and Human Services: Food and Drug Administration: Center for Devices and Radiological Health*, pages 18–34, 2019.

[85] Practice for evaluating characteristics of ultrasonic search units.

[86] Robert E. Apfel and Christy K. Holland. Gauging the likelihood of cavitation from short-pulse, low-duty cycle diagnostic ultrasound. *Ultrasound in Medicine and Biology*, 1991.

[87] J-L. Laborde, C. Bouyer, J.-P. Caltagirone, and A. Gérard. Acoustic bubble cavitation at low frequencies. *Ultrasonics*, 36(1-5):589–594, February 1998.

[88] J.-L. Laborde, C. Bouyer, J.-P. Caltagirone, and A. Gérard. Acoustic cavitation field prediction at low and high-frequency ultrasounds. *Ultrasonics*, 36(1-5):581–587, February 1998.

[89] Kenji Yoshida, Kazuya Obata, Akira Tsukamoto, Takashi Ushida, and Yoshiaki Watanabe. Limited damage of tissue mimic caused by a collapsing bubble under low-frequency ultrasound exposure. *Ultrasonics*, 54(6):1603–1609, August 2014.

[90] Ana L. Lopez-Sanchez and Lester W. Schmerr. Determination of an ultrasonic transducer's sensitivity and impedance in a pulse-echo setup. *IEEE Transactions on Ultrasonics, Ferroelectrics, and Frequency Control*, 53(11):2101–2112, 2006.

[91] Douglas C Montgomery. *Design and Analysis of Experiments*, volume 1. Wiley, Hoboken, 8th edition, feb 2012.

[92] Robert J Bobber. *Underwater electroacoustic measurements*. Peninsula publishing, 1988.

[93] Stephen P Robinson. Review of methods for low-frequency transducer calibration in reverberant tanks. *National Physical Laboratory Report - NPL*, 1999.

[94] SP Robinson and GR Doré. Uncertainties in the calibration of hydrophones at npl by the three-transducer spherical-wave reciprocity method in the frequency range 10 khz on 500 khz. *Unknown*, 1994.

[95] Nykolai Bilaniuk and George S. K. Wong. Speed of sound in pure water as a function of temperature. *The Journal of the Acoustical Society of America*, 93(3):1609–1612, March 1993.

[96] American Institute of Ultrasound in Medicine et al. *Acoustic output measurement standard for diagnostic ultrasound equipment*. American Institute of Ultrasound in Medicine, 1998.

[97] Jason Matthew Sempsrott. Experimental evaluation of acoustic saturation. Master's thesis, University of Illinois at Urbana-Champaign, 2000.

[98] Byung-Jin Kwon. A development of underwater acoustic tonpilz transducer with the piezoelectric single crystal. *Journal of the Korean Institute of Electrical and Electronic Material Engineers*, 29(9):532–538, 2016.

[99] Kanji Ono, Hideo Cho, Hartmut Vallen, and Robert T M'Closkey. Transmission sensitivities of contact ultrasonic transducers and their applications. *Sensors*, 21(13):4396, 2021.

[100] Jineesh George, DD Ebenezer, and SK Bhattacharyya. Receiving sensitivity and transmitting voltage response of a fluid loaded spherical piezoelectric transducer with an elastic coating. *The journal of the acoustical society of america*, 128(4):1712–1720, 2010.

[101] T Miyama, T Nada, T Inoue, S Takahashi, and M Konno. Investigation for tonpilz piezoelectric transducers with acoustic matching plates. In *IEEE 1987 Ultrasonics Symposium*, pages 779–784. IEEE, 1987.

[102] Polat Kurt, Murat Şansal, Istek Tatar, Cihangir Duran, and Sadettin Orhan. Vibro-acoustic design, manufacturing and characterization of a tonpilz-type transducer. *Applied Acoustics*, 150:27–35, 2019.

[103] Anuj Bhatia and Philip Peng. Ultrasound-guided procedures for pain management. In *Essentials of Pain Medicine*, pages 725–736.e1. Elsevier, 2018.

[104] John E. Aldrich. Basic physics of ultrasound imaging. *Critical Care Medicine*, 35(Suppl):S131–S137, May 2007.

[105] R FINE. Image-guided breast biopsy. In *Surgical Pitfalls*, pages 433–454. Elsevier, 2009.

[106] Manoj K. Karmakar and Wing H. Kwok. Ultrasound-guided regional anesthesia. In *A Practice of Anesthesia for Infants and Children*, pages 988–1022.e4. Elsevier, 2019.

[107] John A. Flynn, Peter Kaczkowski, Ken Linkhart, and Ronald E. Daigle. Arbitrary waveforms using a tri-state transmit pulser. In *2013 IEEE International Ultrasonics Symposium (IUS)*. IEEE, July 2013.

[108] Verasonics. Arbitrary waveform generation with the verasonics research ultrasound platform, Feb., 2016 [Online].

[109] Rehman Ali, Scott Hsieh, and Jeremy Dahl. Open-source gauss-newton-based methods for refraction-corrected ultrasound computed tomography. In Nicole V. Ruiter and Brett C. Byram, editors, *Medical Imaging 2019: Ultrasonic Imaging and Tomography*. SPIE, March 2019.

[110] M. Sabry Hassouna and A. A. Farag. Multistencils fast marching methods: A highly accurate solution to the eikonal equation on cartesian domains. *IEEE Transactions on Pattern Analysis and Machine Intelligence*, 29(9):1563–1574, 2007.

[111] Cuiping Li, Nebojsa Duric, Peter Littrup, and Lianjie Huang. In vivo breast sound-speed imaging with ultrasound tomography. *Ultrasound in medicine & biology*, 35(10):1615–1628, 2009.

[112] Gail A. Van Norman. Drugs, devices, and the FDA: Part 2. *JACC: Basic to Translational Science*, 1(4):277–287, June 2016.

[113] P. Mukherjee, S. Roy, D. Ghosh, and S. K. Nandi. Role of animal models in biomedical research: a review. *Laboratory Animal Research*, 38(1), July 2022.

[114] Paul Zarogoulidis, Ioannis Kioumis, Georgia Pitsiou, Konstantinos Porpodis, Sofia Lampaki, Antonis Papaiwannou, Nikolaos Katsikogiannis, Bojan Zaric, Perin Branislav, Nevena Secen, et al. Pneumothorax: from definition to diagnosis and treatment. *Journal of thoracic disease*, 6(Suppl 4):S372, 2014.

[115] Berthold Jany and Tobias Welte. Pleural effusion in adults—etiology, diagnosis, and treatment. *Deutsches Ärzteblatt international*, May 2019.

[116] FA Duck. Propagation of sound through tissue. *The Safe Use of Ultrasound in Medical Diagnosis*, pages 4–15, 2000.

[117] T. Koch, S. Lakshmanan, K. Raum, M. Wicke, D. Mörlein, and S. Brand. Sound velocity and attenuation of porcine loin muscle, backfat and skin. In Olaf Dössel and Wolfgang C. Schlegel, editors, *World Congress on Medical Physics and Biomedical Engineering, September 7 - 12, 2009, Munich, Germany*, pages 96–99, Berlin, Heidelberg, 2010. Springer Berlin Heidelberg.

[118] Tim Koch, Sannachi Lakshmanan, Sebastian Brand, Michael Wicke, Kay Raum, and Daniel Mörlein. Ultrasound velocity and attenuation of porcine soft tissues with respect to structure and composition: Ii. skin and backfat. *Meat Science*, 88(1):67–74, 2011.

[119] Tim Koch, Sannachi Lakshmanan, Sebastian Brand, Michael Wicke, Kay Raum, and Daniel Mörlein. Ultrasound velocity and attenuation of porcine soft tissues with respect to structure and composition: I. muscle. *Meat Science*, 88(1):51–58, 2011.

[120] Tainsong Chen, Jiunn-Shyong Tzeng, and Chii-Jen Lin. A novel method to measure acoustic speed of bone tissue. *Ultrasound in Medicine and Biology*, 23(9):1337–1341, 1997.

[121] Kathryn R. Nightingale, Charles C. Church, Gerald Harris, Keith A. Wear, Michael R. Bailey, Paul L. Carson, Hui Jiang, Kurt L. Sandstrom, Thomas L. Szabo, and Marvin C. Ziskin. Conditionally increased acoustic pressures in nonfetal diagnostic ultrasound examinations without contrast agents: A preliminary assessment. *Journal of Ultrasound in Medicine*, 34(7):1–41, July 2015.

Appendix A

Publication One

Starting on the next page, our publication related to Electrical Impedance Tomography is presented in its original form. It was officially published in the Respiratory Physiology and Neurobiology Journal on August 13, 2021.

Respiratory Physiology & Neurobiology 294 (2021) 103773

Contents lists available at ScienceDirect

Respiratory Physiology & Neurobiology

journal homepage: www.elsevier.com/locate/resphysiol

Electrical impedance tomography detects changes in ventilation after airway clearance in spinal muscular atrophy type I

Andre Viera Pigatto [a], Tzu-Jen Kao [b], Jennifer L. Mueller [c,*], Christopher D. Baker [d], Emily M. DeBoer [d], Oren Kupfer [d]

[a] School of Biomedical Engineering, Colorado State University, Fort Collins, CO 80523, United States
[b] GE Research, Niskayuna, NY 12309, United States
[c] School of Biomedical Engineering and Department of Mathematics, Colorado State University, Fort Collins, CO 80523, United States
[d] Department of Pediatrics, Section of Pulmonary Medicine, University of Colorado School of Medicine, Aurora, CO 80045, United States

ARTICLE INFO

Edited by Dr. M. Dutschmann

Keywords:
Spinal muscular atrophy
Electrical impedance tomography
Mechanical insufflation-exsufflation

ABSTRACT

The effect of mechanical insufflation-exsufflation (MIE) for airway clearance in patients with spinal muscular atrophy type I (SMA-I) on the distribution of ventilation in the lung is unknown, as is the duration of its beneficial effects. A pilot study to investigate the feasibility of using three dimensional (3-D) electrical impedance tomography (EIT) images to estimate lung volumes pre- and post-MIE for assessing the effectiveness of mechanical insufflation-exsufflation (MIE) was conducted in 6 pediatric patients with SMA-I in the neuromuscular clinic at Children's Hospital Colorado. EIT data were collected before, during, and after the MIE procedure on two rows of 16 electrodes placed around the chest. Lung volumes were computed from the images and compared before, during, and after the MIE procedure to assess the ability of EIT to estimate changes in lung volume during insufflation and exsufflation. Images of pulsatile pulmonary perfusion were computed in subjects able to perform breath-holding. In four of the six subjects, lung volumes during tidal breathing increased after MIE (average change from pre to post MIE was 58.8±55.1 mL). The time-dependent plots of lung volume computed from the EIT data clearly show when the MIE device insufflates and exsufflates air and the rest periods between mechanical coughs. Images of pulmonary pulsatile perfusion were computed from data collected during breathing pauses. The results suggest that EIT holds promise for estimating lung volumes and ventilation/perfusion mismatch, both of which are useful for assessing the effectiveness of MIE in clearing mucus plugs.

1. Introduction

Spinal muscular atrophy is a progressive genetic disease affecting about 1 in 11,000 newborn babies each year (Pearn, 1973; Sugarman et al., 2012) characterized by anterior horn cell disease leading to weakness and atrophy of the skeletal muscles. It typically affects the proximal muscles more severely than distal muscles. Approximately one in 50 people in the United States is a carrier of the disease (Sugarman et al., 2012), which is caused by a missing or dysfunctional SMN1 gene (Lefebvre et al., 1995). The most common and most severe form is spinal muscular atrophy type I (SMA-I). Children with SMA-I cannot sit by themselves and have progressive bulbar and respiratory muscle weakness leading to inability to feed, aspiration, and respiratory failure. Respiratory muscle weakness prevents effective coughing and leads to the accumulation of mucus in the lungs that can result in air trapping, atelectasis, infection, and pneumonia. Respiratory complications are the leading cause of death in patients with SMA-I (Zerres and Rudnik-Schöneborn, 1995; Finkel et al., 2014; Kolb et al., 2017). In recent years, three SMA-specific therapies have been approved (Finkel et al., 2017; Al-Zaidy and Mendell, 2019; Food and Drug Administration, 2020), but not all patients are receiving them (Schorling et al., 2020). Assessing respiratory function in SMA-I is challenging since many patients are unable to perform standard pulmonary function tests due to age or bulbar function.

Mechanical insufflation-exsufflation (MIE) is used for airway clearance in patients with SMA-I, but there are many open questions about its optimal use and the duration of its beneficial effects. Knowing the effect of MIE on the distribution of ventilation in the lung could help answer these questions, yet at present, a clinical tool is lacking. Electrical impedance tomography (EIT) is a safe, non-invasive, non-ionizing

* Corresponding author at: Department of Mathematics, 101 Weber Building, Colorado State University, Fort Collins, CO 80523-1874, United States.
E-mail address: mueller@math.colostate.edu (J.L. Mueller).

https://doi.org/10.1016/j.resp.2021.103773
Received 5 December 2020; Received in revised form 6 April 2021; Accepted 5 August 2021
Available online 13 August 2021

Table 1
Subject characteristics at the time of the study.

Subject	Sex	Age	BMI or Weight-for-length (WFL)	SpO_2(%)	Respiratory support during study	Drug Nusinersen (N) Onasemnogene (O)	SMA Genotype
1	F	2 years	WFL = 33 PCTL	97	non-invasive	N and O	0 SMN1, 2 SMN2
2	M	5 years	BMI = 8 PCTL	99	non-invasive	N	0 SMN1, 2 SMN2
3	F	8 years	BMI <1 PCTL	96	non-invasive	N	0 SMN1, 2 SMN2
4	M	11 months	WFL = 6 PCTL	95	none	N and O	0 SMN1, 2 SMN2
5	F	5 years	BMI <1 PCTL	94	invasive	N	0 SMN1, 2 SMN2
6	M	3 years	BMI = 1 PCTL	n/a	none	N	0 SMN1, 3 SMN2

imaging modality that can be performed as-needed, even during MIE. In EIT imaging, electrodes are placed on the skin around the torso, a low-frequency imperceptible current is applied, and the resulting voltages are measured on the electrodes (Holder, 2005; Brown, 2003; Frerichs et al., 2017; Martins et al., 2019). The measured data is used to solve an inverse problem numerically to compute the conductivity distribution in the chest. Since air, blood, muscle, and lung tissue all have different conductivity values, dynamic images of ventilation and perfusion can be formed from the reconstructions. Clinical validation against CT images has shown that EIT is effective for obtaining images of regional ventilation distribution (Frerichs et al., 2002a, b; Costa et al., 2009; Smit et al., 2004; Victorino et al., 2004). Regional information used to derive measures of spatial and temporal ventilatory heterogeneity have been used to detect changes in patients with chronic asthma pre- and post-bronchodilator inhalation (Frerichs et al., 2016) and cystic fibrosis (Lehmann et al., 2016). Cystic fibrosis patients were also the subjects of studies in which changes in EIT-derived spirometry measures demonstrated a positive correlation with standard spirometry (Krueger-Ziolek et al., 2016; Muller et al., 2018), and regions of air trapping were identified using EIT derived ventilation/perfusion maps (Mueller et al., 2018). Changes in lung volume using EIT images collected during spirometry have shown excellent correlation with pneumotachograph measurements (Coulombe et al., 2005; Marquis et al., 2006). EIT has also been shown to be effective for monitoring pulsatile pulmonary perfusion (Carlisle et al., 2010; Smit et al., 2004; Reinius et al., 2015), which is also relevant for SMA-1 patients because of the ventilation/perfusion mismatch that can result from their respiratory weakness (Iwan et al., 2019).

Lung volume measurement in children poses a challenge, particularly in patients with neuromuscular disorders. Traditional measurements of lung function include spirometry and lung volume measurement by plethysmography or gas dilution. Spirometry requires participation such that children younger than 5–6 years old cannot do them reliably. Plethysmography and gas dilution studies are limited by low lung volumes such that those with chest wall restriction may not be able to produce reliable results. These tests also cannot be done in patients on invasive or noninvasive ventilator support. Infant pulmonary function tests require sedation and can be misleading as artificial insufflation and exsufflation of the lungs during this technique overcomes respiratory muscle weakness. EIT may provide a non-invasive method of obtaining lung volume estimates without sedation. Here we present the results of a pilot study of six patients with SMA-I that demonstrates the feasibility of using regional ventilation and perfusion images from EIT data to obtain estimates of lung volumes before, during, and after MIE.

2. Materials and methods

2.1. Data collection

This study was conducted in accordance with the amended Declaration of Helsinki. Data were collected at Children's Hospital Colorado (CHCO) in Aurora, Colorado, under the approval of the institutional review board (IRB) (approval number 18–1843). Informed parental consent and children's informed assent were obtained prior to participation. Six patients ages 4.0 ± 2.6 years diagnosed with SMA-I participated. Subject characteristics at the time of the study are provided in Table 1.

Two rows of 16 disposable pediatric ECG electrodes (Phillips 13951C) were placed around the thorax of the patient with an additional electrode serving as a ground on the lower abdomen. Data were collected before, during, and after the MIE procedure with the subject in the supine position. MIE settings were determined according to patient tolerance and therapist or physician experience, and are shown in Table 2, where Pi is the inspiratory pressure in cm H_2O, Ti is the inspiratory time in seconds, Pe is the expiratory pressure in cm H_2O, Te is the expiratory time in seconds, and Tp is the pause time in between cough cycles in seconds. The operation mode can set to automatic or patient triggered. In automatic mode, the device begins a cough cycle without regard to patient respiratory effort. In patient triggered mode, the patient initiates a cough cycle with inspiratory effort, and thus there is no set pause time. An oscillation setting can also be used; airflow is oscillated on inhalation or exhalation with frequency in Hz and amplitude in cm H_2O, as documented.

The EIT data collected before and after the MIE procedure was during tidal breathing. Note that the number of frames collected per data set and per subject varied due to subject-dependent conditions, such as initiation of speech, a cough, or significant movement. Data for pulsatile pulmonary perfusion images were collected during breath-holding. Fig. 1 shows the electrode placement of two rows of 16 electrodes around the subject's chest for the EIT imaging.

The EIT data were collected using the GENESIS prototype EIT system from GE Research. The GENESIS system is a real-time, 32-channel 3D EIT system that collects data up to 20 frames per second at 10 kHz (Ashe et al., 2014). It is a simultaneous multiple current source EIT system (SMS-EIT), which means that AC currents are applied simultaneously on

Table 2
MIE settings per subject at the time of the study. Here Pi is the inspiratory pressure in cm H_2O, Ti is the inspiratory time in seconds, Pe is the expiratory pressure in cm H_2O, Te is the expiratory time in seconds, and Tp is the pause time in between cough cycles in seconds. Frequency is in Hz and amplitude in cm H_2O.

Subject	Pi	Ti	Pe	Te	Tp	Mode	Oscillation, Frequency (F), Amplitude (A)	Interface
1	35	1.5	35	1.5	1.3	Automatic	No	Mask
2	40	2	40	2	NA	Patient triggered	No	Mask
3	35	1.5	35	1.5	1.5	Automatic	No	Mask
4	25	1	25	1	NA	Patient triggered	No	Mask
5	30	2	30	2	2	Automatic	On inhalation & exhalation, F = 12, A = 8	Tracheostomy
6	25	1	25	1.5	NA	Patient triggered	No	Mask

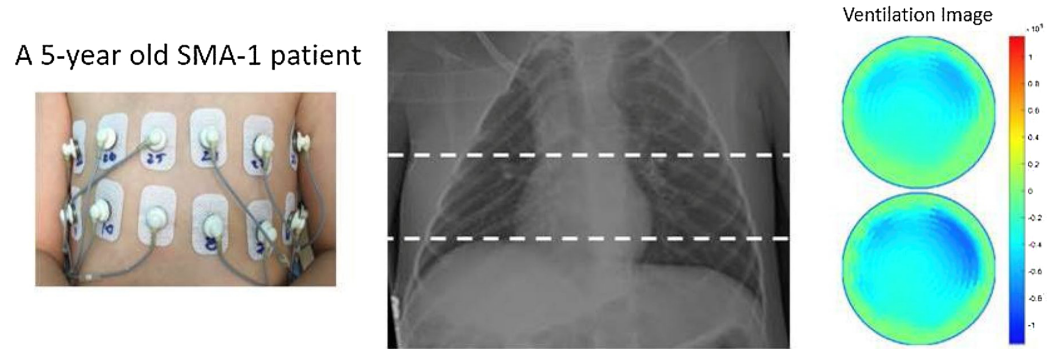

Fig. 1. Left: Two rows of electrodes were placed on each of the patients, as seen here, for Subject 2. Center: Chest x-ray of Subject 2 taken the same day as the EIT data collection. The white lines indicate the average level of the electrode planes. Right: EIT image of the relative conductivity at full inspiration for Subject 2. The upper circle is a cross-sectional image of the relative conductivity in the chest in the plane of the upper row of electrodes, displayed in DICOM format. Likewise, the lower circle is a cross-sectional image of the relative conductivity in the chest in the plane of the lower row of electrodes, displayed in DICOM format.

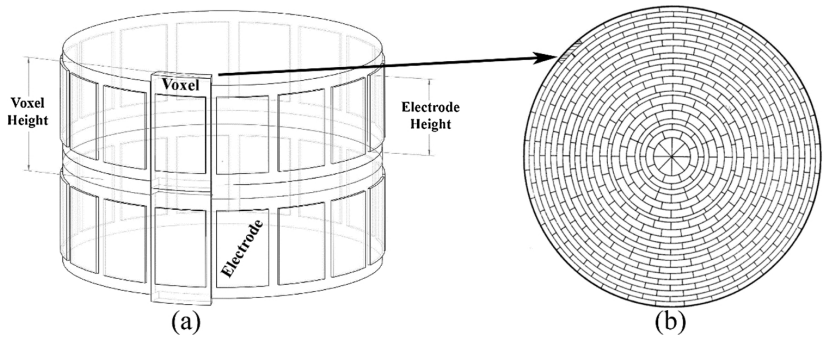

Fig. 3. (a) Illustration of the electrodes position and voxel geometry, (b) Joshua tree mesh.

all electrodes, and the resulting voltages are measured on all of the electrodes. In this work, trigonometric current patterns are applied with a maximum amplitude of 0.11 mA RMS. That is, the amplitude of the current I^{k_1} on the l^{th} electrode for the j^{th} current pattern is given by the formula:

$$I_l^k = M \begin{cases} \cos(k\theta_l),\ k = 1, \ldots,\ 8; \\ (-1)^{r+1} cos((k-8)\theta_l),\ k = 9, \ldots,\ 16; \\ (-1)^{r+1},\ k = 17; \\ \sin((k-17)\theta_l),\ k = 18, \ldots,\ 24; \\ (-1)^{r+1} \sin((k-24)\theta_l),\ k = 25, \ldots,\ 31; \end{cases}$$

$$r = \begin{cases} 1,\ l = 1, \ldots,\ 16 \\ 2,\ l = 17, \ldots,\ 32 \end{cases}$$

$$\theta_l = \begin{cases} \dfrac{2\pi l}{16},\ l = 1, \ldots,\ 16 \\ \dfrac{2\pi(l-16)}{16},\ l = 17, \ldots,\ 32 \end{cases}$$

where θ_l is the angle the lth electrode makes with the reference angle 0 degrees, which corresponds to electrodes 1 and 17, where electrode 17 is directly above electrode 1. This geometry is shown in Fig. 3 (a). A 496 element Joshua tree mesh was chosen in the r_θ plane for reconstruction, as shown in Fig. 3 (b). Data were collected during tidal breathing before and after the MIE procedure.

2.2. Image reconstruction and calculation of volumes of inspired air

Dynamic 3D images of the conductivity in the chest were computed off-line using a one-step iterative reconstruction method based on the ToDLeR algorithm (Blue et al., 2000). A reference frame representing maximal expiration was first chosen from a principal component analysis of the data, and each frame in the reconstruction represents the conductivity change in the thorax relative to the reference frame. In this implementation of the algorithm, the patient's chest is approximated by a cylinder, and the Joshua tree mesh was chosen to define pixels in a 2D cross-sectional slice of the cylinder. Reconstructions of the conductivity are displayed in DICOM format with the cross-section for the lower row of electrodes in the bottom half of the figure and the cross-section for the upper row of electrodes in the top half of the figure. Voxels of lower conductivity than the reference frame are blue, and those of higher conductivity are red.

The inspired volume of air was estimated for each frame in the dynamic reconstructions from the conductivity values in the EIT image using a method also used for computing ventilation/perfusion ratios (Muller et al., 2015). This method provides a voxel-wise volume fraction of air. Multiplying the volume fraction of air in each voxel by the volume of the voxel and summing over all of the voxels in the lung region results in an estimate of the volume of air in the entire lung at a given time. In particular, the volume was calculated by the following. Let p denote a given voxel in the lung region and let $\sigma_a(p,t)$ denote the conductivity in the pth voxel at the time t corresponding to a given frame. The local volume fraction of air in the pth voxel at time t, $f_a(p,t)$, is related to the conductivity by

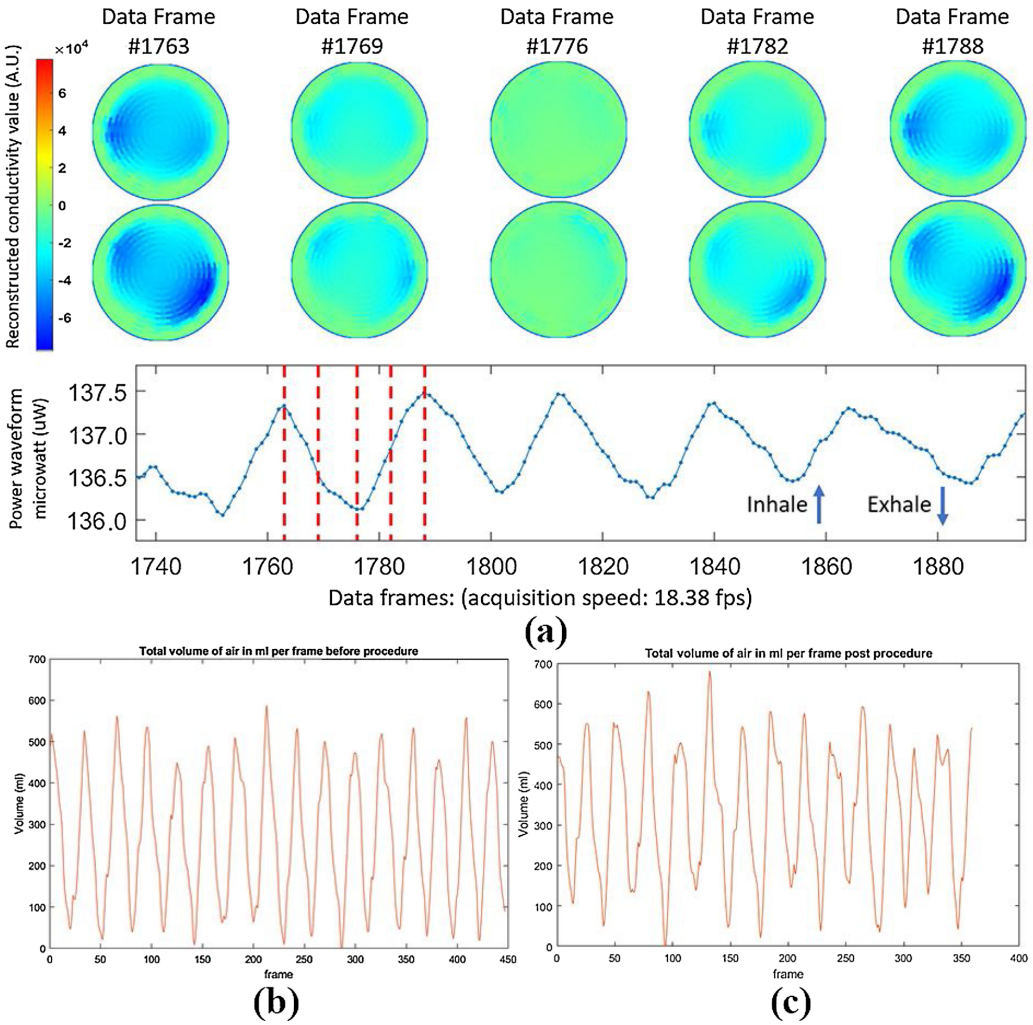

Fig. 4. (a) Five frames in a sequence of data collected during tidal breathing post-MIE in Subject 1. The bottom row of images are plots of relative conductivity values in the plane of the bottom row of electrodes, and the top row of images are plots of relative conductivity values in the plane of the upper row of electrodes. Images are in DICOM orientation. The power waveform is found below the images, and the red lines indicate to which frame each image corresponds. (b) Volume of inspired air by frame for Subject 1 before the MIE procedure, and (c) after the MIE procedure.

$$\sigma_a(p,t) = \sigma_{aM}(1 - f_a(p,t)) + \sigma_{am} f_a(p,t)$$

where σ_{aM} and σ_{am} are the maximum and minimum values, respectively, of the conductivity over all voxels and over the entire data collection period of interest. Then it is easy to see that the volume fraction of air can be computed from the conductivity distribution by

$$f_a(p,t) = \frac{\sigma_a(p,t) - \sigma_{aM}}{\sigma_{am} - \sigma_{aM}}$$

The lung region was segmented and identified from the post-MIE data set by a threshold method. Any voxel whose minimum value of relative conductivity over the entire sequence of frames never falls below half the average value of the maximum and minimum conductivity values over the whole dynamic data set (i.e., $0.5(\sigma_{aM} + \sigma_{am})$) was considered to be too conductive to be included as a lung voxel. Any voxel whose maximum value of relative conductivity over the entire sequence of frames exceeds 90 % of the maximum value of the conductivity over all voxels and over the entire data collection period of interest was also considered to be too conductive to be a lung voxel and, therefore either belongs to the heart or is an artifact. Finally, voxels in the six outer rings of the upper Joshua tree mesh and the four outer rings of the lower Joshua tree mesh, which could represent non-lung tissue because of increased distance from the electrode to lung (such as in the upper axilla), were excluded from the analysis.

To compute the volume of air in the entire lung at time t, one then multiplies $f_a(p,t)$ by the volume of the p^{th} voxel and sums over all of the voxels in the lung region. In this work, the volume of a voxel was one half the distance between the upper and lower rows of electrodes multiplied by the cross-sectional area of the corresponding pixel in the Joshua tree mesh.

2.3. Images of pulsatile pulmonary perfusion

Reconstructions of pulsatile pulmonary perfusion were computed by

Table 3
Average volume of inspired air at maximum inspiration during tidal breathing by subject. The values were computed by taking the average over the total amplitudes in the plots of volumes of inspired air by frame, such as those in Fig. 4 (b) and (c).

Average volume of inspired air at maximum inspiration during tidal breathing (average ± SD)				
Subject	**Before Procedure (ml)**	**After Procedure (ml)**	**Change (ml)**	**Change (%)**
1	485 ± 42.2	480 ± 46.6	−5.00 ± 44.5	−1.04 ± 9.21
2	559 ± 41.3	524 ± 29.0	−35.0 ± 35.7	−6.46 ± 6.59
3	722 ± 18.3	740 ± 15.6	18.0 ± 17.0	2.46 ± 2.33
4	195 ± 45.5	371 ± 44.1	176 ± 44.8	62.2 ± 15.8
5	827 ± 150	870 ± 95.3	43.0 ± 125	5.07 ± 14.8
6	455 ± 105	611 ± 36.7	156 ± 78.7	29.3 ± 14.8
Average	**541 ± 175**	**569 ± 148**	**58.8 ± 55.1**	**15.3 ± 10.0**

the same method as the ventilation images, with a reference frame chosen empirically from the power waveform to correspond to mid-systole. When data is collected for a sufficiently long time, there are typically very short periods of breath-holding in the patient's normal tidal breathing pattern. The data from this period can be used to compute reconstructions that show pulsatile pulmonary perfusion.

3. Results

3.1. Images of regional ventilation and regional and global lung volumes

Fig. 4 (a) shows five frames from the ventilation sequence for Subject 1 post-MIE with red lines in the power waveform plot found below the images indicating the frame for each image. The power waveform of the impedance measurement was computed as the inner product of the measured voltages and applied currents and provides a plot of frame versus power in microwatts. A peak in the waveform corresponds to maximal inhalation and a trough to exhalation. Thus, respiratory rates can be calculated easily from the power waveform as well. In the images, blue regions indicate voxels of inspired air. Regional changes in ventilation are evident over these five frames during the ventilation cycle. Volumes of inspired air by frame calculated from tidal breathing data collected before and after MIE procedure for this subject are shown in Fig. 4 (b) and (c). The average maximum inspired volume is reported in Table 3, computed by taking the average over all local maxima in the plots of volumes of inspired air by frame (such as those in Figs. 4 (b) and (c)). The average change in lung volume at full inspiration during tidal breathing from pre to post MIE calculated from Table 3 was found to be 58.8 ± 55.1 mL.

EIT data were also collected during the MIE procedure, and volumes of inspired air were computed for each frame. Fig. 5 is a plot of the volume inspired air per frame for Subject 3 calculated as described above for EIT data collected during the MIE procedure. The plot clearly shows when the device insufflates and exsufflates air and the rest periods between cough simulations.

Four-time snapshots of ventilation images pre-and post-MIE for Subject 4 are shown in Fig. 6 (a) and (b), respectively. Red lines from the power waveform indicate to which point in the respiratory cycle the image corresponds. In each figure, one image corresponding to full exhalation is included. This image appears quite homogeneous since the reference image for the conductivity was chosen to be a frame corresponding to full exhalation. The irregular shape of the power waveform in Fig. 6 (a) preceding frame 100 likely corresponds to a short period breath-holding between frames 15 and 60, and again between frames 80 and 95. Another pause can be observed between frames 162 and 182. Similarly, the irregular shape of the power waveform in Fig. 6 (b) preceding frame 35 and between frames 140 and 190 are likely caused by short periods of breath-holding. In the images, blue regions indicate voxels of inspired air.

Fig. 6 (a) shows Subject 4's lungs poorly and non-uniformly ventilated prior to the MIE treatment. The left lung receives more volume, and the upper lobes fill more than the lower lobes. After the MIE treatment, the ventilation distribution is more homogeneous and both of the lower lobes are more aerated, as seen in Fig. 6 (b). The increase in recruited lung volume is also supported by an average increase in inspired volume of 176 ± 44.8 mL, reported in Table 3.

Lung volumes per quadrant were also computed for each subject. Fig. 7 shows plots of the lung volume per frame for Subjects 2 and 4. The quadrants were defined by dividing the segmented lung regions in the upper and lower electrode planes into left and right lungs, following anatomical left and right (ie, consistent with DICOM presentation). While Subject 2 did not show significant improvement in lung volume after MIE, one can see from Fig. 7 that the significant improvement shown by Subject 4 following MIE is most pronounced in the lower left lung. The upper left lung and lower right lung also demonstrated

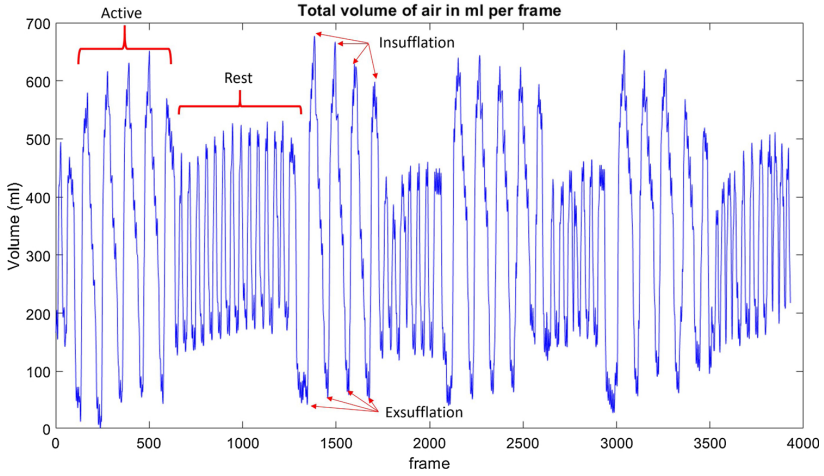

Fig. 5. EIT data was collected during the MIE procedure, and volumes of inspired air were computed for each frame. The plot clearly shows when the device insufflates and exsufflates air and the rest periods between cough simulations.

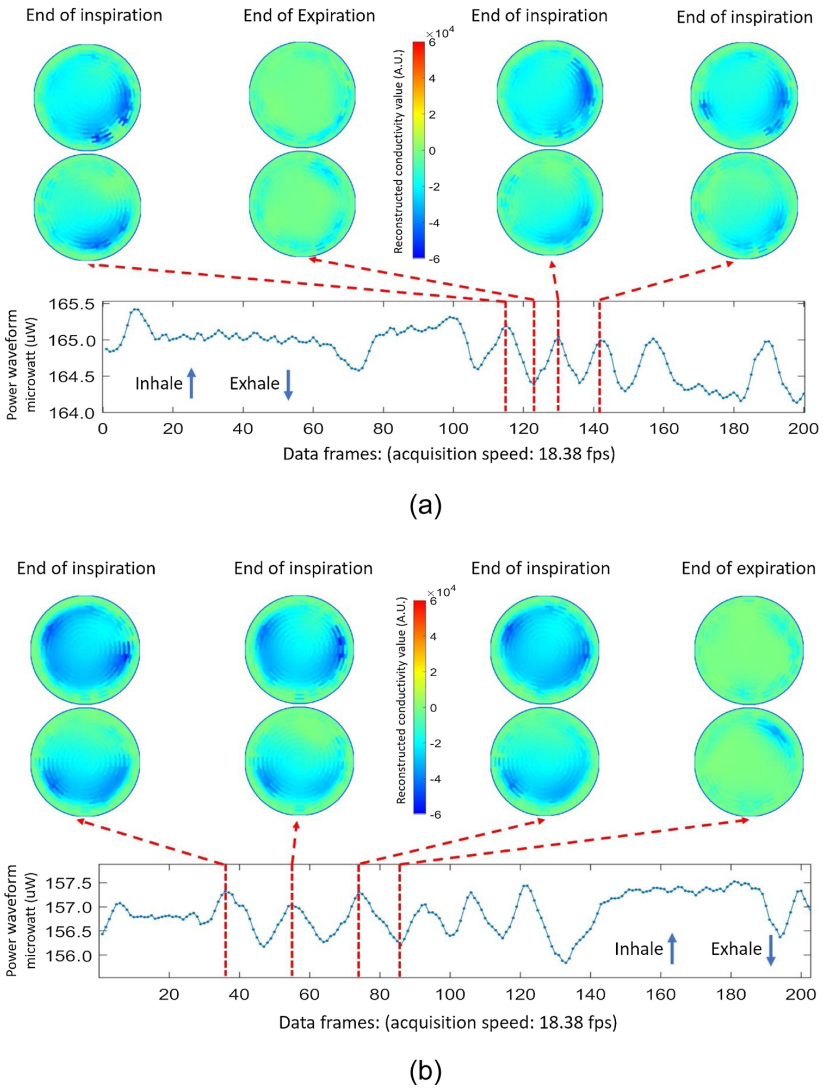

Fig. 6. (a) Four-time snapshots of ventilation images for Subject 4 pre-MIE treatment. Ventilation data was processed for frame # 119, 121, 123, and 142 during normal breathing. (b) Four-time snapshots of ventilation images for Subject 4 post-MIE treatment. Ventilation data was processed for frame # 36, 55, 74, 92, during normal breathing.

consistently higher lung volumes after MIE in this subject, and the upper right lung only improved slightly.

3.2. *Images of pulmonary perfusion*

Fig. 8 (a) shows the power waveform for Subject 2 during tidal breathing, and how the power waveform can be used to identify the frames comprising a breathing pause. Fig. 8 (b) shows two snapshots of pulsatile pulmonary perfusion images from Subject 2, reconstructed from data collected during the short breathing pause indicated in Fig. 8 (a) that occurred during normal breathing. The images corresponding to diastole and systole are shown in Fig. 8 (b). The highly conductive blood-filled voxels appear red in the images since they are more conductive than those voxels were during the reference image of mid systole. Thus, the heart appears red during diastole, and the lungs appear red during systole. Voxels that are less conductive than they were in the reference image appear blue, and so the heart appears blue during systole, and the lungs appear blue during diastole. Fig. 8 (b) shows bilateral lung perfusion with greater perfusion in the left hemithorax. While corresponding ventilation images show greater ventilation in the left lung compared to the right lung, as shown in Fig. 1, perfusion to dorsal regions is greater than ventilation to analogous regions. These figures are time snapshots from the movie in the supplemental material, also found at https://www.math.colostate.edu/~mueller/eit_lab_movies.html, which shows the dynamic changes in conductivity due to ventilation in the left-most animation and the dynamic changes in conductivity due to pulsatile perfusion in the animation on the right. In the movie, the ventilation and perfusion differences in the dorsal region are evident in all frames. Thus, ventilation and perfusion are mismatched between the ventral and dorsal regions in this supine patient.s

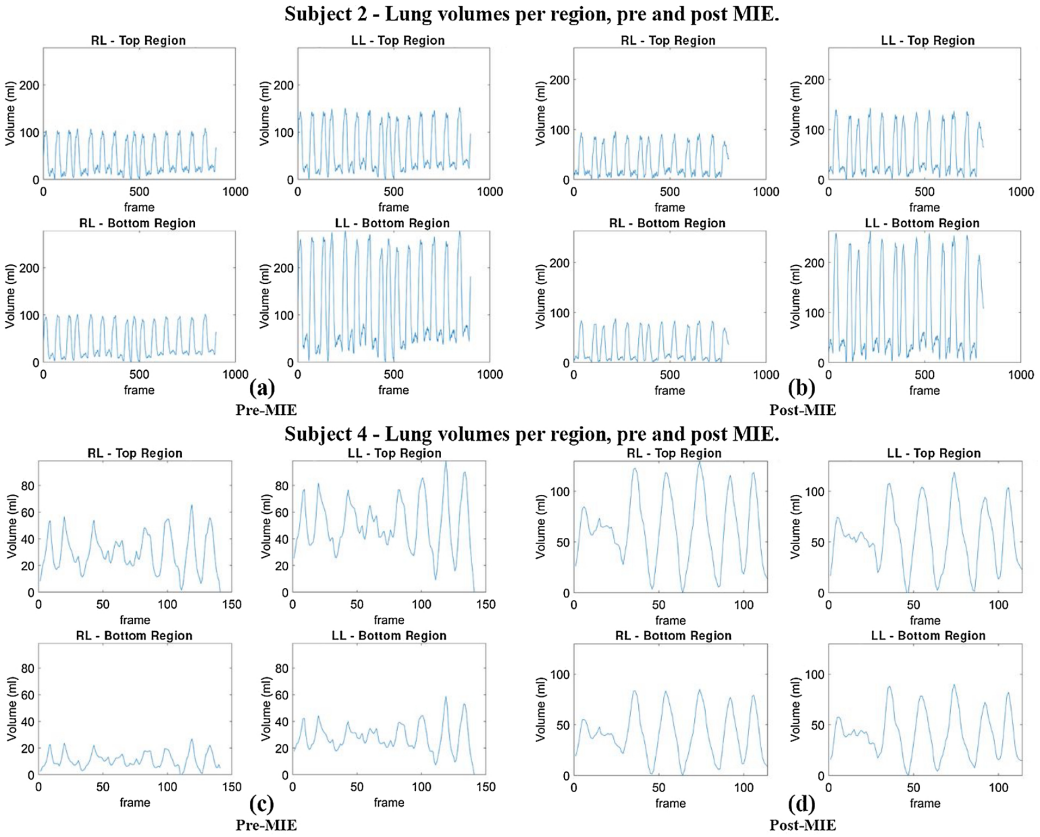

Fig. 7. Lung volumes by quadrant; left lung (LL) and right lung (RL): (a) pre and (b) post MIE for Subject 2, (c) pre and (d) post for Subject 4.

3.3. Statistical analysis

The lung volume amplitude per breath during tidal breathing, measured pre- and post-procedure, for multiple breath cycles, data were analyzed using the Minitab 19 statistics tool. An analysis of variance test was conducted with a confidence interval of 95 % (F-Table $\alpha = 0.05$) for a total of 94 samples. The ANOVA residuals showed a normal distribution, and the equal variances premise was not violated, and thus, ANOVA was considered an appropriate test for this study (Montgomery, 2012). The primary analysis, conducted considering the data collected from all subjects, showed that the airway clearance procedure significantly affected the average lung volume amplitude (F-Value = 4.50; P-Value = 0.037). A more in-depth analysis, conducted per subject, showed that for subjects 2, 3, 4, and 6, the procedure significantly affected the average lung volume amplitude (F-Values = 6.25, 4.70, 38.8, 7.92; P-Values = 0.0200, 0.0480, 0.000, 0.0310, respectively). Therefore, a significant change in volume amplitude was not observed on Subjects' 1 and 5 data (F-Value = 0.0800 and 0.230; P-Value = 0.785 and 0.650). Fig. 9 shows the interval plot for the mean volume amplitude per subject before and after the airway clearance procedure.

From Fig. 9, it is noticeable that for subjects 1 and 5, the mean volume amplitude intervals pre and post-procedure overlap, which corroborates with the results found through ANOVA. For subjects 5 and 6, a narrower confidence interval was observed after MIE, which indicates that the volume of air inspired and expired per breathing cycle after conducting the procedure was more consistent. Analyzing the confidence intervals from subjects 2, 3, 4, and 6, it is clear that the mean volume amplitude increased after MIE. However, it is essential to point out that the statistical analysis was conducted based on a small population. Thus, the results here presented are a representation of the subjects that participated in this study only. Therefore, further investigation is required to analyze the overall effectiveness of the MIE procedure.

4. Discussion

This is the first study investigating EIT as a tool for assessing lung function pre and post MIE in any patient population and for obtaining regional ventilation and perfusion images in patients with SMA. It is evident from the plots of estimated lung volume in Fig. 5 from EIT data collected during MIE that the volumes clearly indicate when the device insufflates and exsufflates air and the rest periods between cough simulations. Such plots could be useful in determining optimal MIE settings and assessing the effectiveness of MIE as well.

From the lung volume estimates provided in Table 3, it is seen that not all patients had large rises in lung volume after MIE, as seen in Table 3. Subjects 1 and 2 exhibited a small decline in lung volume after MIE, as measured by EIT. This may be due to several factors. First, clinical titration of MIE settings is not rigorous. MIE settings are determined by patient tolerance and therapist or physician experience. Perhaps more MIE coughs or higher settings would have cleared airways and permitted lung volume recruitment. Second, since the MIE was performed by the family during a clinic visit, the timing and MIE settings may have been suboptimal to achieve adequate airway clearance. Subject 2 demonstrated through a history of chest x-rays, a conical chest,

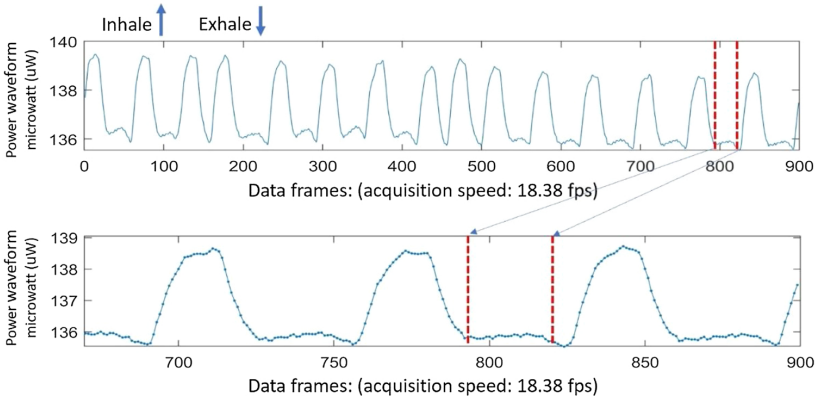

(a)

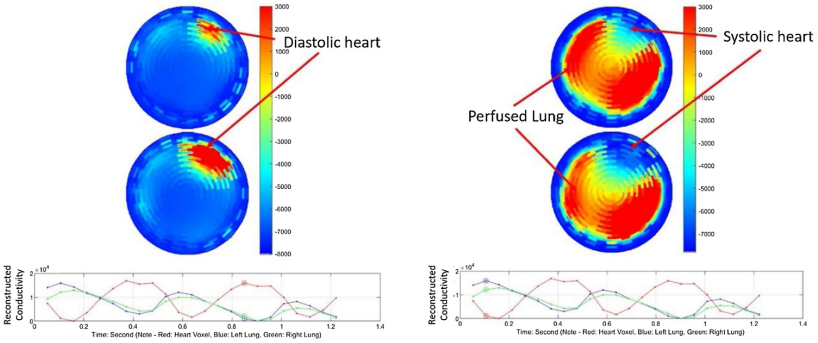

(b)

Fig. 8. (a) Perfusion Data was processed between frame # 792 - 818 during a short breathing pause between two normal breaths. The power waveform was used to identify the frames comprising the breathing pause as seen here for Subject 2. (b) Left: Relative conductivity image for a frame in which the heart is in diastole for Subject 2. The plots underneath show time traces of the relative conductivity in a voxel from the heart region (plotted in red) superimposed with the time traces for voxels from the left lung (plotted in blue) and the right lung (plotted in green). The dots indicate the time snapshot shown here.

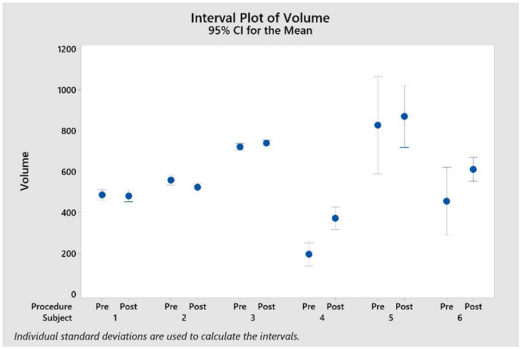

Fig. 9. mean total lung volume amplitude per subject with a 95 % confidence interval.

and a small right lung (see Fig. 2). The small right lung was also evident in the ventilation images (see Fig. 1 and the movie in the supplemental materials) and in the lung volumes by region in Fig. 7, in which the lower right lung volumes per breath are seen to be less than half the volumes in the lower left lung, both pre and post MIE. In the future, real-time lung volume data from EIT may be used to determine effective MIE settings more rigorously, and the results underscore the need for a method of monitoring whether the application of MIE in a patient has indeed improved lung function and reduced ventilation/perfusion mismatch.

Detection of ventilation/perfusion mismatch in patients with SMA-I can facilitate interventions to prevent hypoxemia and respiratory failure. Ventilation/perfusion mismatch can occur as a result of mucus plugging, which can persist after improper airway clearance, underscoring the importance of monitoring the effectiveness of MIE. SMA-I patients are also prone to atelectasis, which decreases distensibility and results in shallow breathing. Low functional residual capacity can then lead to further atelectasis, increasing ventilation/perfusion mismatch and potential hypoxemic respiratory failure (Awad and Agarwal, 2017). EIT's ability to detect and monitor ventilation/perfusion mismatch and lung volumes regionally could be useful for in-home detection of problems and interventions such as a change in MIE settings or frequency of use, or a need for a clinic visit.

The reconstructions in Fig. 8 (b) demonstrate that breath-holding is not required to obtain images of pulsatile pulmonary perfusion, which are needed to assess ventilation/perfusion mismatch. The time traces of the heart and lung voxels are out of phase as the heart beats, as is expected. The heart region is red during diastole since it contains more of the conductive blood than it does during the reference frame, which is mid cardiac contraction, and blue during systole when it has emptied the

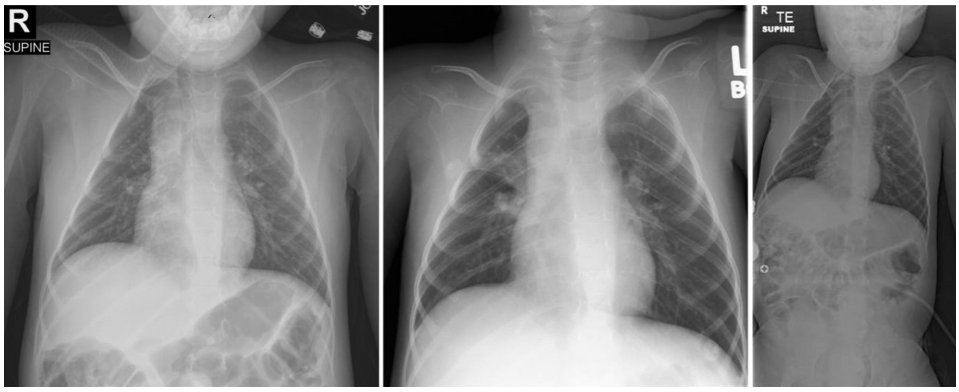

Fig. 2. Left: Archival chest x-ray of Subject 2 from 2015. Right: Archival chest x-ray of Subject 2 from 2018. Both demonstrate the conical lung shape and the small size of the right lung.

conductive blood. It is also evident that there is a larger heart volume in the plane of the lower row of electrodes than the upper row. Thus, changes in ventilation and perfusion during spontaneous breathing, mechanically supported breathing, and MIE can be evaluated with EIT. Baseline differences in the ventilation of the right and left lungs can be observed and correlate with chest X-ray inflation; the x-ray image can be found on the supplemental material.

Figs. 1 and 8, together with the movie of ventilation and pulsatile perfusion provided in the supplemental material show mismatched ventilation and perfusion (V/Q) with mostly ventral ventilation and more dorsal perfusion in Subject 2. This corresponds to known V/Q patterns in supine patients. This subject was normoxic with SpO2 95 % in room air on non-invasive ventilatory support. As with most patients with SMA type 1, this subject is always supine due to respiratory mechanics, and we, therefore, assume that the described ventilation and perfusion patterns observed here are chronic. A small increase in mucus burden may overwhelm the pre-existing V/Q imbalance resulting in rapid and profound oxygen desaturations. This is a novel description of ventilation and perfusion distribution in spinal muscular atrophy and could help understand respiratory fragility in this disease.

A limitation of this study is that the lung volume estimates calculated from the EIT data were not validated by spirometry or plethysmography due to the unique challenges posed by the subject population (age and bulbar dysfunction) and goals of the study. Due to difficulties in measuring lung volumes in patients with neuromuscular disorders, there is a need for a non-invasive modality that does not require sedation and can be used as-needed. EIT has the potential to fulfill this unmet need.

There are other limitations. Although EIT is a non-invasive imaging method that has clear benefits to give insight into ventilation and perfusion, the resolution is coarse, and so small obstructions such as a mucus plug can only be inferred from ventilation/perfusion mismatch or low lung volumes in a certain region, rather than directly from the images. However, regions of atelectasis or edema are distinguishable in EIT images. Change in lung volume after MIE suggests a transient problem such as atelectasis or mucus obstruction and may require a more careful, post-data collection analysis to identify the cause. A lack of change in lung volume may be due to ineffective MIE settings, insufficient MIE coughs to mobilize and expel mucus, pulmonary hypoplasia from chest wall disorder, or intrinsic airway properties such as tracheobronchomalacia. Unlike children with asthma and CF, patients with SMA have a more conical chest, as was seen in Subject 2. Although the 3D EIT helps to accommodate changes in chest wall shape from apex to base, we extrapolate the mid-lung measures to more peripheral lung regions. Each patient served as their own control with EIT data obtained before and after MIE. Thus, we assume that changes in EIT measurements are not due to significant changes in chest shape but are the result of changes in electrical impedance related to acute changes in ventilation.

This study measured lung volume immediately after MIE and not over an extended period. Future work is needed to investigate if MIE leads to sustained improvement in ventilation. With further validation, EIT may also be used to measure lung volume in children with SMA who are too young to perform spirometry. Repeating EIT measurements over time could provide longitudinal data that support clinical decisions regarding continuing or reducing respiratory support, including airway clearance and non-invasive ventilation. This is especially important as the natural history of SMA is changing with SMA-specific therapeutics, and EIT measures could be used to monitor the effect of novel medications and other therapies on lung function in SMA.

In summary, the results of this study demonstrate that EIT has potential as a clinical tool for assessing lung volume before and after mechanical insufflation-exsufflation for airway clearance in patients with spinal muscular atrophy type I (SMA-I). Changes in regional ventilation distribution after MIE treatments are visible in the ventilation images, and lung volumes computed from segmented EIT images showed an increase in four of the six patients. These images give insight into ventilation and perfusion that are unable to be obtained noninvasively using other modalities.

Declaration of Competing Interest

Tzu-Jen Kao is employed by GE Research. Other authors have no declaration of interest to declare.

Acknowledgments

The authors thank Allison Keck for recruiting the volunteers that took part in this study and her assistance as Research Coordinator. They also wish to thank the children and families who participated in the study.

Appendix A. Supplementary data

Supplementary material related to this article can be found, in the online version, at doi:https://doi.org/10.1016/j.resp.2021.103773.

References

Al-Zaidy, S.A., Mendell, J.R., 2019. From clinical trials to clinical practice: practical considerations for gene replacement therapy in SMA type 1. Pediatr. Neurol. 100, 3–11.

Ashe, J., Shoudy, D., Boverman, G., Sabatini, J., Kao, T.J., Amm, B., 2014. A high precision parallel current drive experimental EIT system. In: 15th International Conference on Biomedical Applications of Electrical Impedance Tomography. Gananoque, Ontario, Canada, April. ISBN 978-0-7709-0577-4.
Awad, S., Agarwal, A., 2017. Respiratory care of patients with neuromuscular diseases. Arkansas Children's Hospitals 1, 1–10.
Blue, R.S., Isaacson, D., Newell, J.C., 2000. Real-time three-dimensional electrical impedance imaging. Physiol. Meas. 21, 1–12.
Brown, B.H., 2003. Electrical impedance tomography (EIT): a review. J. Med. Eng. Technol. 27, 97–108.
Carlisle, H.R., Armstrong, R.K., Davis, P.G., Schibler, A., Frerichs, I., Tingay, D.G., 2010. Regional distribution of blood volume within the preterm infant thorax during synchronized mechanical ventilation. Intensive Care Med. 36 (12), 2101–2108.
Costa, E., Lima, R., Amato, M., 2009. Electrical impedance tomography. Curr. Opin. Crit. Care 15, 18–24.
Coulombe, N., Gagnon, H., Marquis, F., Skrobik, Y., Guardo, R., 2005. A parametric model of the relationship between EIT and total lung volume. Physiol. Meas. 26 (4), 401–411.
Finkel, R.S., et al., 2014. Observational study of spinal muscular atrophy type I and implications for clinical trials. Neurology 83 (9), 810–817.
Finkel, R.S., et al., 2017. Nusinersen versus sham control in infantile-onset spinal muscular atrophy. N. Engl. J. Med. 377 (18), 1723–1732.
U.S. Food, Drug Administration, 2020. FDA Approves Oral Treatment for Spinal Muscular Atrophy. FDA News Release.
Frerichs, I., Hinz, J., Herrmann, P., Weisser, G., Hahn, G., Dudykevych, T., Quintel, M., Hellige, G., 2002a. Detection of local lung air content by electrical impedance tomography compared with electron beam CT. J. Appl. Physiol. 93 (2), 660.
Frerichs, I., Hinz, J., Herrmann, P., Weisser, G., Hahn, G., Quintel, M., Hellige, G., 2002b. Regional lung perfusion as determined by electrical impedance tomography in comparison with electron beam CT imaging. IEEE Trans. Med. Imaging 21, 646–652.
Frerichs, I., Zhao, Z., Becher, T., Zabel, P., Weiler, N., Vogt, B., 2016. Regional lung function determined by electrical impedance tomography during bronchodilator reversibility testing in patients with asthma. Physiol. Meas. 37 (6), 698.
Frerichs, I., Amato, M.B., Van Kaam, A.H., Tingay, D.G., Zhao, Z., Grychtol, B., Bodenstein, M., Gagnon, H., Böhm, S.H., Teschner, E., Stenqvist, O., Mauri, T., Torsani, V., Camporota, L., Schibler, A., Wolf, G.K., Gommers, D., Leonhardt, S., Adler, A., Fan, E., Lionheart, W.R., Riedel, T., Rimensberger, P.C., Sipmann, F.S., Weiler, N., Wrigge, H., 2017. Chest electrical impedance tomography examination, data analysis, terminology, clinical use and recommendations: consensus statement of the Translational EIT development study group. Thorax 72 (1), 83–93.
Holder, D.S., 2005. Appendix to electrical impedance tomography: methods, history and applications; introduction to biomedical electrical impedance tomography. Bristol: Institute of Physics Publishing 1, 423–449.
Iwan, F.A., Yeng, Y.W.W., Thirupathirao, V., Michael, L., 2019. Rehabilitation in spinal muscular atrophy. J. Int. Soc. Phys. Rehab. Med. 2 (1), 62–70.
Kolb, S.J., et al., 2017. Natural history of infantile-onset spinal muscular atrophy. Ann. Neurol. 82 (6), 883–891.
Krueger-Ziolek, S., Schullcke, B., Zhao, Z., Gong, B., Moeller, K., 2016. Determination of regional lung function in cystic _brosis using electrical impedance tomography. Curr. Dir. Biomed. Eng. 2 (1), 633–636.
Lefebvre, S., Bürglen, L., Reboullet, S., Clermont, O., Burlet, P., Viollet, L., Benichou, B., Cruaud, C., Millasseau, P., Zeviani, M., Le Paslier, D., Frézal, J., Cohen, D., Weissenbach, J., Munnich, A., Melki, J., 1995. Identification and characterization of a spinal muscular atrophy-determining gene. Cell 80 (1), 155–165.
Lehmann, S., Leonhardt, S., Ngo, C., Bergmann, L., Ayed, I., Schrading, S., Tenbrock, K., 2016. Global and regional lung function in cystic fibrosis measured by electrical impedance tomography. Physiol. Meas. 51 (11), 1191–1199.
Marquis, F., Coulombe, N., Costa, R., Gagnon, H., Guardo, R., Skrobik, Y., 2006. Electrical impedance tomography's correlation to lung volume is not influenced by anthropometric parameters. J. Clin. Monit. Comput. 20 (1), 201–207.
Martins, Td.C., Sato, A.K., de Moura, F.S., de Camargo, E.D.L.B., Silva, O.L., Santos, T.B. R., Zhao, Z., Möeller, K., Amato, M.B.P., Mueller, J.L., Lima, R.G., Tsuzuki, Md.S.G., 2019. A review of electrical impedance tomography in lung applications: theory and algorithms for absolute images. Annu. Rev. Control 48, 442–471.
Montgomery, D.C., 2012. Design and Analysis of Experiments, 8th ed., vol. 1. Wiley, Hoboken. pp. 752.
Mueller, J.L., Muller, P., Mellenthin, M., Murthy, R., Capps, M., Alsaker, M., Deterding, R., Sagel, S.D., Deboer, E., 2018. Estimating regions of air trapping from electrical impedance tomography data. Physiol. Meas. 39 (5), 05NT01.
Muller, P.A., et al., 2015. Estimating a regional ventilation-perfusion index. Physiol. Meas. 36 (6), 1283–1295.
Muller, P.A., Mueller, J.L., Mellenthin, M., Murthy, R., Capps, M., Wagner, B.D., Alsaker, M., Deterding, R., Sagel, S.D., Hoppe, J., 2018. Evaluation of surrogate measures of pulmonary function derived from electrical impedance tomography data in children with cystic fibrosis. Physiol. Meas. 39 (4), 045008.
Pearn, J.H., 1973. The gene frequency of acute Werdni- Hoffmann disease (SMA type 1). A total population survey in North-East England. J. Med. Genet. 10 (3), 260–265.
Reinius, H., Borges, J.B., Fred_en, F., Jideus, L., Camargo, E.D., Amato, M.B., Hedenstierna, G., Larsson, A., Lennmyr, F., 2015. Real-time ventilation and perfusion distributions by electrical impedance tomography during one-lung ventilation with capnothorax. Acta Anaesthesiol. Scand. 59 (3), 354–368.
Schorling, D.C., et al., 2020. Advances in treatment of spinal muscular atrophy - new phenotypes, new challenges, new implications for care. J. Neuromuscul. Dis. 7 (1), 1–13.
Smit, H., Noordegraaf, A.V., Marcus, J., Boonstra, A., Vries, P., Postmus, P., 2004. Determinants of pulmonary perfusion measured by electrical impedance tomography. Eur. J. Appl. Physiol. 92 (1), 45–49.
Sugarman, E.A., Nagan, N., Zhu, H., Akmaev, V.R., Zhou, Z., Rohlfs, E.M., Flynn, K., Hendrickson, B.C., Scholl, T., Sirko-Osadsa, D.A., Allitto, B.A., 2012. Pan-ethnic carrier screening and prenatal diagnosis for spinal muscular atrophy: clinical laboratory analysis of & 72 400 specimens. Eur. J. Hum. Genet. 20 (1), 27–32.
Victorino, J., Borges, J., Okamoto, V., Matos, G., Tucci, M., Caramez, M., Tanaka, H., Sipmann, F., Santos, D., Barbas, E.A.C., 2004. Imbalances in regional lung ventilation: a validation study on electrical impedance tomography. Am. J. Respir. Crit. Care Med. 169 (7), 791–800.
Zerres, K., Rudnik-Schöneborn, S., 1995. Natural history in proximal spinal muscular atrophy. Clinical analysis of 445 patients and suggestions for a modification of existing classifications. Arch. Neurol. 52 (5), 518–523.

Appendix B

Publication Two

Starting on the next page, our article related to the Tonpilz transducer design and calibration is presented in its original form. It was presented at the 44th Annual International Conference of the IEEE Engineering in Medicine and Biology Society (IEEE EMBC 2022), which was held in Glasgow, Scotland, on July 11-15, 2022.

Design and calibration of a Tonpilz transducer for low frequency medical ultrasound tomography

A. V. Pigatto, *Member, IEEE*, L. Giacobbo, A. Lisibach, E. M. Lopes Filho, R. G. Lima and J. L. Mueller

***Abstract*— The design and performance of a transducer for low frequency ultrasound tomography is presented, motivated by recent research demonstrating that acoustic waves transmitting at frequencies between 10 kHz and 750 kHz penetrate the lungs and may be useful for thoracic imaging. An adaptation of the traditional Tonpilz design was developed, vibrational amplitude and electrical impedance were measured, and an optimal frequency was determined. The design is found to meet the desired mechanical, electrical, and safety specifications. Thus, it was considered a promising option for the target application of pulmonary imaging with ultrasound computed tomography between 50 and 200 kHz; highest efficiency achieved around 125 kHz and 156 kHz, and beam divergence of 40°.**

I. Introduction

Conventional ultrasound has been studied as a thoracic bedside technology for diagnosis and monitoring [3], [18], but due to the lack of signal penetration into lung tissue, US images often contain more information in their artifacts than in the images themselves [33]. More recently, the potential of lung point-of-care ultrasound for evaluating the pulmonary status of COVID-19 patients, as well as monitoring treatment and disease progression, has gained interest [6], [9], [29], [39] for respiratory critical care. However, artifacts are an important part of the characteristic findings. For instance, B-lines are a comet-tail-type artifact arising from the pleural line associated with interstitial lung disease [30]. They have been consistently reported in patients with COVID-19 pneumonia [23], [29] and may correspond to clinical severity of COVID-19 [29]. Additionally, A-lines are a normal horizontal reverberation artifact indicating an aerated lung associated with recovery [23]. The need for skilled technicians to perform the data collection [4] and interpret the images and artifacts is a significant obstacle in the adoption of lung ultrasound in ICU patients. B-mode ultrasound is the conventional mode and was used in the studies cited above. Sound waves of frequencies in the range of 2 to 10 MHz are generated and images are computed from measurements of the reflections of the acoustic waves. However, the propagation of acoustic waves is much richer and contains more information than just reflections of acoustic pulses, motivating tomographic ultrasound for pulmonary imaging.

Tomographic ultrasound has been developed for breast imaging (see, for example, [7], [26]–[28]), but mainly in the MHz range. A computer simulation study of breast imaging with USCT in the frequency range of 300 - 500 kHz demonstrated that a spatial resolution of about 2–3 mm can be achieved when operating at the wavelength of about 5 mm even using a stationary 3D scheme with a few fixed sources and no rotating elements [10], but existing experimental and commercial systems operate above 1 MHz. The MHz frequency range poses a problem for pulmonary imaging, as the acoustic waves primarily reflect off of the lung pleura with little to no penetration through the lung tissue. Research [25] has shown that there are three frequency bands in which acoustic signals behave in distinct ways in the human thorax. Between 1 and 10 kHz transmission is absent. Above 1 MHz, there is also no transmission through healthy lungs. However, there is an efficient frequency range for acoustic transmission between 10 and 750 kHz, with signal attenuation increasing as frequency increases. These properties pose an opportunity for bedside pulmonary monitoring in the ICU using low frequency ultrasound tomography. However, the low frequency signal, the geometry of the thorax, and the safety constraints of medical ultrasound pose a challenge in transducer design, and commercial transducers are not available for this application. Low frequency guided waves have been demonstrated to have potential for complementing dual X-ray absorptiometry in screening for osteoporosis [35], but require separate transducers for transmitting and receiving. A low frequency transducer design for quantitative cortical bone assessment was proposed in [12] with a main broadband response ranging from about 70 kHz to 110 kHz. A few research studies have shown new designs of low frequency ultrasound transducers for chronic wound treatment [22], trans-dermal drug transport [16], and accurate placement of spine screws [17]. However, those transducers are designed for their specific application and would not be suitable for Ultrasound Computed Tomography (USCT) due to their operation frequency range, dimensions or sensitivity.

In this work, a novel version of the Tonpilz design [34] is proposed as a solution for low frequency medical ultrasound tomography. Tonpilz transducers are composed of a stack of piezoelectric materials pressed between a light

This project was supported by Award Number R21EB024683 from the National Institute of Biomedical Imaging and Bioengineering. The content is solely the responsibility of the authors and does not necessarily represent the official view of the National Institute of Biomedical Imaging and Bioengineering or the National Institutes of Health.

A. V. Pigatto, is with the School of Biomedical Engineering, Colorado State University, Fort Collins, CO 80523 USA (e-mail: pigatto.andre@gmail.com).

L. Giacobbo and A. Lisbach, are with the Department of Engineering, Bern University of Applied Sciences, Bern, Switzerland 3012.

E. M. Lopes Filho and R.G. Lima, are with the Department of Mechanical Engineering, Polytechnic School of the University of Sao Paulo, Sao Paulo, SP 05508-010 Brazil.

J. L. Mueller, is with the Department of Mathematics and the School of Biomedical Engineering, Colorado State University, Fort Collins, CO 80523 USA (e-mail: mueller@math.colostate.edu).

head and a heavy tail mass [31], and can operate as either a projector or receiver, being commonly used in underwater sonar applications. The resonance frequency of a Tonpilz transducer depends on its design and the masses of its components, and thus it can operate in the low frequency range (below 500 kHz) [13], [36]. Previous work on the Tonpilz design includes the use of stacked piezocomposites to facilitate lower frequency resonant operation than would be possible with a single layer and electrical impedance matching to typical transmission circuitry [5]. An equivalent circuit method was proposed in [24] to analyze the transmitting voltage response spectrum of a planar array of Tonpilz transducers with center frequency 100 kHz, and then used to improve the design to maximize the bandwidth. With the goal of tomographic thoracic imaging, an understanding of the transducer properties such as the temperature sensitivity, directivity, and acoustic power is necessary for obtaining optimal performance and assessing the safety of its use. An alternative numerical/analytical method for determining the directivity-dependent receiving sensitivity of general electro-acoustic transducers is presented in [11] and demonstrated on a Tonpilz transducer. A non-resonant design for low frequency transducers was proposed in [1] for disbond detection in the automotive industry has promise as an alternative to the Tonpilz design presented here, if sufficient amplitude could be achieved, which would require further study beyond the results presented in [1].

One common characteristic of Tonpilz transducers, however, is that they are oddly shaped which is undesirable for a tomographic application. In our design, we were able to develop a more compact transducer by distributing the tail mass laterally, using different materials and integrating the stress rod to the piston, which also provided the casing and protection to the internal components. We also developed a piston with a curved head to achieve a broader angular dependence than a typical transducer. Through simulations and experiments we demonstrate that the design and prototype presented here meets both design and safety considerations for the application of pulmonary imaging, paving the way for future work in animal studies.

II. Methodology and Hardware Description

A. Transducer Design

The transducer parameters were determined based on the following design goals: the ability to operate at a frequency within the range of 20 kHz to 750 kHz, an external diameter of 25 mm or less, and a thickness less than or equal to 11 mm. The dimensional restrictions were imposed by the goal of thoracic USCT imaging with two rows of transducers placed circumferentially on the chest.

Tonpilz transducers are widely used in sonar applications due to their low cost, high acoustic power and simple structure [37]. A standard Tonpilz transducer is composed of a tail mass, a stack of piezoelectric ceramic rings (PZT) and a head mass that weighs less than half of the tail mass [20], [31]. This topology is known for achieving a resonance frequency that no longer depends only on the PZT but on the masses of the parts used in its construction [13], [36]. Furthermore, lower working frequencies can be achieved than those found on commercial transducers, motivating an adaptation of the traditional Tonpilz construction method.

1) Simulation: A model of the experimental transducer was developed and analyzed using the Finite Element Method (FEM). A render of the 3D model is found in Figure 1.

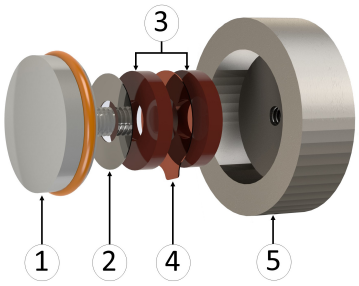

Fig. 1. Virtual model of the experimental transducer.

As shown in Figure 1, the transducer is composed of the tail mass (5), two PZT8 ceramics (3) separated by a thin copper sheet (4), a washer (2) and a piston (1); a silicone rubber o-ring is used to seal the gap between the piston and the housing. A cylindrical spacer (not shown in Figure 1) is used to ensure proper alignment of the PZTs and washers by filling the gap between the PZTs and the piston's bolt.

The main constructive novelties when compared to the standard Tonpilz are the following:

- The tail mass is laterally distributed, providing housing for the ceramics and piston, and reducing the overall transducer thickness.
- The stress rod is integrated to the piston structure, enabling the development of a thinner and lighter piston
- The piston head is curved, increasing the beam divergence, which is essential for the application.

Several characteristics of the transducer were simulated and analyzed through the design process, such as the resonance frequency modes, the directivity, and the mechanical stresses on each part. The final physical dimensions and construction materials were determined iteratively based on the application requirements.

2) Fabrication: After determining the optimal dimensions and materials through computational analysis, the transducer parts were fabricated with the aid of a milling machine with a tolerance of ± 0.001". The tail mass was built using 304 stainless steel, the washer was manufactured on stainless steel 301, and the piston was machined in 6061 T6 aluminum. The application of different materials to the tail mass and piston increases the disparity between these two masses and ensures that the highest fraction of the displacement generated by the PZTs is transferred to the piston and not to the tail mass. Both the tail mass and piston are connected to the electric ground, while the internal copper sheet supplies

the excitation signal to the PZTs, ensuring a safe operation. The cable that connects the transducer to the UST system was built using an RG-316 shielded cable and a male SMT terminal as shown in Figure 2. As seen in Figure 2, no bolts

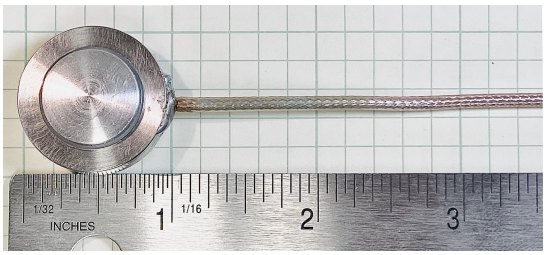

Fig. 2. Final assembled transducer.

are used to attach the piston to the tail mass since the threads were already machined on the piston's structure. An ACT Piezoclamping ® prestress measurement tool was used to ensure the application of a prestress load of 16.4 $\pm$ 0.45 MPa to the PZTs.

B. Experimental Protocol

The impedance and vibrational amplitude of each transducer was experimentally measured within the selected frequency range of 120 to 170 kHz. The collected data was then compared to the simulation results.

1) Impedance Measurement: The transducer impedance was measured in an open air configuration using a continuous sinusoidal sweep signal with a voltage amplitude of 20 V_{pp} for the selected frequency range. Figure 3 shows the configuration of the hardware used on the experiment.

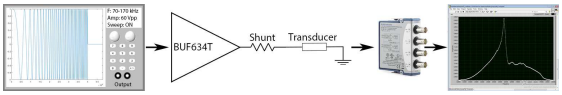

Fig. 3. Impedance measurement experimental setup.

As shown in Figure 3, a function generator (SRS DS360 Ultra Low Distortion) was used to generate a voltage sweep, which was amplified by a BUF634T high-speed buffer, and excited the shunt resistor and transducer. The voltage was measured on the buffer's output and on the shunt using a NI-9775 Digitizer Module at a sampling rate of 2 MHz. The signal was collected using LabVIEW and processed in MATLAB to determine the impedance and resonance frequencies.

2) Displacement Measurement: A PSV 300 vibrometer was used to measure the velocity and displacement of the transducer's piston. A sinusoidal sweep with selected frequency range and an amplitude of 60 V_{pp} was applied to the transducer. Figure 4 shows the hardware configuration used for the experiment.

As shown in Figure 4, a TiePie Handyscope HS5 Digital oscilloscope is controlled by a laptop with MATLAB, which sets the frequency and amplitude of the excitation signal. The

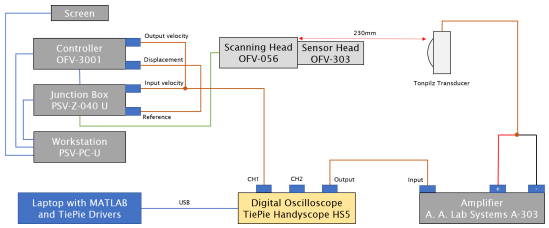

Fig. 4. Displacement measurement experimental setup.

generated signal was amplified by a A-303 amplifier and supplied to the transducer, which was located at 230 mm from the vibrometer. The vibration characteristics of the center piston were measured. The velocity and displacement amplitudes converted to a voltage signal by the controller and junction box, then digitized by the oscilloscope. The signal was sent to MATLAB, to calculate the velocity and displacement for the current frequency. The frequency increments were 100 Hz, and the vibrometer displacement range was set to 0.5 μm/V. After collecting the data, the transmission sensitivity (displacement per unit input voltage) was determined.

III. Results and Discussion

A. Simulation Results

The model of the transducer was implemented with a tail mass of external diameter 25 mm, a thickness of 8 mm, and a piston of size 16 mm wide and 10 mm tall. The depth and width of the cavity on the tail mass were set to 5 mm and 17 mm, respectively. The curvature of the surface of the piston head was optimized, using FEM simulations. The goal was to obtain the highest total radiated acoustic power and a radiation pattern suitable for the application. The results are shown in section III-A.1. For the selected configuration a mechanical analysis was performed to ensure the durability of the transducer; the results are shown in section III-A.2.

1) Acoustic Data: To determine the optimal curvature of the piston head, heights (denoted by hini in Figure 5) from 0.5 mm to 1.5 mm were evaluated using a step size of 0.1 mm. After the first round of simulations, the range from 0.885 mm to 0.905 mm was examined with a higher resolution, leading to Figure 5.

From Figure 5, one sees that the piston head curvature height that results in the highest total radiated power is 0.885 mm. However, through further analysis of the radiation pattern, a curvature height of 0.895 mm was chosen for the final design. Even though that lowers the total radiated power by 18 mW, corresponding to a decrease of approximately 1%, a more desirable radiation pattern was achieved. Moreover, the resonance frequency was found to be 152.6 kHz, and the peak radiated power at that frequency was 1934 mW. The thermal index (TI) that can be achieved when operating at this frequency at maximum power is 1.40 [32], which represents 23% of the maximum value approved by the FDA [8], and thus, is considered safe.

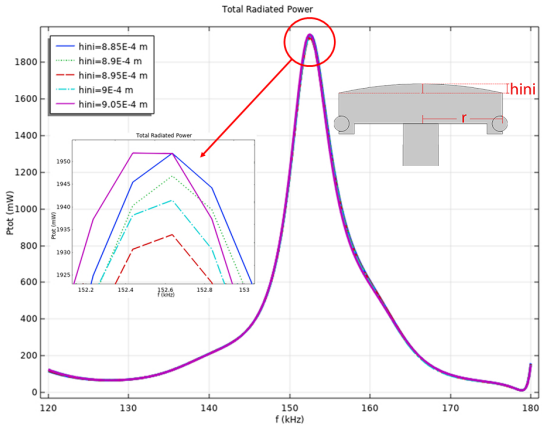

Fig. 5. Maximum irradiated power for different piston head curvatures.

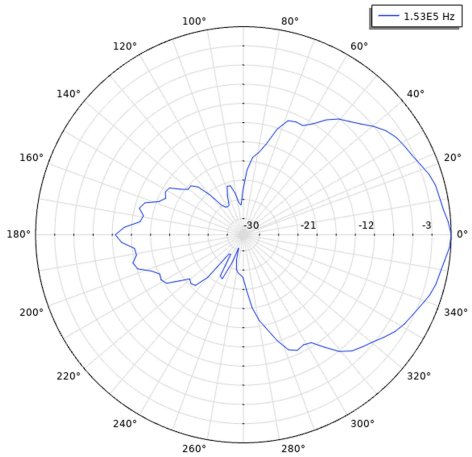

(a) radiation pattern in dB

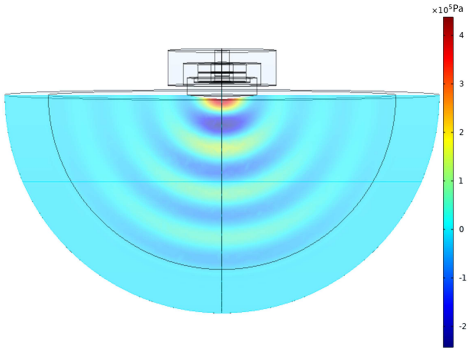

(b) acoustic pressure map for a height h of 8.95e-4 m (denoted $hini$ in Figure 5) and a frequency of 153 kHz.

Fig. 6. Acoustic simulations in water.

Figure 6 illustrates the radiation pattern and the acoustic pressure map of the transducer when excited with a sinusoidal source with an amplitude of 84.5 V_{pp} and a frequency of 153 kHz.

As seen in Figure 6 (a), the beam divergence, that is the angle from the acoustic axis to the point where the acoustic pressure has decreased to one half (-6dB), is 40°. The maximum acoustic pressure achieved was found to be 0.438 MPa. The mechanical index (MI) was introduced by Apfel and Holland in 1991 [2], for the purpose of quantifying the potential for bio-effects due to transient cavitation. Acoustic cavitation is a concern at this frequency range, and has been studied in [14], [15], [38]. A maximum acoustic pressure of 0.438 MPa results in a mechanical index of 1.12 using the formula in [2]. The FDA approved maximum MI for diagnostic imaging is 1.9 [8].

2) Structural Analysis: To analyze the structural behavior of the transducer, a static and dynamic stress analysis was conducted. The von Mises stress was determined by applying the maximal voltage to the transducer and a torque of 0.3 Nm is used during its assembly. The results are shown on Figure 7.

As shown in Figure 7 (a), the maximum static stress of 100 MPa occurs on the piston bolt. This static stress is caused by the force necessary to compress the PZTs and internal parts of the transducer and is solely dependent on the manual torque applied to the piston during assembly. In Figure 7 (b) one sees that the maximum stress of 2.8 MPa, caused by the vibration of the PZTs, occurs on the piston's rear surface. Therefore, considering both sources of deformation combined, a safety factor of 2.33 is achieved since the yield strength of the material is 240 MPa. Furthermore, different tightening torques were simulated, and the results have shown that the application of a torque larger than 0.3 Nm did not improve the transducers acoustic characteristics.

B. Experimental Results

The main purpose of the study was to evaluate the variability of the electrical impedance, resonance frequencies, and displacement amplitude among different transducers, using the selected frequency range. Thirty five transducers were built and characterized. The results are shown in sections III-B.1 to III-B.3.

1) Electrical Impedance: The measurements were taken on the selected range of 120 kHz to 170 kHz to focus on the operational frequency range used for this application. Figure 8 shows the magnitude of the electrical impedance of four representative transducers.

As seen in Figure 8, there is a substantial variation in the magnitudes of the electrical impedance, depending on the frequency and the transducer.

- The extremal values for the different transducers occur at different frequencies and have different values.
- The variations at the second peaks are considerably larger than the variations around 125 kHz .

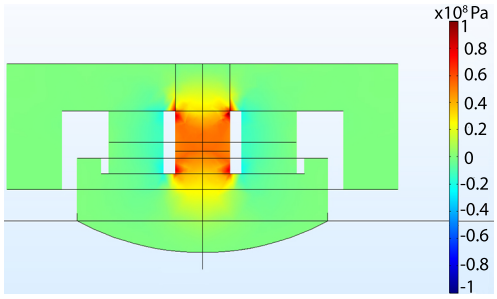

(a) static mechanical stress.

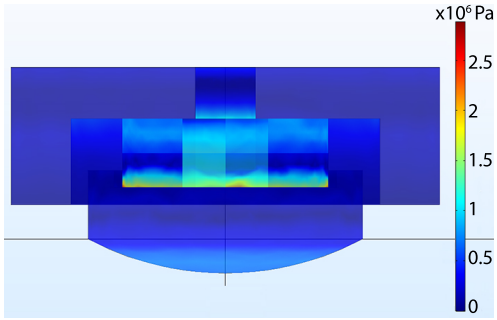

(b) dynamic mechanical stress.

Fig. 7. Simulated mechanical stresses.

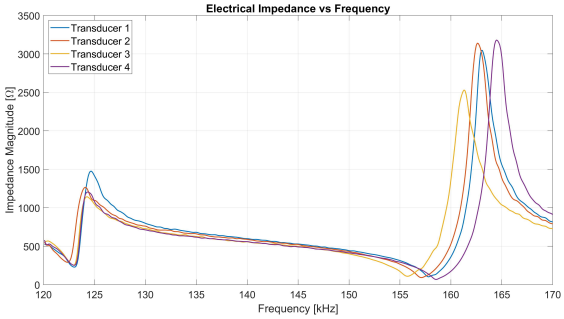

Fig. 8. Electrical impedance magnitude as a function of the applied signal frequency of transducers 1, 2, 3 and 4.

These differences are important since they are related to the transducer sensitivity when operating at a specific frequency [19]. Therefore, after analyzing all the data collected for all transducers, it was determined that the USCT will be operated at the frequencies of 125 kHz and 156 kHz in future studies. By operating the system at two frequencies one is able to explore the characteristics of the received signal at two different operation regimens; at the resonance frequency (156 kHz), and between the two resonance frequency modes (125 kHz). When operating between resonance modes, the sensitivity per transducer is lower, but the variability of the sensitivity among transducers is also lower, which is desirable when collecting data on a tomographic configuration. When operating at 156 kHz, the individual sensitivity is higher, however, more variation among transducers is expected. Thus, since this is a pilot study, we decided to investigate both options.

2) Displacement Measurement: The displacement amplitude measurement data was analyzed and the characteristics of each transducer were extracted. A subset of the measurements is shown in Figure 9. A substantial variation in the displacement magnitude is observed, again depending on frequency and transducer.

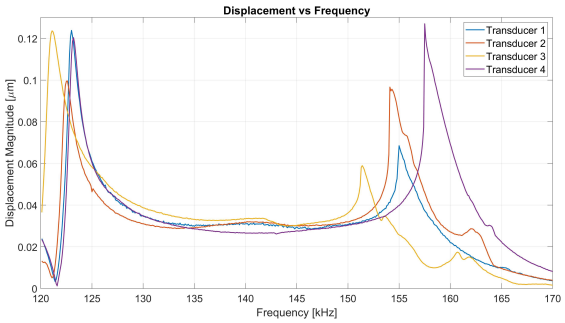

Fig. 9. Displacement magnitude in function of the applied signal frequency of transducers 1, 2, 3 and 4.

It is clear that not only the magnitude varies with frequency and among transducers, but the maximal values do not necessarily occur for the same resonance mode. For transducer 3, a higher displacement magnitude was achieved on the resonance mode closer to 122 kHz, whereas for transducer 4, it was achieved closer to 156 kHz. In the region between the 125 kHz and 150 kHz the magnitude for all transducers is between 0.027 μm and 0.033 μm. A similar behavior was also observed on the electrical impedance measurements, and therefore, agrees with the frequency previously chosen to be used on the application.

3) Statistical Analysis: The statistical significance of the impedance and displacement data, collected during the experiment, was analyzed through an analysis of variance test with a confidence interval of 99% (F-Table α=0.01). The controlled variable considered was the transducer, and the response factors were the maximum and minimum impedance, displacement and sensitivity values, and also, the frequency to which they occur. The ANOVA residuals for all the response variables showed a normal distribution, and the equal variances premise was not violated, and thus, it was considered that ANOVA is an adequate test for this experiment [21]. ANOVA has shown that the resonance frequency, the maximum and minimum displacement, the electrical impedance, and the sensitivity, when the transducer is operating at its own resonance frequency and at fixed frequencies of 125 kHz and 156 kHz, significantly vary among transducers (f-values $\geq$ 27.08 and p-values $\leq$ 0.001).

The results in Table I and Figure 10 show that even though the average electrical impedance is higher at 125 kHz, the

displacement of the piston is larger at that frequency. Also, the variability at 125 kHz is lower than at 156 kHz, thus, it is considered that 125 kHz might be the best operation frequency for the transducers.

Frequency	125 kHz	156 kHz
Elec. impedance	955 $\pm$ 210 Ω	433 $\pm$ 242 Ω
Displacement	0.066 $\pm$ 0.02 μm	0.049 $\pm$ 0.03 μm

TABLE I

THE AVERAGE IMPEDANCE AND DISPLACEMENT OF THE TRANSDUCERS AT THE TWO FREQUENCIES

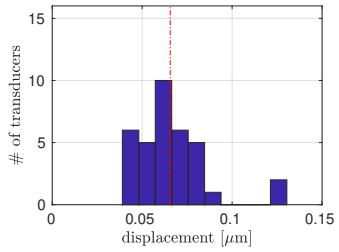

(a) 125 kHz

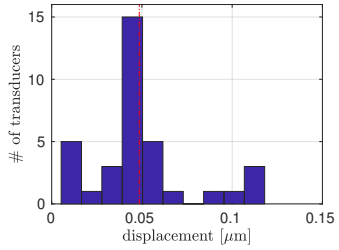

(b) 156 kHz

Fig. 10. Histograms for the displacements

If each of the transducers were operated at their resonance frequency, displacements of 0.110 $\pm$ 0.03 μm and 0.109 $\pm$ 0.03 μm could be achieved for the first and second resonant modes. However, each transducer is used to emit and receive signals in a tomographic configuration, and thus, varying the frequency of the transmitted signal would make the image reconstruction process more complicated, and also increase the disparity between the sensitivity of the transmitting and the receiving transducers that compose the array.

4) Transducer calibration: As seen in section III-B.3, there was significant variability in the sensitivity of the transducers. After analyzing and comparing the magnitude of the impedance and displacement, a strong correlation ($r = 0.91$) was found between the frequency corresponding to the minimum impedance and maximum displacement for both resonance modes (around 125 kHz and 156 kHz). However, there was no correlation ($r = -0.07$) between the impedance magnitude at resonance frequency and displacement. Therefore, a calibration approach based only on impedance would not be sufficient to compensate for the sensitivity variation of the transducers, and hence a calibration based on the displacement is proposed. The displacement magnitude was measured at the center of the transducer's piston three times using the vibrometer. The variability among samples collected per transducer was evaluated and only the third sample was used for calibration under the assumption that the vibrometer has reached steady-state temperature by the third measurement. The measurements were then analyzed, and the absolute value of displacement at the operating frequencies of 125 kHz and 156 kHz was determined for each transducer.

The sensitivity of each transducer was determined based on the displacement reached at the operating frequency and the excitation voltage. The average sensitivity was 1.809 $\pm$ 0.5879 nm/V and 1.812 $\pm$ 0.5979 nm/V for the frequencies of 125 and 156 kHz, respectively. A calibration table was filled with the sensitivity coefficients. The rows represent the transducer number, and columns, the normalized sensitivity at each operating frequency.

The table was used to calibrate data collected in a tomographic configuration (32 transducers radially distributed on the same plane). The coefficients are applied to the raw, time-dependent, data twice; once for the transmitting transducer and once for each of the receiving transducers, as shown in Equation (1).

$$\text{Voltage}_c = \frac{\text{Voltage}_r}{\text{Coeff}_r.\text{Coeff}_t}, \tag{1}$$

where Voltage_c is the calibrated voltage, Voltage_r is the raw received signal and Coeff_r and Coeff_t are the calibration coefficients of the receiving and transmitting transducers.

For a segment of data collected on transducer 25, when the signal is transmitted by transducer 32, for example, the data is divided by the normalized sensitivity coefficient of transducer 25 and 32. That approach compensates for the differences in sensitivity for both sending and receiving channels individually, which is essential for a proper tomographic reconstruction.

IV. CONCLUSION

This study aimed to develop a Tonpilz transducer capable of operating on a low frequency range (frequencies below 750 kHz) for the application of pulmonary USCT. The maximum acceptable external dimensions of the transducer were determined, and several simulations were conducted to analyze its behavior. Through the acoustic analysis, it was shown that the maximum acoustic pressure achieved is safe for use on human patients and that the beam divergence is adequate for the application. The structural analysis results have shown that the safety factor is 2.33 and that the assembly torque is responsible for 98% of the mechanical stress on the piston structure.

The sensitivity of the transducers was determined based on the piston's displacement for a known excitation source. Sta-

tistical analysis have shown that the sensitivity varies significantly among devices. Therefore, a calibration method based on the transducer piston's displacement was implemented to compensate for the variability on the characteristics of both transmitting and receiving transducers.

ACKNOWLEDGMENT

We thank Martin Hofmann from the University of Bern for the support and advice for the displacement measurements.

REFERENCES

[1] J.M. Allin and P. Cawley. Design and construction of a low frequency wide band non-resonant transducer. *Ultrasonics*, 41(3):147–155, May 2003.

[2] Robert E. Apfel and Christy K. Holland. Gauging the likelihood of cavitation from short-pulse, low-duty cycle diagnostic ultrasound. *Ultrasound in Medicine and Biology*, 1991.

[3] Y. Beaulieu and P.E. Marik. Bedside ultrasonography in the ICU: part 2. *Chest*, 128(3):1766–1781, 2005.

[4] M. Blaivas, A. Kirkpatrick, and A. Sustic. Future directions and conclusions. *Crit. Care Med.*, 35:S305–S307, 2007.

[5] A Cochran, P Reynolds, and G Hayward. Progress in stacked piezocomposite ultrasonic transducers for low frequency applications. *Ultrasonics*, 36(10):969–977, October 1998.

[6] David L. Convissar, Lauren E. Gibson, Lorenzo Berra, Edward A. Bittner, and Marvin G. Chang. Application of lung ultrasound during the COVID-19 pandemic: A narrative review. *Anesthesia & Analgesia*, 131(2):345–350, 2020.

[7] Neb Duric, Peter Littrup, Cuiping Li, Olivier Roy, Steve Schmidt, John Seamans, Andrea Wallen, and Lisa Bey-Knight. Whole breast tissue characterization with ultrasound tomography. In Johan G. Bosch and Neb Duric, editors, *Medical Imaging 2015: Ultrasonic Imaging and Tomography*, volume 9419, pages 81 – 88. International Society for Optics and Photonics, SPIE, 2015.

[8] FDA. Marketing Clearance of Diagnostic Ultrasound Systems and Transducers; Guidance for Industry and Food and Drug Administration Staff. *U.S. Department of Health and Human Services: Food and Drug Administration: Center for Devices and Radiological Health*, pages 18–34, 2019.

[9] Luna Gargani, Hatem Soliman-Aboumarie, Giovanni Volpicelli, Francesco Corradi, Maria Concetta Pastore, and Matteo Cameli. Why, when, and how to use lung ultrasound during the COVID-19 pandemic: enthusiasm and caution. *European Heart Journal - Cardiovascular Imaging*, 21(9):941–948, 06 2020.

[10] A.V. Goncharsky, S.Y. Romanov, and S.Y. Seryozhnikov. A computer simulation study of soft tissue characterization using low-frequency ultrasonic tomography. *Ultrasonics*, 67:136–150, April 2016.

[11] Christian Henke. A numerical modeling strategy for passive electro-acoustic transducers. *Ultrasonics*, 102:106065, March 2020.

[12] Koussila Kassou, Youcef Remram, Pascal Laugier, and Jean-Gabriel Minonzio. Dispersion characteristics of the flexural wave assessed using low frequency (50–150 kHz) point-contact transducers: A feasibility study on bone-mimicking phantoms. *Ultrasonics*, 81:1–9, November 2017.

[13] Valsala Kurusingal. Tonpilz transducer array for wideband sonar applications. In *2019 IEEE International Ultrasonics Symposium (IUS)*, pages 1750–1752, 2019.

[14] J-L. Laborde, C. Bouyer, J.-P. Caltagirone, and A. Gérard. Acoustic bubble cavitation at low frequencies. *Ultrasonics*, 36(1-5):589–594, February 1998.

[15] J.-L. Laborde, C. Bouyer, J.-P. Caltagirone, and A. Gérard. Acoustic cavitation field prediction at low and high frequency ultrasounds. *Ultrasonics*, 36(1-5):581–587, February 1998.

[16] Seungjun Lee, N.B. Smith, and K.K. Shung. Ultrasound mediated transdermal in vivo transport of insulin with low profile cymbal arrays. In *2002 IEEE Ultrasonics Symposium, 2002. Proceedings.*, volume 2, pages 1423–1426 vol.2, 2002.

[17] Peiyang Li, Weiwei Shao, Tingyi Jiang, Zhangjian Li, Suoyuan Li, Junjie Fan, Liming Cai, Yaoyao Cui, and Jun Shen. Development of a miniaturized low-frequency transducer for accurate placement of screw implants in the spine. In *2019 IEEE International Ultrasonics Symposium (IUS)*, pages 1815–1818, 2019.

[18] D.A. Lichtenstein. Ultrasound in the management of thoracic disease. *Crit. Care Med.*, 35:S250–S261, 2007.

[19] Ana L. Lopez-Sanchez and Lester W. Schmerr. Determination of an ultrasonic transducer's sensitivity and impedance in a pulse-echo setup. *IEEE Transactions on Ultrasonics, Ferroelectrics, and Frequency Control*, 53(11):2101–2112, 2006.

[20] R.J. Meyer, T.C. Montgomery, and W.J. Hughes. Tonpilz transducers designed using single crystal piezoelectrics. In *OCEANS '02 MTS/IEEE*, volume 4, pages 2328–2333 vol.4, 2002.

[21] Douglas C Montgomery. *Design and Analysis of Experiments*, volume 1. Wiley, Hoboken, 8th edition, feb 2012.

[22] Olivia Ngo, Evan Niemann, Vivinya Gunasekaran, Prabagar Sankar, Miriam Putterman, Alec Lafontant, Sumati Nadkarni, Rose Ann Dimaria-Ghalili, Michael Neidrauer, Leonid Zubkov, Michael Weingarten, David J. Margolis, and Peter A. Lewin. Development of low frequency (20-100 kHz) clinically viable ultrasound applicator for chronic wound treatment. *IEEE Transactions on Ultrasonics, Ferroelectrics, and Frequency Control*, 66(3):572–580, 2019.

[23] QY. Peng, XT. Wang, LN. Zhang, and Chinese Critical Care Ultrasound Study Group (CCUSG). Findings of lung ultrasonography of novel corona virus pneumonia during the 2019-2020 epidemic. *Intensive Care Med*, 46:849–850, 2020.

[24] Seonghun Pyo and Yongrae Roh. Structural design of an acoustic planar array transducer by using the equivalent circuit method. *Ultrasonics*, 108:106219, December 2020.

[25] D. Rueter, H. P. Hauber, D. Droeman, P. Zabel, and Stefan Uhlig. Low-frequency ultrasound permeates the human thorax and lung: A novel approach to non-invasive monitoring. *Ultraschall in der Medizin*, 31(1):53–62, 2010.

[26] Mark Sak, Peter Littrup, Rachel Brem, and Neb Duric. Whole Breast Sound Speed Measurement from US Tomography Correlates Strongly with Volumetric Breast Density from Mammography. *Journal of Breast Imaging*, 2(5):443–451, 07 2020.

[27] G Y Sandhu, C Li, O Roy, S Schmidt, and N Duric. Frequency domain ultrasound waveform tomography: breast imaging using a ring transducer. *Physics in Medicine & Biology*, 60(14):5381, 2015.

[28] Gursharan Yash Sandhu, Erik West, Cuiping Li, Olivier Roy, and Neb Duric. 3D frequency-domain ultrasound waveform tomography breast imaging. In Neb Duric and Brecht Heyde, editors, *Medical Imaging 2017: Ultrasonic Imaging and Tomography*, volume 10139, pages 56 – 69. International Society for Optics and Photonics, SPIE, 2017.

[29] J. A Shaw, E. H Louw, and C. F. N. Koegelenberg. Lung ultrasound in COVID-19: Not novel, but necessary. *Respiration*, 99:545–547, 2020.

[30] J.A. Shaw, F. von Groote-Bidlingmaier, and C.F.N. Koegelenberg. Transthoracic ultrasound, Palange P, Rhode G, editors: ERS. In *Handbook of Respiratory Medicine. 3rd ed.*, pages 160–167. European Respiratory Society (ERS), 2019.

[31] Charles H. Sherman and John L. Butler. *Transducers and Arrays for Underwater Sound*. Springer New York, 2007.

[32] Hazel C. Starritt and Francis A. Duck. Safety. In *Clinical Ultrasound*, pages 51–60. Churchill Livingstone, jan 2011.

[33] C.L. Tobin, Y.C. Lee, F. Gleeson, D. Feller-Kopman, and N. Rahman. *Pleural ultrasound for clinicians: a text and e-book*. CRC Press, 2014.

[34] Robert J. Urick. *Principles of Underwater Sound*. (McGraw–Hill, New York, 1893.

[35] Florian Vogl, Bernd Friesenbichler, Laura Hüsken, Inès A. Kramers de Quervain, and William R. Taylor. Can low-frequency guided waves at the tibia paired with machine learning differentiate between healthy and osteopenic/osteoporotic subjects? a pilot study. *Ultrasonics*, 94:109–116, April 2019.

[36] Chunying Wang, Yu Lan, and Wenwu Cao. Tonpilz transducer head mass selection based on excitation signal type. *Applied Acoustics*, 176:107852, 2021.

[37] Qingshan Yao and Leif Bjørnø. Broadband tonpilz underwater acoustic transducers based on multimode optimization. *IEEE Transactions on Ultrasonics, Ferroelectrics, and Frequency Control*, 1997.

[38] Kenji Yoshida, Kazuya Obata, Akira Tsukamoto, Takashi Ushida, and Yoshiaki Watanabe. Limited damage of tissue mimic caused by a collapsing bubble under low-frequency ultrasound exposure. *Ultrasonics*, 54(6):1603–1609, August 2014.

[39] Yao Zhang, Heng Xue, Mixue Wang, Nan He, Zhibin Lv, and Ligang Cui. Lung ultrasound findings in patients with coronavirus disease (COVID-19). *American Journal of Roentgenology*, 216(1):80–84, 2021.

Appendix C

Publication Three

Starting on the next page, our article related to Electrical Impedance Tomography is presented in its original form. It was presented at the International Conference of Bioelectromagnetism, Electrical Bioimpedance, and Electrical Impedance Tomography (ICBEM-ICEBI-EIT 2022), held online on June 28 - July 1, 2022.

ICBEM Bioelectromagnetism ICEBI Electrical Bioimpedance EIT Electrical Impedance Tomography

Proceedings of the International Conference of Bioelectromagnetism, Electrical Bioimpedance, and Electrical Impedance Tomography June 29 – July 1, 2022 / Kyung Hee University, Seoul, Korea

Ventilation Volume of Mechanically Ventilated Patients from EIT Data on a Novel Electrode Solution : A Case Study

Nilton Barbosa da Rosa Junior[1], Jennifer Mueller[1,2], Andre Vieira Pigatto[1], Tzu-Jen Kao[3], Nancy Stoffel[3], Cheryl Bromirski[3], David Davenport[3], Patrick Offner[4] and Ellen Burnham[4]

[1]School of Biomedical Engineering, Colorado State University, Fort Collins, USA
[2]Department of Mathematics, Colorado State University, Fort Collins, USA
[3]GE Research, Niskayuna, USA
[4]Department of Medicine, University of Colorado Anschutz Medical Campus, Aurora, USA

Correspondence: Nilton Barbosa da Rosa Junior, e-mail: nilton@colostate.edu

Abstract–Monitoring patients receiving mechanical ventilation is a leading application of electrical impedance tomography. Electrical impedance tomography has been shown to be a viable imaging modality for bedside lung monitoring, which can provide visual information about regional ventilation and pulmonary perfusion. However, a significant challenge in its use for patients receiving mechanical ventilation is efficient and safe electrode placement. The purpose of this paper is to present results from a case study in which a novel electrode solution is being used in a larger study to image patients with acute respiratory distress syndrome. Data was collected during a spontaneous breathing trial using the General Electric simultaneous multiple current source prototype electrical impedance tomography system, and 3-D conductivity difference images were computed using a linearization-based reconstruction algorithm. Regional lung volume estimates were computed from the images. The images show good agreement with the chest x-ray that showed suspected pleural fluid accumulation and atelectesis, and the dynamic global lung volume estimate was in good agreement with the volume range provided by the ventilator.

Keywords: EIT; real-time lung monitoring; acute respiratory distress syndrome; lung volume estimates.

1. Introduction

Patients with ARDS (acute respiratory distress syndrome) are treated with mechanical ventilation, which reinflates the airways over time. Various methods have been used to monitor patients undergoing mechanical ventilation including monitoring blood gases and pressure-volume curves, but these quantities do not provide regional information about lung aeration, which is important because an aeration imbalance can lead to collapse of dependent lung zones and overdistension of non-dependent regions, potentially resulting in lung injury. Electrical impedance tomography has been shown to be a viable imaging modality for bedside lung monitoring, which can provide visual information about regional ventilation and pulmonary perfusion.

One challenge in the use of EIT for imaging mechanically ventilated patients is electrode placement. Patients are typically sedated, and rolling the patient to apply the electrodes comes with the risk of dislodging the endotracheal tube or tracheostomy and patient discomfort. Thus, it is important to have a fast and reliable method of electrode application. A novel textile electrode solution was developed to address this problem and is being used in an ongoing study of patients with acute respiratory distress syndrome at Anschutz Hospital in Aurora, CO. Here we present a case study of the results on one mechanically ventilated patient in the ICU undergoing a spontaneous breathing trial. The images are compared to a chest x-ray and reveal good agreement in the detection of fluid accumulation in the lung. Real-time regional lung volume estimates are computed from the EIT images and compared to the global ventilator values.

2. Materials and methods

2.1 EIT system and data collection

The study was conducted in accordance with the amended Declaration of Helsinki. Data were collected at Anschutz Hospital in Aurora, CO under the approval of the institutional review board (approval number 21-3315). Here we present preliminary results from data collected on one 73 year-old male patient with primary diagnoses of acute hypercapnic

respiratory failure (AHRF) and pulmonary edema receiving mechanical ventilation. The WEAT was placed, and EIT data was collected with the patient in supine position. PEEP was set at 5 cm H20. The EIT data was collected using the GE SMS-EIT prototype system described in [Ashe et al, 2014] The system is a 32 channel real-time simultaneous multiple current source system, that collects data at 18 frames per second at 10 kHz. In this work, the 3-D trigonometric current patterns specified in [Kao et al, 2020] are applied with a maximum amplitude of 0.11 mA RMS.

2.2 Electrode placement solution: WEATs

An easy-to-apply array of electrodes is essential to efficient work flow in the hospital environment. The textile design, consisting of two independent halves, is shown in Figure 1. The wearable electrode applicator textile (WEAT) consists of two rows of 16 electrodes arranged in two C-shapes to enable 3-D imaging. The ends of the C-shape meet at the sternum and the spine, which has the advantages of not constricting the chest during breathing. The WEAT is made in a variety of sizes with the intent of maintaining a gap of approximately 3 to 4 cm between the electrodes at the sternum and spine. The leads come together in four groups of eight, and so two connectors under each arm connect the WEAT to the EIT system. A ground electrode is attached separately to the subject's shoulder or abdomen.

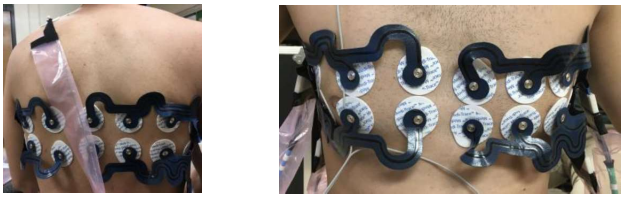

Figure 1. Two views of the WEAT on a healthy volunteer.

2.3 ToDLeR algorithm and lung volume computation

The ToDLeR algorithm [Blue et al, 2000] with the real-time implementation described in [Kao et al, 2020] on a cylinder was modified to account for uneven electrode placement and varying height between the two rows of the electrodes, while keeping the cylindrical model in this work. A reference frame representing maximal expiration was chosen from a principal component analysis of the data, and 3-D difference images of the conductivity were computed relative to the reference frame on two vertically stacked 496-voxel Joshua tree meshes [Cheney et al, 1990] with height 7.5 cm. The reconstructions are displayed in DICOM format, and the cross-section through the lower row of electrodes is displayed in the bottom image of the figure and the cross-section through the upper row of electrodes is displayed as the upper image. Voxels of lower conductivity than the reference frame are blue, and those of higher conductivity are orange/red.

For each frame, the inspired volume of air in each voxel was estimated from the conductivity values in the EIT image using the method from [Muller et al, 2015] and [Pigatto et al, 2021]. We review the method here. For a given voxel p in the segmented lung region, let $\sigma_a(p,t)$ denote the conductivity in the pth voxel at time t corresponding to a given frame. The volume fraction $\mathrm{f}_a(p,t)$, of air in the pth voxel at time t, is related to the conductivity in the pth voxel at time t by

$$\sigma_a(p,t) = \sigma_{aM}(1\text{-}\mathrm{f}_a(p,t)) + \sigma_{am}\mathrm{f}_a(p,t), \tag{1}$$

where σ_{aM} and σ_{am} are the maximum and minimum values, respectively, of the conductivity over all voxels and over the entire data collection period of interest. The volume fraction of air can then be computed by

$$\mathrm{f}_a(p,t) = \frac{\sigma_a(p,t)-\sigma_{aM}}{\sigma_{am}-\sigma_{aM}} \tag{2}$$

The lung region was identified and segmented by a threshold method. Any voxel with a minimum relative conductivity value that remains larger than $0.5(\sigma_{aM} + \sigma_{am})$ over the entire data set was considered to be too conductive to be included as a lung voxel. Any voxel with maximum relative conductivity value over the entire data set exceeding 90% of σ_{aM} was also considered to be too conductive to be a lung voxel. Finally, voxels that have peak-to-peak conductivity smaller than 30% of the highest peak-to-peak voxel conductivity, which could represent voxels with small variations close to the electrodes (such as in the upper axilla), were excluded from the computations.

The images were divided into four quadrants to represent the upper left lung (ULL), upper right lung (URL), lower left lung (LLL) and lower right lung (LRL). To compute the volume of air in each quadrant at time t, the sum of $\mathrm{f}_a(p,t)$ multiplied by the volume of the p^{th} voxel was taken over all of the voxels in the quadrant. In this work, the volume of a voxel was one half the distance between the upper and lower rows of electrodes multiplied by the cross-sectional area of the corresponding pixel in the Joshua tree mesh. The global lung volume was the sum of the volume in each quadrant.

3. Results

The patient received a chest x-ray as part of his standard care, which is shown in Figure 2. The radiology report stated, "… there is a new right basilar opacity suspected to reflect a combination of pleural fluid and underlying atelectesis, however pneumonia is not excluded." The EIT conductivity difference images for three frames in the data collection sequence are shown in Figure 3. The three frames correspond to a full inspiration, mid inspiration, and full expiration, with frame 2489 as reference. The total lung volumes computed by the method described in Section 2 are also plotted in Figure 2 for a portion of the sequence. The computed lung volume (Global Volume) ranged from 238 ml to 769 ml, which is in very good agreement with the range of exhaled tidal volume (VTE) provided by the ventilator of 200 to 1000 ml (See Figure 2).

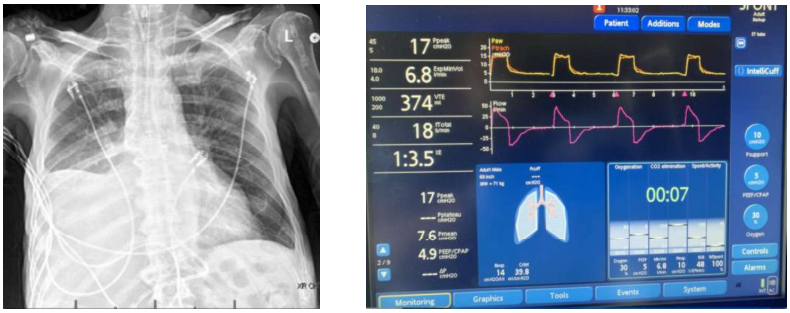

Figure 2. Chest x-ray taken two days after the EIT data collection. Radiology report indicates a right basilar opacity suspected to reflect a combination of pleural fluid and underlying atelectesis, but pneumonia is not excluded.

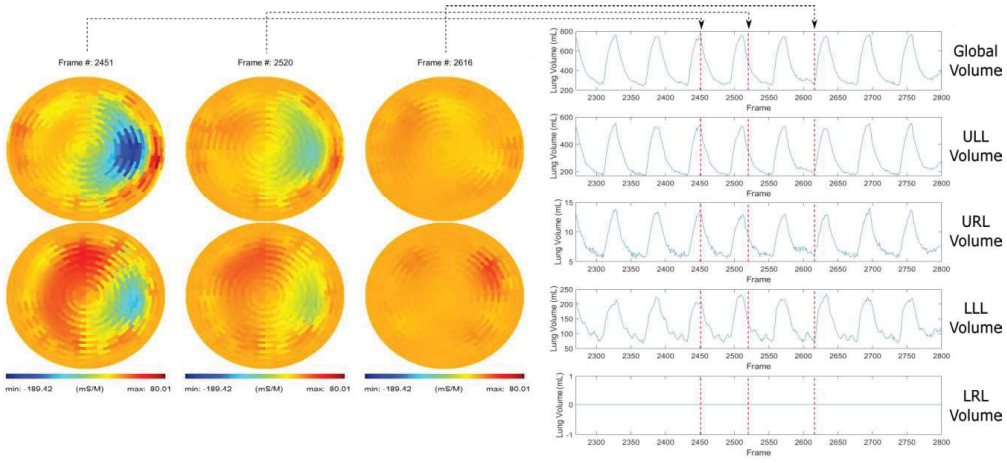

Figure 3. EIT conductivity difference images displayed in DICOM orientation for three frames in the data collection sequence. These frames are indicated by dashed red lines in the line plots below, which depict the lung volumes computed from the EIT images globally (Global Volume), in the upper left lung (ULL), upper right lung (URL), lower left lung (LLL), and lower right lung (LRL).

4. Discussion

One motivation for the design of the WEAT is to avoid restricting patient breathing by constricting the chest with elastic material. Recently, [Zhang et al, 2020] reported that an EIT electrode belt could reduce lung volumes in subjects with pre-existing lung diseases including respiratory muscle weakness patients and COPD patients. Therefore, a better electrode solution for fragile ICU patients is needed. While the WEAT does not constrict the chest, it does permit non-uniform electrode placement, which is then best accounted for in the reconstruction algorithm, and requires placement measurements by the attending clinician.

Regarding the images, at full inspiration (frame # 2451), the upper-left lung (ULL) and lower-left lung (LLL) show regions of ventilation represented by lower conductivity, while the upper-right lung (URL) only shows very few voxels

that are being ventilated. The lower-right lung (LRL) shows highly conductive areas that are not being ventilated. This patient did not receive a CT scan as part of his care, and so comparisons can only be made with the chest x-ray in Figure 2. The regional ventilation in the EIT image is consistent with the chest x-ray and radiologist's report.

The method of computation of the lung volume estimates from the EIT images was also used in [Kao et al, 2020] to compute lung volume estimates in six healthy volunteers who performed a breathing maneuver with a volumetric incentive spirometer, and the volume of air inhaled was calculated from the EIT images. The relative errors between the total inhaled volume reported by the spirometer and the average calculated volume from the EIT images for each of the subjects were 6.5%, 1.5%, 9.2%, 47.2%, 4.4%, and 6.9%. In this study, we see that the global lung volume ranges from 238 ml to 769 ml, which is in very good agreement with the VTE on the ventilator, which ranged from 200 to 1000 ml. Further validation studies are needed to assess the accuracy of the computed lung volumes, both regionally and globally.

5. Conclusions

Preliminary results from this case study using the novel wearable electrode applicator textile (WEAT) demonstrate that the SMS-EIT system together with the WEAT provides 3-D conductivity difference images and regional lung volume estimates that detect ventilation deficiencies in real time and can quantify regional lung volumes. This is part of a larger study in which a statistical analysis will be performed to support quantitative results.

Acknowledgments

This project was supported by Award Number 3R01EB026710-02S1 from the National Institute Of Biomedical Imaging And Bioengineering. The content is solely the responsibility of the authors and does not necessarily represent the official view of the National Institute Of Biomedical Imaging And Bioengineering or the National Institutes of Health. We would also like to the staff in the medical ICU at the University of Colorado Hospital for their role in the data collection.

References

Ashe J, Shoudy D, Boverman G, Sabatini, Kao T J and Amm B 2014 A high precision parallel current drive experimental EIT system. *In 15th International Conference on Biomedical Applications of Electrical Impedance Tomography* **2014**

Blue R S, Isaacson D, and Newell J C 2000 Real-time three-dimensional electrical impedance imaging *Physiological Measurement,* **21,** 1-12

Cheney M, Isaacson D, Newell J C, Simske S and Goble J 1990 NOSER: An algorithm for solving the inverse conductivity problem *International Journal of Imaging systems and technology*, **2(2)**, 66-75

Kao T J, Amm B, Isaacson D, Newell J C, Saulnier G J and Mueller J L 2020 A 3D Reconstruction Algorithm for Real-time Simultaneous Multi-Source EIT Imaging for Lung Function Monitoring *bioRxiv*

Muller P A, Li T, Isaacson D, Newell J C, Saulnier G J, Kao T J, and Ashe J 2015 Estimating a regional ventilation-perfusion index. *Physiological measurement*, **36(6)**, 1283–1295

Pigatto A V, Kao T K, Mueller J L, Baker C D, DeBoer E M and Kupfer O 2021 Imaging ventilation before and after airway clearance therapy in spinal muscular atrophy using electrical impedance tomography *Respir Physiol Neurobiol*, **294**

Zhang N, Jiang H, Zhang C, Li Q, Li Y, Zhang B, Deng J, Niu G, Yang B, Frerichs I, Moeller K, Fu F and Zhao Z 2020 The influence of an electrical impedance tomography belt on lung function determined by spirometry in sitting position *Physiol Meas*, **41(4)**, 044002

Appendix D

Acoustic Maps

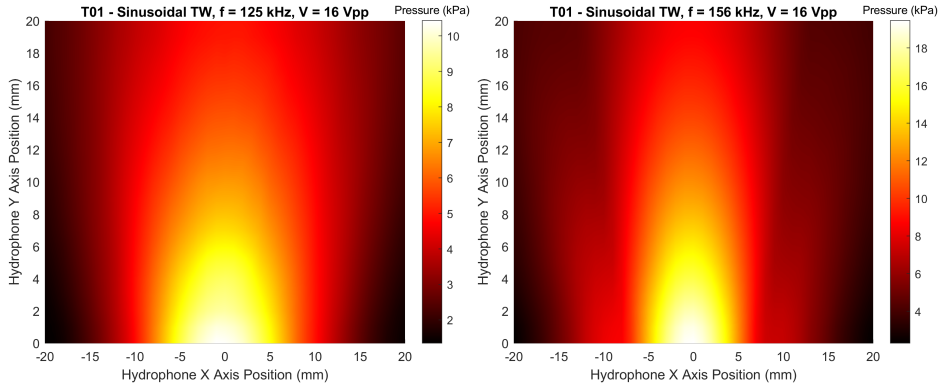

(a) Transducer 1, F = 125 kHz.

(b) Transducer 1, F = 156 kHz.

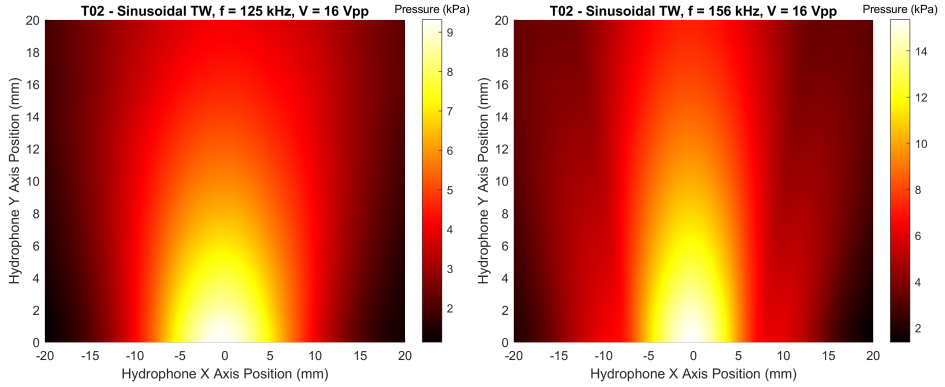

(c) Transducer 2, F = 125 kHz.

(d) Transducer 2, F = 156 kHz.

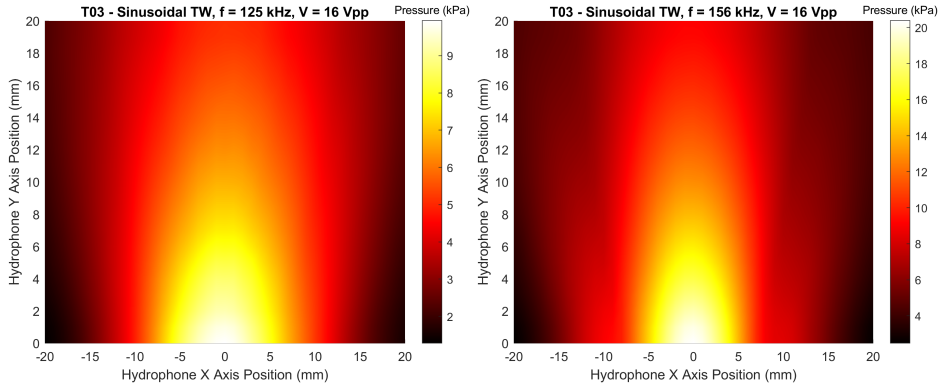

(e) Transducer 3, F = 125 kHz.

(f) Transducer 3, F = 156 kHz.

Figure D.1: Acoustic pressure maps of transducers 1, 2, and 3 when transmitting a sinusoidal signal.

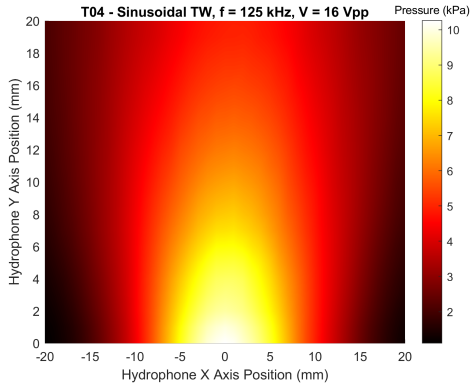

(a) Transducer 4, F = 125 kHz.

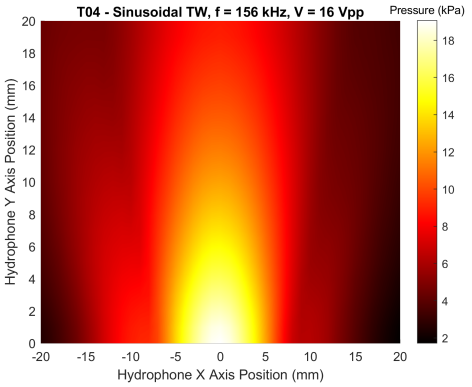

(b) Transducer 4, F = 156 kHz.

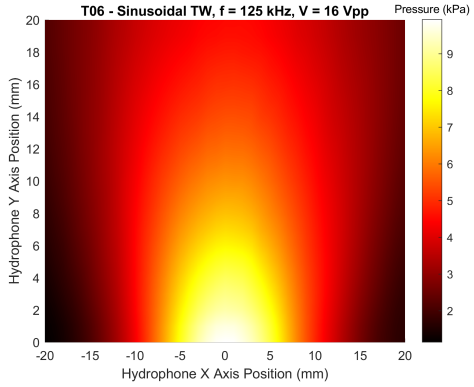

(c) Transducer 6, F = 125 kHz.

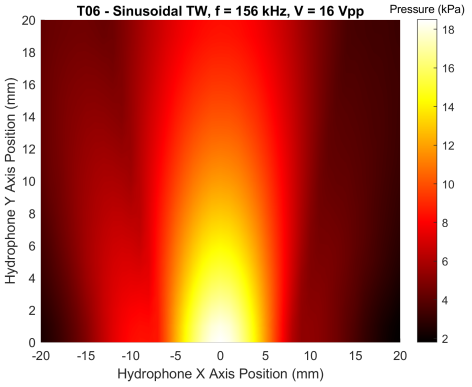

(d) Transducer 6, F = 156 kHz.

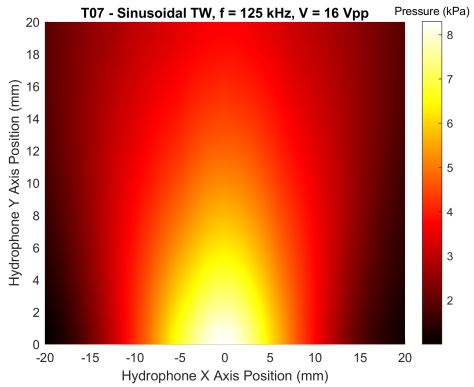

(e) Transducer 7, F = 125 kHz.

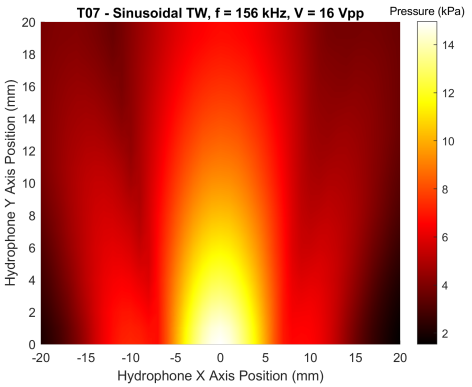

(f) Transducer 7, F = 156 kHz.

Figure D.2: Acoustic pressure maps of transducers 4, 6, and 7 when transmitting a sinusoidal signal.

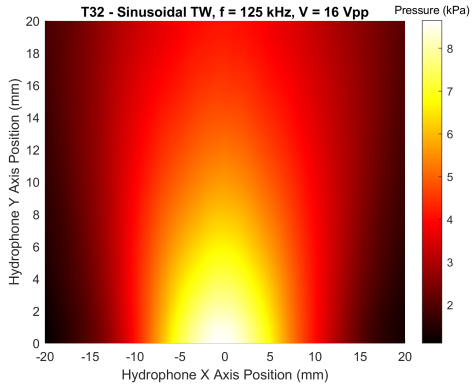

(a) Transducer 32, F = 125 kHz.

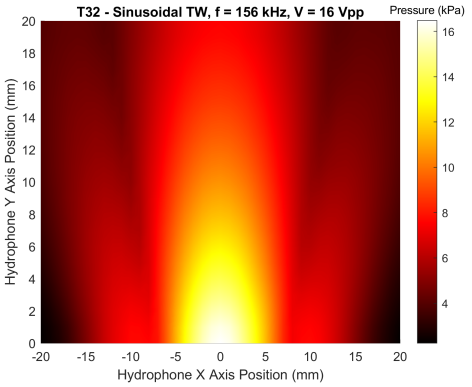

(b) Transducer 32, F = 156 kHz.

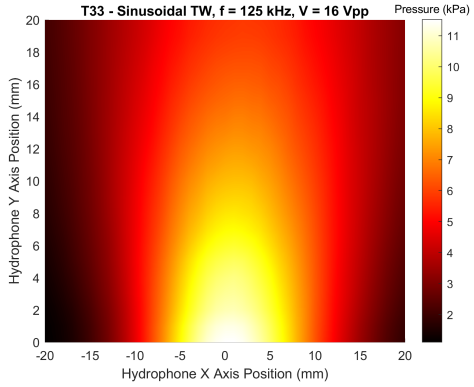

(c) Transducer 33, F = 125 kHz.

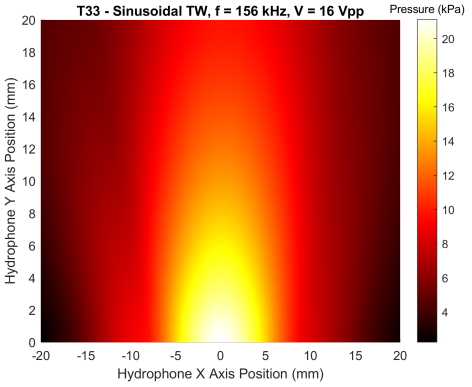

(d) Transducer 33, F = 156 kHz.

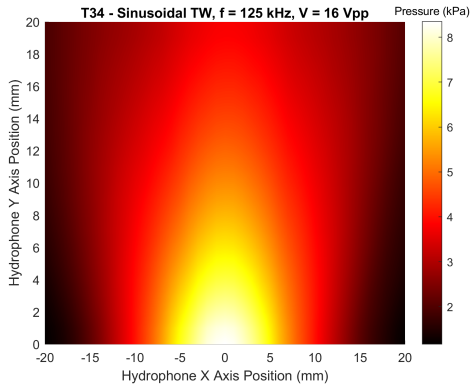

(e) Transducer 34, F = 125 kHz.

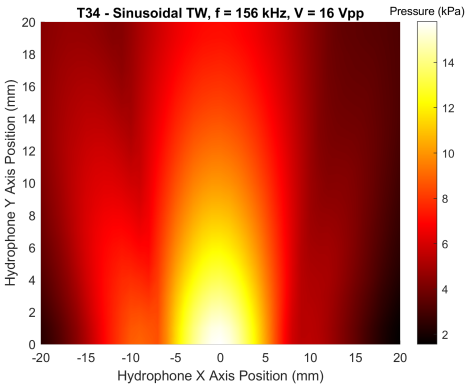

(f) Transducer 34, F = 156 kHz.

Figure D.3: Acoustic pressure maps of transducers 32, 33, and 34 when transmitting a sinusoidal signal.

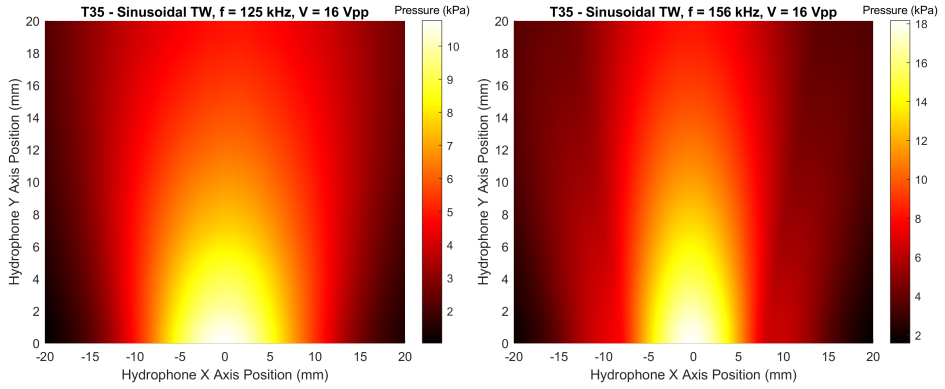

(a) Transducer 35, F = 125 kHz.

(b) Transducer 35, F = 156 kHz.

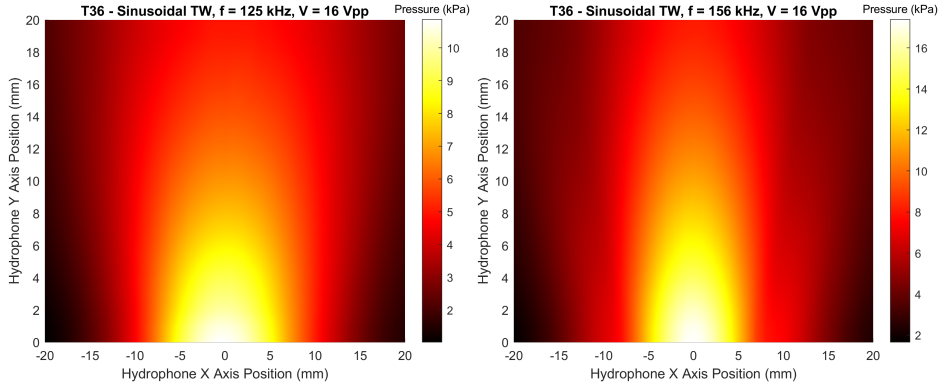

(c) Transducer 36, F = 125 kHz.

(d) Transducer 36, F = 156 kHz.

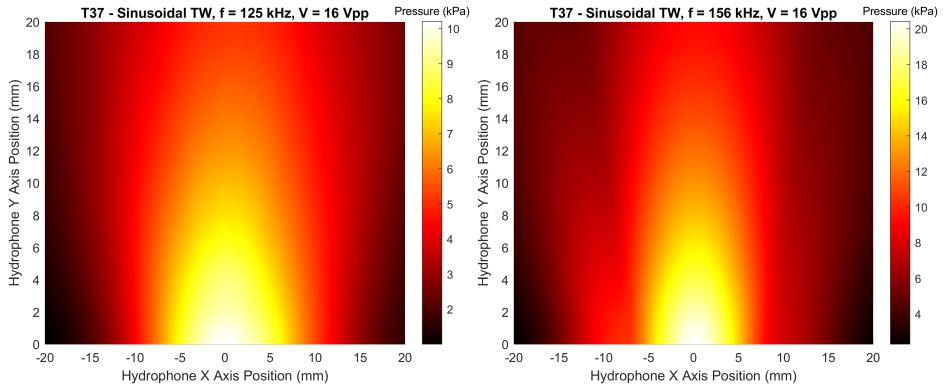

(e) Transducer 37, F = 125 kHz.

(f) Transducer 37, F = 156 kHz.

Figure D.4: Acoustic pressure maps of transducers 35, 36, and 37 when transmitting a sinusoidal signal.

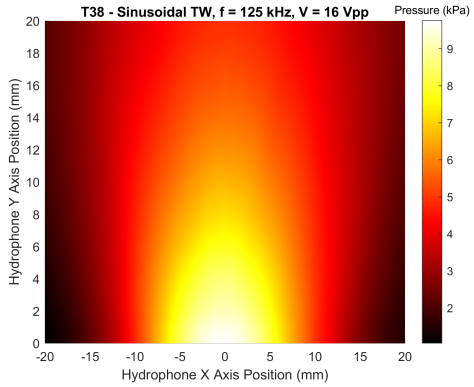

(a) Transducer 38, F = 125 kHz.

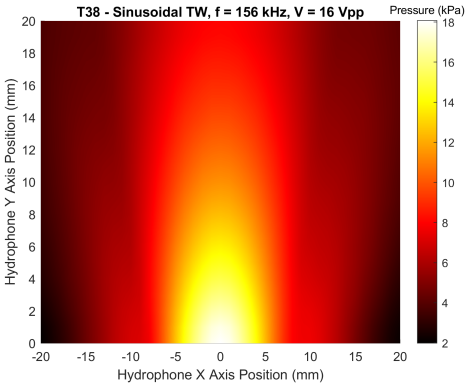

(b) Transducer 38, F = 156 kHz.

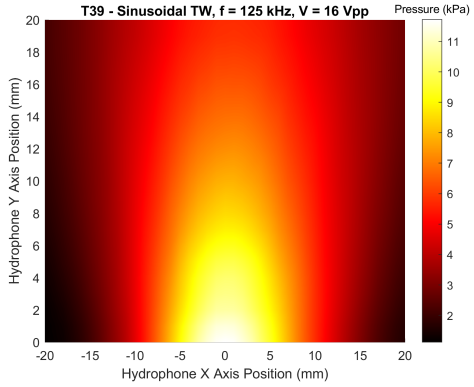

(c) Transducer 39, F = 125 kHz.

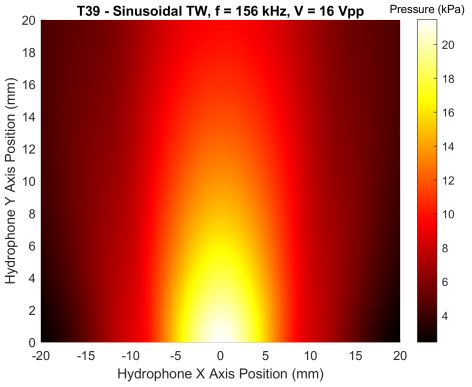

(d) Transducer 39, F = 156 kHz.

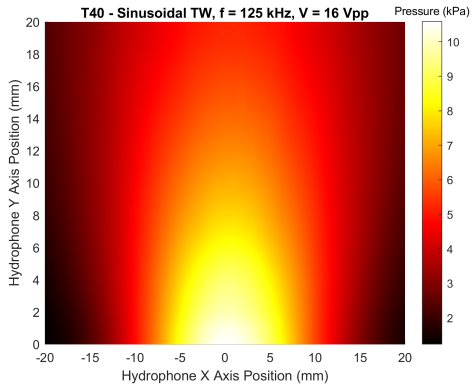

(e) Transducer 40, F = 125 kHz.

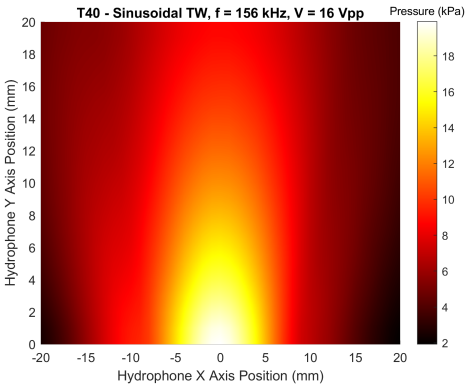

(f) Transducer 40, F = 156 kHz.

Figure D.5: Acoustic pressure maps of transducers 38, 39, and 40 when transmitting a sinusoidal signal.

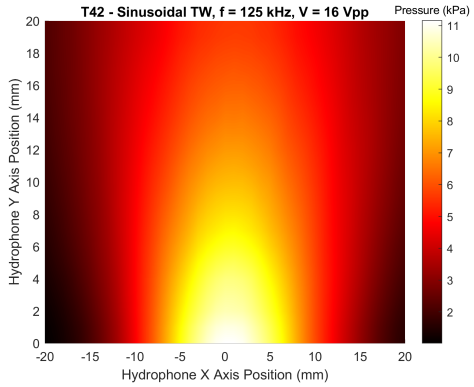

(a) Transducer 42, F = 125 kHz.

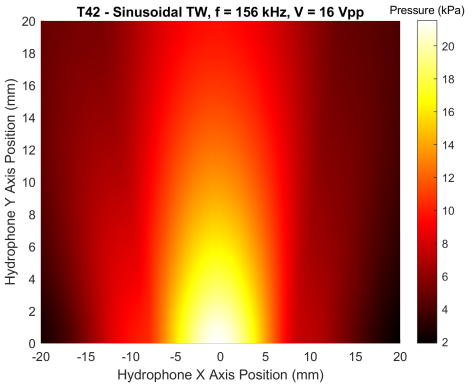

(b) Transducer 42, F = 156 kHz.

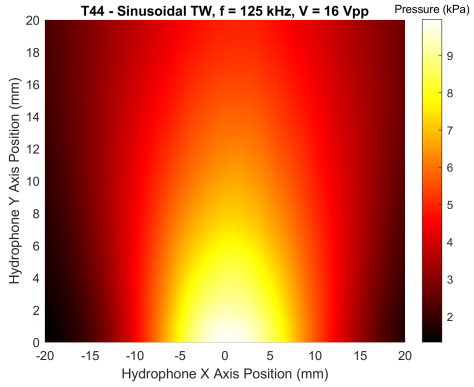

(c) Transducer 44, F = 125 kHz.

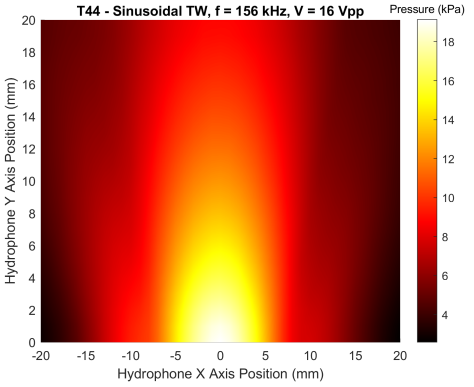

(d) Transducer 44, F = 156 kHz.

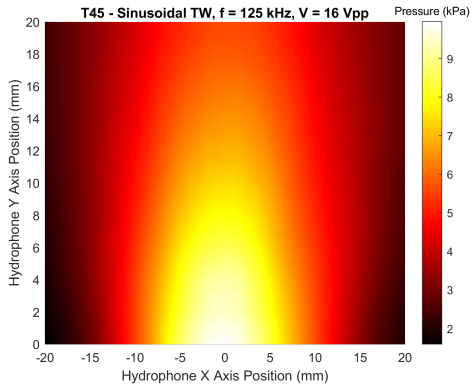

(e) Transducer 45, F = 125 kHz.

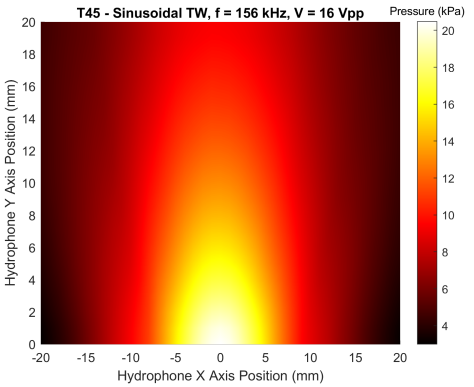

(f) Transducer 45, F = 156 kHz.

Figure D.6: Acoustic pressure maps of transducers 42, 44, and 45 when transmitting a sinusoidal signal.

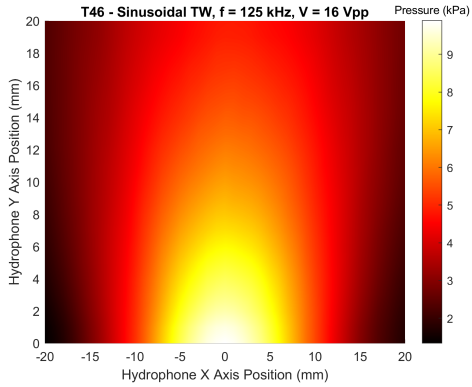

(a) Transducer 46, F = 125 kHz.

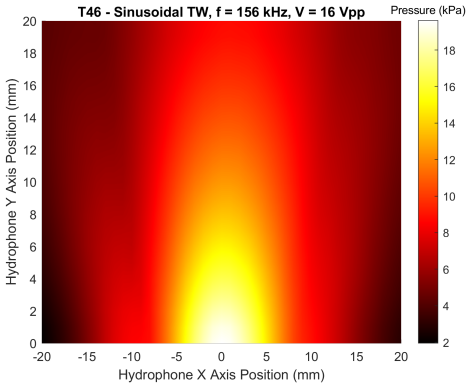

(b) Transducer 46, F = 156 kHz.

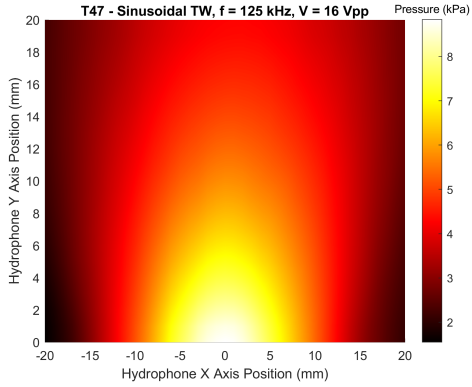

(c) Transducer 47, F = 125 kHz.

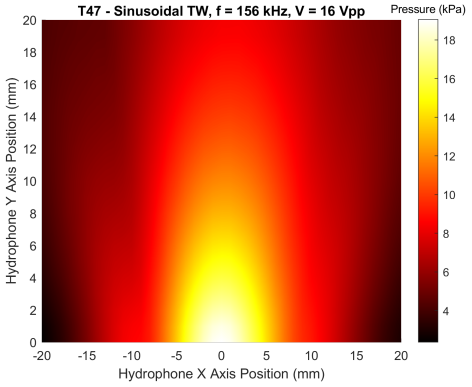

(d) Transducer 47, F = 156 kHz.

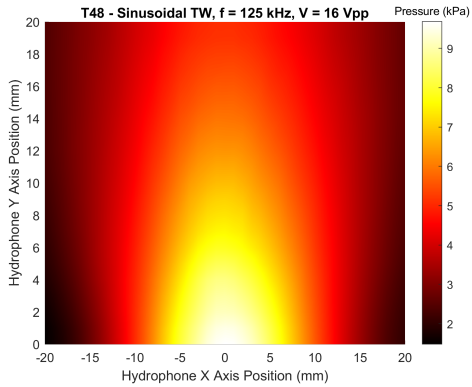

(e) Transducer 48, F = 125 kHz.

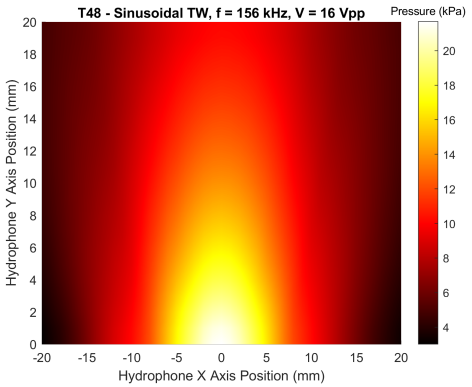

(f) Transducer 48, F = 156 kHz.

Figure D.7: Acoustic pressure maps of transducers 46, 47, and 48 when transmitting a sinusoidal signal.

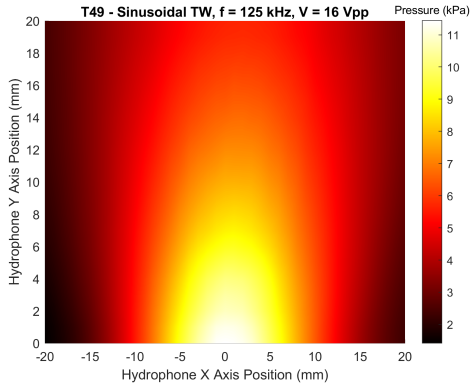

(a) Transducer 49, F = 125 kHz.

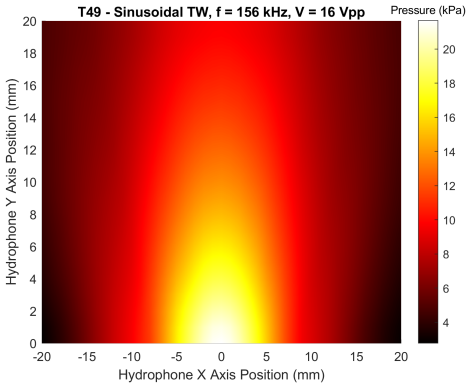

(b) Transducer 49, F = 156 kHz.

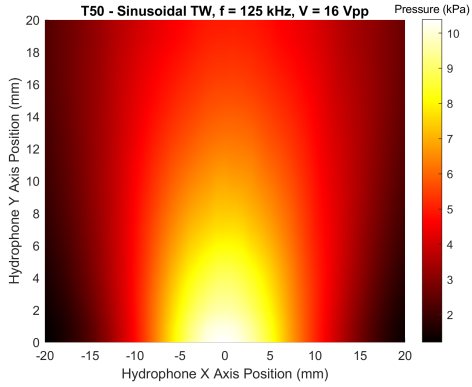

(c) Transducer 50, F = 125 kHz.

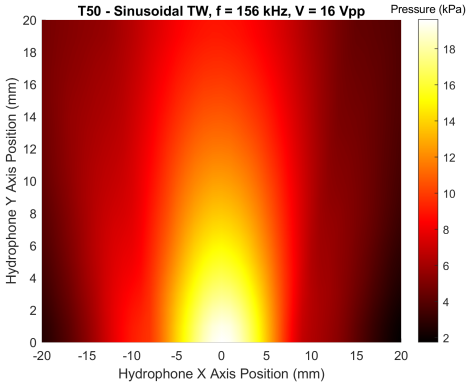

(d) Transducer 50, F = 156 kHz.

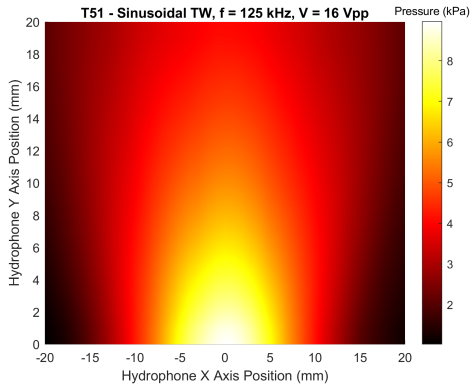

(e) Transducer 51, F = 125 kHz.

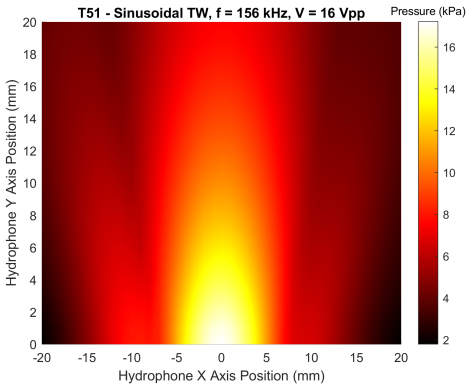

(f) Transducer 51, F = 156 kHz.

Figure D.8: Acoustic pressure maps of transducers 49, 50, and 51 when transmitting a sinusoidal signal.

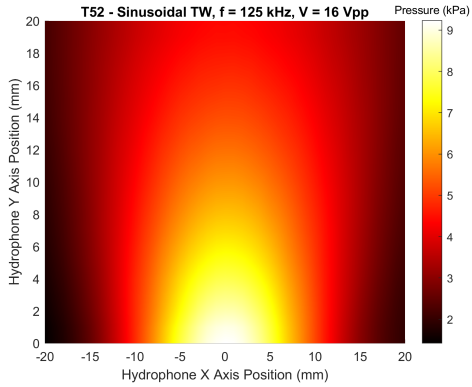

(a) Transducer 52, F = 125 kHz.

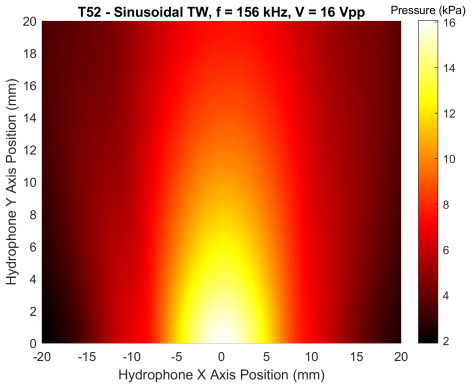

(b) Transducer 52, F = 156 kHz.

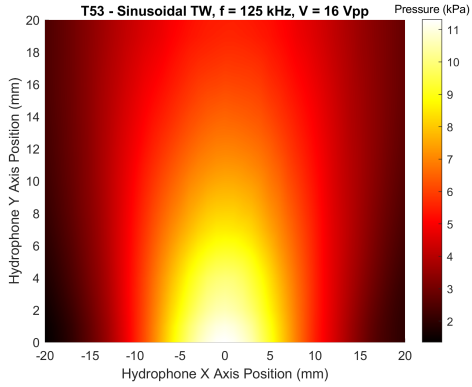

(c) Transducer 53, F = 125 kHz.

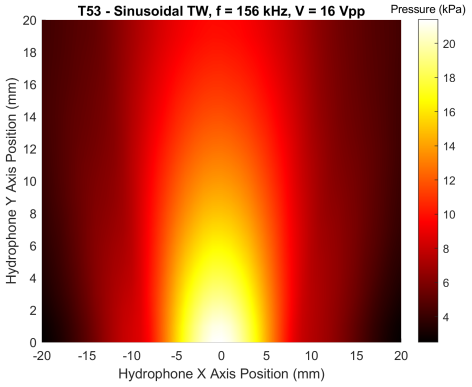

(d) Transducer 53, F = 156 kHz.

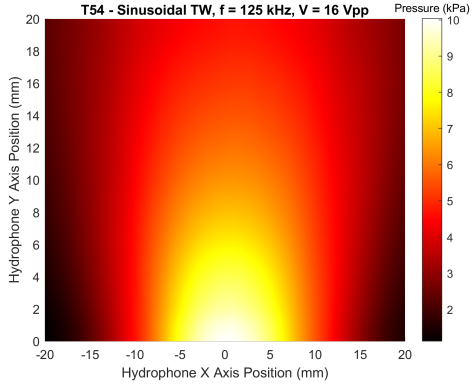

(e) Transducer 54, F = 125 kHz.

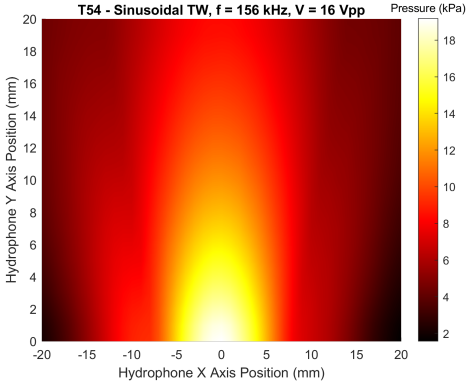

(f) Transducer 54, F = 156 kHz.

Figure D.9: Acoustic pressure maps of transducers 52, 53, and 54 when transmitting a sinusoidal signal.

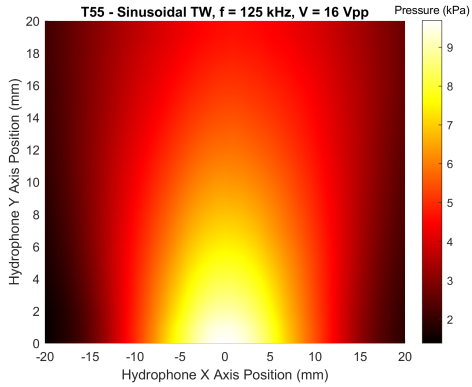

(a) Transducer 55, F = 125 kHz.

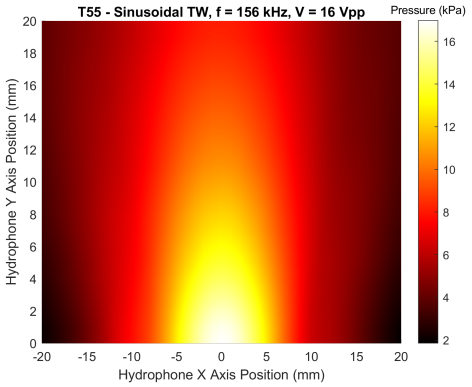

(b) Transducer 55, F = 156 kHz.

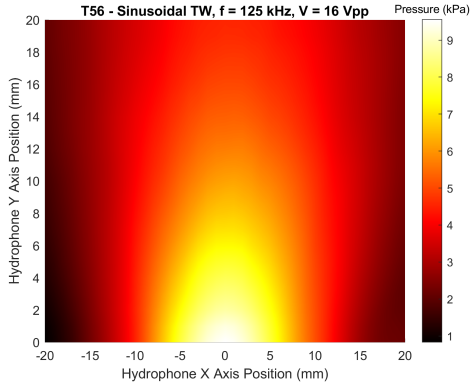

(c) Transducer 56, F = 125 kHz.

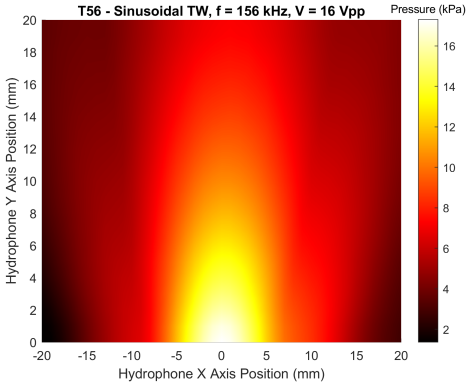

(d) Transducer 56, F = 156 kHz.

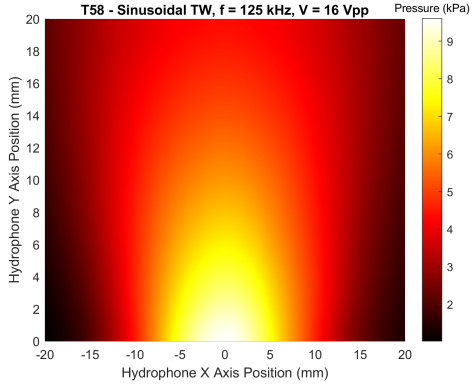

(e) Transducer 58, F = 125 kHz.

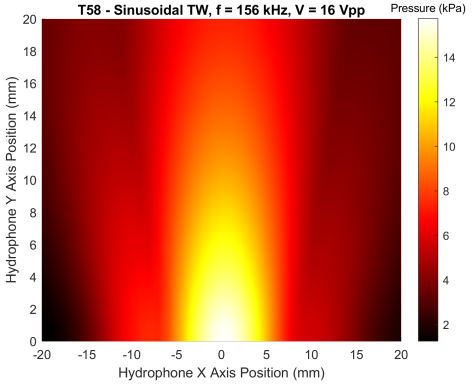

(f) Transducer 58, F = 156 kHz.

Figure D.10: Acoustic pressure maps of transducers 55, 56, and 58 when transmitting a sinusoidal signal.

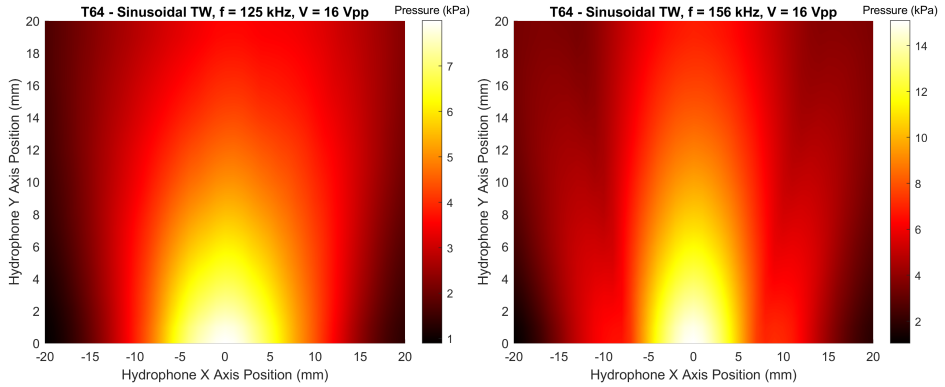

(a) Transducer 64, F = 125 kHz.

(b) Transducer 64, F = 156 kHz.

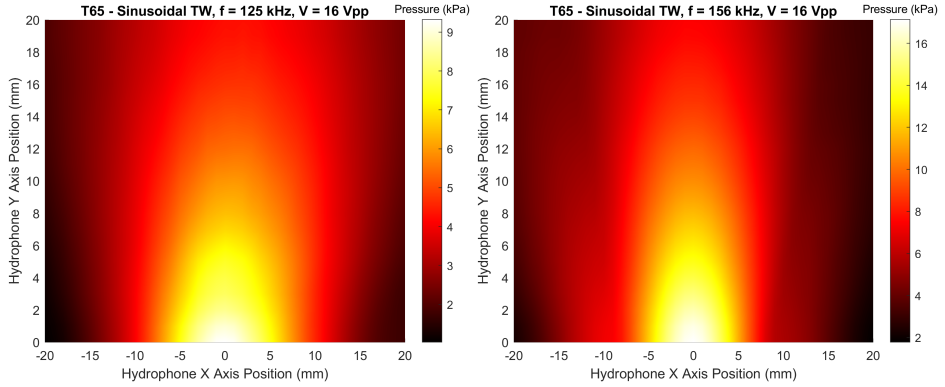

(c) Transducer 65, F = 125 kHz.

(d) Transducer 65, F = 156 kHz.

Figure D.11: Acoustic pressure maps of transducers 64 and 65 when transmitting a sinusoidal signal.

Appendix E

Pressure Profiles

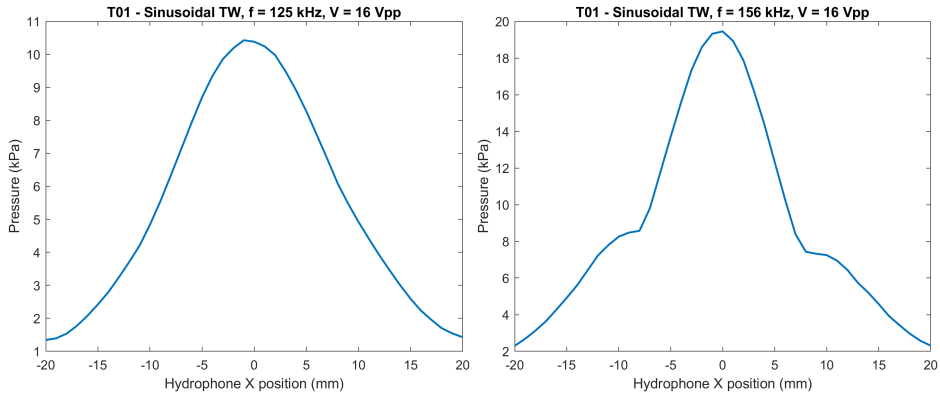

(a) Transducer 1, F = 125 kHz.

(b) Transducer 1, F = 156 kHz.

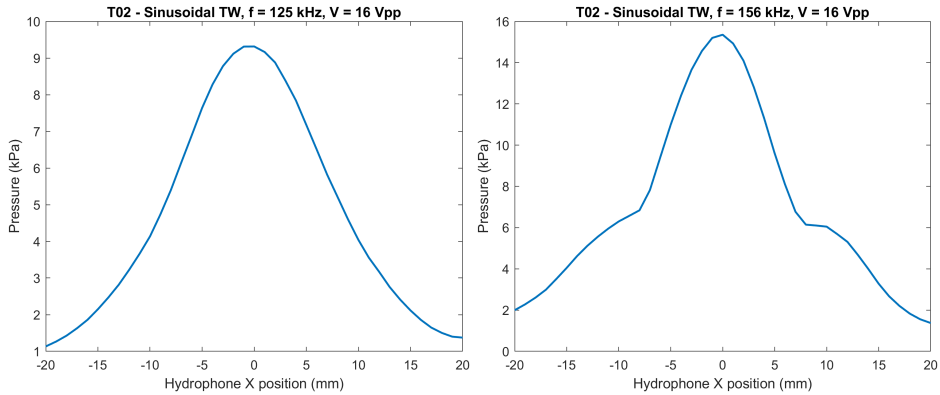

(c) Transducer 2, F = 125 kHz.

(d) Transducer 2, F = 156 kHz.

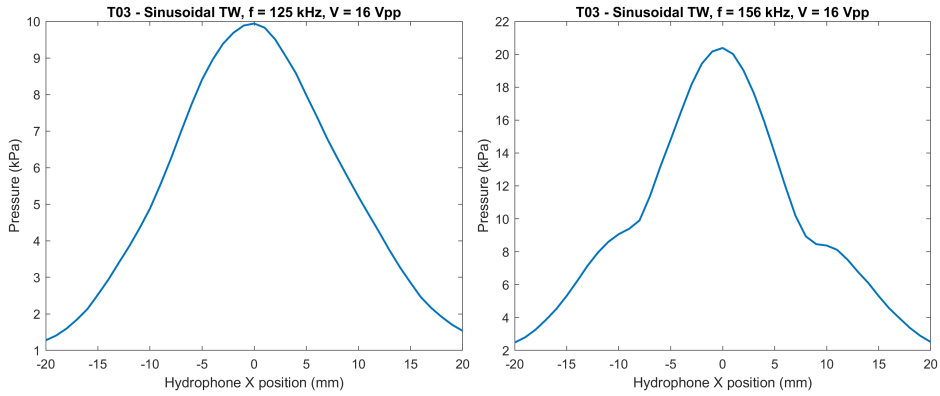

(e) Transducer 3, F = 125 kHz.

(f) Transducer 3, F = 156 kHz.

Figure E.1: Acoustic pressure profiles of transducers 1, 2, and 3 when transmitting a sinusoidal signal.

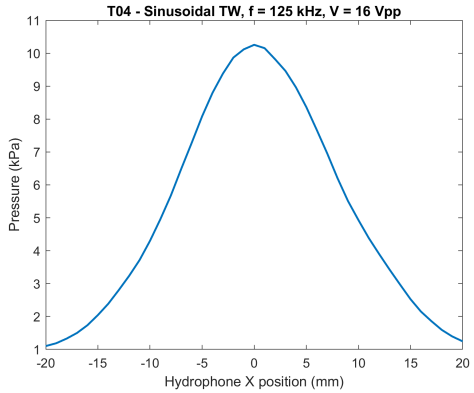

(a) Transducer 4, F = 125 kHz.

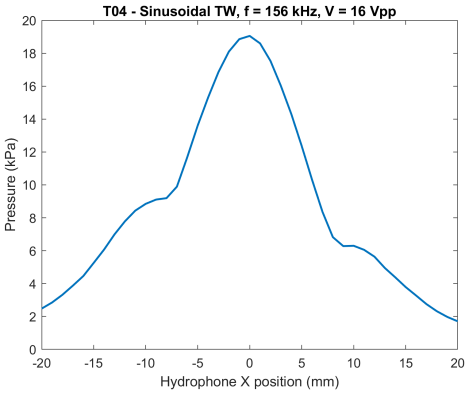

(b) Transducer 4, F = 156 kHz.

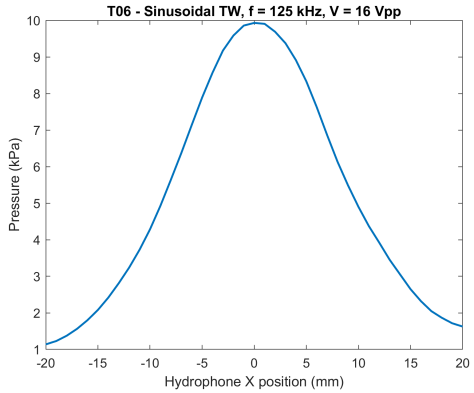

(c) Transducer 6, F = 125 kHz.

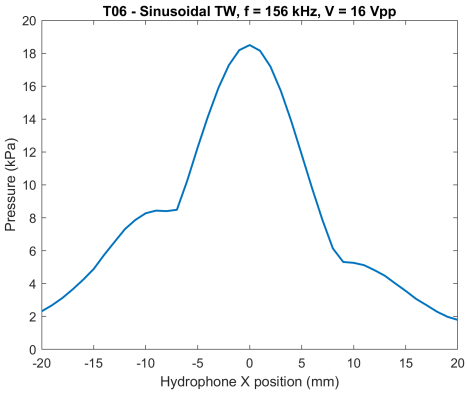

(d) Transducer 6, F = 156 kHz.

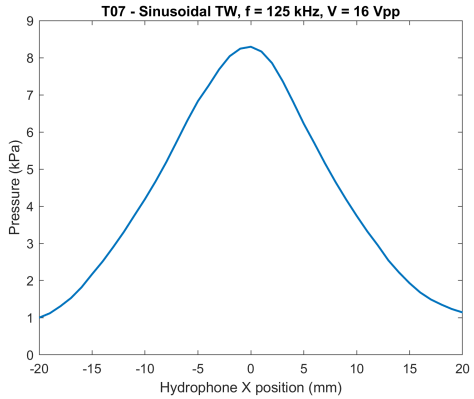

(e) Transducer 7, F = 125 kHz.

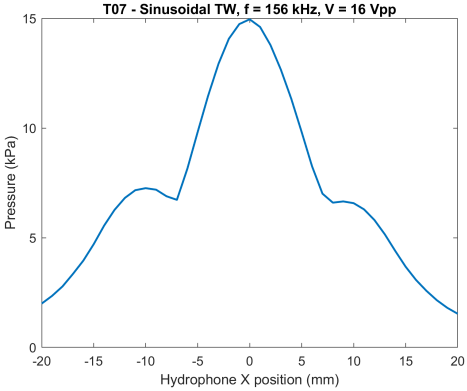

(f) Transducer 7, F = 156 kHz.

Figure E.2: Acoustic pressure profiles of transducers 4, 6, and 7 when transmitting a sinusoidal signal.

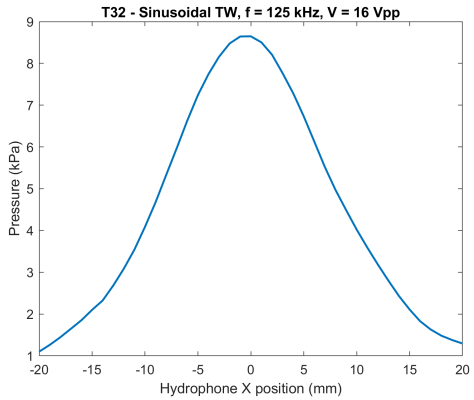

(a) Transcducer 32, F = 125 kHz.

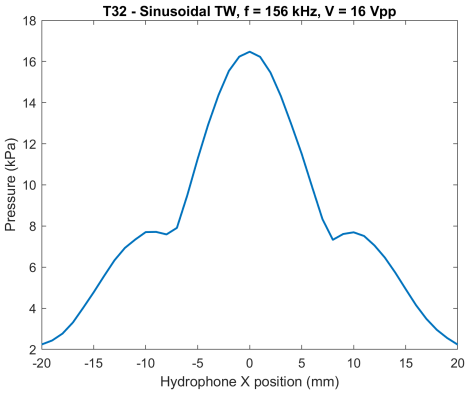

(b) Transcducer 32, F = 156 kHz.

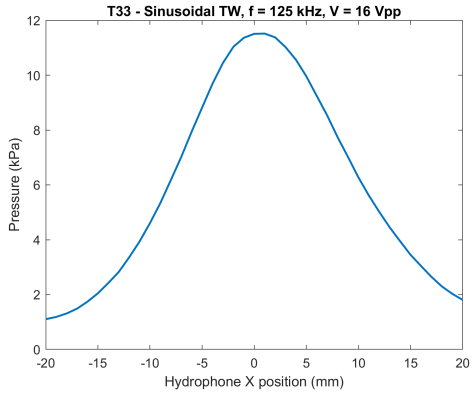

(c) Transcducer 33, F = 125 kHz.

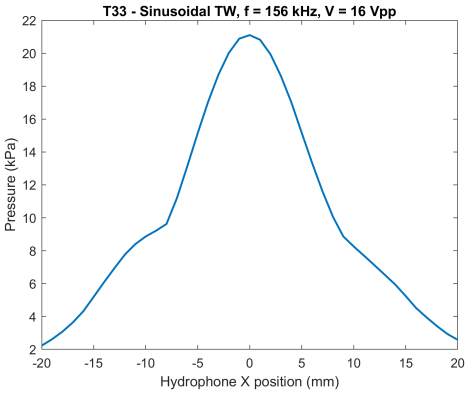

(d) Transcducer 33, F = 156 kHz.

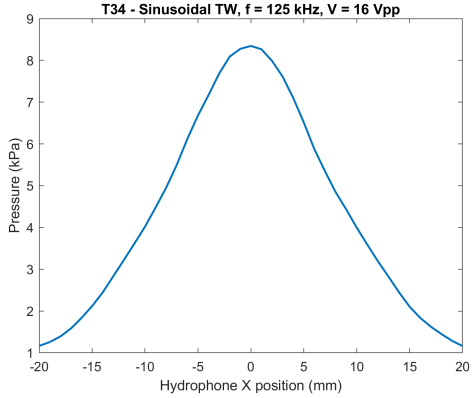

(e) Transcducer 34, F = 125 kHz.

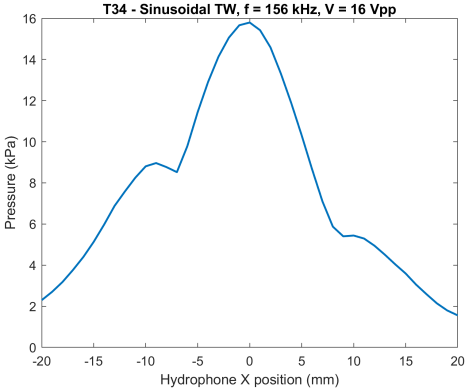

(f) Transcducer 34, F = 156 kHz.

Figure E.3: Acoustic pressure profiles of transducers 32, 33, and 34 when transmitting a sinusoidal signal.

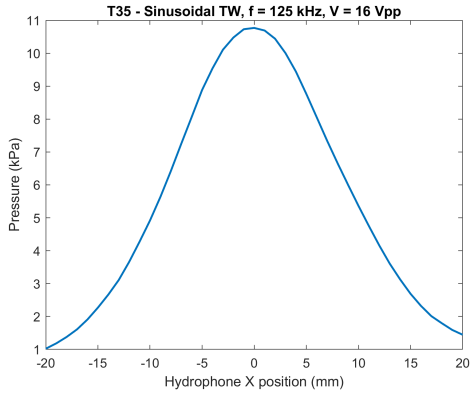

(a) Transducer 35, F = 125 kHz.

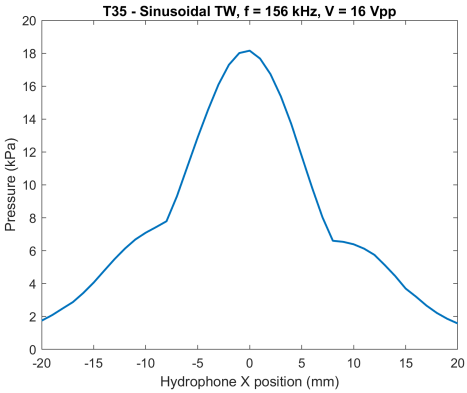

(b) Transducer 35, F = 156 kHz.

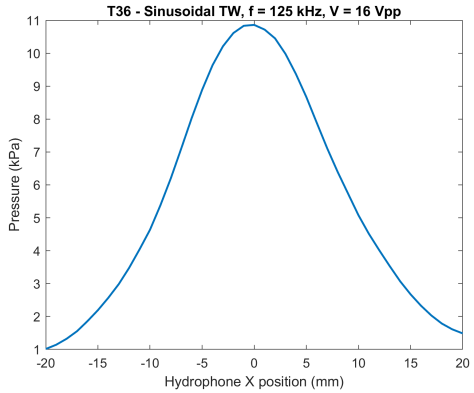

(c) Transducer 36, F = 125 kHz.

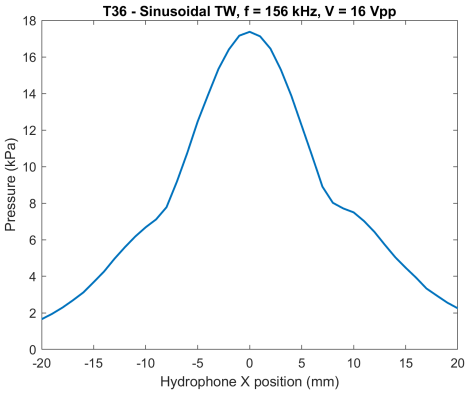

(d) Transducer 36, F = 156 kHz.

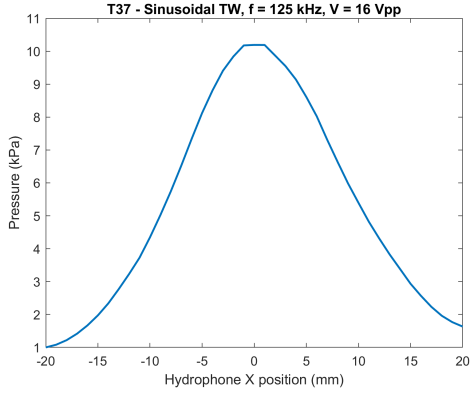

(e) Transducer 37, F = 125 kHz.

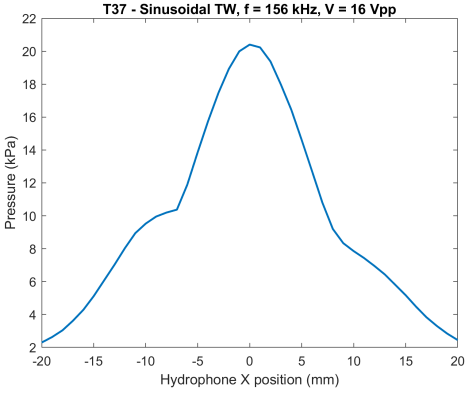

(f) Transducer 37, F = 156 kHz.

Figure E.4: Acoustic pressure profiles of transducers 35, 36, and 37 when transmitting a sinusoidal signal.

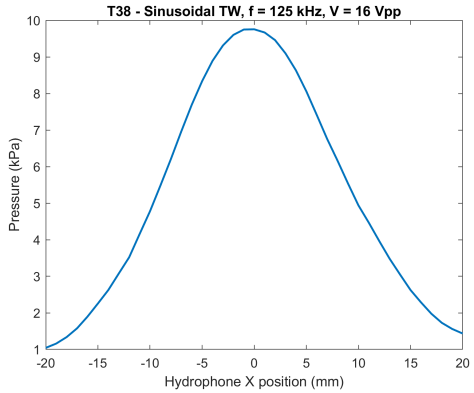

(a) Transducer 38, F = 125 kHz.

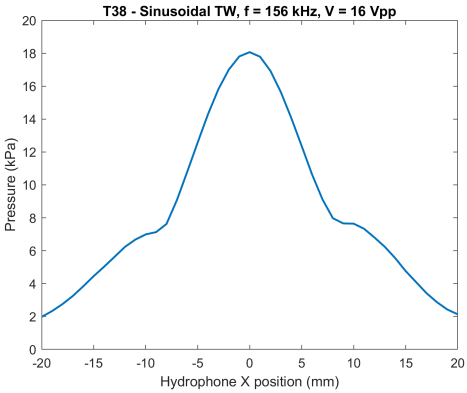

(b) Transducer 38, F = 156 kHz.

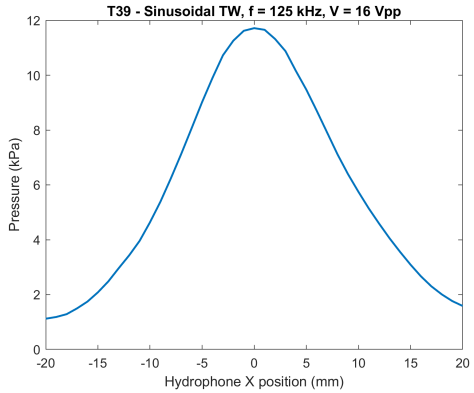

(c) Transducer 39, F = 125 kHz.

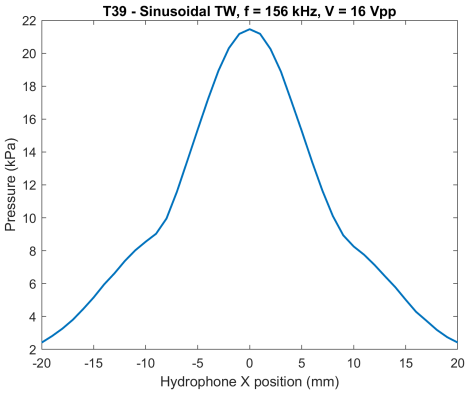

(d) Transducer 39, F = 156 kHz.

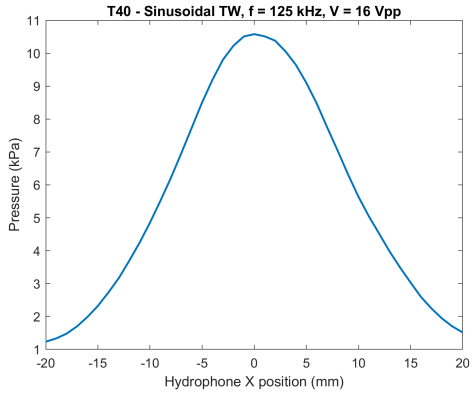

(e) Transducer 40, F = 125 kHz.

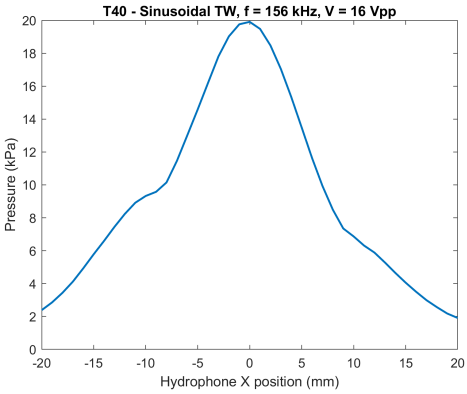

(f) Transducer 40, F = 156 kHz.

Figure E.5: Acoustic pressure profiles of transducers 38, 39, and 40 when transmitting a sinusoidal signal.

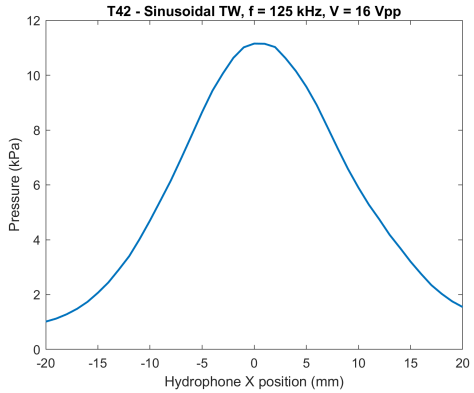

(a) Transducer 42, F = 125 kHz.

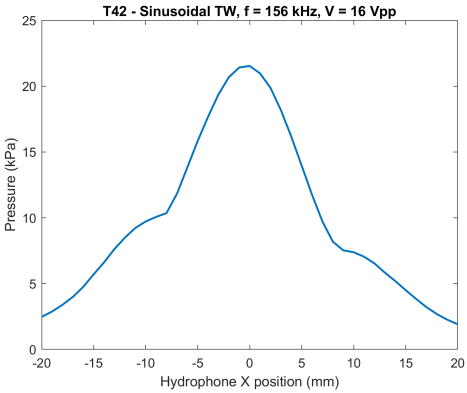

(b) Transducer 42, F = 156 kHz.

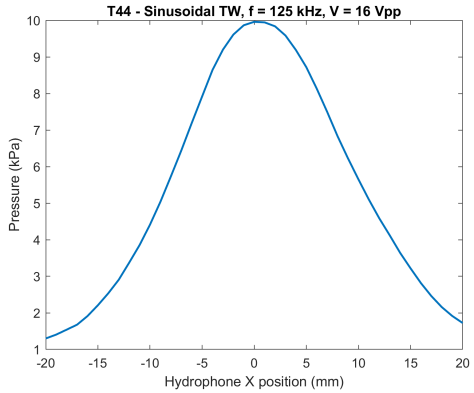

(c) Transducer 44, F = 125 kHz.

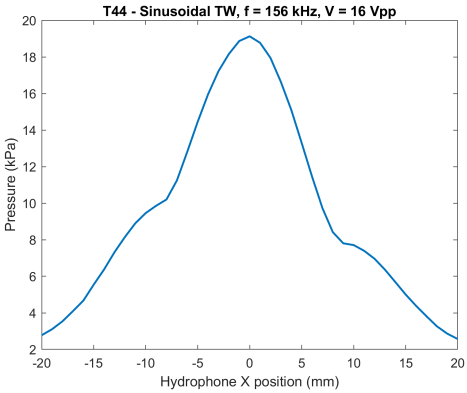

(d) Transducer 44, F = 156 kHz.

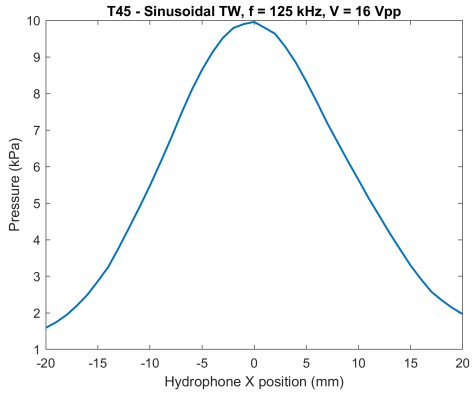

(e) Transducer 45, F = 125 kHz.

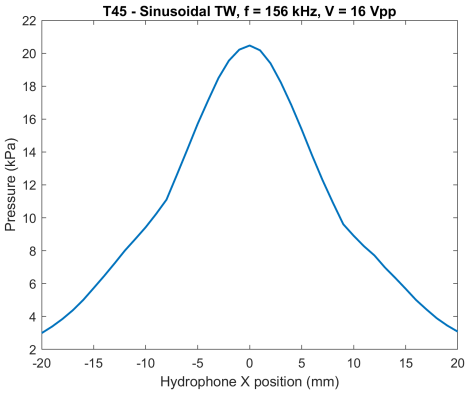

(f) Transducer 45, F = 156 kHz.

Figure E.6: Acoustic pressure profiles of transducers 42, 44, and 45 when transmitting a sinusoidal signal.

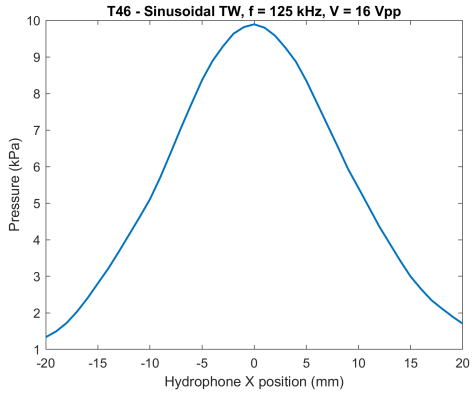

(a) Transducer 46, F = 125 kHz.

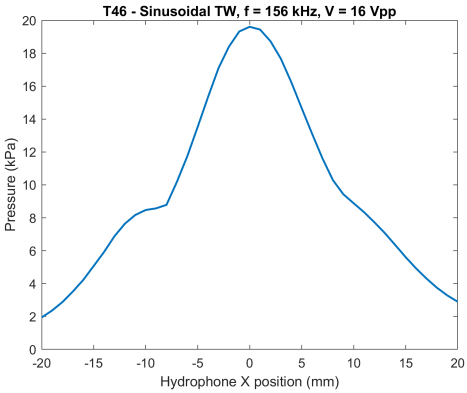

(b) Transducer 46, F = 156 kHz.

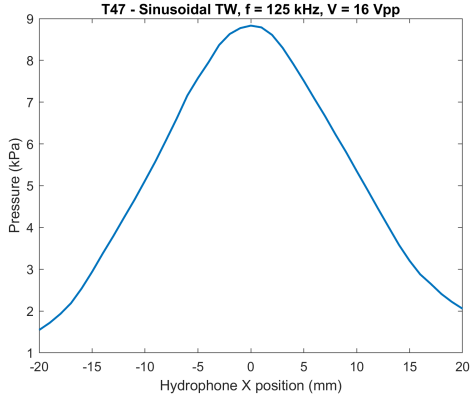

(c) Transducer 47, F = 125 kHz.

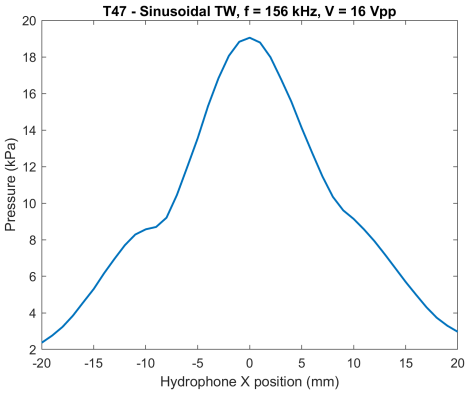

(d) Transducer 47, F = 156 kHz.

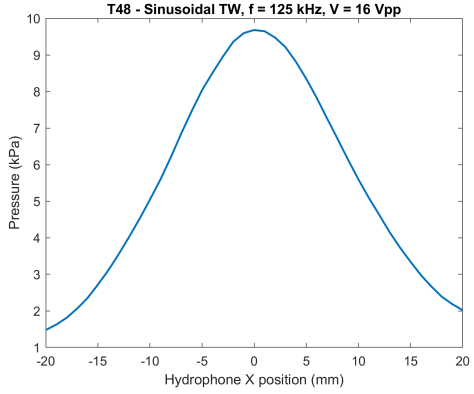

(e) Transducer 48, F = 125 kHz.

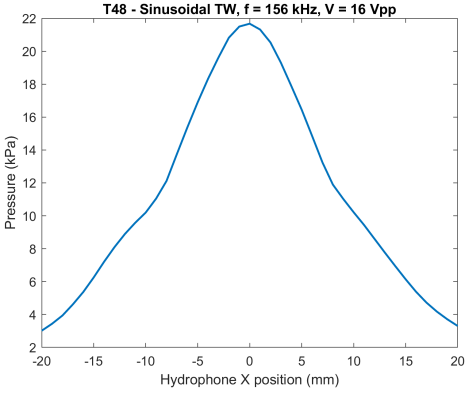

(f) Transducer 48, F = 156 kHz.

Figure E.7: Acoustic pressure profiles of transducers 46, 47, and 48 when transmitting a sinusoidal signal.

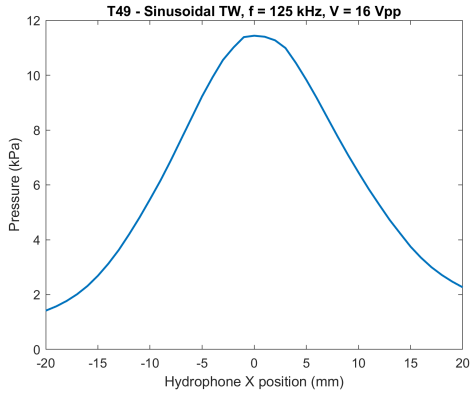

(a) Transcducer 49, F = 125 kHz.

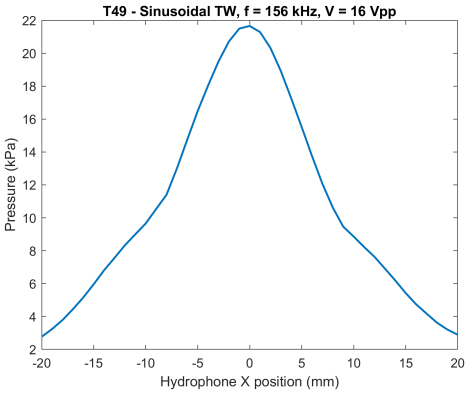

(b) Transcducer 49, F = 156 kHz.

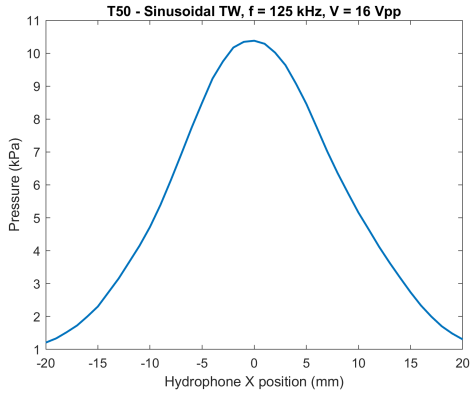

(c) Transcducer 50, F = 125 kHz.

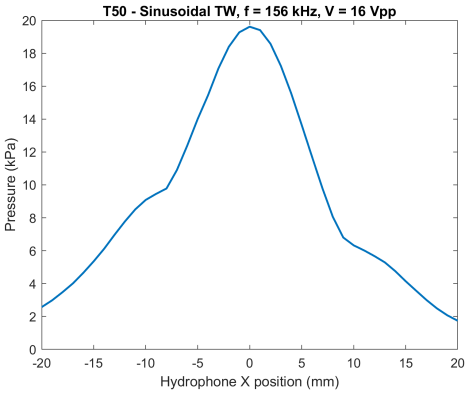

(d) Transcducer 50, F = 156 kHz.

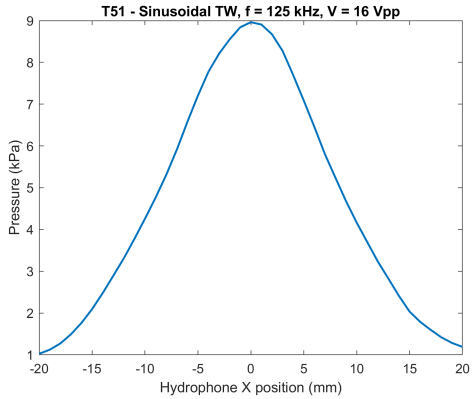

(e) Transcducer 51, F = 125 kHz.

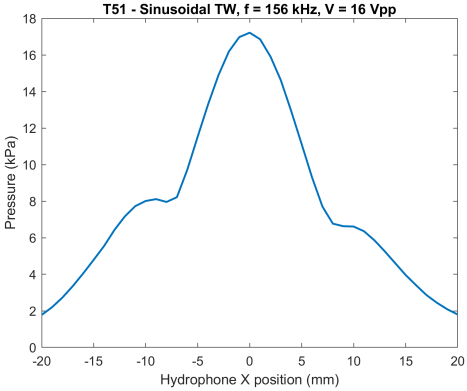

(f) Transcducer 51, F = 156 kHz.

Figure E.8: Acoustic pressure profiles of transducers 49, 50, and 51 when transmitting a sinusoidal signal.

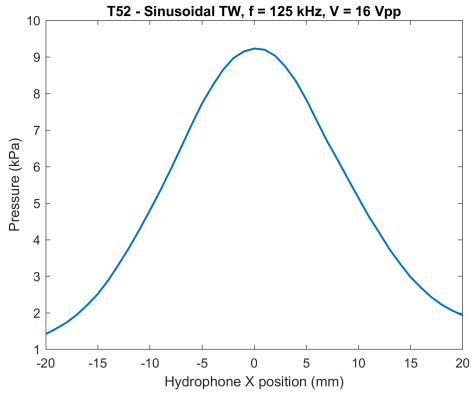

(a) Transducer 52, F = 125 kHz.

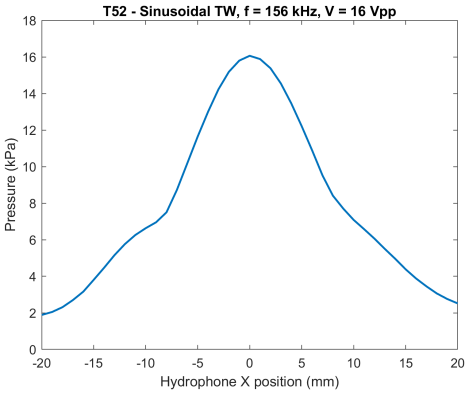

(b) Transducer 52, F = 156 kHz.

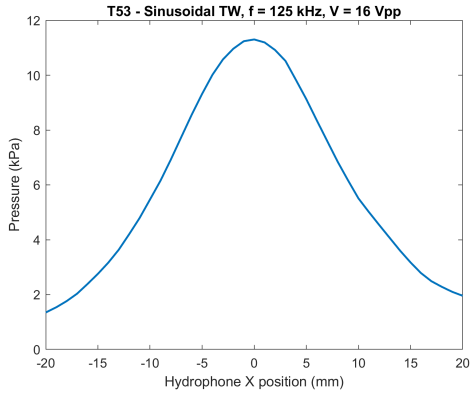

(c) Transducer 53, F = 125 kHz.

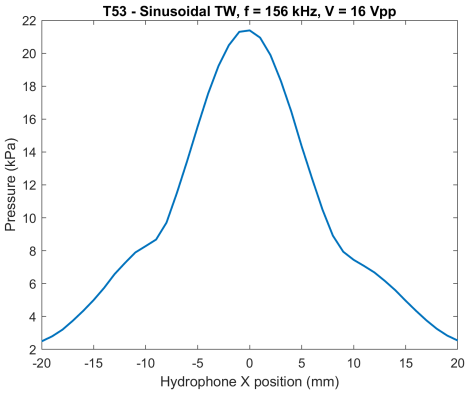

(d) Transducer 53, F = 156 kHz.

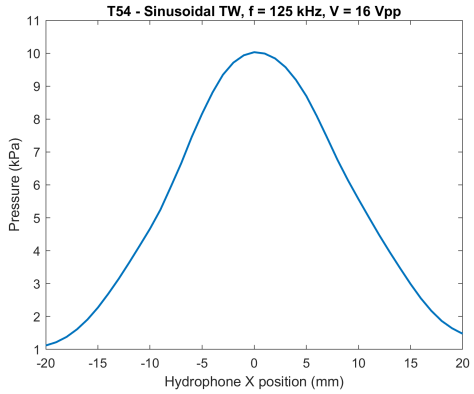

(e) Transducer 54, F = 125 kHz.

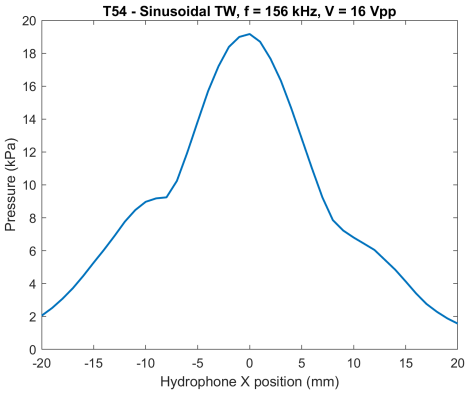

(f) Transducer 54, F = 156 kHz.

Figure E.9: Acoustic pressure profiles of transducers 52, 53, and 54 when transmitting a sinusoidal signal.

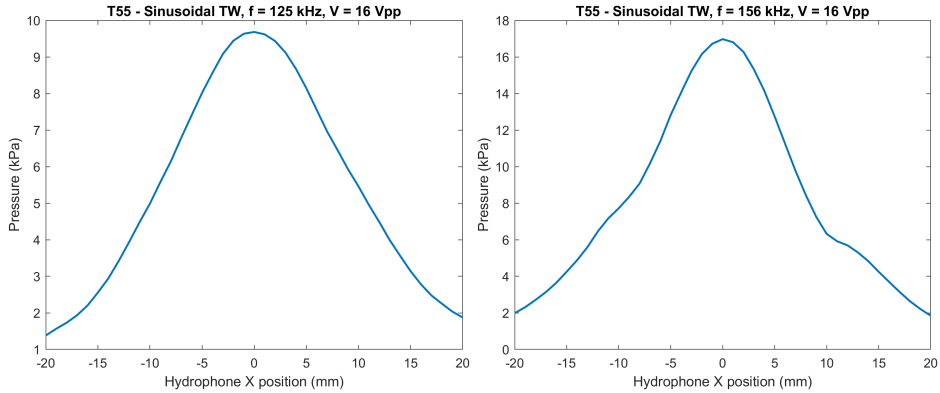

(a) Transducer 55, F = 125 kHz.

(b) Transducer 55, F = 156 kHz.

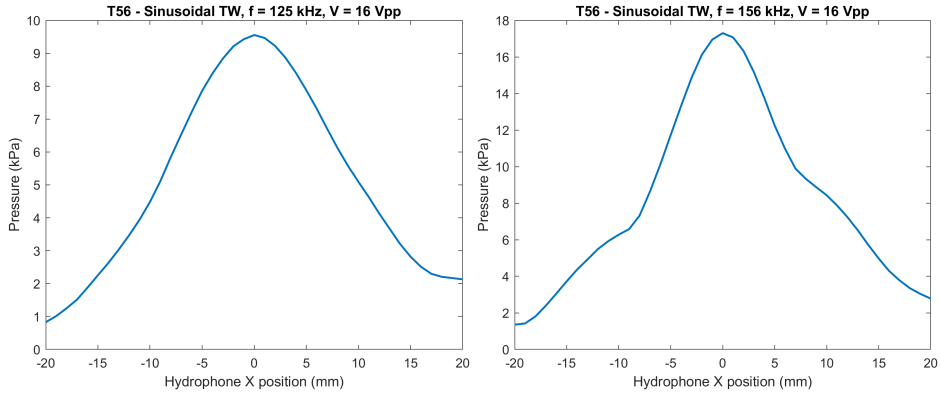

(c) Transducer 56, F = 125 kHz.

(d) Transducer 56, F = 156 kHz.

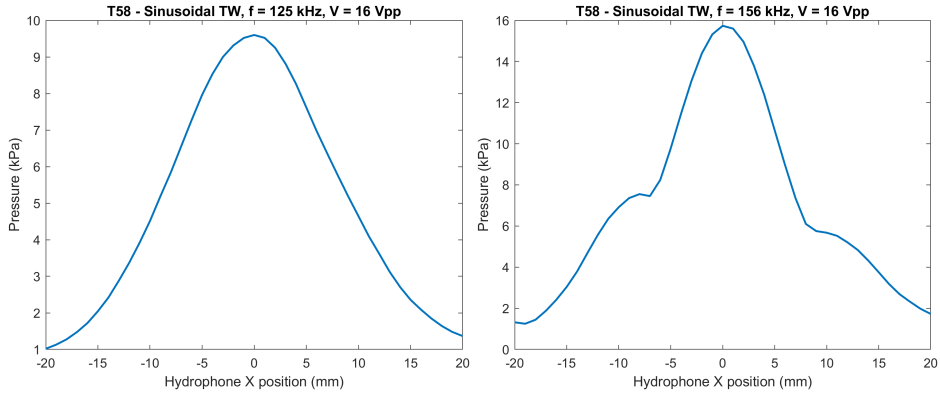

(e) Transducer 58, F = 125 kHz.

(f) Transducer 58, F = 156 kHz.

Figure E.10: Acoustic pressure profiles of transducers 55, 56, and 58 when transmitting a sinusoidal signal.

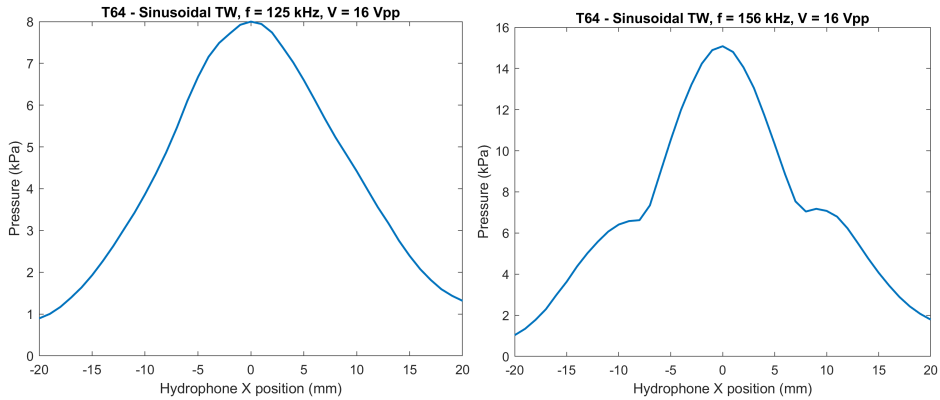

(a) Transducer 64, F = 125 kHz.

(b) Transducer 64, F = 156 kHz.

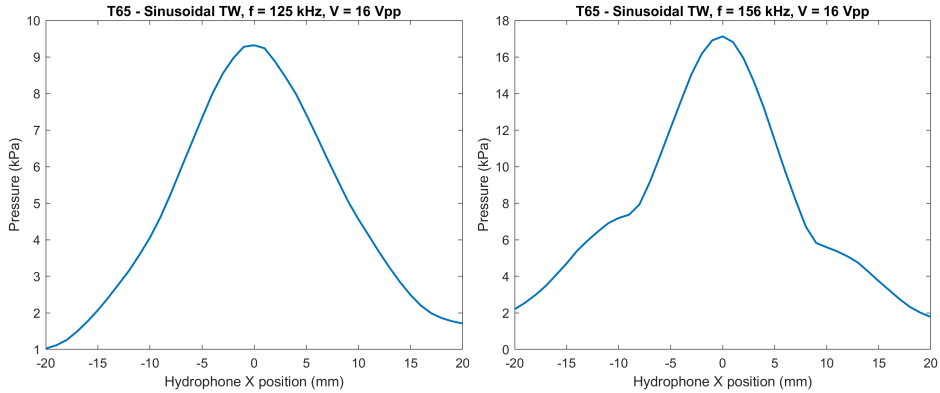

(c) Transducer 65, F = 125 kHz.

(d) Transducer 65, F = 156 kHz.

Figure E.11: Acoustic pressure profiles of transducers 64 and 65 when transmitting a sinusoidal signal.

Appendix F

Voltage Maps

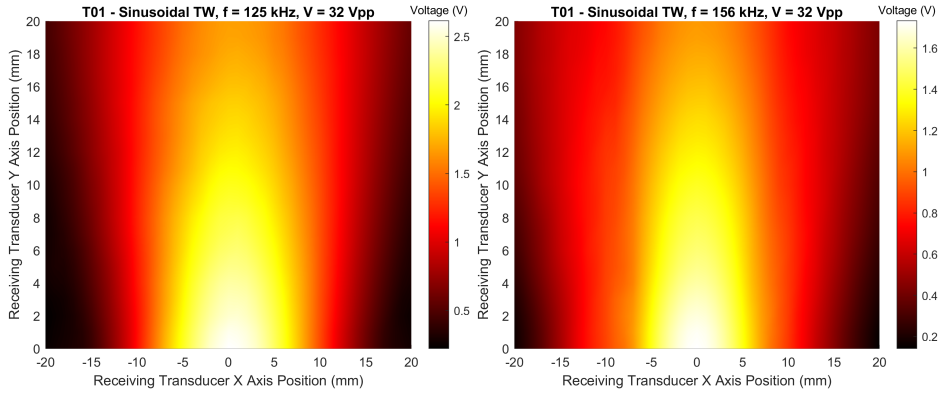

(a) Transducer 1, F = 125 kHz.

(b) Transducer 1, F = 156 kHz.

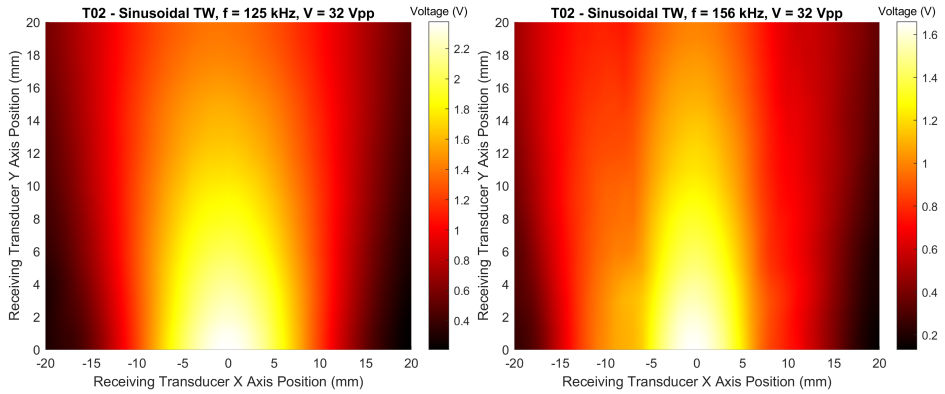

(c) Transducer 2, F = 125 kHz.

(d) Transducer 2, F = 156 kHz.

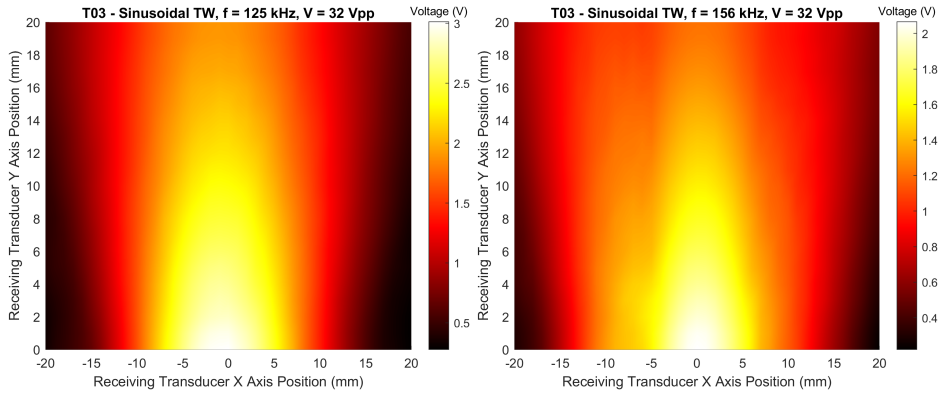

(e) Transducer 3, F = 125 kHz.

(f) Transducer 3, F = 156 kHz.

Figure F.1: Received voltage maps of transducers 1, 2, and 3 when transmitting a sinusoidal signal.

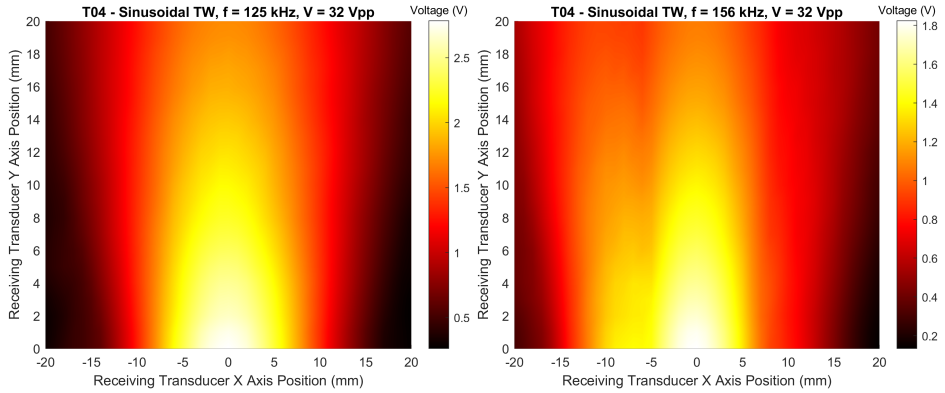

(a) Transducer 4, F = 125 kHz.

(b) Transducer 4, F = 156 kHz.

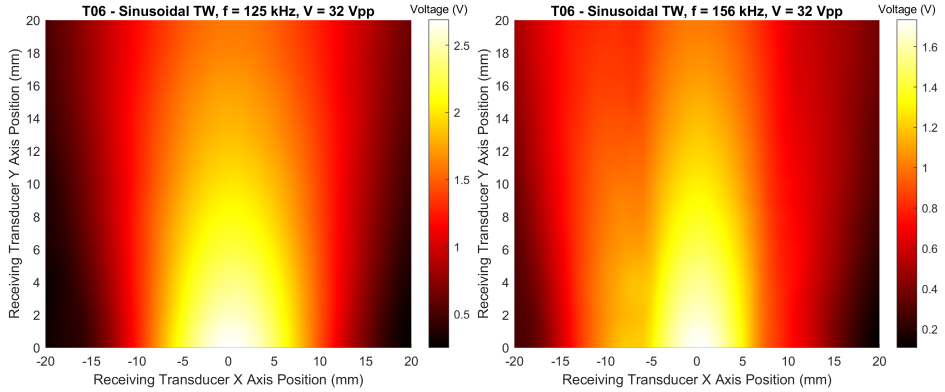

(c) Transducer 6, F = 125 kHz.

(d) Transducer 6, F = 156 kHz.

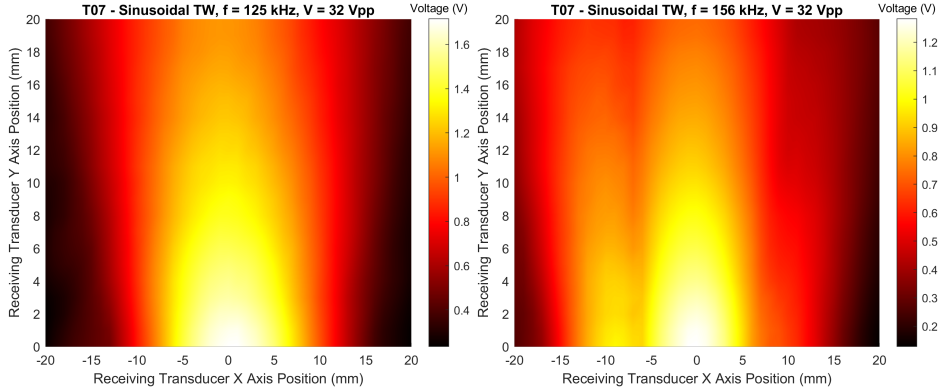

(e) Transducer 7, F = 125 kHz.

(f) Transducer 7, F = 156 kHz.

Figure F.2: Received voltage maps of transducers 4, 6, and 7 when transmitting a sinusoidal signal.

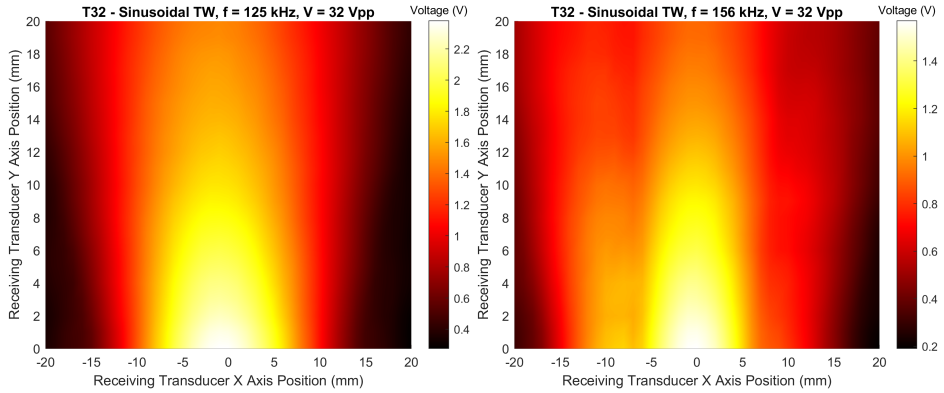

(a) Transducer 32, F = 125 kHz.

(b) Transducer 32, F = 156 kHz.

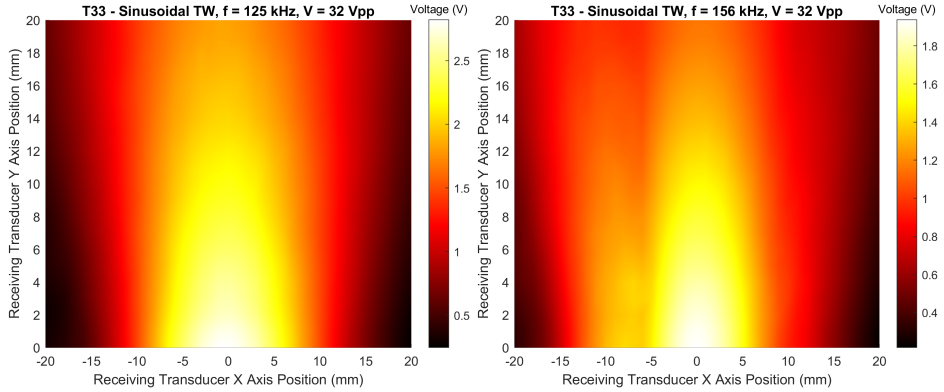

(c) Transducer 33, F = 125 kHz.

(d) Transducer 33, F = 156 kHz.

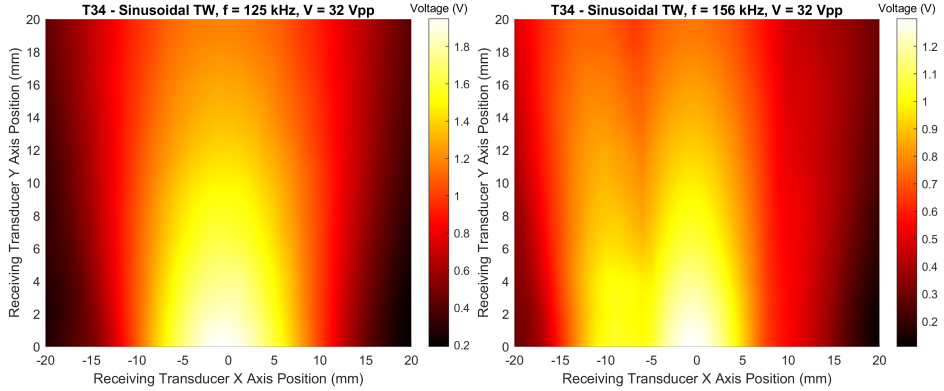

(e) Transducer 34, F = 125 kHz.

(f) Transducer 34, F = 156 kHz.

Figure F.3: Received voltage maps of transducers 32, 33, and 34 when transmitting a sinusoidal signal.

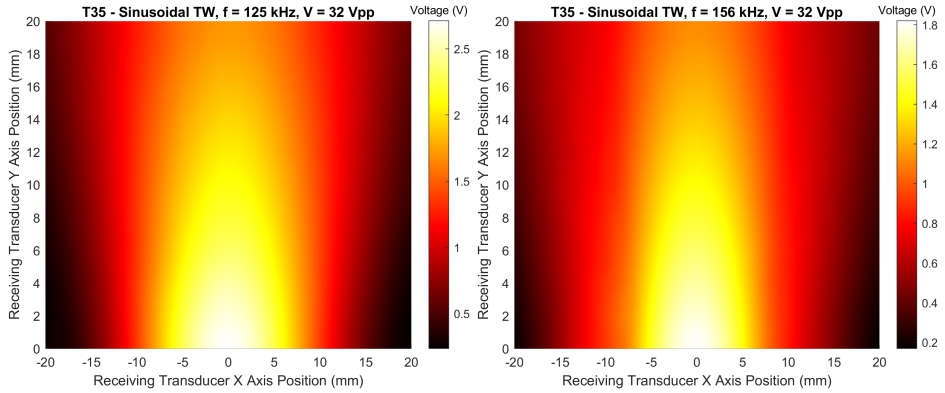

(a) Transducer 35, F = 125 kHz.

(b) Transducer 35, F = 156 kHz.

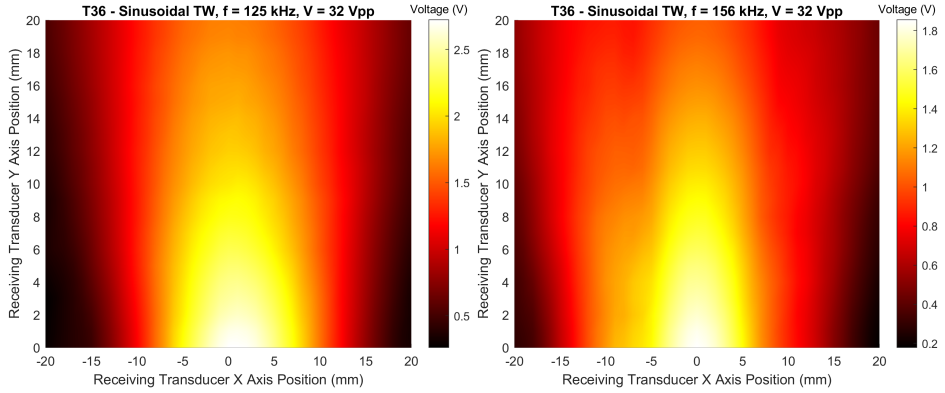

(c) Transducer 36, F = 125 kHz.

(d) Transducer 36, F = 156 kHz.

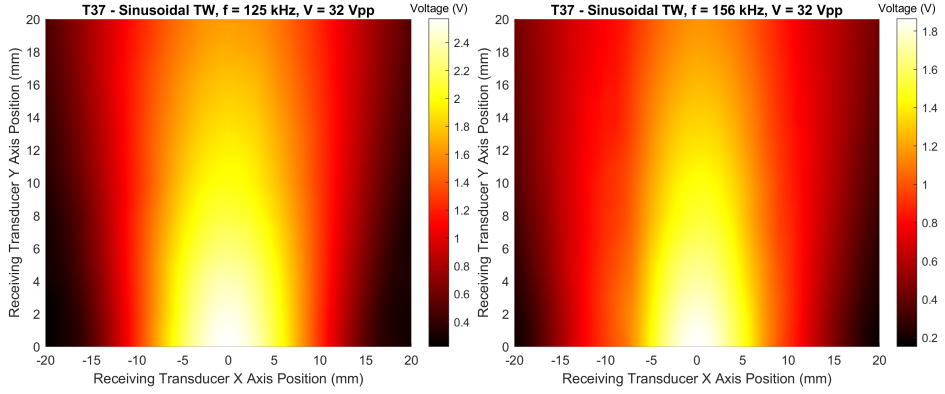

(e) Transducer 37, F = 125 kHz.

(f) Transducer 37, F = 156 kHz.

Figure F.4: Received voltage maps of transducers 35, 36, and 37 when transmitting a sinusoidal signal.

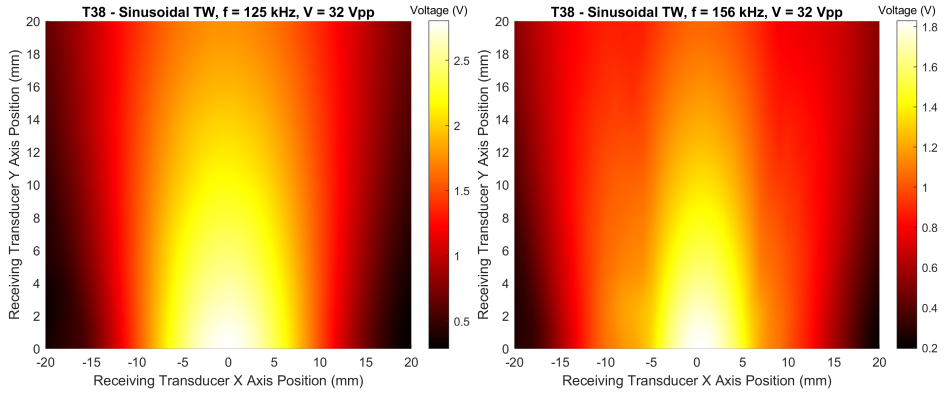

(a) Transducer 38, F = 125 kHz.

(b) Transducer 38, F = 156 kHz.

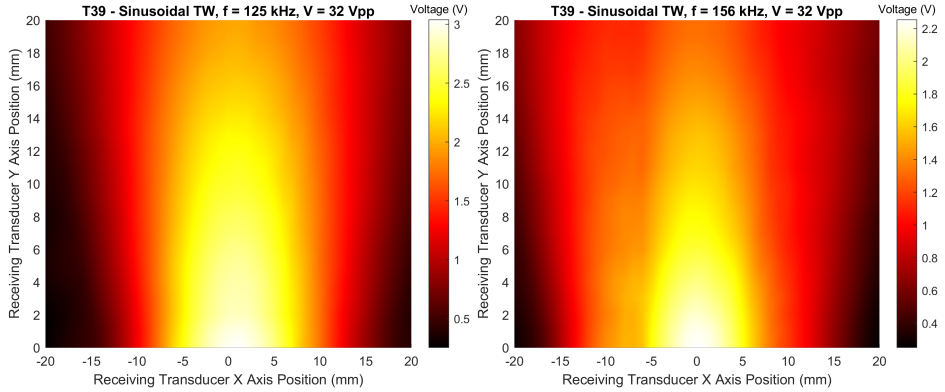

(c) Transducer 39, F = 125 kHz.

(d) Transducer 39, F = 156 kHz.

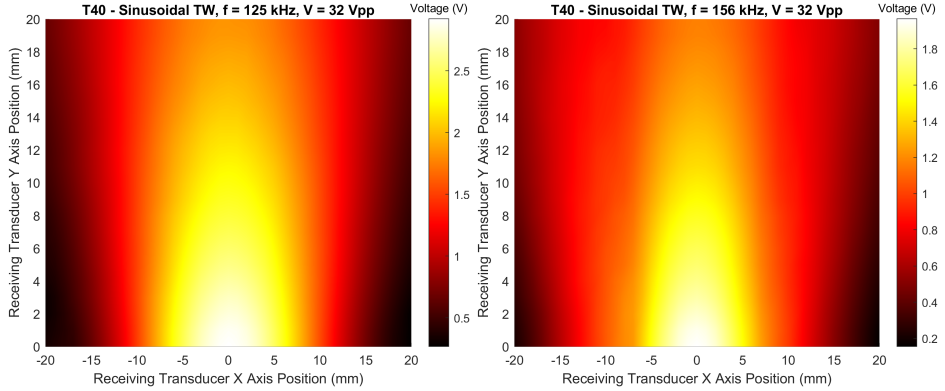

(e) Transducer 40, F = 125 kHz.

(f) Transducer 40, F = 156 kHz.

Figure F.5: Received voltage maps of transducers 38, 39, and 40 when transmitting a sinusoidal signal.

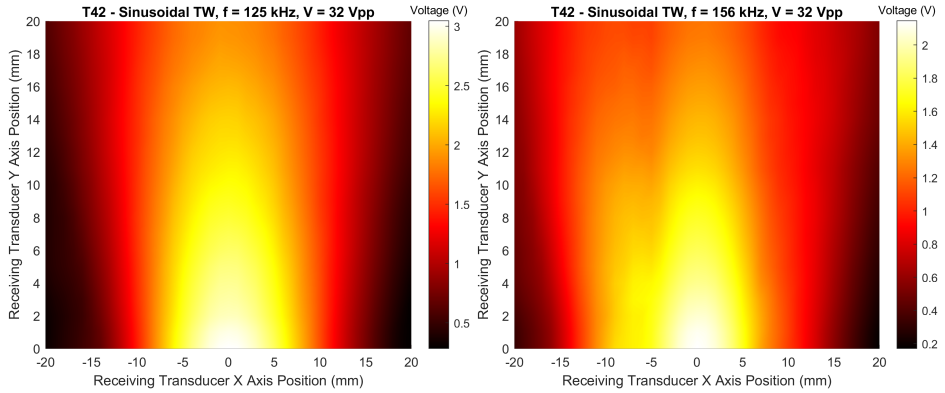

(a) Transducer 42, F = 125 kHz.

(b) Transducer 42, F = 156 kHz.

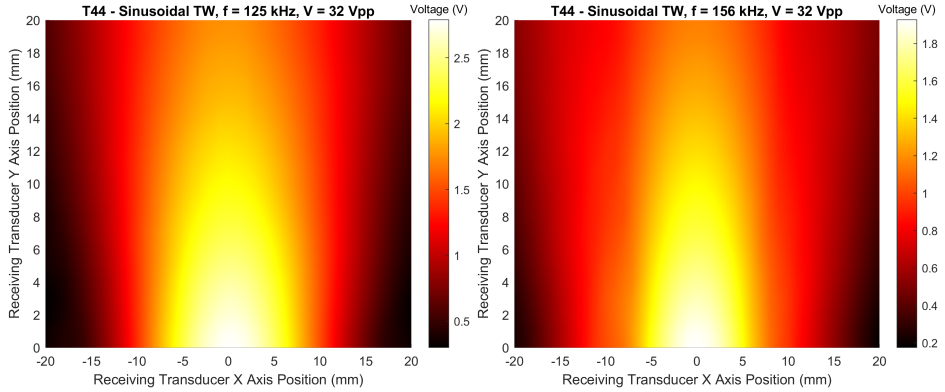

(c) Transducer 44, F = 125 kHz.

(d) Transducer 44, F = 156 kHz.

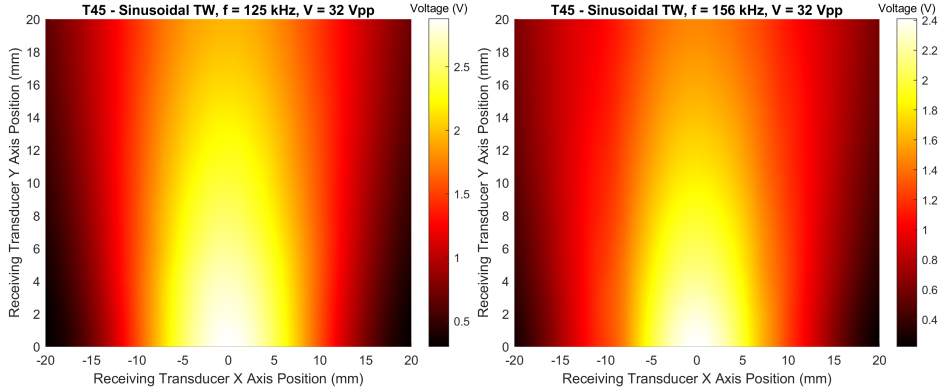

(e) Transducer 45, F = 125 kHz.

(f) Transducer 45, F = 156 kHz.

Figure F.6: Received voltage maps of transducers 42, 44, and 45 when transmitting a sinusoidal signal.

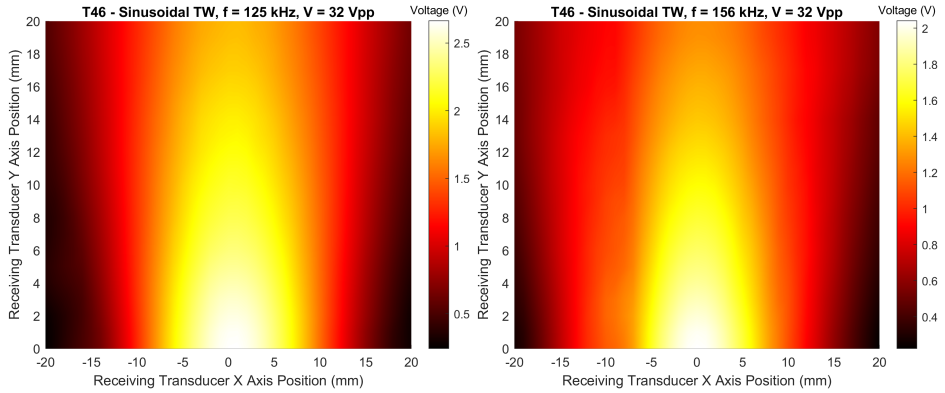

(a) Transducer 46, F = 125 kHz.

(b) Transducer 46, F = 156 kHz.

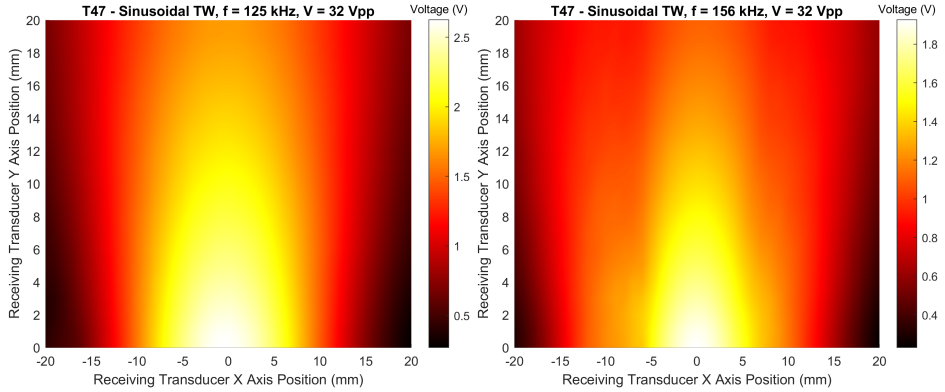

(c) Transducer 47, F = 125 kHz.

(d) Transducer 47, F = 156 kHz.

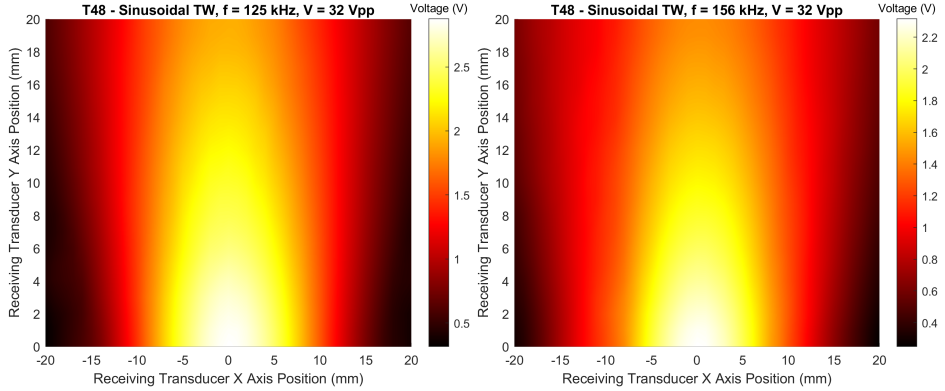

(e) Transducer 48, F = 125 kHz.

(f) Transducer 48, F = 156 kHz.

Figure F.7: Received voltage maps of transducers 46, 47, and 48 when transmitting a sinusoidal signal.

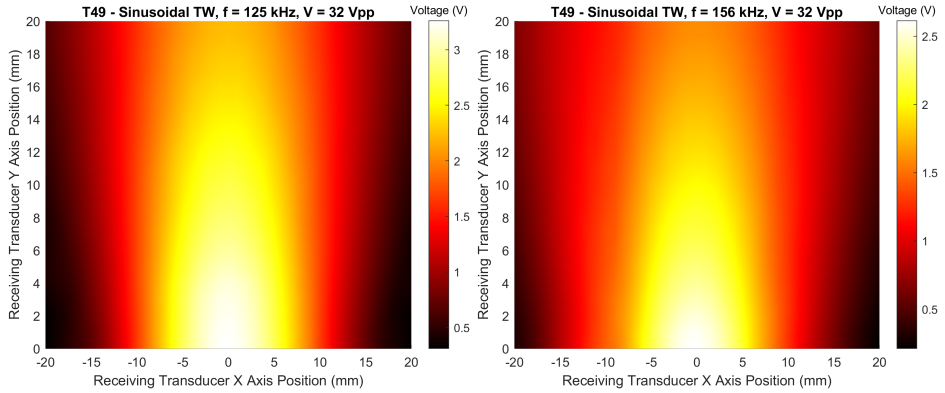

(a) Transducer 49, F = 125 kHz.

(b) Transducer 49, F = 156 kHz.

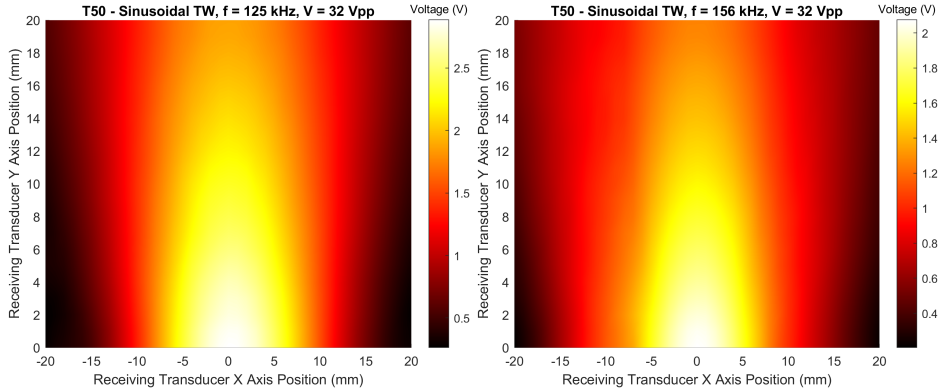

(c) Transducer 50, F = 125 kHz.

(d) Transducer 50, F = 156 kHz.

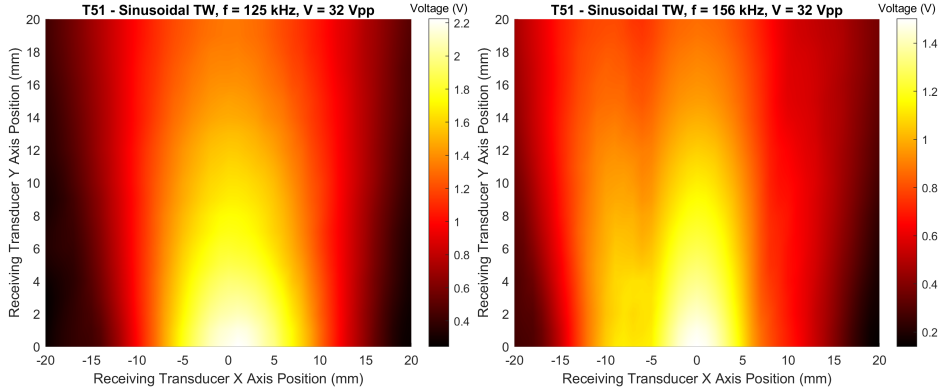

(e) Transducer 51, F = 125 kHz.

(f) Transducer 51, F = 156 kHz.

Figure F.8: Received voltage maps of transducers 49, 50, and 51 when transmitting a sinusoidal signal.

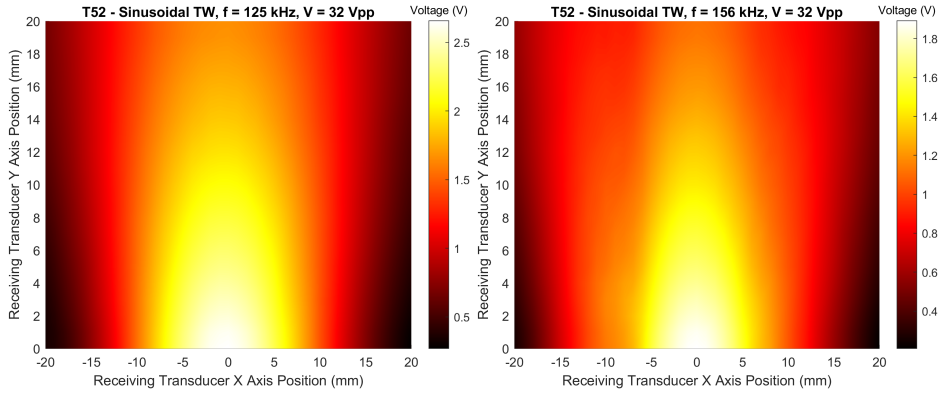

(a) Transducer 52, F = 125 kHz.

(b) Transducer 52, F = 156 kHz.

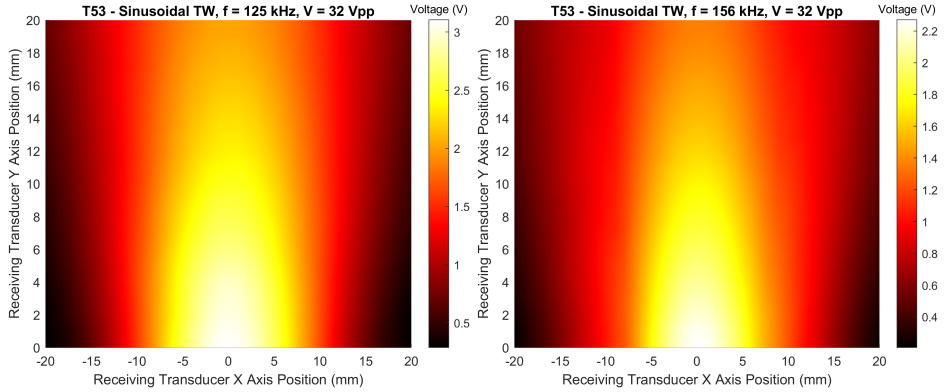

(c) Transducer 53, F = 125 kHz.

(d) Transducer 53, F = 156 kHz.

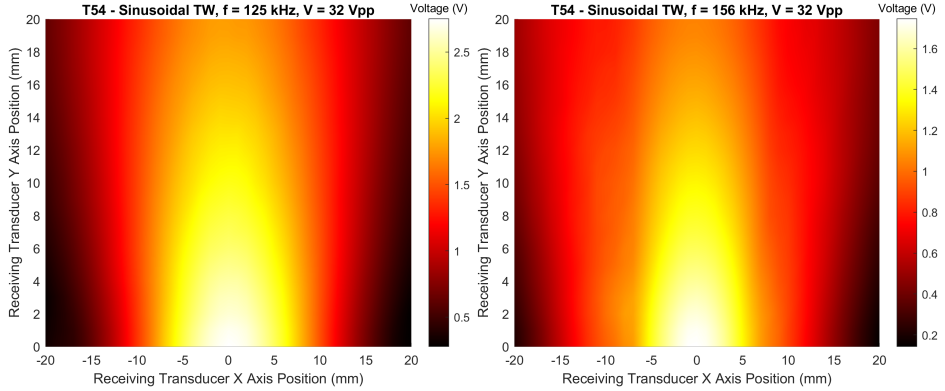

(e) Transducer 54, F = 125 kHz.

(f) Transducer 54, F = 156 kHz.

Figure F.9: Received voltage maps of transducers 52, 53, and 54 when transmitting a sinusoidal signal.

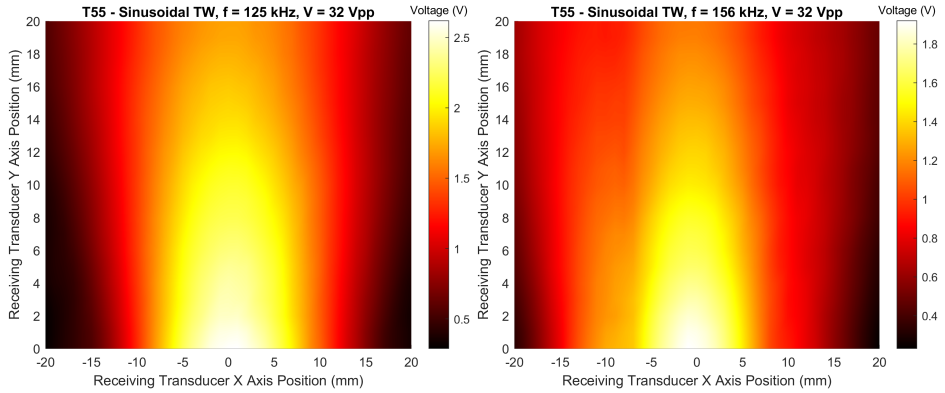

(a) Transducer 55, F = 125 kHz.

(b) Transducer 55, F = 156 kHz.

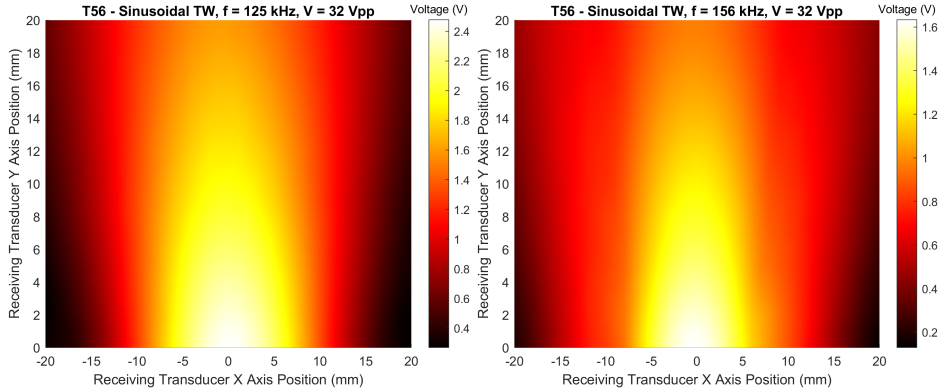

(c) Transducer 56, F = 125 kHz.

(d) Transducer 56, F = 156 kHz.

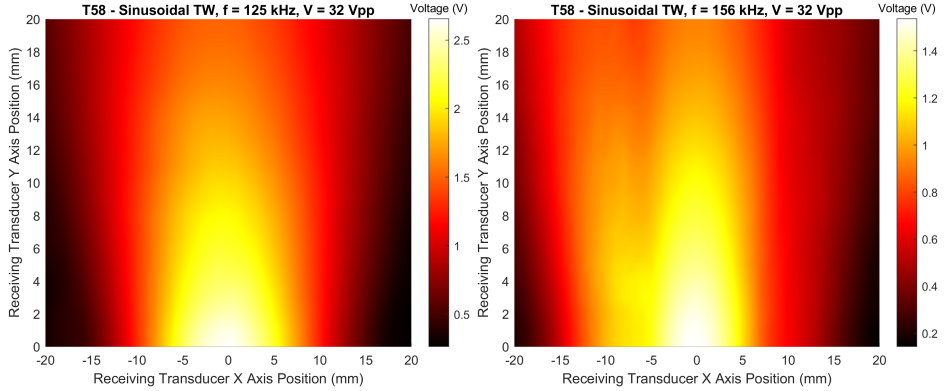

(e) Transducer 58, F = 125 kHz.

(f) Transducer 58, F = 156 kHz.

Figure F.10: Received voltage maps of transducers 55, 56, and 58 when transmitting a sinusoidal signal.

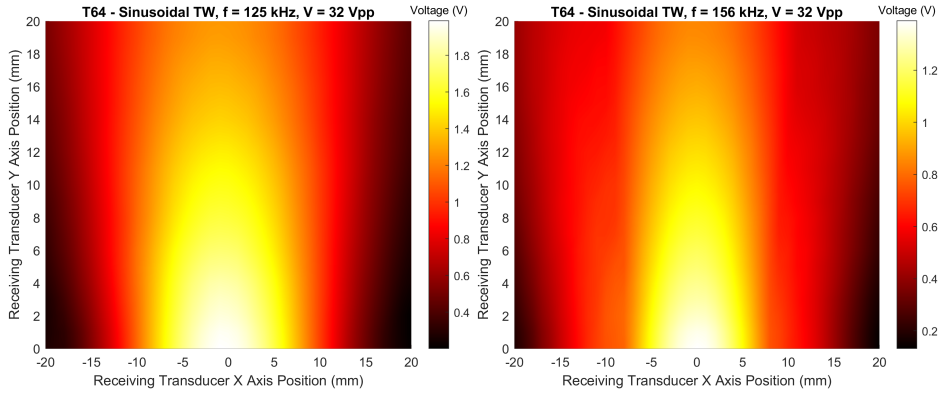

(a) Transducer 64, F = 125 kHz. **(b)** Transducer 64, F = 156 kHz.

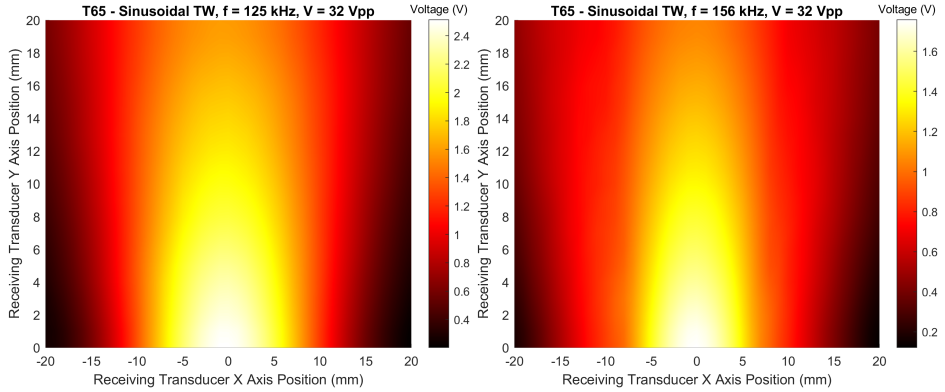

(c) Transducer 65, F = 125 kHz. **(d)** Transducer 65, F = 156 kHz.

Figure F.11: Received voltage maps of transducers 64 and 65 when transmitting a sinusoidal signal.

Appendix G

Voltage Profiles

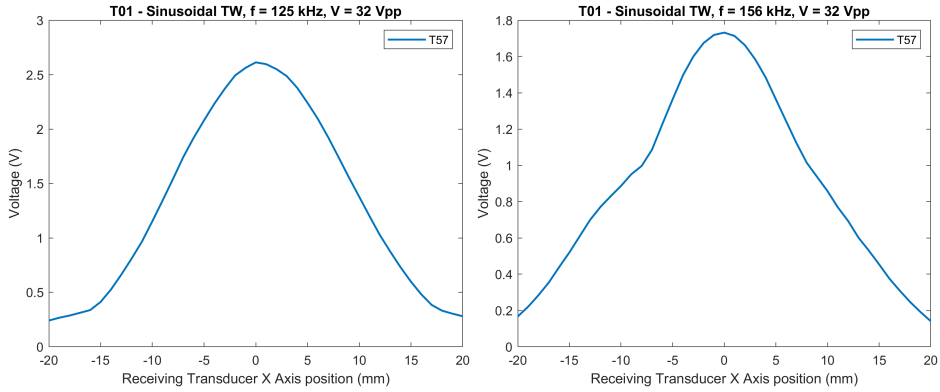

(a) Transducer 1, F = 125 kHz.

(b) Transducer 1, F = 156 kHz.

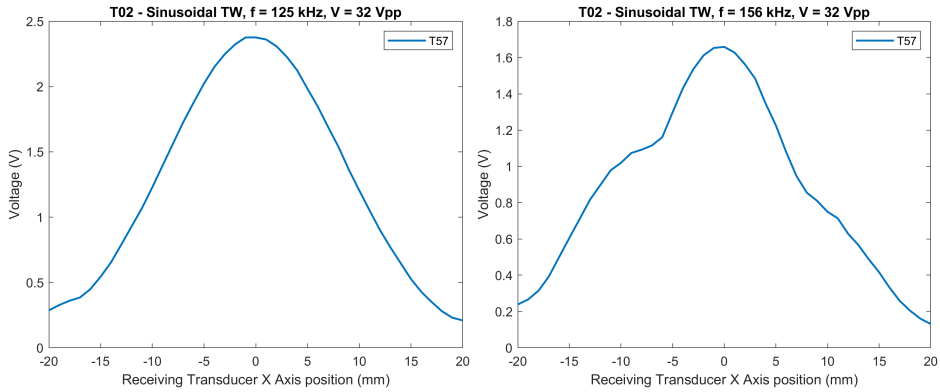

(c) Transducer 2, F = 125 kHz.

(d) Transducer 2, F = 156 kHz.

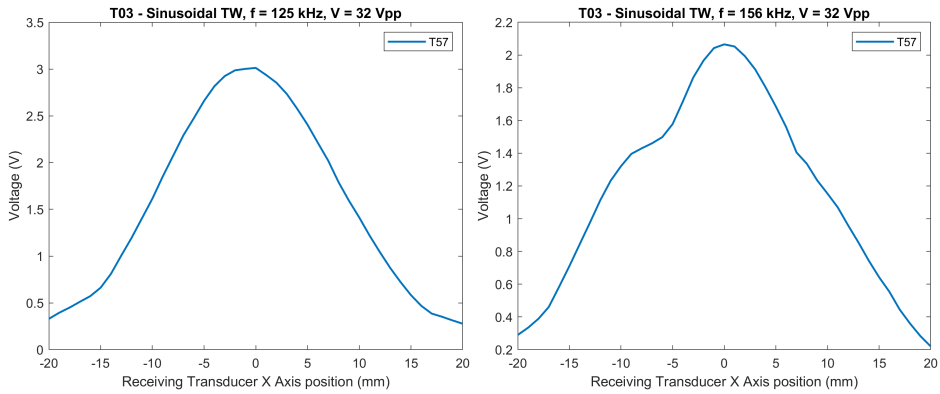

(e) Transducer 3, F = 125 kHz.

(f) Transducer 3, F = 156 kHz.

Figure G.1: Received voltage profiles of transducers 1, 2, and 3 when transmitting a sinusoidal signal.

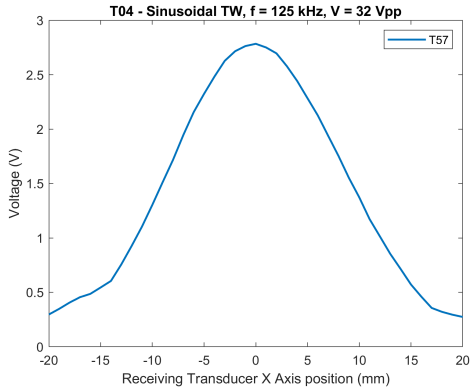

(a) Transducer 4, F = 125 kHz.

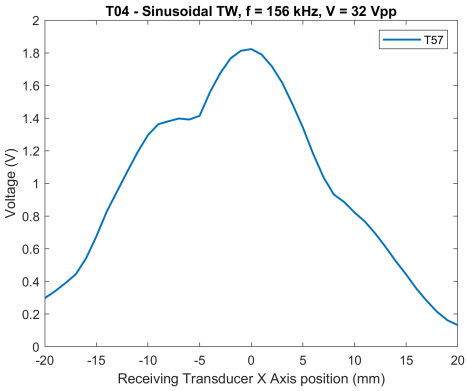

(b) Transducer 4, F = 156 kHz.

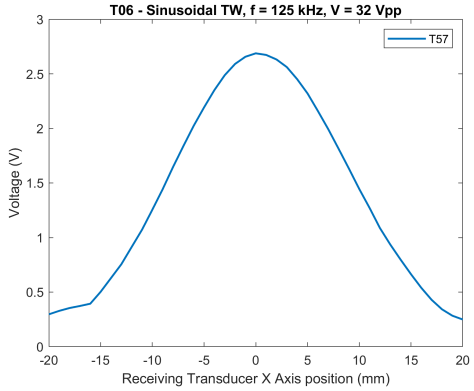

(c) Transducer 6, F = 125 kHz.

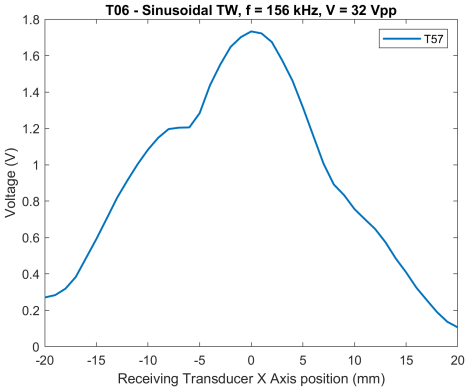

(d) Transducer 6, F = 156 kHz.

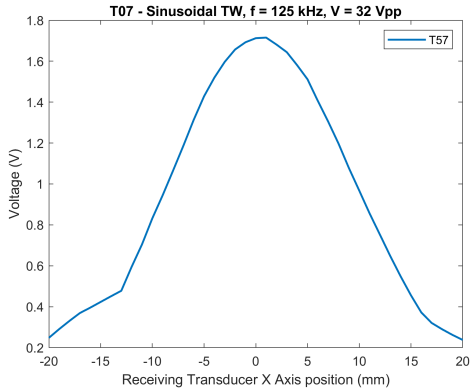

(e) Transducer 7, F = 125 kHz.

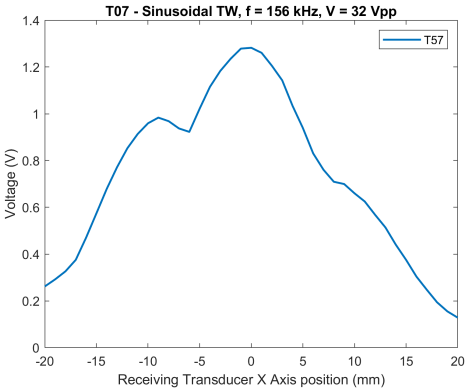

(f) Transducer 7, F = 156 kHz.

Figure G.2: Received voltage profiles of transducers 4, 6, and 7 when transmitting a sinusoidal signal.

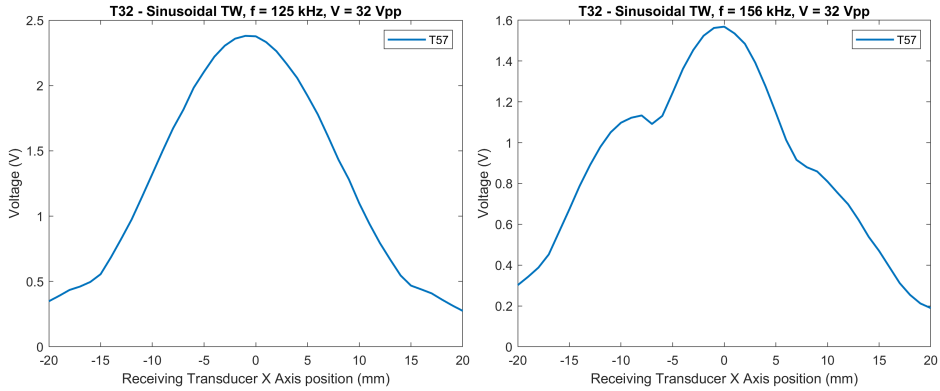

(a) Transducer 32, F = 125 kHz.

(b) Transducer 32, F = 156 kHz.

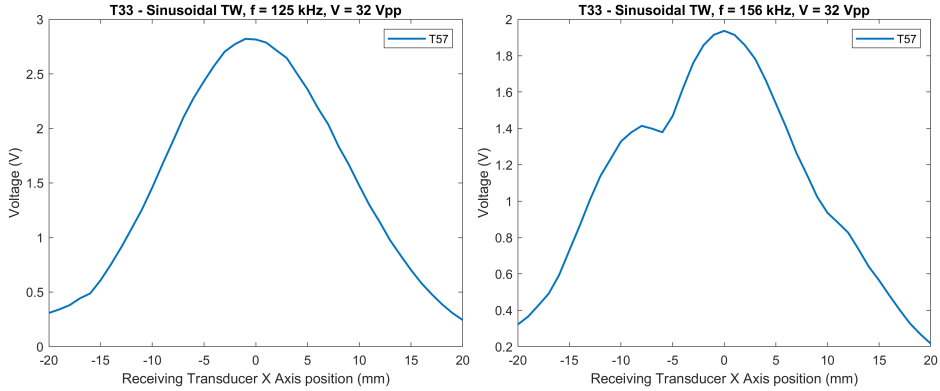

(c) Transducer 33, F = 125 kHz.

(d) Transducer 33, F = 156 kHz.

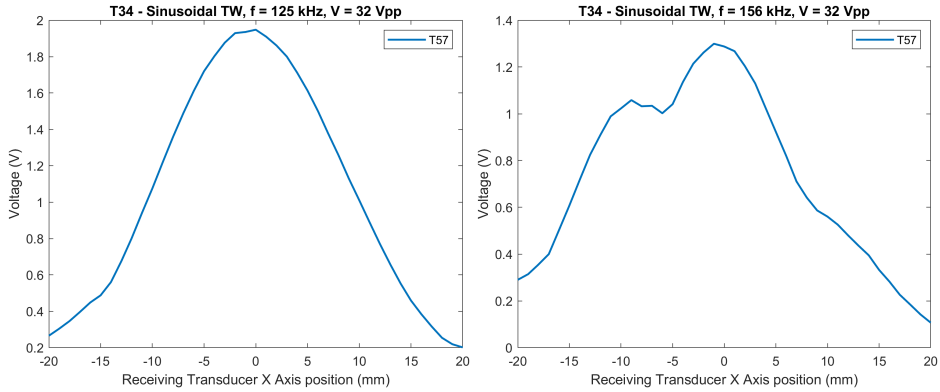

(e) Transducer 34, F = 125 kHz.

(f) Transducer 34, F = 156 kHz.

Figure G.3: Received voltage profiles of transducers 32, 33, and 34 when transmitting a sinusoidal signal.

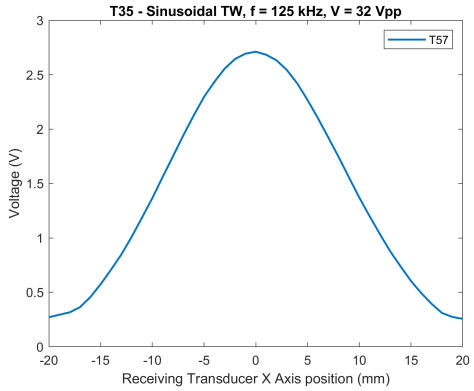

(a) Transducer 35, F = 125 kHz.

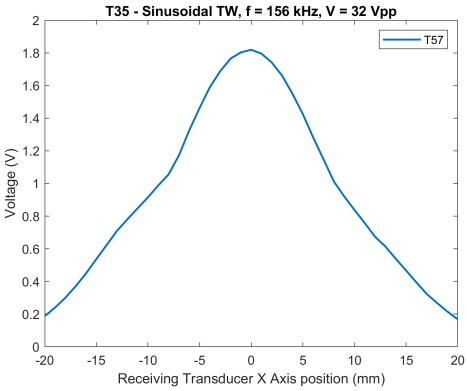

(b) Transducer 35, F = 156 kHz.

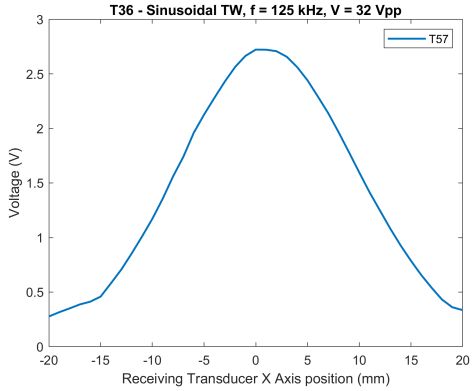

(c) Transducer 36, F = 125 kHz.

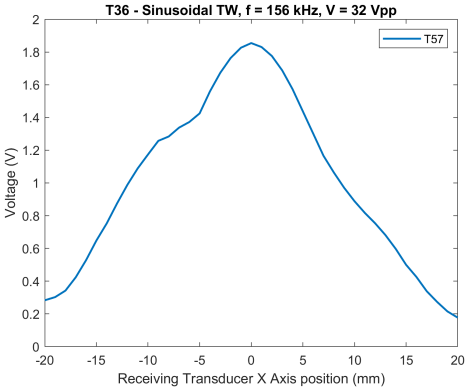

(d) Transducer 36, F = 156 kHz.

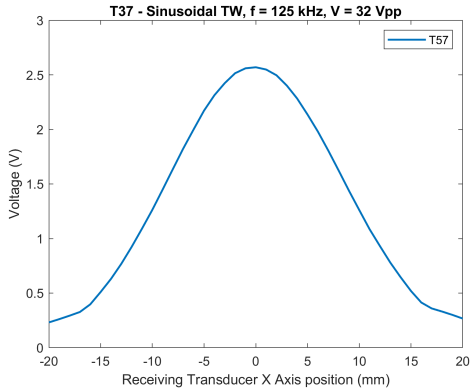

(e) Transducer 37, F = 125 kHz.

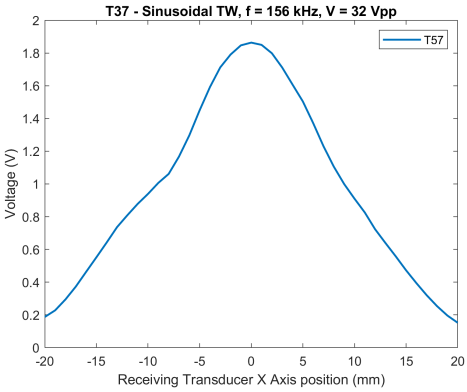

(f) Transducer 37, F = 156 kHz.

Figure G.4: Received voltage profiles of transducers 35, 36, and 37 when transmitting a sinusoidal signal.

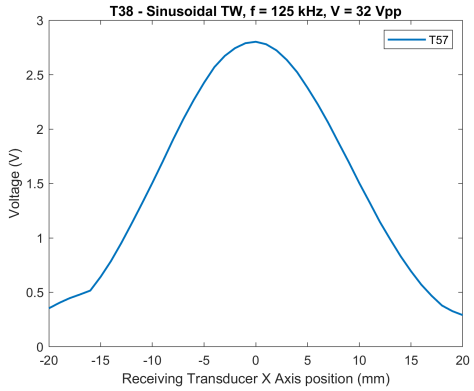

(a) Transducer 38, F = 125 kHz.

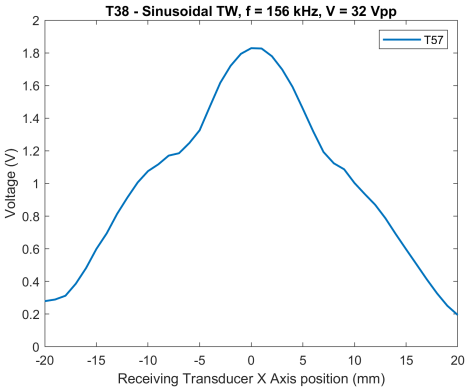

(b) Transducer 38, F = 156 kHz.

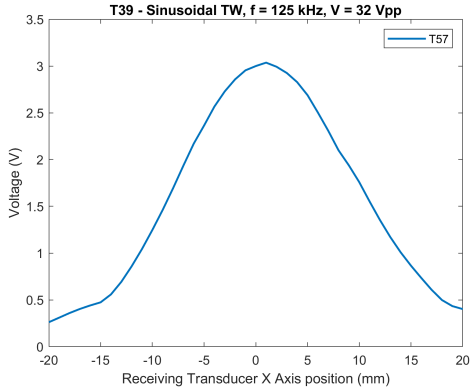

(c) Transducer 39, F = 125 kHz.

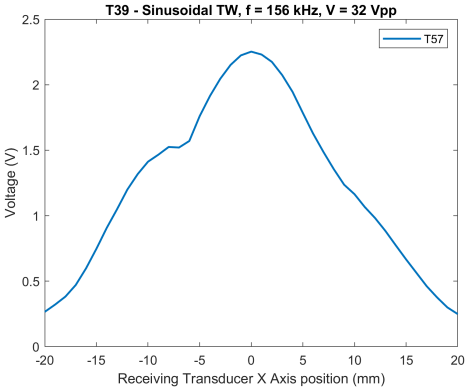

(d) Transducer 39, F = 156 kHz.

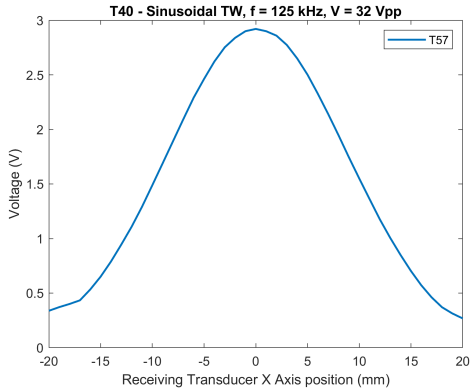

(e) Transducer 40, F = 125 kHz.

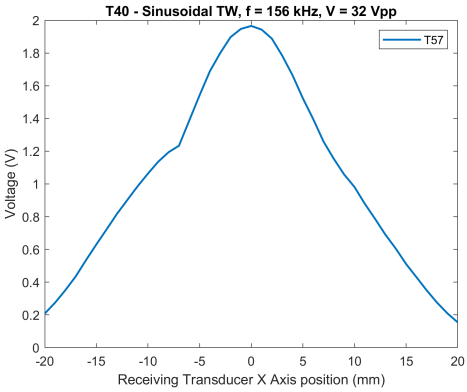

(f) Transducer 40, F = 156 kHz.

Figure G.5: Received voltage profiles of transducers 38, 39, and 40 when transmitting a sinusoidal signal.

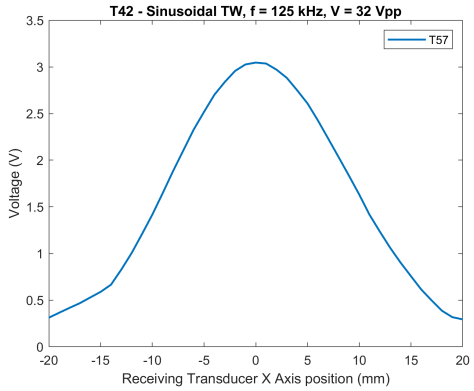

(a) Transducer 42, F = 125 kHz.

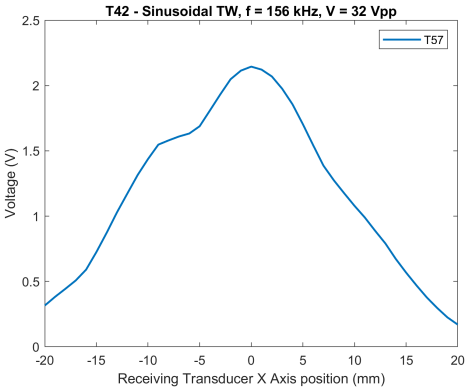

(b) Transducer 42, F = 156 kHz.

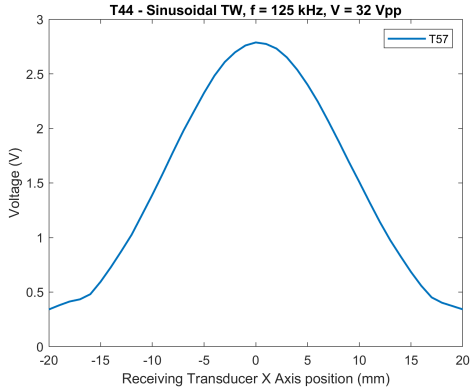

(c) Transducer 44, F = 125 kHz.

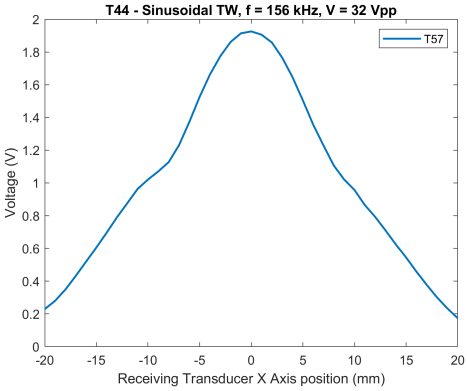

(d) Transducer 44, F = 156 kHz.

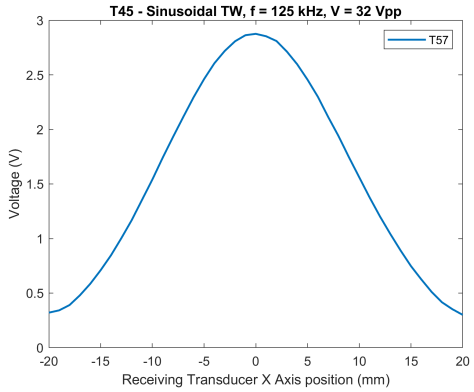

(e) Transducer 45, F = 125 kHz.

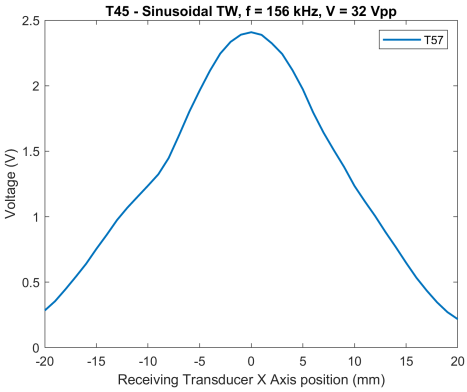

(f) Transducer 45, F = 156 kHz.

Figure G.6: Received voltage profiles of transducers 42, 44, and 45 when transmitting a sinusoidal signal.

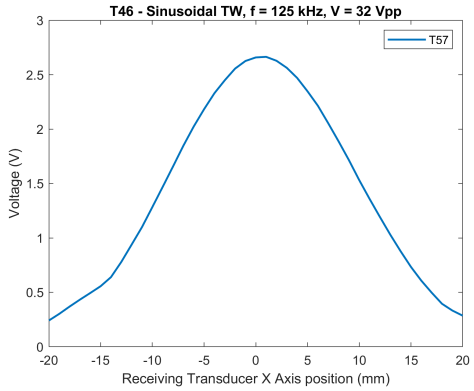

(a) Transducer 46, F = 125 kHz.

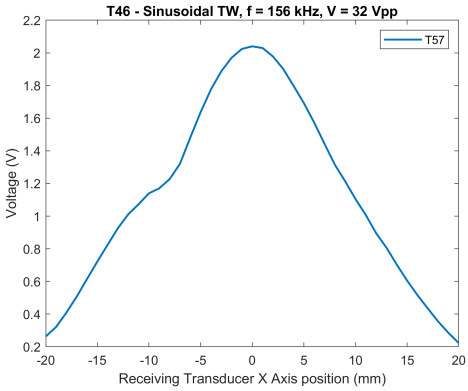

(b) Transducer 46, F = 156 kHz.

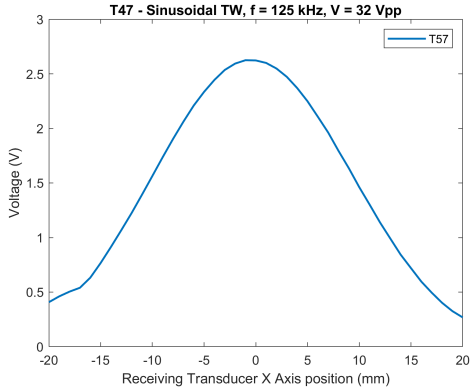

(c) Transducer 47, F = 125 kHz.

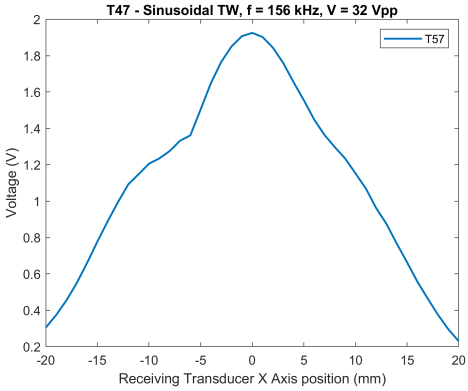

(d) Transducer 47, F = 156 kHz.

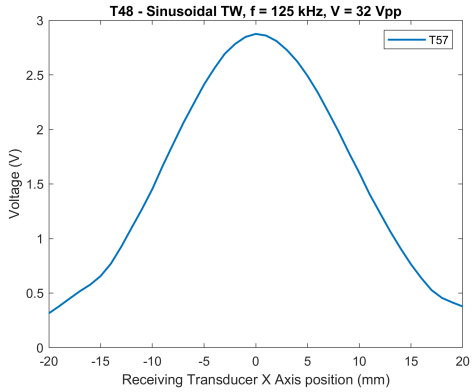

(e) Transducer 48, F = 125 kHz.

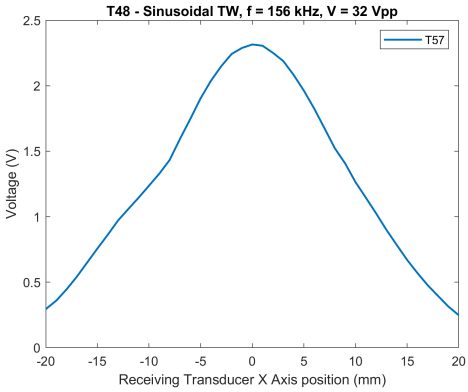

(f) Transducer 48, F = 156 kHz.

Figure G.7: Received voltage profiles of transducers 46, 47, and 48 when transmitting a sinusoidal signal.

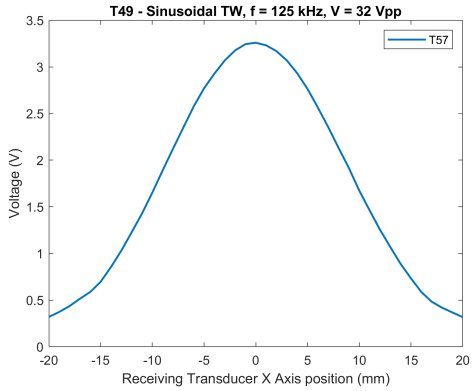

(a) Transducer 49, F = 125 kHz.

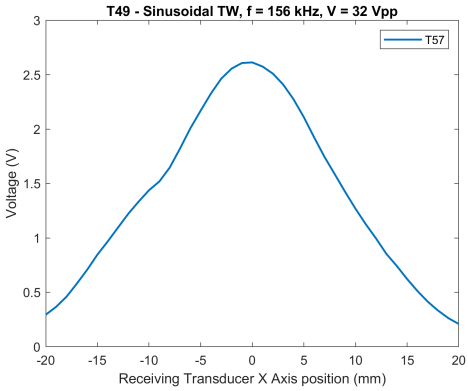

(b) Transducer 49, F = 156 kHz.

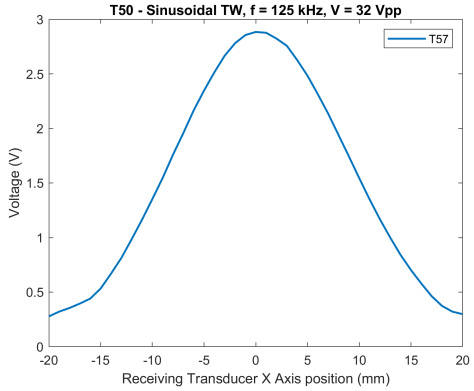

(c) Transducer 50, F = 125 kHz.

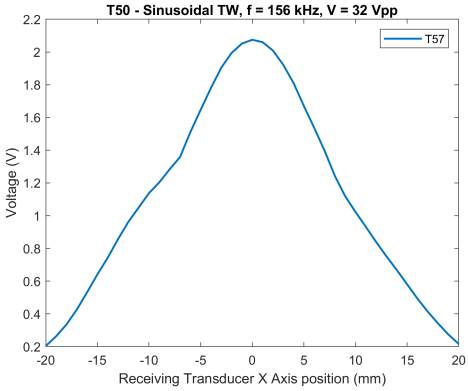

(d) Transducer 50, F = 156 kHz.

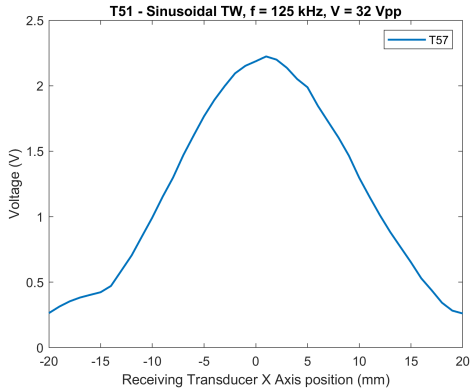

(e) Transducer 51, F = 125 kHz.

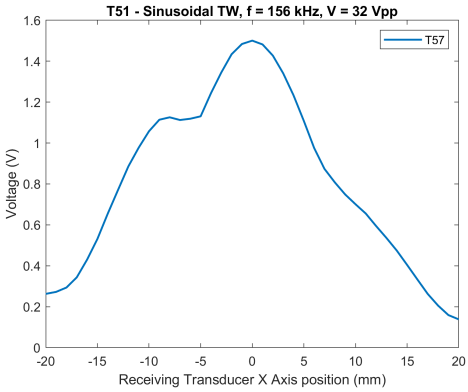

(f) Transducer 51, F = 156 kHz.

Figure G.8: Received voltage profiles of transducers 49, 50, and 51 when transmitting a sinusoidal signal.

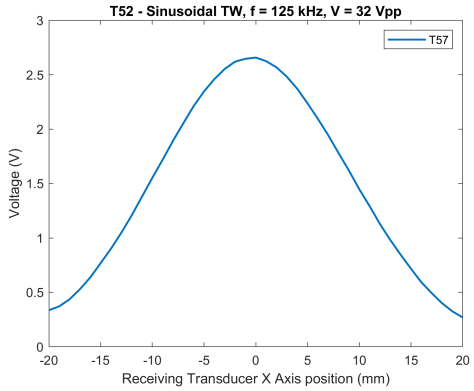

(a) Transducer 52, F = 125 kHz.

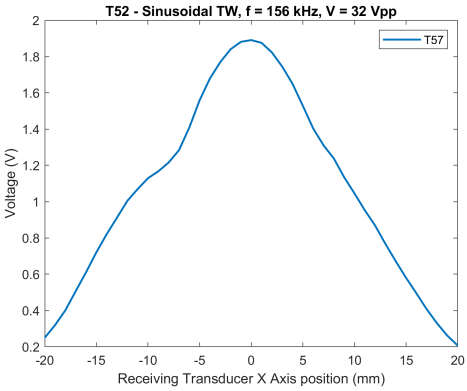

(b) Transducer 52, F = 156 kHz.

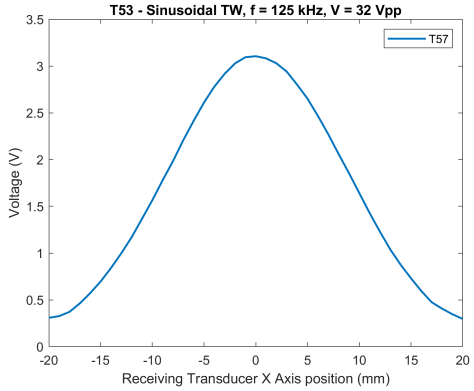

(c) Transducer 53, F = 125 kHz.

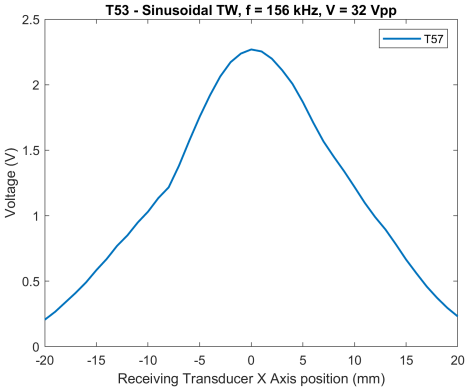

(d) Transducer 53, F = 156 kHz.

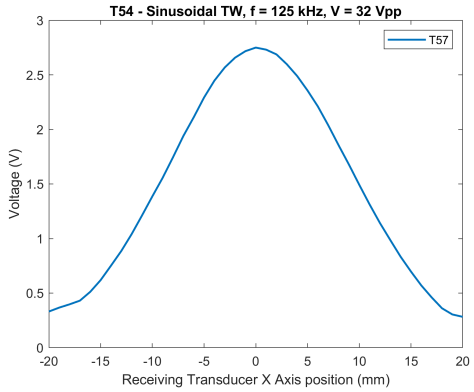

(e) Transducer 54, F = 125 kHz.

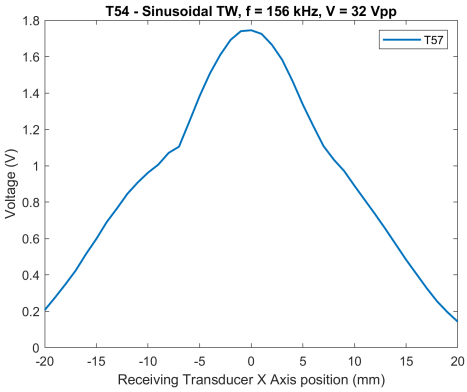

(f) Transducer 54, F = 156 kHz.

Figure G.9: Received voltage profiles of transducers 52, 53, and 54 when transmitting a sinusoidal signal.

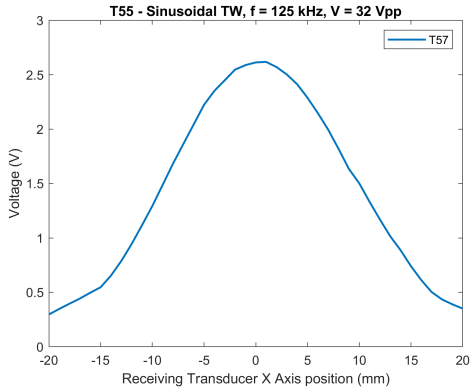

(a) Transducer 55, F = 125 kHz.

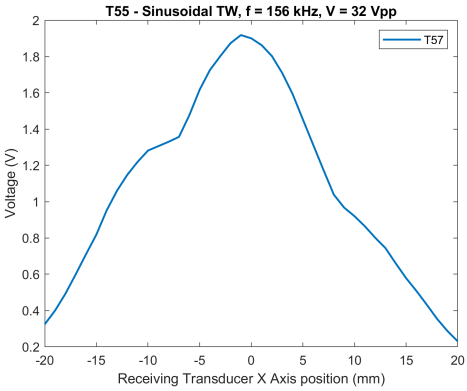

(b) Transducer 55, F = 156 kHz.

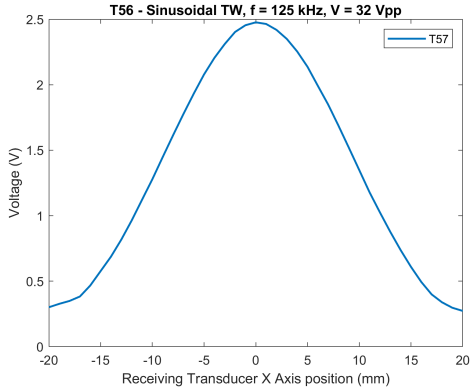

(c) Transducer 56, F = 125 kHz.

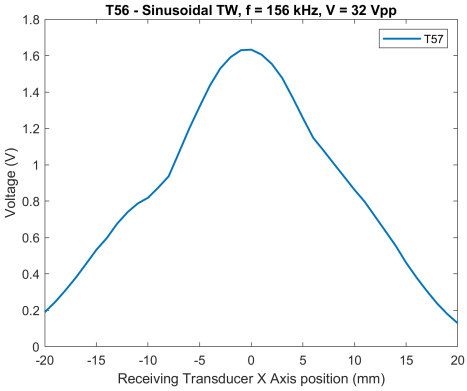

(d) Transducer 56, F = 156 kHz.

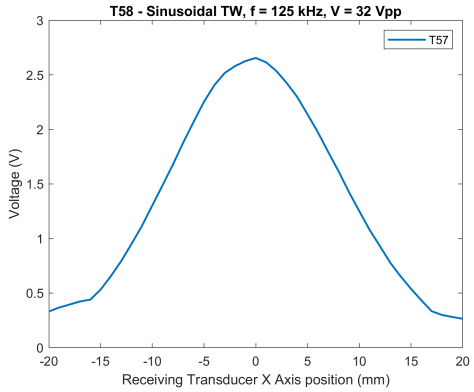

(e) Transducer 58, F = 125 kHz.

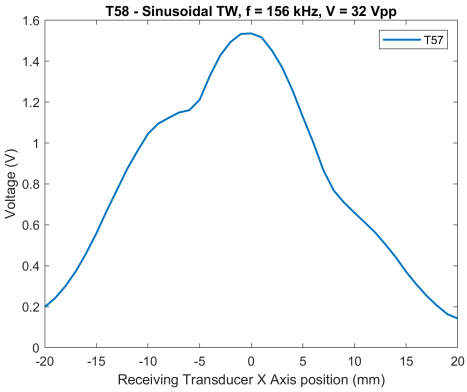

(f) Transducer 58, F = 156 kHz.

Figure G.10: Received voltage profiles of transducers 55, 56, and 58 when transmitting a sinusoidal signal.

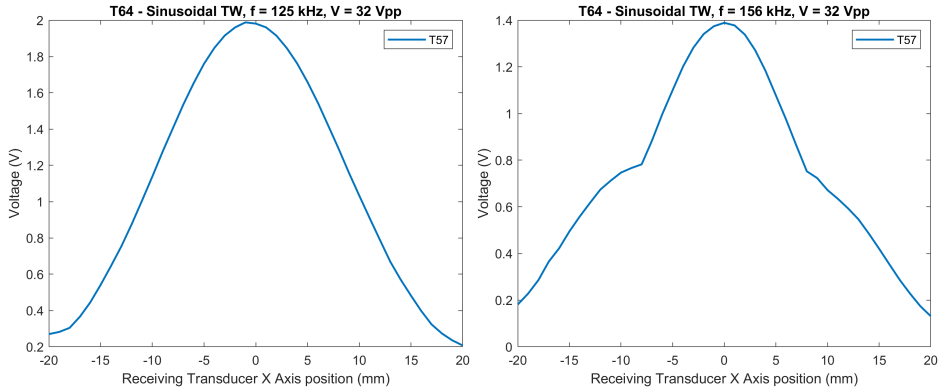

(a) Transducer 64, F = 125 kHz.

(b) Transducer 64, F = 156 kHz.

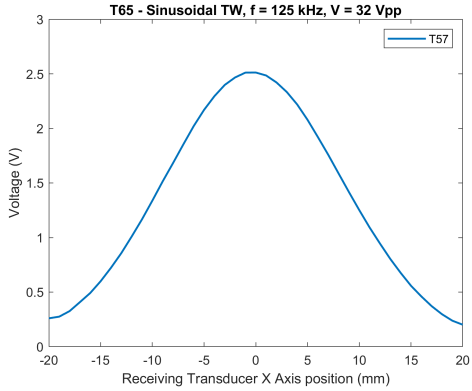

(c) Transducer 65, F = 125 kHz.

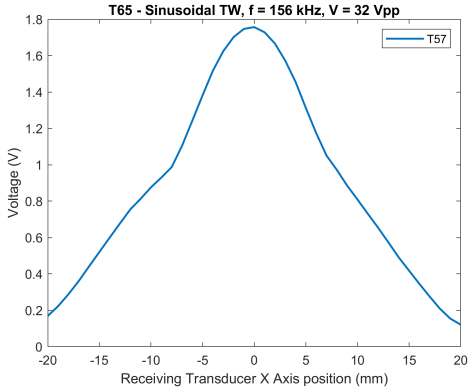

(d) Transducer 65, F = 156 kHz.

Figure G.11: Received voltage profiles of transducers 64 and 65 when transmitting a sinusoidal signal.